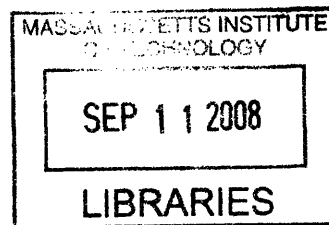


Addition and Recombination Reactions of Unsaturated Radicals Using a Novel Laser Kinetics Spectrometer

by

Huzeifa Ismail
B.A./M.S., Chemistry
Brandeis University



Submitted to the Department of Chemistry
in partial fulfillment of the requirements for the degree of

Doctor of Philosophy

at the

MASSACHUSETTS INSTITUTE OF TECHNOLOGY

June 2008

© Massachusetts Institute of Technology 2008. All rights reserved.

Author.....
Department of Chemistry
June 26, 2008

Certified by.....
William H. Green
Department of Chemical Engineering
Thesis Supervisor

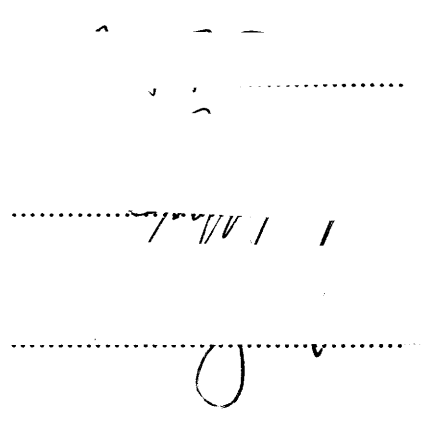
Accepted by.....
Robert W. Field
Chairman, Department Committee on Graduate Students

This doctoral thesis has been examined by a committee of the Department of Chemistry that included

Professor Robert W. Field
(Chairperson)

Professor Jeffrey I. Steinfeld

Professor William H. Green
(Thesis Supervisor)



The image shows faint handwritten signatures and dotted lines corresponding to the names of the committee members. The first signature is partially visible above the first name. The second signature is written over the dotted line for Professor Jeffrey I. Steinfeld. The third signature is written over the dotted line for Professor William H. Green.

In dedication to my Aqa Moula (TUS)

Addition and Recombination Reactions of Unsaturated Radicals Using a Novel Laser Kinetics Spectrometer

by

Huzeifa Ismail

Submitted to the Department of Chemistry
on June 30, 2008 in partial fulfillment of the
requirements for the degree of
Doctor of Philosophy in Physical Chemistry

Abstract

This thesis describes the construction of a novel, low-noise laser kinetics spectrometer. A quasi-CW (picosecond pulse), tunable Ti:Sapphire laser is used to detect various transient species in laser flash photolysis kinetics experiments via direct absorption. The spectral range of the laser, when used with a harmonic generator, covers most of the visible wavelength region, allowing for the detection of a wide array of organic radical species. Paired with a temperature-and pressure-controlled flow reactor equipped with a Herriott-type optical multiple pass cell, transient absorptions of ~ 0.0001 can be measured, corresponding to cross section - concentration products of less than $1 \times 10^{-7} \text{ cm}^{-1}$. The flexibility and high sensitivity of this instrument allows direct and accurate measurement of many important transient intermediates in combustion and atmospheric chemistry.

Using this instrument, we report the self-reaction rate coefficient of vinyl and allyl radicals. Vinyl iodide and allyl iodide are used as precursors to generate respective radicals via laser-flash photolysis at 266 nm. Second order chemical reactions require an accurate determination of the initial radical concentration, which we determined using direct laser absorption by I atom at 1315 nm. The current study finds the self-reaction rate constant for vinyl radical to be more than a factor of two slower than previous studies and allyl self reaction rate constant to be 50% faster than values reported in the literature. The absorption cross sections of the vinyl radical at 404, 423.2, & 445 nm and allyl radical at 404 & 408 nm are also determined. This thesis also reports measurements of rate coefficients for the reaction of vinyl radical with various alkenes: ethylene, propene, isobutene, 1-butene, and 2-butene, performed over a temperature range of 300 K to 700 K at 100 Torr. The measured vinyl radical disappearance rates compare well with *ab initio* quantum calculations. The combined measurements and calculations provide improved estimates for other vinyl + alkene reactions.

Thesis Supervisor: William H. Green
Title: Professor of Chemical Engineering

Acknowledgements

Upon completion of the thesis, I would like express my sincere gratitude to several people. This project has been a roller coaster ride of sorts, and without the steadfast help of the following brilliant people, I would not have seen the light at the end of the tunnel.

First and foremost, I would like to thank my mentor Professor Bill Green. Bill showed a lot of faith in me by entrusting me with a great deal of responsibility and intellectual freedom during the course of my Ph.D. which included letting me manage the construction of the new Combustion Dynamic Laboratory and allowing me build the entire version 1 & version 2 of the Laser Kinetics Spectrometer (LKS). I will always remember him for his infallible optimism, which was greatly needed during my time here. In the Green Group, I would like to thank several people: Bryan M. Wong who taught me everything I know today about pressure dependence and quantum chemistry; James W. Taylor, who trained me for all the initial experimental capabilities in the Green Group and helped me construct version one of the LKS; C. Franklin Goldsmith, who conducted all the theoretical calculations for the vinyl + alkenes chemical system to help us understand our experimental data; and lastly my UROP, Paul Abel, whose assistance was imperative during the construction of Combustion Dynamic Laboratory and version 2 of the instrument. Paul also was the main reason we were able automate the LKS.

Secondly, I would like to acknowledge Professor Bob Field and many members of his Group. Bob has also been a great mentor to me at MIT. Not only did he provide me with technical assistance for various experiments I conducted at MIT, but his support always kept me focused. I faced some very difficult situations at MIT and thought about quitting the Ph.D. program, but it was Bob who provided a great deal of encouragement for me to stay. Additionally, I have borrowed endless pieces of equipment from the Field Group including (an excimer laser, YAG lasers, chemicals, and optics). In the Field Group, I would like to thank several former and current members including: Dr. Hans Bechtel for helping me setup and align the photolysis laser; Dr. Jeff Kay

for assisting on the alignment of the Ti-Sapphire probe laser; and Adam Steeves who helped in various aspects in the design and construction of the LKS and proofread all my presentations and papers. I will also treasure that Adam and Jeff's friendship that I have had for last six years at MIT.

In summer of 2005, after the failure of the version 1 of the LKS, I was fortunate enough to be able to go for a research internship at Sandia National Laboratories. There, I got a chance to work with Dr. Craig A. Taatjes and Leonard Jusinski. At Sandia, not only was I able to work on couple of very interesting chemical systems, but more importantly, I learned exactly why the version 1 of my instrument failed. Additionally, it was Craig and Len who introduced me to the vinyl chemical system, which has become the staple for our lab and this thesis.

Of course, I also want to thank my wife Ummehani, for the love and support she has given me for last four years. Recently, my wife gave birth to our beautiful daughter Sakina, and for that as well, I thank her.

Lastly, but most importantly, I would like to thank my parents. They sacrificed a great deal to move to United States. Due to the political instability and lack of educational opportunities in Pakistan, my father felt that he must make the leap to move to the United States and settle his family down. He gave up a lucrative business and professional career in Pakistan to come here and take up a sub-par job. When financially things became difficult, my mother worked sixteen hour days, just to break even. My parents were willing to bear all these hardships, because they truly believed in the value of a good education for their children. Their efforts have paid off, as I have taken full advantage of their hard work.

To have the means to attend a prestigious institution, and to have the chance to obtain the highest degree it can offer, is a testament for what they set out to achieve. Therefore, I would like to take this moment to thank my parents and sincerely acknowledge them. For without them, I would not be here.

Huzeifa Ismail, Ph.D., Physical Chemistry

Table of Contents

Approval Page.....	ii
Acknowledgements	vii
Table of Contents.....	x
List of Tables	xii
List of Figures and Illustrations	xiv
1. Introduction	1
2. Gas Phase Cyclohexadienyl Experiments	7
2.1. Motivation	7
2.2. Introduction.....	8
2.3. Experimental setup.....	12
2.4. Results	17
2.5. Discussion	20
2.5.1. Thermal lensing	21
2.5.2. Limitation of the instrument	24
2.5.2.1. Laser noise	24
2.5.2.2. Bubbler over flow.....	26
2.5.2.3. Manual control.....	28
2.5.2.4. Digitization error.....	29
2.5.3. Problems in chemical system	30
2.6. Conclusions.....	31
3. Multipass Laser Kinetics Spectrometer	33
3.1. Introduction.....	33
3.2. Chemical systems.....	34
3.3. Herriott cell	39
3.4. Ti-Sapphire probe laser	45
3.4.1. Noise reduction	48
3.5. Photolysis laser.....	50
3.6. Flow cell design and vacuum system.....	51
3.7. Flow & pressure control	53
3.8. Temperature control system.....	57
3.9. Automation & acquisition	60
3.10. Validation	62
4. Self Reaction of Vinyl Radical.....	63
4.1. Introduction.....	63
4.2. Experimental details.....	64
4.3. Results	76
4.3.1. I* quenching and Φ_{I^*} (C_2H_3I) determination	76
4.3.1.1. Method #1:.....	76
4.3.1.2. Method #2:.....	79
4.3.1.3. Method #3:.....	80
4.3.2. Vinyl radical self reaction rate constant (k_1)	81
4.3.3. Vinyl radical spectrum & visible cross section.....	84
4.4. Discussion	88
4.5. Conclusion	90

5.	Self reaction of allyl radical	91
5.1.	Introduction.....	91
5.2.	Experimental details.....	93
5.3.	Results.....	96
5.3.1.	Φ_{1*} (C_3H_5I) determination	96
5.3.2.	Allyl radical self reaction rate constant (k_4)	101
5.3.3.	Allyl visible spectrum and cross section (σ).....	104
5.4.	Discussion	109
5.5.	Conclusion	114
6.	Reaction of vinyl radical with various alkenes	116
6.1.	Introduction.....	116
6.2.	Experimental details.....	120
6.3.	Theoretical calculations	131
6.3.1.	<i>Ab initio</i> calculations	131
6.3.2.	Pressure dependence calculations.....	132
6.3.3.	End product studies in RMG.....	133
6.4.	Results.....	135
6.4.1.	Vinyl + ethylene.....	135
6.4.1.1.	Kinetic study.....	135
6.4.1.2.	Comparison to previous studies	138
6.4.1.3.	Modeling of product studies using RMG	142
6.4.2.	Vinyl + propene.....	148
6.4.3.	Vinyl + butenes.....	150
6.5.	Discussion	155
6.6.	Conclusion	156
7.	Ongoing & Future Chemical Systems.....	158
7.1.	Vinyl + O_2	158
7.1.1.	Introduction	158
7.1.2.	Experimental details	162
7.1.3.	Results	165
7.1.3.1.	Spectrum.....	165
7.1.3.2.	Kinetic study (k_{10}).....	169
7.1.4.	Conclusions and future work.....	175
7.2.	Allyl + O_2	177
7.2.1.	Introduction	177
7.2.2.	Experimental details	179
7.2.3.	Results	179
7.2.3.1.	Spectrum.....	179
7.2.3.2.	Kinetic study (k_{11}).....	185
7.2.4.	Conclusions and future work.....	187
7.3.	IO & OIO	188
7.4.	Benzyl & Phenoxy Radical.....	192
	References	198

List of Tables

Table 3.1: Radical chemical systems that can be studied using the laser kinetics spectrometer	35
Table 3.2: Inventory of Herriott mirrors	42
Table 3.3: Number of passes vs. temperature.....	43
Table 3.4: Comparison of Xenon Arc lamp and Ti:Sapphire Laser.....	44
Table 3.5: Pump laser power requirement at different Ti:Sapphire wavelengths	47
Table 3.6: Various lenses to expand the photolysis beams.....	50
Table 4.1: Experimental conditions for self reaction of vinyl radical	70
Table 4.2: Determination of k_1 using various methods to determine $[C_2H_3]_0$	82
Table 4.3: Comparison of self reaction rate of vinyl radical from literature and from the current study	89
Table 5.1: Experimental conditions for the self reaction of allyl radical at 20 Torr.	95
Table 5.2: k_4 determination using various methods to determine $[C_3H_5]_0$	101
Table 5.3: Temperature dependence of $\sigma_{C_3H_5}$ at 408 nm and at 20 Torr.....	108
Table 5.4: Comparison of allyl radical self-reaction rate constants with previous literature	111
Table 6.1: Conditions and results for experiments to measure k_5	125
Table 6.2: Conditions and results for experiments to measure k_6	126
Table 6.3: Conditions and results for experiments to measure k_7 for 1-butene.	128
Table 6.4: Conditions and results for experiments to measure k_8 for 2-butene.	129
Table 6.5: Conditions and results for experiments to measure k_9 for isobutene.....	130
Table 6.6: Comparison of Vinyl + Ethylene (k_5) rate constants from literature and from the current study.....	137
Table 7.1: Conditions and results of experiments to measure the reaction of vinyl with $O_2(k_{10})$	163

Table 7.2: Conditions and results of experiments to measure reaction of allyl with O_2	180
Table 7.3: Conditions and results of experiments to measure equilibrium constants for $C_3H_5 + O_2 \leftrightarrow C_3H_5OO^a$	181

List of Figures and Illustrations

Figure 2.1: A typical ring closing reaction mechanism. Cyclohexadienyl radical is a key intermediate in benzene formation.	8
Figure 2.2: Cyclohexadienyl + O ₂ forms benzene + HO ₂ via three distinct pathways. Berho <i>et al.</i> conducted experiments under relatively low [O ₂] because of apparatus limitations. They never observed the equilibrium reactions k ₀ A and k ₀ B. Berho ²⁴ proposed a different mechanism with a direct reaction (k _{direct}) and stated that k ₀ A and k ₀ B have significant barriers therefore equilibrium reaction is not observed. Radical additions to O ₂ , in general, do not have significant barriers. In the present study, the experiments are conducted at higher [O ₂] to determine the equilibrium coefficient k ₀ A and k ₀ B.	11
Figure 2.3: Experimental Setup of the version 1 of the laser kinetics spectrometer.	12
Figure 2.4: Diagram of flow distribution system in the version 1 of the laser kinetics spectrometer. Sierra and MKS flow controllers are used to control the gas flows. Check-valves are placed between the bubblers and flow controllers to prevent back flow.	14
Figure 2.5: Recorded transient signal 248 nm photolysis of C ₆ H ₈ /DTBP/Ar mixture at room temperature and 380 Torr of total pressure. [C ₆ H ₈] = 4 × 10 ¹⁸ molecules cm ⁻¹ and [DTBP]=1 × 10 ¹⁸ molecules cm ⁻¹	18
Figure 2.6: Pseudo-first-order plot of experimental absorption with respect to [O ₂] at a temperature of 298 K and a pressure of 380 Torr.	19
Figure 2.7: a) Thermal lensing signal at microsecond time scale. The characteristic oscillating acoustic spikes had periodicity of 250 μs. The transient signal increases after photolysis laser. b) Thermal lensing signal at millisecond time scale, which resembles a transient absorption signal.	22
Figure 2.8: Screen shot of the digital oscilloscope, showing the line synchronous noise. Noise measured out of Spectra Physics Millennia Xs at 5 ms/div (a) and 200 us/div (b). There is a sinusoidal and sharp 'spiky' component to the noise which is synchronous to the line frequency (60Hz). Both traces were taken at 2 mV/div in the vertical axis.	25
Figure 2.9: Pump laser noise spectrum comparing Spectra Physics Millennia and Coherent Verdi. This was provided to us by Prof. Franz X. Kärtner from Research Laboratory of Electronics at MIT.	27
Figure 2.10: Transient signal with digitization error in Agilent/HP digital oscilloscope	30

Figure 3.1. The Herriott multi-pass resonator is shown with incorporation of an on-axis pump laser. Changing the diameter of the pump laser changes the overlap with the probe laser. L is the distance between the two mirrors.	38
Figure 3.2: Diagram of the optical setup to correct for the astigmatism in the probe beam and mode-match the Herriott resonator. A total of four cylindrical lenses are used to correct horizontal (H) and vertical (V) astigmatism separately in the probe beam. A mode-matching lens with long focal length (>500 mm) sits on a translation stage. The focal length of the lens and physical location of the lens should be adjusted to ensure the beam is mode-matched in such a way that it is focusing when it exits the cavity.	41
Figure 3.3: Diagram of the probe laser setup.	46
Figure 3.4: a) Characteristic noise of just the probe laser in time domain. b) noise of the signal after reference beam was subtracted using a differential amplifier. c) Power spectrum of probe laser without (blue) and with differential amplifier (red). Time domain traces were taken after 500 averages. Frequency domain were acquired after 2000 averages.	49
Figure 3.5: Diagram of flow-cell	52
Figure 3.6: Diagram of the flow control system.	54
Figure 3.7: Diagram of the bubbler setup.	56
Figure 3.8: Diagram of the temperature control system.....	57
Figure 3.9: Temperature profile along the longitudinal axis of the flow cell under experimental conditions of 100 Torr and 3000 sccm of He flow. The temperature profile is taken with a thermocouple vacuum feed-through, which can be translated in the longitudinal axial direction using Cajon [®] fitting. The ISO-100 to 1/4 inch Cajon [®] coupler is attached to one of the six-way crosses. The temperature probe is translated every 1 inch to acquire this Figure.....	59
Figure 3.10: Instrumental control software written in LabView.	61
Figure 3.11: The red trace is on resonance of C ₂ H ₃ at 423.2 nm. The blue trace is off resonance taken at 418.0 nm. The inset shows a section of the vinyl radical absorption spectrum as reported by Shahu et al., ⁶⁰ with the probe wavelengths of the two traces shown by vertical arrows.....	62
Figure 4.1: Diagram of experimental apparatus with I-atom probe laser.....	65
Figure 4.2: Transient absorption signal for I atom at 1315.14 nm upon photolysis of vinyl iodide at 266 nm. A prompt decay is observed on the 1315.14 nm probe laser. The I(² P _{1/2}) atoms are quenched on a short time scale to yield ground state iodine atoms with a unit efficiency. I(² P _{3/2}) population is solely removed via diffusion and recombination processes.	

O ₂ (a) and ethylene (b) induced decay (S _i) and the total absorption (S _f) are obtained via back extrapolated based on single exponential fit (--).....	69
Figure 4.3: Transient absorption signal for vinyl radical. The second order fit to the decay is shown as a red line, with the corresponding residuals shown on top.	75
Figure 4.4: Pseudo-first-order I* quenching rate k' vs. [O ₂] at a temperature of 293 K and a pressure of 20 Torr.....	77
Figure 4.5: I traces with [O ₂] higher then 1%.....	78
Figure 4.6: Pseudo-first-order plot of I* quenching rate k' vs. [C ₂ H ₄] at a temperature of 293 K and a pressure of 20 Torr	79
Figure 4.7: Measured rate constant for the self reaction of vinyl radical at various initial vinyl concentrations. The error bar on each data point is based on propagated error.	83
Figure 4.8: Low resolution spectrum attained in the present study for vinyl radical and it is compared to high resolution spectrum by Shahu <i>et al.</i> ⁸⁰ .	85
Figure 4.9: Plots of the absorption cross sections at 404nm (a), 423.2nm (b), and 445nm (c) for the vinyl radical as a function of initial vinyl concentration. The error bars are based on propagated error.	86
Figure 5.1: Transient absorption signal for allyl radical. The second order fit to the decay is shown as a red line, with the corresponding residuals shown on top.	97
Figure 5.2: Transient absorption signal for I atom at 1315.14 nm upon photolysis of allyl iodide at 266 nm. All the traces were taken at room temperature, 100 Torr of total pressure, [C ₃ H ₅ I] ≈ 4 × 10 ¹⁵ molecules/cm ³ , and [C ₃ H ₅] = 1.7 × 10 ¹³ molecules/cm ³ . A prompt gain is observed on the 1315.14 nm probe laser. The I(² P _{1/2}) atoms are quenched on a short time scale to yield ground state iodine atoms. I(² P _{3/2}) population is removed via diffusion slowly and recombination processes. The signals S _i and S _f are obtained via extrapolating to t=0 based on single exponential fit (--).....	99
Figure 5.3: Branching ratio (Φ _{I*}) for Allyl Iodide at 266 nm at various oxygen concentrations.	100
Figure 5.4: Measured rate constant for the self reaction of allyl radical at various initial allyl concentrations. The error bars on each data point are based on propagated error.	102
Figure 5.5: Temperature dependence of the allyl self reaction rate constant (k ₁). Solid circles: experimental results of the current study at 20 Torr. The error bars on each experimental data point is based on propagated error. Solid line is the Arrhenius fit for the present data (solid circles); Dotted line is the result from Klippenstein <i>et al.</i> Number sign (#)	

measured by van den Bergh & Callear. Dashed line and cross (×) are the results reported by Tulloch <i>et al.</i> , using our estimate of the propagated uncertainty. Plus (+) are results from Boyd <i>et al.</i> and star (*) is rate reported by Jenkin <i>et al.</i> at room temperature.	103
Figure 5.6: Low resolution spectrum acquired in the present study for allyl radical and it is compared to high resolution spectrum by Tonokura <i>et al.</i> ³⁰	105
Figure 5.7: Plots of the absorption cross sections at 404nm (a) and 407.5nm (b) for the allyl radical as a function of initial allyl concentration. The error bars are based on propagated error.	107
Figure 6.1: Observed decay rate (k') of vinyl + ethylene, measured at various repetition rates of the photolysis laser. The k' fluctuated by only 3% and produced no systematic changes.	123
Figure 6.2: Recorded decay of C_2H_3 at 700 K and 100 Torr for the conditions $[C_3H_6] = 0$ molecules cm^{-1} (triangles), $[C_3H_6] = 2.2 \times 10^{16}$ molecules cm^{-1} (squares) and $[C_3H_6] = 1.4 \times 10^{17}$ molecules cm^{-1} (circles). Every 150th point is shown for clarity. b) Pseudo-first-order C_2H_3 decay rate k' vs. $[C_3H_6]$, at 700 K and 100 Torr.	124
Figure 6.3: A simplified reaction scheme for the vinyl + alkene reaction system. $k_{5,9} = k_a + k_b + k_c$	131
Figure 6.4: Temperature dependence of the total rate constant of the reaction of vinyl with ethylene. Open circles: experimental results of the current study at 100 Torr; filled circles: experimental results of the current study at 15 Torr; open squares: results reported by Shestov <i>et al.</i> ¹¹⁸ Dotted line is the Arrhenius fits for high pressure data set for present study. Master equation calculations for 15 Torr (dashed line) and 100 Torr (solid line) are shown.	136
Figure 6.5: Master equation predictions for the product branching of the reaction between vinyl radical and ethylene at 15 Torr and 100 Torr.	141
Figure 6.6: Experimental and RMG predicted yield of 1-butene versus total pressure.	143
Figure 6.7: Experimental and RMG predicted yield of 1,3-butadiene versus total pressure.	143
Figure 6.8: Experimental and RMG predicted yield of 1,5-hexadiene versus total pressure.	144
Figure 6.9: Experimental and RMG predicted yield of 1,7-Octadiene versus total pressure.	144
Figure 6.10: Temperature dependence of the total rate constant of the reaction of vinyl with propene. Filled circles: experimental results for 100 Torr; Open circles: experimental results for 15 Torr; open triangles: experimental results for 25 Torr. The dotted line is the Arrhenius fits	

(100 Torr) for the present data sets, and master equation calculations (100 Torr) are shown as the solid line.....	149
Figure 6.11: Temperature dependence of the total rate constant of the reaction of vinyl with various butene. Experimental results of the current study at 100 Torr; Open triangle: 1-butene; open circle: 2-butene; open square: isobutene; Dotted lines are the 2 parameter Arrhenius fits for each data sets. Master equation calculations (100 Torr) are shown as the solid line.....	152
Figure 6.12: a) Low resolution spectrum of the background signal for vinyl + isobutene system taken at 700 K and 100 Torr. The background signal is attributed to 2-methyl-allyl radical b) Transient absorption of the background signal. The spectrum is taken at 0.8 ms. The background signal lasts for ~5 ms, before returning to baseline.....	153
Figure 7.1. a) Recorded decay of C_2H_3 at 675 K and 10 Torr at various $[O_2]$. At high $[O_2]$, red and the green trace, the interference from the background signal is significant. b) A vinyl off-resonance trace was acquired at 426.2 nm and subtracted from the on-resonance signal and the resultant trace is fitted to a single exponential.	166
Figure 7.2. a) Low resolution spectrum recorded in the present study of photo-products of $C_2H_3I/He/O_2$ mixture after 266 nm photolysis (red trace) at 298 K and 5 Torr. It is compared to high resolution spectrum of Spietz <i>et al.</i> (grey trace). b) Spietz's spectrum is subtracted from the spectrum in the present study (blue trace), which yields a diffuse band from 400 to 432 nm.	168
Figure 7.3. Temperature dependence of the total rate constant of the reaction of vinyl with O_2 . Solid markers are experimental results of the current study at various pressures; The line markers are experimental results from various previous studies; Dotted lines are theoretical results from previous studies.....	170
Figure 7.4. Transient absorption of allyl radical at three different temperatures; data are offset for clarity. All three traces are taken at 20 Torr total pressure and $[O_2] = 1.8 \times 10^{15}$ molecules cm^{-3} . At 300 K (circle) the decay is fitted to simple exponential. At 400 K (triangle), equilibrium is established between $C_3H_5 + O_2 \leftrightarrow C_3H_5OO$, therefore, a biexponential model is fitted to the ally decay. At 500 K (square), the decay reverts to a second order decay, corresponding to allyl reacting with itself or I atoms. Oxygen has little effect on the decay of allyl radical at 500 K.....	182
Figure 7.5. a) Low resolution spectrum for $C_3H_5I/He/O_2$ mixture after 266 nm photolysis (blue trace) at 300 K, 20 Torr, and $[O_2] = 3.0 \times 10^{15}$ molecules cm^{-3} . Three different transient species are thought to be convoluted in the spectrum. b) From 400-410 nm, the initial fast spike is due to absorption from allyl radical. The slow background signal is due to absorption unknown species. c) The absorption from the unknown species, which we believe is from C_3H_5OO isomers, ends at ~440 nm. The	

rise time for the unknown species is 0.6 ms under our experimental conditions. d) From 440-490 nm, the absorption is due to OIO radical and rise this is species changes to 1.5 ms. Our spectrum for OIO compares well with the high resolution spectrum of Spietz *et al.* (grey trace).184

Figure 7.6. A van't Hoff plot of the measured equilibrium constants (K_p) for $C_3H_5 + O_2 \leftrightarrow C_3H_5OO$. The experimental data (O) were taken at various oxygen concentrations. The straight line through the data points was obtained by a least squares fit to determine the thermodynamic parameters for the equilibrium reaction. The slope of this line is $\Delta H^0/R$ and the y-intercept is $\Delta S^0/R$186

Figure 7.7: a) Low resolution spectrum recorded in the present study of photoproducts of $C_6H_5C_2H_2Cl/He$ mixture after 266 nm photolysis (circle) at 300 K and 20 Torr. Inserts are transient absorption signals at different wavelengths.194

Figure 7.8: Low resolution spectrum recorded in the present study of photoproducts of $C_6H_5OCH_3/He$ mixture after 266 nm photolysis at 300 K and 20 Torr (square). High resolution spectrum of Tonokura and Koshi (grey traces) compare well with the present study.195

Chapter 1

1. Introduction

Many important chemical processes such as combustion, pyrolysis and oxidation of organic compounds in the atmosphere are very complex, involving hundreds to thousands of chemical reactions. The need for accurate predictive models for such chemical systems has been apparent for many decades; it is very difficult to design a new fuel or new combustion device if one cannot predict with any confidence whether or not the new system will work better than existing technology. The Green Group, using state-of-the-art thermochemical techniques (combined with quantum chemistry when applicable), have developed an open-source, extensible automatic reaction model generation (RMG) program that combines a rate-based iterative model generation algorithm¹ with the integrated pressure-dependence algorithm². Using RMG, it is now becoming possible to accurately predict combustion chemistry in detail for fuels containing molecules in the gasoline range. RMG has been used successfully in various sophisticated chemical systems, including: Steam cracking of n-hexane³, ethane pyrolysis^{4,5}, and the oxidation of neopentane fuel⁶. Though fairly robust and internally consistent, RMG simulations still yield significant prediction error, due to the complexity of the model, which usually involves more than 10^3 species and 10^4 reactions, raising a host of practical and numerical issues at many different scales.

One important problem RMG faces is that in these models, only a fraction of the rate parameters are known experimentally. Accurate estimates for all significant rate coefficients are required in order to model combustion processes. Most of the reactions in these models involve large (more than 3 carbon atoms) free radicals and have neither *ab initio* nor experimental rate coefficients available. Experimental investigations of radicals would vastly improve these large kinetic models, and also help improve the theory for estimating these reaction rates. Although the kinetics of smaller radicals such as OH⁷, NH₂⁸, and CH₃⁹ are well understood, this is not the case for larger radicals. Particularly, rate coefficients for the reactions of unsaturated free radicals have not been characterized due to various computational and experimental challenges.

The goals of my Ph.D. project were to develop, construct and implement an experimental kinetics instrument which would determine reaction rate coefficients of various large unsaturated radicals, crucial experimental information for RMG. Like RMG, such an instrument would have to be robust, fast, automated and diverse in the types of radicals it can probe.

Many obstacles hamper the investigation of the reactivity of such radicals. Their high reactivity demands fast time resolution, and because of the high reactivity their concentrations are typically very low, requiring high detection sensitivity. Some high-sensitivity techniques such as electron paramagnetic resonance (ESR) and mass spectroscopy are not suited for fast radical kinetic experiments, since the maximum rate constants that can be measured are 10^{-15} to 10^{-14} cm³ molecules⁻¹ s⁻¹. In laser flash photolysis, large concentrations of radicals are formed instantaneously, and there is enough time resolution to observe this high signal before it decays. Most other methods work

on longer timescales, so they do not see the high peak concentration of the radical formed after a sub-microsecond photolysis pulse. Slower techniques such as ESR and mass spectrometry maintain a steady-state radical concentration which can mask the relevant kinetics.

The optical spectra of large radicals are broad and lack resolvable structure to allow definitive identification. Laser-induced fluorescence (LIF) has limited applicability since many radicals with broad spectra do not fluoresce due to pre-dissociation or collisional quenching. Also, kinetic information can be masked due to internal conversion or intersystem crossing processes. Similarly, in multi-photon ionization (MPI), the intermediate excited state of the radical often pre-dissociates rapidly, resulting in low ionization yields¹⁰.

Direct absorption (via Laser-Flash Photolysis), therefore, is a much more straightforward technique to extract absolute concentrations. The problem with direct absorption is its sensitivity. In contrast to LIF and MPI, which are zero-background techniques, direct absorption always has a background due to the noise in the probe light. To improve this problem, our setup uses a very stable quasi-CW (picosecond pulse), tunable Ti:Sapphire laser as a probe source. This laser is coupled to a harmonic generator, yielding a spectral range that covers most of the visible wavelength region and allows for the detection of a wide array of organic radical species. Since the probe laser uses all solid state components, it has very low noise level. In addition, the probe beam is very stable and well collimated, allowing us to incorporate a multi-pass Herriott configuration^{11,12}.

According to Beer's Law,

$$\frac{I}{I_0} = \exp(-\sigma[C]l) \quad (1.1)$$

where I is the light intensity out of the cell, I_0 is the initial intensity, σ is the absorption cross section, $[C]$ is the concentration of the absorber, and l is the path length; the weak absorbance of a given chemical can be increased significantly by increasing the path length. Another advantage of our technique is that the entire kinetic time trace can be acquired in a single photolysis shot, which drastically reduces the effects of photolysis laser fluctuations, a major source of error in kinetics measured using the cavity ring-down technique. The combination of the low noise of the probe laser and long path length, allows us to increase the sensitivity of the instrument, make accurate peak assignments, and determine the absorption cross section at higher precision.

Chapter 2 of the thesis discusses the use of version 1 of the laser kinetics spectrometer (LKS) to probe for cyclohexadienyl radical via direct absorption in the gas phase. The design of this instrument and the cyclohexadienyl chemical system have been addressed by the theses of Leah M. Ruslen¹³ and James W. Taylor¹⁴. Therefore, a short overview of this chemical system is given to act as motivation for re-designing LKS and switching the chemical system to succeed in the LKS project.

Many problems we faced in the cyclohexadienyl experiments, we address in the design of version 2 of the LKS. The details of the design and operation procedure are described in Chapter 3. The new design of the LKS has several interesting features which include: incorporation of a Herriott cell with path lengths up to 60 meters; use of differential amplification to further reduce the probe laser noise; and automated flow, temperature (298-700K), and pressure (0-1 atm) control.

Chapters 4 and 5 describe the rate coefficient determination of the self reaction rate coefficients of vinyl and allyl radicals, respectively. Vinyl iodide

and allyl iodide are used as precursors and a 266 nm photolysis beam is used to generate the radical of interest. An added complication with the determination of second order rate coefficients is that they require an accurate determination of the initial radical concentration. This problem is addressed by determining the I atom concentration by using direct absorption at 1315 nm. Upon photolysis, since the I atoms produced from vinyl iodide and allyl iodide are produced in both the ground state ($^2P_{3/2}$) and the electronically excited state ($^2P_{1/2}$), various methods are discussed regarding how the time-dependent I traces were analyzed and the initial I atom concentrations were deduced. Lastly, the absorption cross sections of various visible absorption lines of vinyl radical and allyl radical are also reported.

Chapter 6 reports measurements of first-order rate coefficients for the reaction of vinyl radical with various alkenes: ethylene, propene, isobutene, 1-butene, and 2-butene, performed over a temperature range of 300-700 K and a pressure range of 15-100 Torr. The experimental rate coefficients were compared to theoretical Rice-Ramsperger-Kassel-Markus (RRKM) coupled with master equation (ME) pressure dependence simulations. Using these calculations, we are also able to predict various product yields in these systems. The theoretical calculations aid in understanding the differences in the rate coefficients of similar classes of reactions.

Lastly, Chapter 7 examines some ongoing and future chemical systems that can be studied using this laser kinetic spectrometer. The ongoing work includes rate constant determination of oxidation of vinyl and allyl radical by O_2 . These systems yielded some very interesting results, but the rate coefficient values were inconclusive due to interference from background chemical species.

Also, low resolution spectra of phenoxyl and benzyl radical are reported as ground work for future chemical systems.

Chapter 2

2. Gas Phase Cyclohexadienyl Experiments

2.1. Motivation

This chapter describes the cyclohexadienyl chemical system and the version 1 of the laser kinetics spectrometer which was used to probe the radical. The gas phase cyclohexadienyl experiments were studied by two former members/collaborators of this group: Leah M. Ruslen¹³ and James W. Taylor¹⁴. In both cases, these experiments were largely unsuccessful. In the present case, once again the cyclohexadienyl experiments yielded inconclusive results. Therefore, the main purpose of this chapter is to describe the limitations of the instrument and cyclohexadienyl chemical system, and to motivate Chapter 3, which describes a thoroughly redesigned version of the laser kinetics spectrometer used to study vinyl and other radical chemical systems.

2.2. Introduction

Cyclohexadienyl radical (C_6H_7) plays an important role in various combustion-relevant processes. For example, the ring closing reactions of unsaturated hydrocarbons are a critical step in nascent formation of benzene under atmospheric conditions and of polycyclic aromatic hydrocarbons (PAH) under combustion conditions¹⁵. Formation of cyclohexadienyl radical is an example of one these ring closing reactions, where the competition between benzene formation and oxidation is of great interest in combustion chemistry. A typical ring closing reaction mechanism is illustrated in Figure 2.1.

The spectroscopy of cyclohexadienyl radicals has been a topic of interest for various studies. The strong ultraviolet absorption of C_6H_7 was first reported by Shida *et al.*¹⁶ and Ohnishi *et al.*¹⁷ in solid matrix studies, where the radical was detected by ESR spectroscopy.

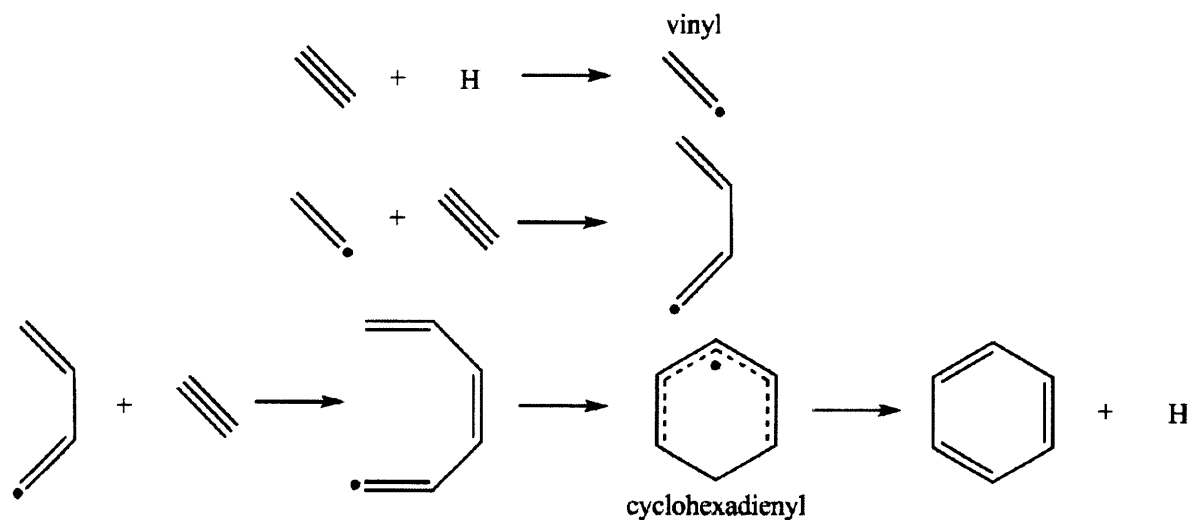
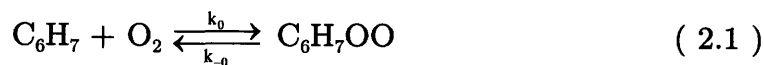


Figure 2.1: A typical ring closing reaction mechanism. Cyclohexadienyl radical is a key intermediate in benzene formation.

Sauer *et al.*¹⁸ and Cooper *et al.*¹⁹ respectively reported liquid phase and gas phase absorption bands for C₆H₇ near 300 nm. Along with a UV band centered at 314 nm, a much weaker ($\times 4000$) absorption transition near 550 nm in solid matrix was reported by Shida *et al.*²⁰ and Jordan *et al.*²¹ Berho *et al.*²² reported the only UV absorption cross section measurement of cyclohexadienyl radical: $\sigma_{\text{C}_6\text{H}_7} = 2.5 \times 10^{-17} \text{ cm}^2$ at 308 nm.

Several kinetic studies in the liquid and gas phase have been conducted via detecting UV and visible absorption of C₆H₇. Effio *et al.*²³ reacted *tert*-butoxyl (C₄H₉O) radical with 1,4-cyclohexadiene (C₆H₈) to generate C₆H₇ at room temperature and reported the visible absorption spectrum of C₆H₇ radical in benzene. In the process, they were also able to measure hydrogen abstraction rate coefficient to be $1.0 \times 10^{-13} \text{ cm}^3 \text{ molecule}^{-1} \text{ s}^{-1}$. In the gas phase, Berho and Lesclaux^{22,24}, using UV absorption, reported the self-reaction and oxidation rate coefficients for C₆H₇.

The oxidation experiments of cyclohexadienyl radical in previous studies yielded contradictory results between liquid and gas phase.



Pan *et al.*^{25,26} and Mailard *et al.*²⁷ measured reaction (2.1) in water and in hydrogen peroxide/benzene solution, respectively. They measured $k_0 = 2 \times 10^{-12} \text{ cm}^3 \text{ molecule}^{-1} \text{ s}^{-1}$ and concluded this reaction to be diffusion limited. The gas phase studies of reaction (2.1) were first performed by Berho *et al.*²⁴. Using flash photolysis coupled to a UV absorption spectrometer, they reported $k_0 = 3 \times 10^{-14} \text{ cm}^3 \text{ molecule}^{-1} \text{ s}^{-1}$, which is about two orders of magnitude slower than

the rate coefficient reported in the liquid phase. In Berho's²⁴ experiment, cyclohexadienyl radicals were generated via a fairly complex mechanism involving C₆H₆/Cl₂/H₂/O₂/N₂ mixtures. This led them to derive a complex chemical mechanism to de-convolute k₀. Estupiñán²⁸ improved upon Berho's²⁴ experiments where Cl was used to abstract H-atoms from 1,4 cyclohexadiene to generate C₆H₇. Estupiñán²⁸ found k₀ to be slightly higher at 6.6 × 10⁻¹⁴ cm³ molecule⁻¹ s⁻¹.

Previous members of our group have extensively studied the oxidation of cyclohexadienyl radical both in liquid and gas phase^{13,14,29}. A thorough liquid phase study was conducted by Taylor^{14,29}, who used *tert*-butoxyl radical to abstract the H-atom from 1,4 cyclohexadiene. Taylor^{14,29} also found reaction (2.1) to be diffusion limited in the liquid phase, and hypothesized that the slow gas phase rate coefficient reported by Berho²⁴ and Estupiñán²⁸ was likely due to combination of several reactions (Figure 2.2) which together appeared to be a slow decay.

In the present study, we intended to study reaction (2.1) in the gas phase to complement the liquid phase study by Taylor^{14,29}. Additionally, cyclohexadienyl radical is reported to have an intense absorption cross section (2.5 × 10⁻¹⁷ cm²) at 300 nm²². Most other unsaturated hydrocarbons have a weak absorption in the accessible spectral range of our probe laser (280 nm < λ < 1 μm) for flash photolysis kinetics experiments. For example, benzyl, allyl and phenyl radical have UV/Vis absorption cross-section of only ~10⁻¹⁹ cm², therefore, more sophisticated detection methods are required to probe them³⁰⁻³². Therefore, cyclohexadienyl radical provided a convenient chemical system for us to test version 1 of our laser kinetics spectrometer. The S/N calculations

indicated that we would detect ~10% absorption signal with a single pass of the probe beam in a one meter long cell.

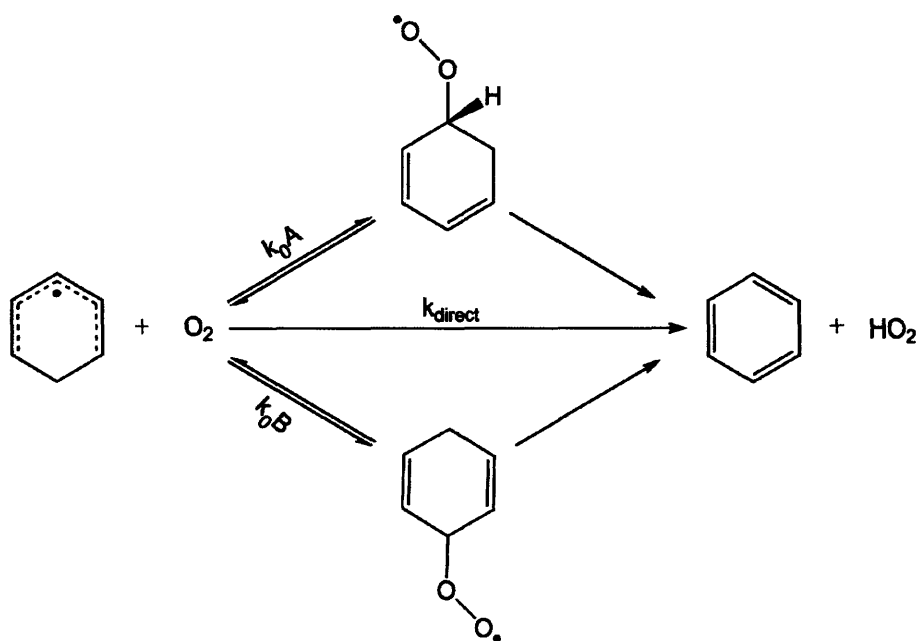


Figure 2.2: Cyclohexadienyl + O_2 forms benzene + HO_2 via three distinct pathways. Berho *et al.* conducted experiments under relatively low $[O_2]$ because of apparatus limitations. They never observed the equilibrium reactions k_{0A} and k_{0B} . Berho²⁴ proposed a different mechanism with a direct reaction (k_{direct}) and stated that k_{0A} and k_{0B} have significant barriers therefore equilibrium reaction is not observed. Radical additions to O_2 , in general, do not have significant barriers. In the present study, the experiments are conducted at higher $[O_2]$ to determine the equilibrium coefficient k_{0A} and k_{0B} .

2.3. Experimental setup

The description of version 1 of the Laser Kinetics Spectrometer can be found elsewhere¹⁴, therefore, only a brief description is presented here. The generation of cyclohexadienyl radical and its reaction with molecular oxygen were measured by a laser flash photolysis-type experiment. The experimental apparatus is shown in Figure 2.3.

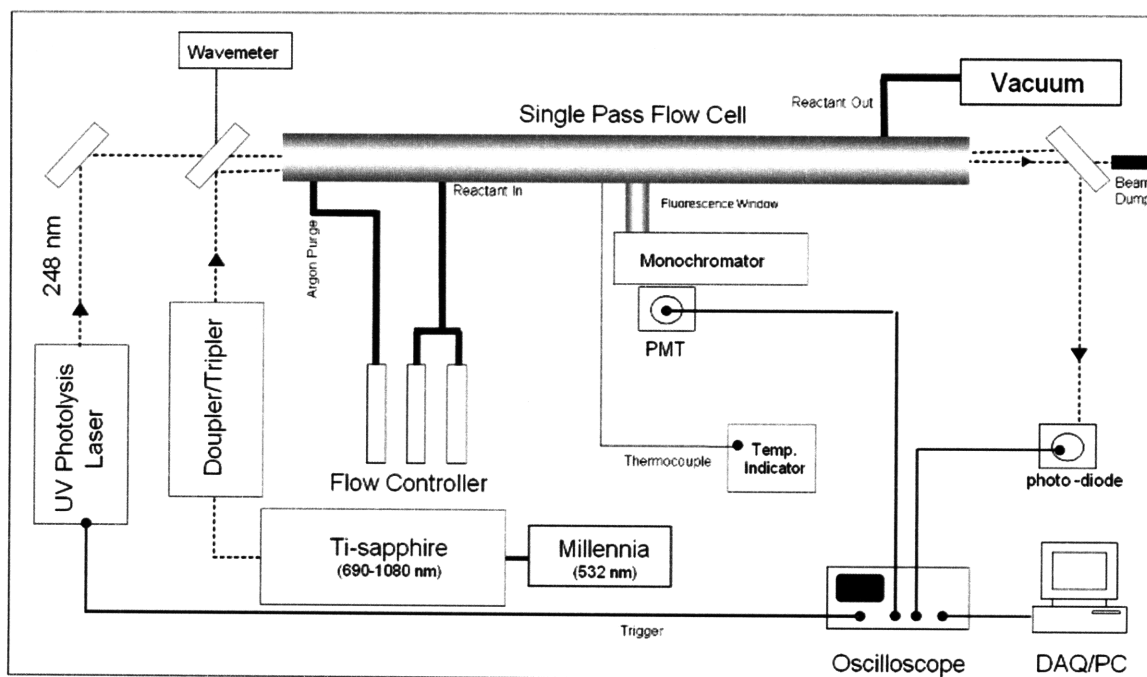
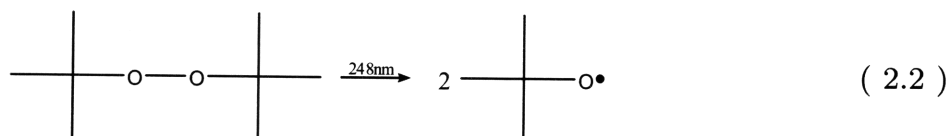
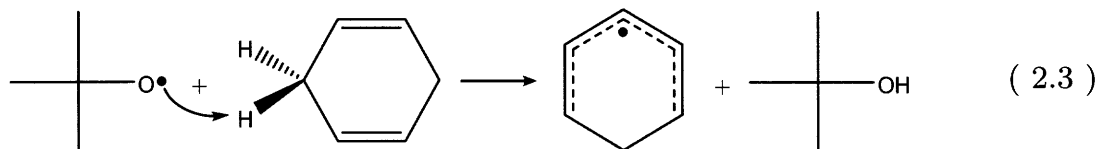


Figure 2.3: Experimental Setup of the version 1 of the laser kinetics spectrometer.

An excimer laser was used to photolyze di-*tert*-butyl-peroxide (DTBP) to produce *tert*-butoxyl radicals:



These radicals react rapidly with excess amounts of 1,4 cyclohexadiene to generate cyclohexadienyl radicals:



Chemicals were purchased from the following suppliers and were used without further purifications: $C_6H_8 \geq 97.0\%$, (Aldrich), DTBP $\geq 98.0\%$ (Aldrich), $O_2 \geq 99.99\%$ (2.0 Grade Airgas), Ar $\geq 99.99\%$ (6.0 grade, Airgas).

The vapor pressures (p_{vap}) of C_6H_8 ($p_{vap} = 77$ Torr) and DTBP ($p_{vap} = 27$ Torr) are relatively low at room temperature, therefore a bubbler setup is incorporated to flow the chemicals into the cell. As shown in Figure 2.4, the vapor mixture was created by sparging Argon through two temperature controlled Ace glass bubblers. The flow of Argon was controlled into the bubbler using a MKS mass flow controller (Figure 2.4).

Two other Argon-calibrated Sierra mass flow controllers were used to flow purge gas to prevent chemical deposition on the windows of the flow cell. A separate oxygen-calibrated Sierra mass flow controller was used to flow O_2 into the flow cell. Total molar flow rates (\dot{n}_{total}) through the cell ranged from 500-2000 cm^3/min .

The internal pressure of the reactor was measured by a MKS capacitance manometer and controlled by hand using a series of bypass needle valves, which were accurate within 10%.

The flow tube was heated using Omega heat tape and controlled using a Variac. The entrance, center, and exit temperatures are monitored using K-type thermocouples and the Variac was adjusted accordingly to increase or

decrease the temperature. Without any insulation, the maximum achievable temperature in the flow cell at maximum Variac setting was found to be 473 K.

The combination of flow rates, organic vapor pressures, cell pressure (P) and cell temperature (T_c), allows us to accurately determine the concentration (c_i) of C_6H_8 and DTBP in experiments:

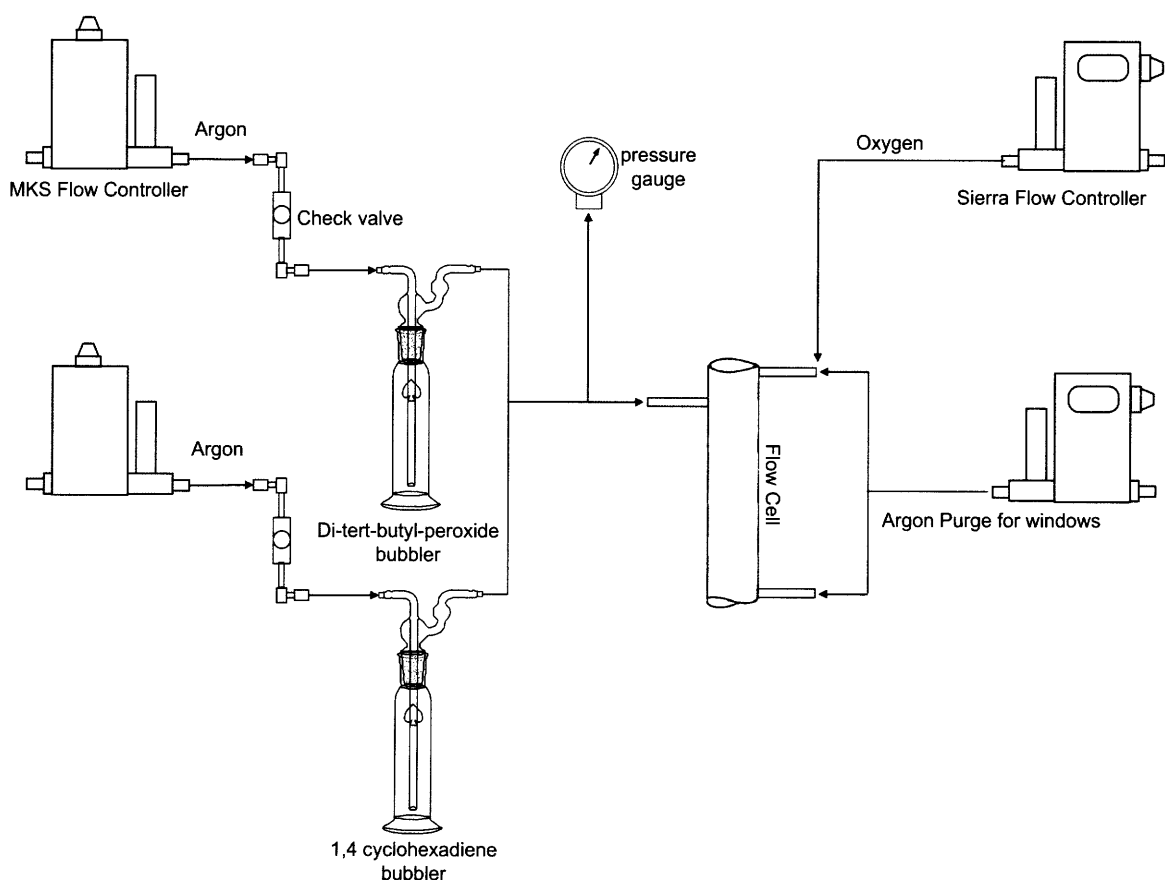


Figure 2.4: Diagram of flow distribution system in the version 1 of the laser kinetics spectrometer. Sierra and MKS flow controllers are used to control the gas flows. Check-valves are placed between the bubblers and flow controllers to prevent back flow.

$$y_i = \frac{p_i^*(T_{bubbler})}{P} \quad (2.4)$$

$$\dot{n}_i = \frac{y_i \dot{n}_i^{Ar}}{1 - y_i} \quad (2.5)$$

$$c_i = \frac{P}{RT_c} \left(\frac{\dot{n}_i}{\dot{n}_{total}} \right) \quad (2.6)$$

In equations (2.4)-(2.6), y_i is the mole fraction of reactant i , p_i^* is the vapor pressure of the organics, \dot{n}_i is the molar flow-rate of reactant i and \dot{n}_i^{Ar} is the flow rate of Argon into the bubbler. The p_i^* is intrinsically temperature dependent ($T_{bubbler}$). The temperature of the bubbler was kept at room temperature for most of the experiments. To increase the organic concentration in the flow cell, bubbler temperature was varied using temperature controlled water bath. The $p_i^*(T_{bubbler})$ for DTBP and C_6H_8 was determined using modified Antoine equations³³. The gas mixture is flowed continuously through a 1.7 meter long stainless steel flow reactor with quartz windows on each end. The gas mixture is continuously pumped out using a roots blower vacuum system.

The gas mixture was exposed to 248 nm radiation produced by a Lambda Physik Compex 102 pulsed-excimer laser filled with a krypton fluoride gas mixture. All the experiments were conducted either by triggering the excimer randomly or by triggering at repetition rates of 0.7 Hz or 1.4 Hz. About 20-40 mJ/pulse of light was directed into the flow reactor using dielectric mirrors. A calibrated Ophir Optronics power meter was used to measure power of the photolysis laser. Several optical configurations were attempted to correct for the astigmatism in the excimer laser, including a cylindrical lens, but none of them gave satisfactory results. Therefore, an iris was incorporated to control the

beam size. Depending on the [DTBP], between 10% to 90% of the 248 nm light was absorbed in the cell.

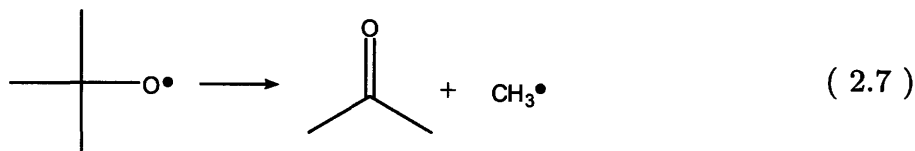
The cyclohexadienyl radicals were probed near the peak of the radical's absorption spectrum²² at 308 nm. The tripled output of a picosecond Ti-Sapphire laser was used to generate this wavelength. A detailed description of this laser system will be presented in the next section. Here a brief overview is given. Nine Watts of cw 532 nm light from a Spectra Physics Millennia Xs was used to pump the Ti-Sapphire oscillator (Spectra Physics Tsunami). The Tsunami was mode-locked at 924 nm, which outputs a train of 1.2 picosecond pulses at a repetition rate of 80 MHz. The Tsunami output is then directed into second and third harmonic generating optics (GWU 23). The output of the laser is stable within 3% (peak-to-peak intensity) over the duration of the experiments. The probe laser was directed into the flow cell using UV-enhanced silver mirrors.

Upon exiting the flow cell, the probe laser was directed into a photo detector through a Schott white glass filter (WG 305) to suppress scattered light from the excimer laser. Several different detection schemes were used to register a voltage proportional to the light intensity. Amongst all the UV sensitive photodiodes tested, ThorLabs Det 210 and ThorLabs PDA155 registered the least noise. In the scheme that used an integrating sphere (Melles Griot 13 SIP 102), a Hamamatsu photomultiplier was used to detect the integrated probe light. The voltage from both detection schemes was amplified using a Femto DHPA-100. Digital and analog filtration schemes were used to reduce high frequency noise greater than 1 MHz. The resulting signal was sent to a digital oscilloscope (Agilent/HP 54642A) and analyzed in Microcal Origin.

2.4. Results

A typical transient absorption signal is shown in Figure 2.5. To confirm that transient absorption was due to cyclohexadienyl radical, several tests were performed. The ideal way to verify that the signal was due to cyclohexadienyl radical was to replicate Berho's²⁴ absorption spectrum from 280-330 nm. Unfortunately, it was very difficult to tune and mode lock the picosecond Ti-Sapphire laser in this range (840-990 nm) with any consistency. The diffuse spectrum of cyclohexadienyl made it almost impossible to obtain an off-resonance signal. Therefore, the cyclohexadienyl signal was attempted to be verified chemically.

First, the precursor chemicals were added to the flow cell in a stepwise fashion. No signal was observed with Ar alone, but when DTBP was flowed into the cell, a weak transient absorption was observed. When the [DTBP] was increased by raising the bubbler temperature, the transient absorption signal also increased. This signal was initially attributed to absorption from acetone ($\sigma_{\text{C}_3\text{H}_6\text{O}}(308 \text{ nm}) = 1.0 \times 10^{-18} \text{ cm}^2$), a product of decomposition of *tert*-butoxyl radical:



Later, we also realized the possibility that this signal could have occurred due to thermal lensing (Section 2.5.1).

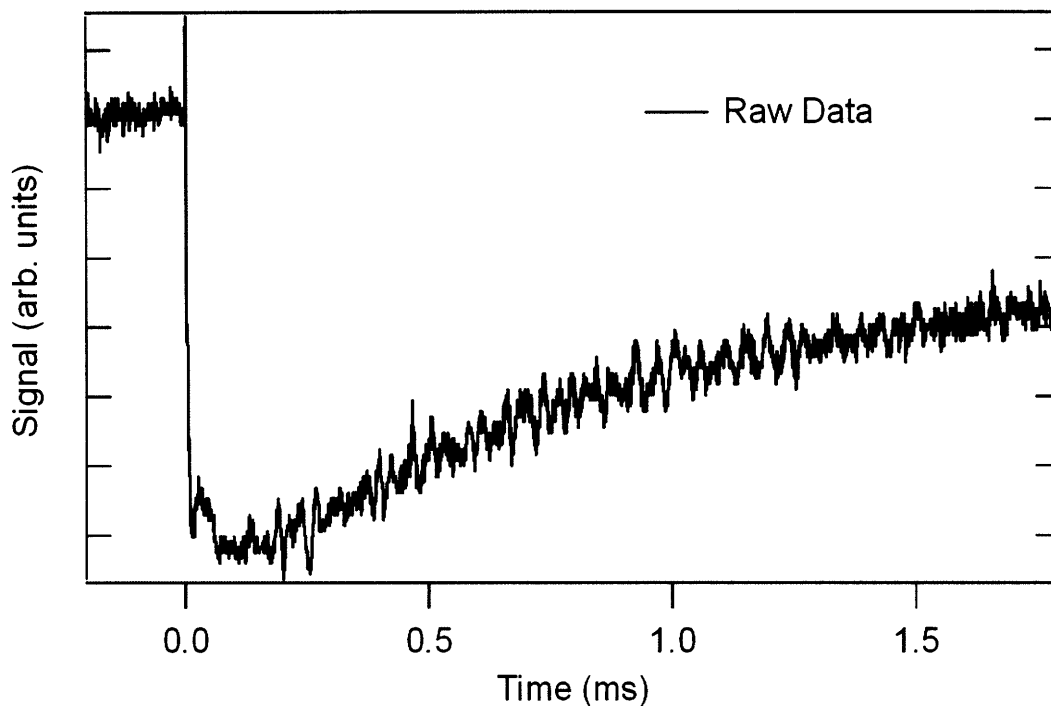


Figure 2.5: Recorded transient signal 248 nm photolysis of C₆H₈/DTBP/Ar mixture at room temperature and 380 Torr of total pressure. [C₆H₈] = 4×10^{18} molecules cm⁻¹ and [DTBP]= 1×10^{18} molecules cm⁻¹

With just cyclohexadiene in the reaction cell, a small absorption signal was again observed. Pure cyclohexadiene does not absorb at 248 nm, but it was found that our cyclohexadiene sample had a 3% benzene impurity. Benzene does absorb at 248 nm. This absorption is associated with electronically excited³⁴ and dissociative³⁵ states of benzene. Therefore, the observed transient signal associated with just cyclohexadiene was most likely due to a triplet state transition from excited state benzene³⁴ or from one of a variety of photo-products of benzene³⁵. This transient signal could also possibly be attributed to thermal lensing.

With both DTBP and C_6H_8 in the reaction cell, a large absorption signal was observed, as shown in Figure 2.5. The time scale of this decay was on the order of ms, which agreed with S/N calculations and previous liquid phase experiments¹⁴.

A second way we tried to verify that transient absorption signals of C_6H_8 /DTBP/Ar mixtures were indeed from cyclohexadienyl radicals was by measuring the decay's dependence on oxygen concentration at room temperature. The $[O_2]$ was varied from $(0.6 - 2.0) \times 10^{18}$ molecules cm^{-3} and the resultant transient absorption signals were fitted to simple exponential decays. Figure 2.6 shows the change in rate of the decay as oxygen concentration is increased. By assuming pseudo first order kinetics, we determined the oxidation rate coefficient of $(1.6 \pm 0.2) \times 10^{-14}$ cm^3 molecule⁻¹ s⁻¹, which is about 75% slower than rate coefficients determined in previous studies by Berho²⁴ and Estupiñán²⁸.

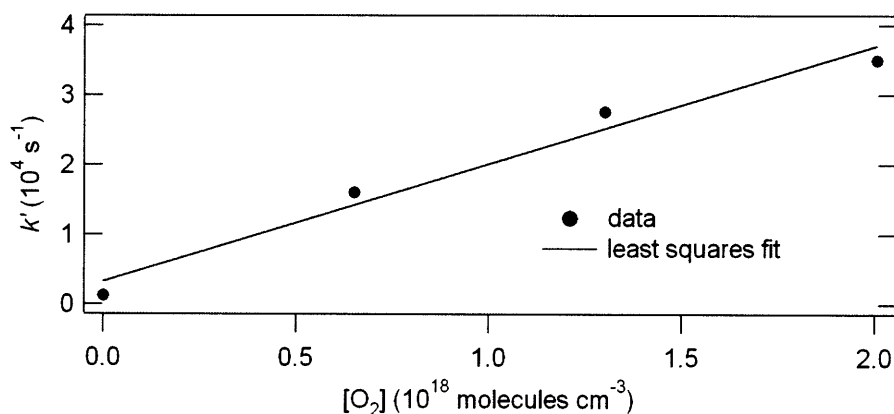


Figure 2.6: Pseudo-first-order plot of experimental absorption with respect to $[O_2]$ at a temperature of 298 K and a pressure of 380 Torr.

The room temperature rate coefficient measurement yielded some evidence that the transient absorption signals of C₆H₈/DTBP/Ar mixtures were from the formation of cyclohexadienyl radical. But in the oxidation experiments at higher temperatures (325-450 K), the cyclohexadienyl decay constants became slower as [O₂] was increased, yielding negative rate coefficients. This could have been potentially due to the fact that the reaction measured was not following first order kinetics at higher temperatures. However, other phenomena, such as thermal lensing, would have had to be ruled out in order to positively identify the presence of cyclohexadienyl radical.

2.5. Discussion

As in the previous studies^{13,14} in this group, the gas phase cyclohexadienyl experiments led to very inconclusive results. One of the reasons this occurred in the present case is that the various limitations in version 1 of the laser kinetics spectrometer produced irreproducible results. Additionally, using C₆H₈/DTBP/Ar mixtures to generate cyclohexadienyl radical led to various secondary chemistry, which in turn caused interference in our measurements. And, lastly, because of thermal lensing and limitations in the version 1 of this instrument, we were never able to positively identify the presence of cyclohexadienyl radical in our system. These issues are discussed in further detail in the next section.

2.5.1. Thermal lensing

Thermal lensing essentially is a lensing effect induced by temperature gradients. Photolytic species such as DTBP or C_6H_8 release heat significant following absorption of light from the photolysis laser. The sudden heat release changes the refractive index of the gas medium creating a temporary thermal lens and causing the probe laser to be steered off of the detector. The thermal lens produced was usually divergent, which caused the probe laser power, as measured by a photodiode, to decrease when monitored along the laser beam axis. Therefore, such a phenomenon is hard to account for since it resembles a real absorption signal (Figure 2.7b). In a few cases, the transient signal probe laser power increased after photolysis, which clearly indicated to us that thermal lensing was occurring, since stimulated emission is very unlikely in our chemical system (Figure 2.7a). The thermal lens signal also had characteristic oscillating acoustic spikes which occurred every 250 μs (Figure 2.7a).

Additionally, the thermal lens signal only occurred in conjunction with all of the reactants and both the laser beams. If any of the components were removed, the signal disappeared. Also, the thermal signal amplitude directly correlated to reactant concentration, which also made it difficult to distinguish the thermal lensing signal from an actual absorption signal.

Several attempts were made to minimize the lensing signal. Instead of using a photodiode for detection, an integrating sphere coupled with a photomultiplier tube was incorporated in our system. Our hope in using an integrating sphere setup was that the small spatial deviations of the probe beam would get

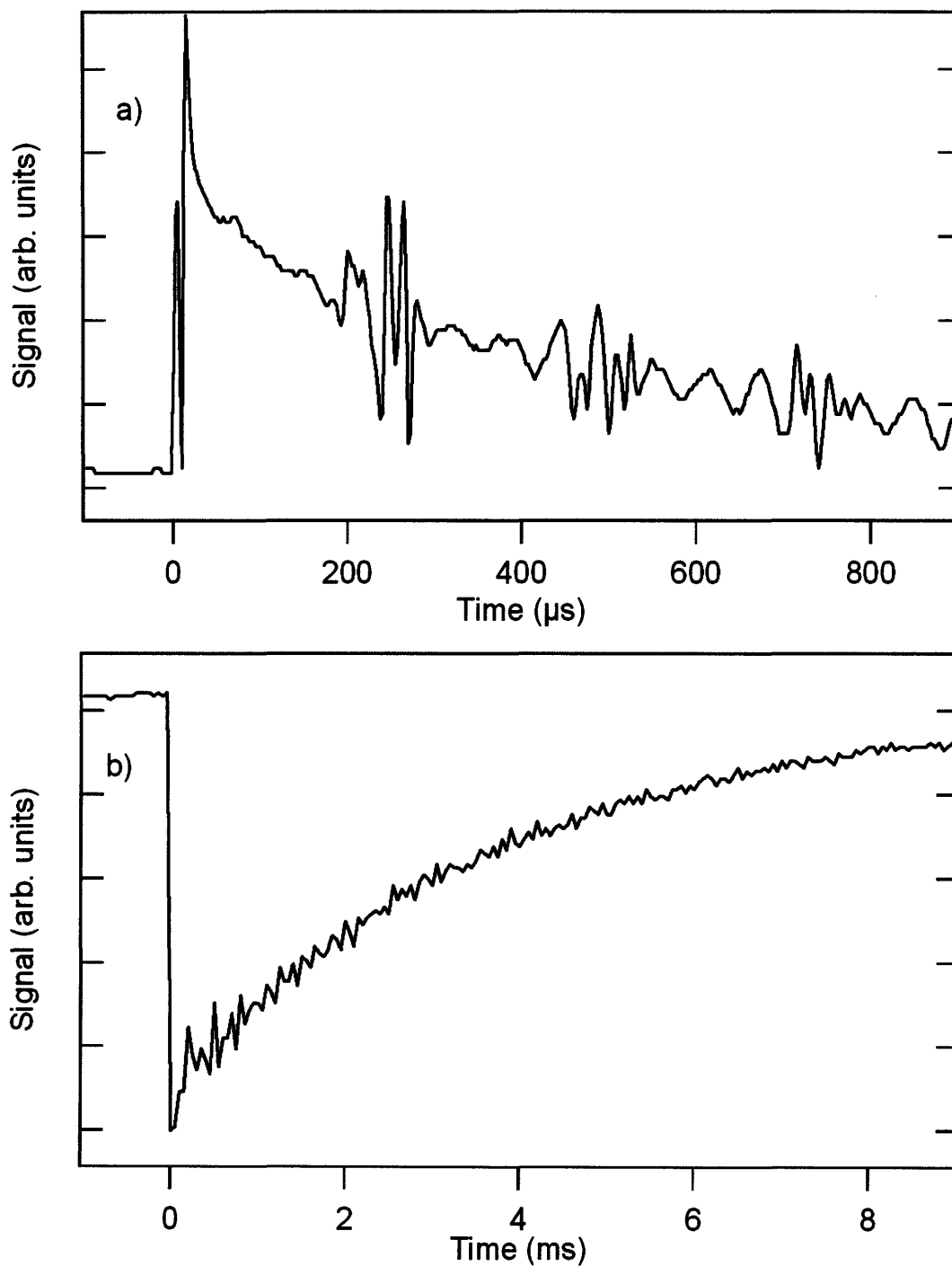


Figure 2.7: a) Thermal lensing signal at microsecond time scale. The characteristic oscillating acoustic spikes had periodicity of 250 μs . The transient signal increases after photolysis laser. b) Thermal lensing signal at millisecond time scale, which resembles a transient absorption signal.

integrated out by having it reflect several times off the partially reflective interior surface of the sphere. Unfortunately, the integrating sphere did not remove the thermal lensing signal.

We also had a discussion about thermal lensing with Professor Kevin Lehmann from Dept. of Chemistry from Princeton University. Professor Lehmann suggested that thermal lensing would be highly dependent on polarizability of the gas medium. Therefore, Prof. Lehmann recommended using Helium instead of Argon as the inert gas since helium's polarizability is much lower compared to Argon³⁶. Switching to Helium as the carrier gas reduced thermal lensing signal by $\sim 4\times$, though it did not completely remove the thermal lensing signal.

Lastly, it was also found that reducing the organic concentration also reduced the thermal lensing signal to almost zero, as long as the probe beam was perfectly aligned and focused into the center of the detection system. Using Helium as the inert gas and low organic concentration yielded some consistent absorption data. But this method was not very reproducible since any slight movement in the probe laser or fluctuation in photolysis power caused thermal lensing to reappear. Also, running the experiments under low organic concentrations led to digitization errors in the acquisition system (Section 2.5.2.4).

2.5.2. Limitation of the instrument

2.5.2.1. Laser noise

One of the main sources of noise in the absorption signal came from line synchronous noise in the probe laser in the millisecond time scale. This characteristic noise is shown as a screen shot of the digital oscilloscope in Figure 2.8. The noise is synchronous to the 60 Hz signal provided by the AC power to the instrument and any of its overtones. Therefore, when the photolysis laser fired at any one of the evenly divisible frequencies (0.5, 1, 2, 3 Hz...), the line noise averaged in phase. When we triggered the photolysis laser asynchronously to the line frequency (0.7 or 1.4 Hz), this noise only averaged away at a high number of shots (> 2000). We also wrote a script in LabView to trigger the photolysis laser randomly, which also yielded unsatisfactory results.

A great deal of effort was put in trying to figure out the source of noise, which was found to ultimately originate from the power supply of Spectra Physics Millennia Xs (pump laser for picosecond Ti-Sapphire laser). We attempted several things to remove this noise including: powering the power supply via an electrical isolator, shielding the entire power supply in a faraday cage, replacing each component of the power supply part by part, replacing the entire power supply, and replacing the pump diodes inside the power supply. None of these actions seemed to remove the line synchronous noise.

We also consulted with Professor Steven B. Leeb in MIT's Department of Electrical Engineering and Professor Franz X. Kärtner in MIT's Research

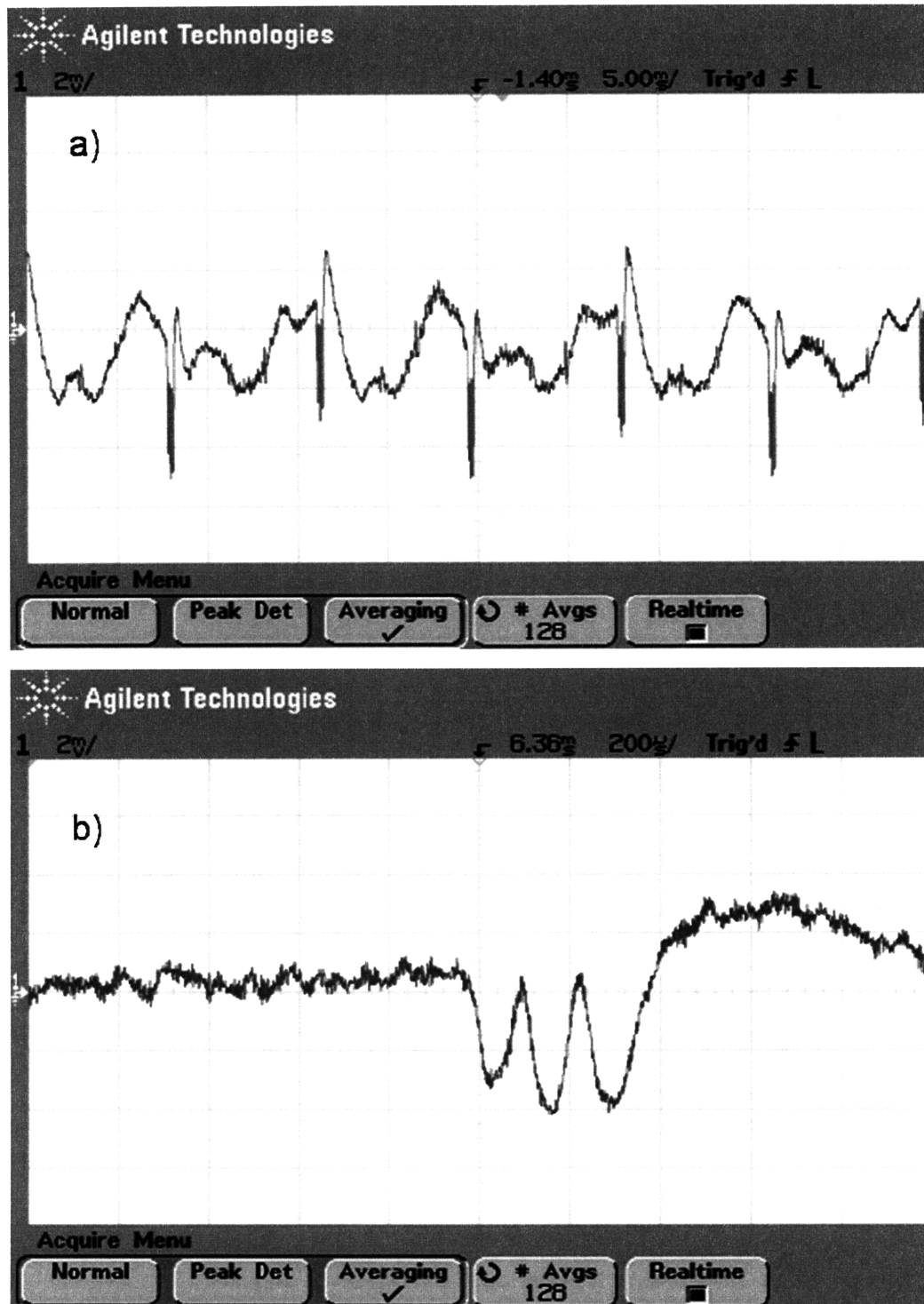


Figure 2.8: Screen shot of the digital oscilloscope, showing the line synchronous noise. Noise measured out of Spectra Physics Millennia Xs at 5 ms/div (a) and 200 us/div (b). There is a sinusoidal and sharp 'spiky' component to the noise which is synchronous to the line frequency (60Hz). Both traces were taken at 2 mV/div in the vertical axis.

Laboratory of Electronics (RLE) to help us resolve the noise issues. Prof. Leeb suggested that if we could acquire the circuit diagram for the Millennium power supply, we could make slight modification to it, by essentially bypassing the transformer and externally providing clean DC power to the pump laser diodes. This could potentially greatly improve the noise specification for the Millennium Laser. We communicated this request to Dr. Kerry Diaz, a vice president of technical sales at Spectra Physics, who indicated to us that due to proprietary reasons, this request could not be accommodated.

Prof. Kärtner from RLE looked into the pump laser noise problem in great detail, and found that the line synchronous noise to be present in all Millennium models. Prof. Kärtner also provided us with a power noise spectrum of a Millennium, along with a comparison to its competitor, a Coherent Verdi (Figure 2.9). As seen in the spectrum, Millennium is significantly more noisy in comparison to the Verdi, particularly in the frequencies ranging from 10^2 to 10^6 Hz, the timescale of most free radical reactions of interest.

2.5.2.2. Bubbler over flow

As shown in Figure 2.4, both C_6H_8 and DTBP were bubbled into the flow cell. A check valve was placed between the bubbler and the flow controller to prevent the back flow of the organic liquids. Unfortunately, the check valve performed very poorly and always leaked liquid into the flow controller during significant pressure fluctuation in the flow cell. Additionally, pressure fluctuations also caused organics to flow in the flow cell in liquid form. There

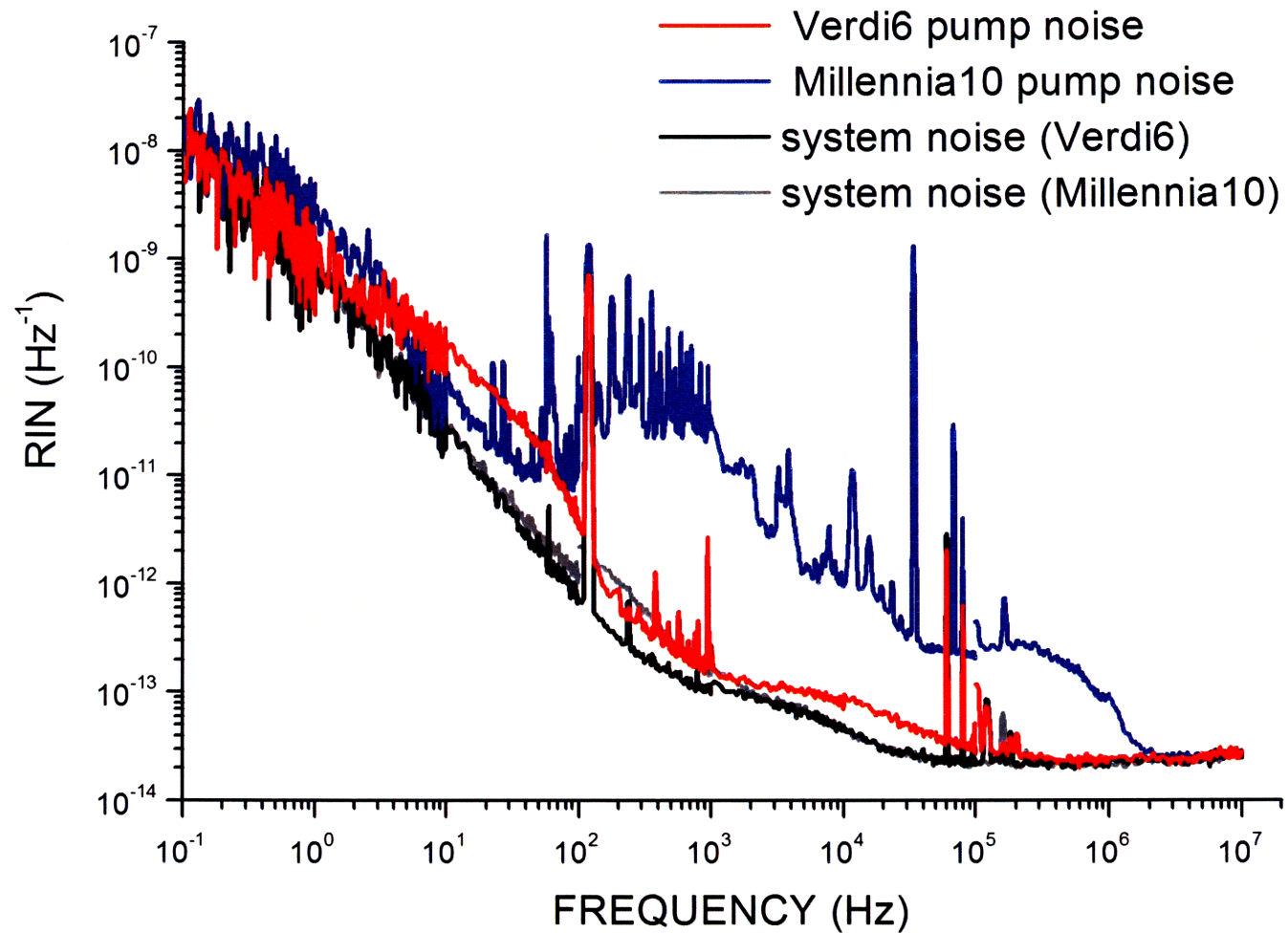


Figure 2.9: Pump laser noise spectrum comparing Spectra Physics Millennia and Coherent Verdi. This was provided to us by Prof. Franz X. Kärtner from Research Laboratory of Electronics at MIT.

was no way to regulate the pressure after the bubbler. This not only caused condensation on the windows for the flow cell, but also caused to us to underestimate the organic concentrations. As seen in Figure 2.4, both the C_6H_8 and DTBP bubbler's exit ports connected to one gas line which allowed liquids to mix within the two bubblers. This problem with the bubbler flow setup was one of the main causes for not being able to generate reproducible results, since it led to large uncertainties in determining the organic concentration.

2.5.2.3. Manual control

As discussed in Section 2.3, various critical components of version 1 of the laser kinetic spectrometer were manually controlled, making it very difficult to reproduce many of the results. In particular, the flow, pressure and temperature control systems were all manually controlled.

All the mass flow controllers in the instrument were controlled via trim pots. In both Sierra and MKS flow controllers, the pots were meant for rough flow adjustment, so it was impossible to fine tune a particular flow setting. Therefore, replicating the flow setting from experiment to experiment was very difficult.

The temperature of the flow cell was also manually controlled by varying the voltage across the heating tape wrapped around the flow cell. The voltage was regulated by variable transformer (Variac), which we could not fine tune and did not generate reproducible temperatures. Often, the Variac overshoot or under-shot the desired temperature, making the stabilization and selection of a particular cell temperature difficult and time consuming.

Lastly, the pressure inside the flow cell was controlled by various needle valves stacked in parallel. Each needle valve was valid within a narrow set of pressure or linear flow rate conditions. Slow drifts in pressure were a constant problem, and needle valve settings had to be constantly adjusted as changes in flow conditions occurred.

Controlling all these variables manually was time consuming, causing acquisition times for typical data trace to be in hours when they should have been in minutes.

2.5.2.4. Digitization error

In the version 1 of the laser kinetics spectrometer, there were also various bugs in the data acquisition system. The signal from the optical detector was sent to a digital oscilloscope (Agilent/HP 54642A) that processed, averaged and digitized the signal, which was then sent via a GPIB interface to a personal computer for further analysis. Under weak transient signals (<2 %), the data after several hundred shots of averaging had significant digitization error. An example of this phenomenon is shown in Figure 2.10. This problem occurred even when the signal was externally amplified. The digitization error was diminished only when the transient signal was > 5%. But this meant we had to run the experiment under high organic concentration, which in turn led to thermal lensing. Several attempts were made to resolve this issue. Eventually, it was discovered that this model of Agilent/HP digital oscilloscope could not internally amplify the averaged signal, unlike its competitors, LeCroy and Tektronix.

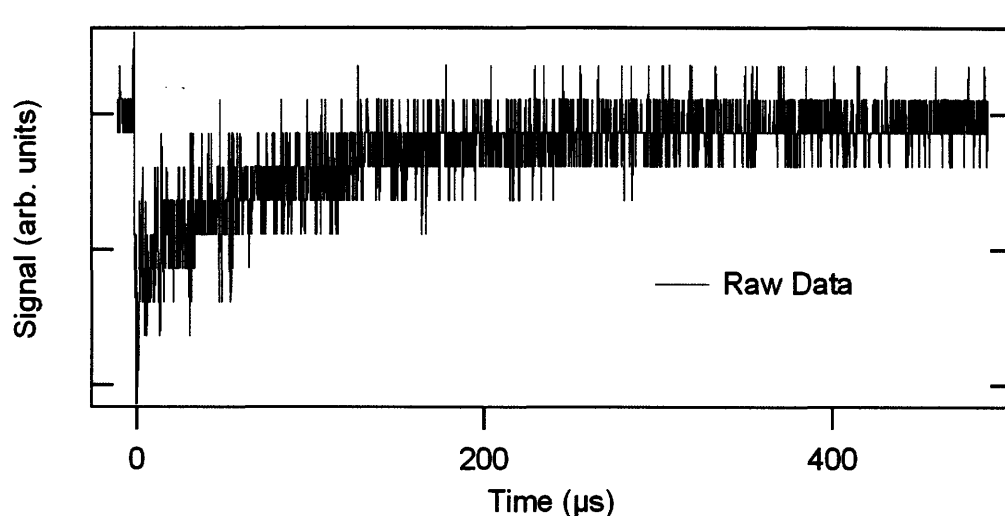


Figure 2.10: Transient signal with digitization error in Agilent/HP digital oscilloscope

2.5.3. Problems in chemical system

Using the cyclohexadienyl chemical system to test version 1 of the laser kinetics spectrometer also had various limitations. As discussed in Section 2.3, 1,4 cyclohexadiene had a 3% benzene impurity which caused significant background interference. Additionally, di-*tert*-butyl-peroxide had a very weak absorption cross section at 248 nm ($\sigma_{\text{DTBP}}(248 \text{ nm}) = 3.0 \times 10^{-19} \text{ cm}^2$). Therefore a significant amount of DTBP had to be used to generate a high radical concentration. High [DTBP] led to thermal lensing which was particularly pronounced since DTBP would be expected to have high polarizability due to its high molecular weight (146.2 amu). Once *tert*-butoxyl radical forms after DTBP photolysis, it can rearrange to form acetone and methyl radical, the kinetics of which compete with the H-abstraction reaction. This reduced the effective yield of cyclohexadienyl radical. Acetone also caused background

interference when probing at 308 nm. Lastly, the cyclohexadienyl was not an ideal chemical system to test version 1 of the spectrometer, because of its broad absorption spectrum (280-310 nm). We were never able to tune the probe laser off-resonance to isolate thermal lensing from actual absorption signal.

2.6. Conclusions

Gas phase experiments were performed using version 1 of the laser kinetics spectrometer. Like the previous gas phase cyclohexadienyl experiments^{13,14}, the results in the present study were inconclusive due the problems with the chemical system and limitations of the experimental apparatus. The problems in the cyclohexadienyl chemical system included:

- Benzene impurity causing possible UV interferences
- Decomposition of *tert*-butoxyl radical to acetone and methyl radical
- Weak absorption cross section of DTBP at 248 nm
- Inability to tune off resonance due to the broad absorption band of cyclohexadienyl radical

In the process, we also identified several limitations in version 1 of the laser kinetics spectrometer which included:

- Line synchronous noise of the probe laser

- Flaw in the bubbler design, leading to significant error in determining organic concentration
- Manual control of several variables in the instruments making the experiments very time consuming and leading to a lack of reproducibility.
- Digitization error in the data acquisition system

We were unable to identify, with any certainty, the presence of cyclohexadienyl radical in our experiments.

Chapter 3

3. Multipass Laser Kinetics

Spectrometer

3.1. Introduction

Direct absorption experiments often involve transient reactive species and lack sensitivity at low concentrations of the probed species. Often in reaction kinetics, the concentration of reactive species must be kept low to target a particular reaction and also, as discussed in Chapter 2, minimize thermal lensing.

Chapter 2 discussed several problems that the cyclohexadienyl chemical system faced as well as the shortcomings of version 1 of the laser kinetics spectrometer. This chapter describes in detail the version 2 the laser kinetics spectrometer, built specifically to study kinetics of vinyl and allyl radicals, which possess many advantages over the cyclohexadienyl system. The instrument described in Chapter 2 lacked the sensitivity to probe vinyl and allyl radicals; this is addressed via addition of a multi-pass cavity to increase the absorption path length. Additionally, the new spectrometer incorporates an improved bubbler design, a differential amplifier to remove line synchronous

probe laser noise and LabView software to automate the entire instrument. This chapter first presents an argument for why the vinyl and allyl chemical systems were selected and then describes the design and operational procedure of version 2 of the laser kinetics spectrometer.

3.2. Chemical systems

The cyclohexadienyl chemical system had several disadvantages and fundamental limitations which were described in Chapter 2. After the failure of the version 1 of the laser kinetics spectrometer, a thorough literature search was conducted to find an optimal chemical system to see which radical kinetics could be measured using a picosecond Ti-Sapphire laser system. The results of the literature search are summarized in Table 3.1. Based on our experience with the cyclohexadienyl system, the ideal chemical would possess the following characteristics:

- the radical of interest should be generated via direct photolysis and not via photolysis of secondary reactions.
- the radical of interest should have the absorption features in the visible range (away from the UV, where interference could occur from background species)

the radical's absorption spectra should have band like structure, so that we can easily tune off-resonance to distinguish the transient signal from thermal lensing. Also the absorption band should be

Table 3.1: Radical chemical systems that can be studied using the laser kinetics spectrometer

Name (m.f)	Peak Absorption (nm)	σ (cm^2)	Precursor	Photolysis wavelength (nm)	Feasibility	Spectrum	Ref
acetyl (CH_3COCH_2)	320	2.0×10^{-18}	acetone	pulse radiolysis	multi-pass	diffuse	37
acetylperoxy ($\text{CH}_3\text{COCH}_2\text{O}_2$)	330	2.0×10^{-18}	acetone/ Cl_2/O_2	355	multi-pass	diffuse	38
allyl (C_3H_5)	402.9	4.0×10^{-19}	allyl-iodide	266	multi-pass	bands	30,39
benzyl ($\text{C}_6\text{H}_5\text{CH}_2$)	447.7	2.2×10^{-18}	benzyl-chloride	193	multi-pass	bands	32
bromine dioxide (OBrO)	491	1.8×10^{-17}	Br_2/O_2	microwave discharge	single-pass	bands	40
bromine monoxide (BrO)	344.1	1.6×10^{-17}	Br_2/O_2	193	single-pass	bands	41
formyl (HCO)	695	1.0×10^{-19}	glyoxal	266	multi-pass	bands	42,43

Table 3.1(continued): Radical chemical systems that can be studied using the laser kinetics spectrometer

Name (m.f)	Peak Absorption (nm)	σ (cm^2)	Precursor	Photolysis wavelength (nm)	Feasibility	Spectrum	Ref
fluroformylradical (FCO_2)	695	1.1×10^{-17}	oxalyl fluoride/ O_2/F_2	193	single-pass	bands	44
iodine dioxide (OIO)	549.3	1.5×10^{-17}	$\text{NO}_2/\text{CF}_3\text{I}$	355	single-pass	bands	45,46
iodine monoxide (IO)	427.2	3.5×10^{-17}	O_2/I_2	193	single-pass	bands	45
iodomethyl (CH_2I)	337.7	4.0×10^{-18}	methyliodide	pulse radiolysis	single-pass	diffuse	47
iodomethy-peroxy (CH_2IO_2)	360	2.5×10^{-18}	methyliodide/ O_2	pulse radiolysis	multi-pass	diffuse	47
methoxymethyl (CH_3OCH_2)	340	1.0×10^{-18}	$\text{SF}_6/\text{dimethyl ether}$	pulse radiolysis	multi-pass	diffuse	48
methylthioyl (CH_3S)	371	2.0×10^{-18}	dimethyldisulfide	248	multi-pass	diffuse	49

Table 3.1(continued): Radical chemical systems that can be studied using the laser kinetics spectrometer

Name (m.f)	Peak Absorption (nm)	σ (cm^2)	Precursor	Photolysis wavelength (nm)	Feasibility	Spectrum	Ref
phenyl (C_6H_5)	504.8	3.0×10^{-19}	chlorobenzene	193	multi-pass	bands	31
phenylperoxy ($\text{C}_6\text{H}_5\text{O}_2$)	470	2.0×10^{-18}	nitrosobenzene	355	multi-pass	diffuse	50
phenoxy ($\text{C}_6\text{H}_5\text{O}$)	390	2.0×10^{-18}	anisole	193	multi-pass	diffuse	51,52
propargyl (C_3H_3)	332.5	4.0×10^{-18}	propargyl chloride	193	single-pass	diffuse	53
vinyl (C_2H_3)	423.2	2.0×10^{-19}	vinyl iodide	266	multi-pass	bands	39,54
vinylloxy ($\text{C}_2\text{H}_3\text{O}$)	348	6.0×10^{-19}	methyl vinyl ether/ O_2	193	multi-pass	diffuse	55,56
vinylperoxy ($\text{C}_2\text{H}_3\text{O}_2$)	380	6.0×10^{-19}	vinyl iodide/ O_2	266	multi-pass	diffuse	57

broader than 13 cm^{-1} , but narrow enough so that one can tune off-resonance within few nm.

- the radical should be generated via 266 or 355 nm photolysis. (We only had the Nd:YAG laser available)

The only chemical systems identified that matched all four of the criteria were vinyl and allyl radical formed via 266 nm photolysis of vinyl iodide and allyl iodide, respectively. Another advantage of these chemical systems is that the visible absorption spectra have been reported in the literature^{54,58}. Vinyl radical also has been well characterized using a similar technique described in this chapter, by our collaborators, Dr. Craig Taatjes, at Sandia National Laboratories in Livermore, CA. A disadvantage was that vinyl and allyl radical systems required a more sensitive technique which was addressed by incorporating a multi-pass Herriott-type-resonator in our instrument.

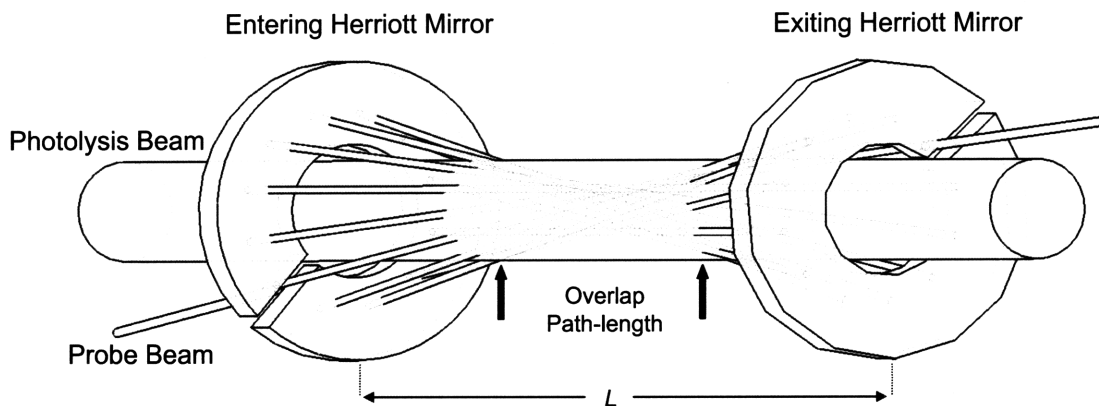


Figure 3.1. The Herriott multi-pass resonator is shown with incorporation of an on-axis pump laser. Changing the diameter of the pump laser changes the overlap with the probe laser. L is the distance between the two mirrors.

3.3. Herriott cell

A diagram of the multi-pass Herriott cell in our current setup is shown in Figure 3.1. The Herriott resonator design and mathematical formulation has been well established in the literature^{11,12,59}; therefore a practical operational procedure will be presented in this section.

In a Herriott resonator, the multiple passes are contained similar to the way off-axis rays are confined in spherical mirrors. The probe laser beam is coupled into the resonating cell via a physical hole in the mirror or an interruption in optical coating in the mirror. After traversing several times in the resonator, the probe beam exits on the opposite mirror in the same fashion as it entered. To maintain a stable cavity, identical spherical mirrors are spaced greater than confocal, but less than twice the radius of curvature of the mirrors. The number of passes achievable in the cavity highly depends on the spacing between the two mirrors (L). In a symmetric resonator, where radius of curvature of the Herriott mirrors (R_c) are equal, Trutna and Byer¹² give a solution for L for any specified number of transits between the resonator (N):

$$L = R_c \left(-1 - \left(\frac{\cos\left(\frac{J(4\pi)}{N+1}\right) + 1}{2} \right)^{1/2} \right) \quad (3.1)$$

Physically, J represents the number of times that the beam completely traverses the mirror before it exits the resonator. From equation 3.1, we see that the number of passes approaches infinity as the cavity length approaches twice the radius of curvature of the mirrors. As shown in Figure 3.1, when the probe beam travels through the Herriott resonator, the individual spots made

by consecutive reflections follow around the end mirrors and map out a circular pattern. The spots made by the probe beam might transverse the circle a number of times before the total angular traversal criteria is met to send the probe beam through the exit (depending the physical location of the slit on the exit mirror). For example, the resonator setup with 11 passes (5 spots on each mirror) making one circular transit or the setup with 21 passes (10 spots on each mirror) making two circular transits has very little difference in spacing between the resonators. Whereas, the spacing between mirrors drastically changes for a 21 pass resonator with one transit versus a 21 pass resonator with 2 transits.

Because the resonator utilizes spherical end mirrors, the beam periodically focuses and de-focuses as it travels back and forth in the resonator. In the ideal case where a properly mode-matched laser enters the resonator with identical mirrors, the beam waist should focus in the center of the cell and the beam spot size on both mirrors should be uniform. For a TEM_{00} beam, mode matching can be accomplished by focusing the laser in the initial pass at the center of the Herriott resonator cavity which will allow the mode to repeat. Unfortunately, due to astigmatism, our doubled/tripled Ti-Sapphire beam is not a perfect TEM_{00} mode which leads to improper mode matching inside the resonator. In principle, improper mode matching manifests itself as non-uniform spot sizes on the Herriott mirrors. Practically speaking, it is not critical that the laser be perfectly mode matched in the resonator, as long as the exiting beam does not clip on the exit slit of the Herriott mirror and the whole beam cleanly makes it to the detector. If the beam clips at any point, it will lead to thermal lensing. Therefore, it is recommended that the cavity not be perfectly mode-matched, so that the probe beam is focused at the exit slit. To facilitate this,

the probe beam is processed through a series of cylindrical lenses to correct for the astigmatism. The probe beam then passes through a spherical (mode-matching) lens with a long focal length (> 500 mm), positioned on a 1 meter long translation stage. The diagram of this optical setup is shown in Figure 3.2. In the current setup, there are several mode matching lenses with various focal lengths that can be used (500, 600, 700, 750, 800, 850, 900, 1000, 1200, 1500, & 2000 mm). The position and the focal length of the mode matching lens should be changed as needed to avoid clipping of the probe beam.

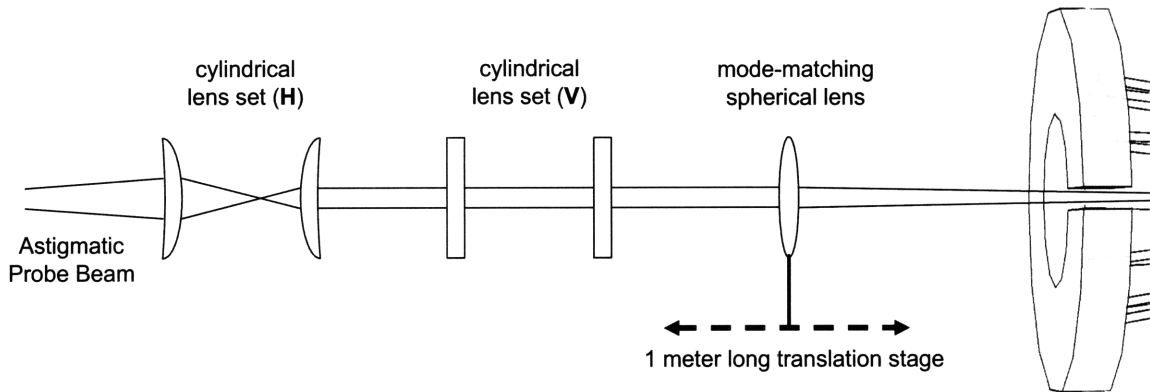


Figure 3.2: Diagram of the optical setup to correct for the astigmatism in the probe beam and mode-match the Herriott resonator. A total of four cylindrical lenses are used to correct horizontal (H) and vertical (V) astigmatism separately in the probe beam. A mode-matching lens with long focal length (>500 mm) sits on a translation stage. The focal length of the lens and physical location of the lens should be adjusted to ensure the beam is mode-matched in such a way that it is focusing when it exits the cavity.

The alignment of the Herriott resonator is fairly straightforward, once the astigmatism is corrected. The required mirror spacing and beam in-coupling angle are determined using formulas derived by Trutna and Byer¹². The probe beam first should be properly aligned through the slit in the entrance mirror onto the exiting mirror. Then the exiting mirror should be adjusted such that

the first reflection is placed into correct position on the entrance mirror. Finally, adjusting the entrance mirror for the second reflection on the exit mirror should coarsely align the resonator. Minor adjustments of the two Herriott mirrors and the angle of the input mirror (for the probe beam) will be required to perfectly center the cavity.

Table 3.2: Inventory of Herriott mirrors

Vendor	Radius of Curvature (mm)	Reflectivity	Coating (nm)	Substrate	Quantity
Rocky Mountain Optics	750	98%	380-550	Zerodur®	2
Rocky Mountain Optics	1000	99.5%	260-350	Quartz	2
Red Optronics	800	99%	380-550	BK7	8
Red Optronics	1200	99%	380-550	BK7	2
Red Optronics	1600	99%	380-550	BK7	2

Several different Herriott mirrors with various coatings and radii of curvature are available for the present setup. All the mirrors are 50.8 mm in diameter and have 20 mm holes drilled in the center. A detailed inventory is summarized in Table 3.2. All the experiments presented in this thesis were conducted using the Herriott mirrors purchased from Red Optronics Inc, with radius of curvature of 800mm and an optical coating effective from 380-550 nm. The mirrors are placed 1520.7 mm apart. This configuration leads to 55 total passes ($N=55$ and $J=4$). Depending on the photolysis beam diameter, overlap path lengths from 25 to 45 meters can be achieved. An experimental observation that we were never able to fully understand is that the number of

passes in the resonator changed when the oven temperature around the cell was increased. We believe this might have been caused by either the thermal expansion of the flow cell or thermal expansion of the substrate of the Herriott mirrors. Table 3.3 summarizes the number of passes achieved as the cell temperature is increased. In high temperature experiments, the exiting mirror of the Herriott resonator might need to be slightly rotated to get the probe beam to exit cleanly. A translational/rotational stage for the exiting mirror is recommended.

Table 3.3: Number of passes vs. temperature.

Temperature (K)	# of passes (N)	Temperature (K)	# of passes (N)
298	55	525	39
325	55	550	39
350	41	575	39
375	41	600	39
400	41	625	39
425	53	650	39
500	53	675	39
525	39	700	39/65

Table 3.4: Comparison of Xenon Arc lamp and Ti:Sapphire Laser

	Newport Xenon Arc Lamp — 6269	Spectra Physics Tsunami-Ti:Sapphire Laser
power (Watts)	150	1
wavelength range (nm)	200-800	230-1080 *
bandwidth		0.7 nm #
# of photon/s at 0.7 nm bandwidth	$\sim 1 \times 10^{18}$	$\sim 4 \times 10^{18}$
beam diameter (mm)	~ 2 ^a	<2 ^b
beam divergence	20° ^a	0.06° ^b
solid angle (sr)	$\sim 4 \times 10^{-1}$ ^c	$\sim 3 \times 10^{-6}$ ^c
photon radiance (photons $\text{s}^{-1}\text{m}^{-2}\text{nm}^{-1}$ sr^{-1})	$\sim 1 \times 10^{22}$ ^a	$\sim 2 \times 10^{27}$ ^c

* full range achieved via doubling and tripling the output of the Ti-Sapphire laser—with some gaps in the middle

at 750 nm for 1.2 ps pulses with 13 cm^{-1} bandwidth

^a quoted from Newport/Oriel manual

^b quoted from Spectra Physics manual

^c calculated

3.4. Ti-Sapphire probe laser

Many different sources of probe light have been traditionally used in flash-photolysis kinetics experiments, including tungsten-halogen lamps, xenon arc lamps, and lasers. An important quantity to consider when choosing an ideal probe source is photon radiance at the desired wavelength.

The ideal probe source should have high radiance over the absorption linewidth of the radical of interest. Also, the radiance of the ideal probe source should be able to be efficiently collected from and transmitted through the flow cell. Table 3.4 compares some of the key parameters between the Ti:Sapphire probe laser and Newport Xenon Arc Lamp (Model # 6253). Both radiation sources differ in beam divergence, which leads to a high solid angle. There are commercial available lamps with collimated output (divergence $\leq 1^\circ$), but these lamps have an order magnitude bigger beam diameter (25 mm). The probe laser's high spectral radiance makes it ideal for a multi-pass cavity. Signal to noise (SNR) calculation shows that if the detector and source are placed 50 meters apart, a laser source gives five order magnitude more signal to noise ratio ($\text{SNR} \approx 5 \times 10^6$) than a lamp source ($\text{SNR} \approx 50$). SNR calculation assumes a lens diameter of 25 mm, and detector with 1 MHz bandwidth and noise equivalent power (NEP) of $1 \times 10^{-11} \text{ W Hz}^{-1/2}$.

A diagram of the probe laser setup is shown in Figure 3.3. The probe laser is generated using a mode-locked Ti:Sapphire laser (1.2 ps at 80 MHz) pumped by a 532 nm diode-pumped solid state continuous-wave (CW) laser. The pump laser, Millennia Xs by Spectra Physics, should be turned on and turned off in the 'Current Mode', but once the specified output requirement is

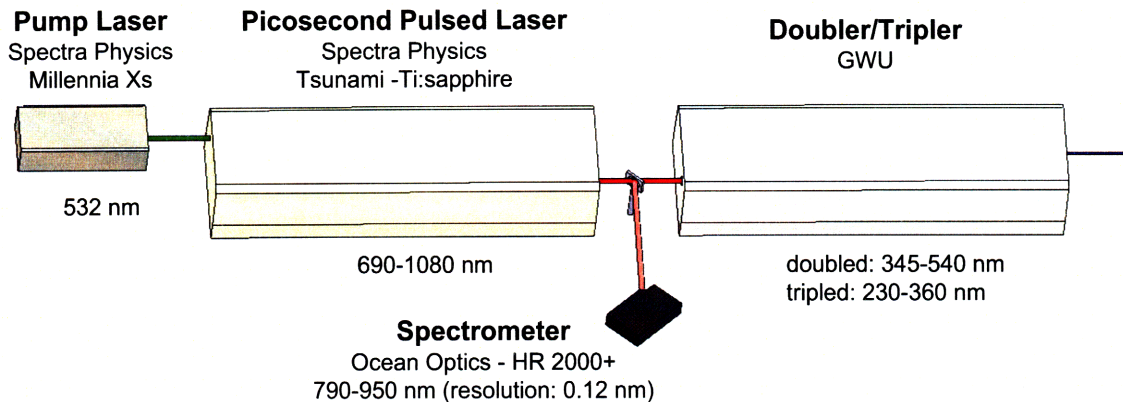


Figure 3.3: Diagram of the probe laser setup.

achieved, it should be run in 'Power Mode'. The pump laser can output up to 10 W of 532 nm light. The requisite pump laser power varies depending on what wavelength is desired out of the Ti-Sapphire. This is summarized in Table 3.5. Both the pump laser and Ti-Sapphire laser crystal required 15° C cooling water in the circulator to maintain a steady crystal temperature.

The Ti-Sapphire laser (Tsunami) emits a train of infrared pulses lasting only 1.2 ps, at a repetition rate of 80 MHz. The Tsunami is tunable via a birefringent filter over the range of 690-1080 nm. There are two optical kits provided for Tsunami. The currently installed optical kit allows for tuning range from 690-980 nm. Several optical components have to be exchanged inside the Ti-Sapphire laser, if wavelengths between 980-1080 nm are required.

The output of the Ti-Sapphire laser is then directed into the GWU 23, where the light can be frequency-doubled or tripled using a BBO (beta-barium borate) crystal to get wavelengths in the UV/Vis region. There are three optical kits available for the GWU which work in different wavelength ranges. The

'Short' kit can double/triple wavelengths between 690-850 nm. The 'Long' kit works between 850-1000 nm. And 'Extra-Long' covers the range from 980-1080 nm.

Table 3.5: Pump laser power requirement at different Ti-Sapphire wavelengths

Ti-Sapphire wavelength range	Required Pump Power from Millennia Xs
690-725 nm	8.5 W
725-775 nm	7.8 W
775-825 nm	6.7 W
825-875 nm	7.5 W
875-900 nm	8.0 W
900-925 nm	9.0 W
925-980 nm	9.5 W
980-1080 nm	>10 W

The picosecond Ti:Sapphire laser can be tuned through its entire spectral range, without any major changes to the optical path. This laser system has excellent stability on the microsecond-to-millisecond time scale, so it can be used as a quasi-CW source, allowing detection of transient absorbances as small as ~ 0.0001 .

Part of the Ti-Sapphire output is reflected into a fiber-optic coupled Ocean Optics High Resolution (HR 2000+) spectrometer to determine the output wavelength. The 13 cm^{-1} uncertainty in wavelength of the probe laser (because of 1.2 ps uncertainty in time domain) requires a spectrometer with ~ 0.6 nm of resolution or better. The spectrometer is currently equipped with a 'H6'

grating with best efficiency range of 500-1100 nm and resolution of ~ 0.12 nm FWHM. At this resolution, the spectral range of the spectrometer is ~ 140 nm. The spectrometer currently is centered at 870 nm, giving a range of 790-950 nm. Since this spectrometer does not cover the entire Ti:Sapphire range, either a new spectrometer should be purchased or the grating of the present spectrometer should be re-centered and re-calibrated by Ocean Optics.

3.4.1. Noise reduction

As discussed in Section 2.5.2.1, line synchronous noise was major problem in version 1 of the laser kinetics spectrometer. The noise issue is addressed in this version by incorporating a balanced detection scheme and performing the subtraction real time. The reference beam (I_0) is generated using a beam-splitter and does not pass through the reactor. I_0 is normalized to the probe beam (I) using a Thorlabs continuously variable metallic neutral density filter (NDC-100C-2M). Both I_0 and I are detected by Thorlabs fixed gain, wide band (200-1000 nm) silicon amplified photodiode (PDA10A). Signal from both detectors are fed into a Stanford Research Systems, differential-low noise-voltage preamplifier (SR 560). The differential preamplifier has a bandwidth of 1 MHz.

The differential amplifier performs exceptionally well in removing the laser noise as evident in Figure 3.4a. We also acquired FFT spectrum of the probe laser before and after subtraction. These results are shown in Figure 3.4b. The differential amplifier does an excellent job at removing noise between 10^1 - 10^5 Hz. At frequencies ranging from 10^5 - 10^6 Hz, the amplifier is not as effective.

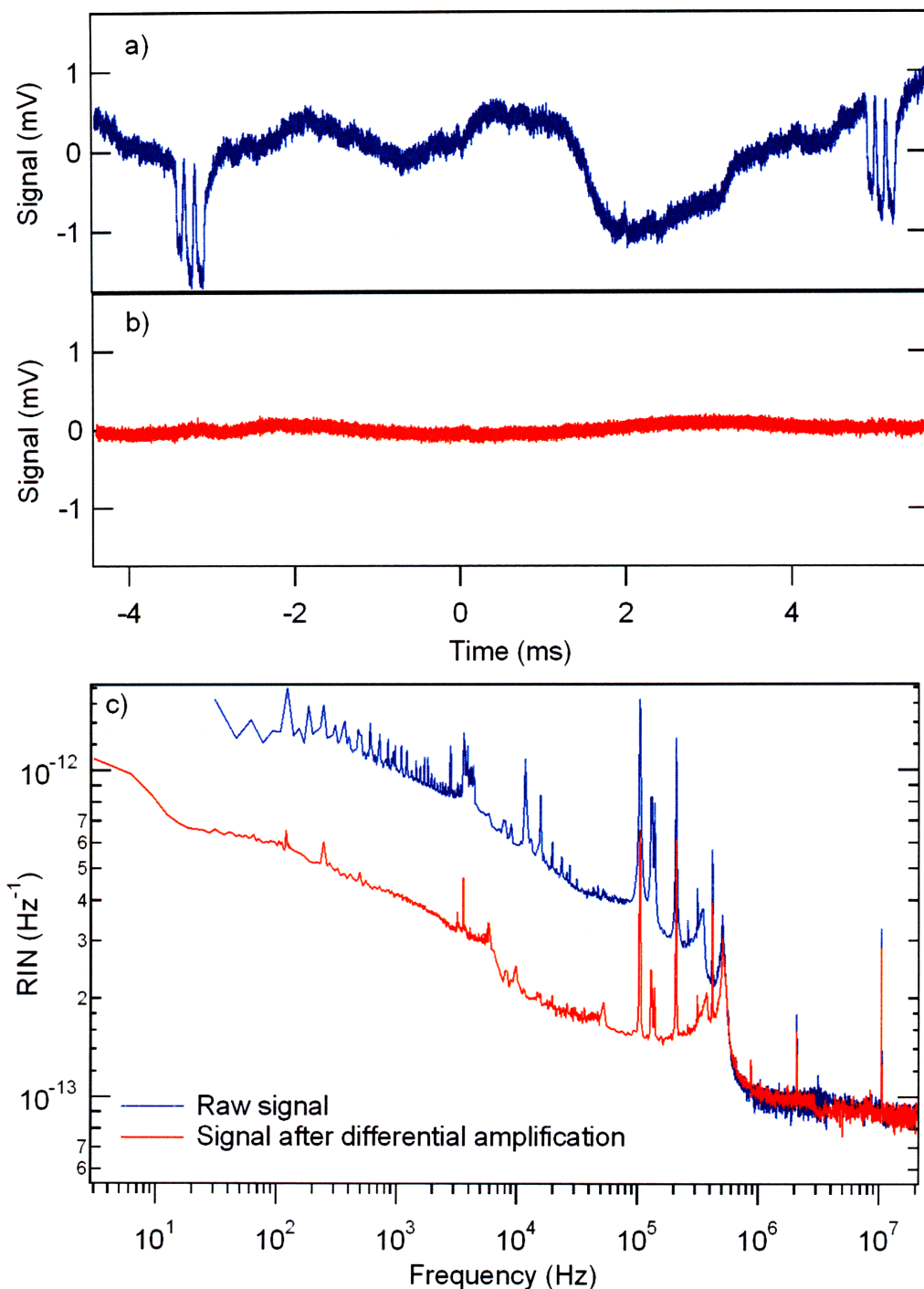


Figure 3.4: a) Characteristic noise of just the probe laser in time domain. b) noise of the signal after reference beam was subtracted using a differential amplifier. c) Power spectrum of probe laser without (blue) and with differential amplifier (red). Time domain traces were taken after 500 averages. Frequency domain were acquired after 2000 averages.

3.5. Photolysis laser

The photolysis laser source utilized for gas phase experiments is the short pulsed (2ns) Coherent Infinity 20/100 Nd:YAG laser. This YAG laser has excellent pulse to pulse stability (10%). The Coherent laser is internally capable of producing doubled (532 nm) and tripled (355 nm) radiation. In the present setup, 532 nm output is doubled again externally using a BBO (or a KDP) crystal to produce 266 nm radiation. The BBO crystal was purchased from Red Optronics. Because the YAG laser has short pulses, both KDP and BBO crystals give excellent conversion efficiencies ($> 40\%$). Approximately, 500 Watts of lamp power led to ~ 200 mJ/pulse of 1064 nm, ~ 100 mJ/pulse of 532 nm and ~ 40 mJ/pulse of 266 nm.

The 266 nm weakly divergent beam exiting the doubling crystal is ~ 0.4 cm in diameter. To increase the overlap path-length in the Herriott cell, the photolysis beam is expanded using telescoping lenses, where a concave lens is used to expand the beam and a convex lens is used to collimate it. As summarized in Table 3.6, photolysis beams of various diameters are attainable by varying the focus of the concave lens.

Table 3.6: Various lenses to expand the photolysis beams

concave lens focal length (mm)	convex lens focal length (mm)	distance between the lenses (mm)	photolysis beam diameter (cm)	overlap pathlength for single-pass (cm)
-75	150	55	1.12	44
-50	150	85	1.44	59
-25	150	110	1.72	72

All the uncoated, UV-grade fused silica lenses were purchased from Thorlabs. It is *absolutely* critical that the photolysis beam pass exactly through the center of each lens, otherwise hot spots are formed within the beam, which can create various problems including ozone formation, damaging of windows, and uneven distribution of radical formation. The hot spots occurs because the optics do not behave ideally on the edges. Therefore, all the telescoping lenses are placed on 3-D translation stages.

After passing through all the lenses and the two windows of the flow cell, ~27-34 mJ/pulsed (depending on the size of the diameter) of 266 nm of photolysis power is available. A calibrated Ophir Optronics power meter is used to measure the power of the photolysis laser continuously.

3.6. Flow cell design and vacuum system

Keeping the Herriott optics outside the flow cell under ambient conditions led to considerable losses of the probe laser due to the back reflection from the windows. Therefore, the Herriott optics are placed inside the vacuum flow cell. A diagram of the flow cell is shown in Figure 3.5. The two Herriott mirrors are enclosed by two ISO-100 six-way crosses purchased from Nor-Cal. Both six-way crosses have a 1/4 inch ports for purge gas to keep the Herriott mirrors and cell windows clean. The six-way cross from which the probe beam enters is attached to ISO-63 flex coupling, which has 3/8 inch port from which reacting gases enter. The six-way cross from which the probe beam exits is

attached to a four way cross (2 NW-40 and 2 ISO-63 coupling). One of the NW-40 connects to the root blower vacuum line. The Roots blower was purchased from Leybold (RUVAC WSU-251) with nominal pumping speed at pump outlet $\sim 250 \text{ m}^3 \text{ h}^{-1}$. From 760 Torr, the ~ 5 liter cell volume (using 1.8 inch o.d. vacuum up to the cell) can be evacuated to ~ 10 mTorr in ~ 20 seconds. The second NW-40 connection attaches to thermocouple feed-through and two Baratron pressure gauges (via a NW-25 3-way cross).

The entrance 6-way cross's window is at Brewster's angle (53.7°). The probe beam and photolysis laser are counter-propagated. Therefore, the Brewster's window is incorporated to avoid the back reflection of photolysis laser from hitting the Herriott mirror from which the probe beam exits. The Brewster's plate required a 5 inch diameter quartz window. The 6-way cross on the exit side requires a 2.25 inch diameter quartz window.

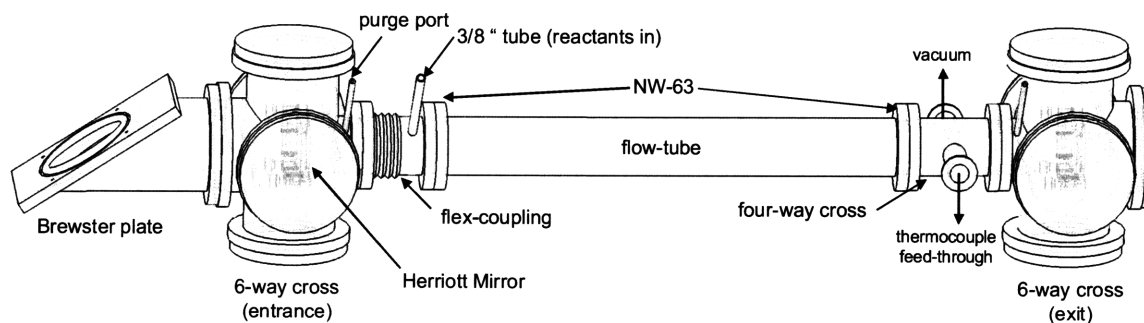


Figure 3.5: Diagram of flow-cell

3.7. Flow & pressure control

The diagram of the flow control system is shown in Figure 3.6. Calibrated MKS mass flow controllers are used to maintain a constant flow of the reactant and buffer gases. In the version 1 of the laser kinetic spectrometer, we incorporated three Sierra Instruments flow controllers. In the present version, the entire instrument is leak test tested using a Varian Helium leak detector. All the Sierra Instruments flow controllers had major leaks at the high pressure end, whereas, none of the MKS mass flow controller had any leaks. Therefore, we recommend using MKS 1179A or M100B flow controllers as the standard flow controllers for this laboratory.

At present, there are eight MKS mass flow controllers incorporated in the instrument, which are all powered and controlled by two MKS Four Channel Power Supply/Readout (247D). Two flow controllers (2000 & 10000 sccm) are used for the hydrocarbon (alkenes, alkynes, etc) flow. A set of two are employed for inert gases (He, N₂ or Ar) and two for oxygen. A set of two special MKS metal sealed flow controllers (1179A) are utilized to flow organics as opposed to viton sealed (100B) flow controllers which react with many of the organics. Each set of two flow controllers is equipped with a by pass valve to clean the gas line. The back pressure behind each flow controller is maintained at 10 PSI.

As discussed in Section 2.4.2.2, we faced several problems in the bubbler setup in the version 1 of the spectrometer. In the present version, a brand new setup is designed to flow the organics. This setup is shown in Figure 3.7. For experiments in which the pressure of the flow cell (P_{cell}) is less than the vapor pressure of the organic (P_{vap}), a simple flask (Chemglass Airfree[®] Cajon[®] storage

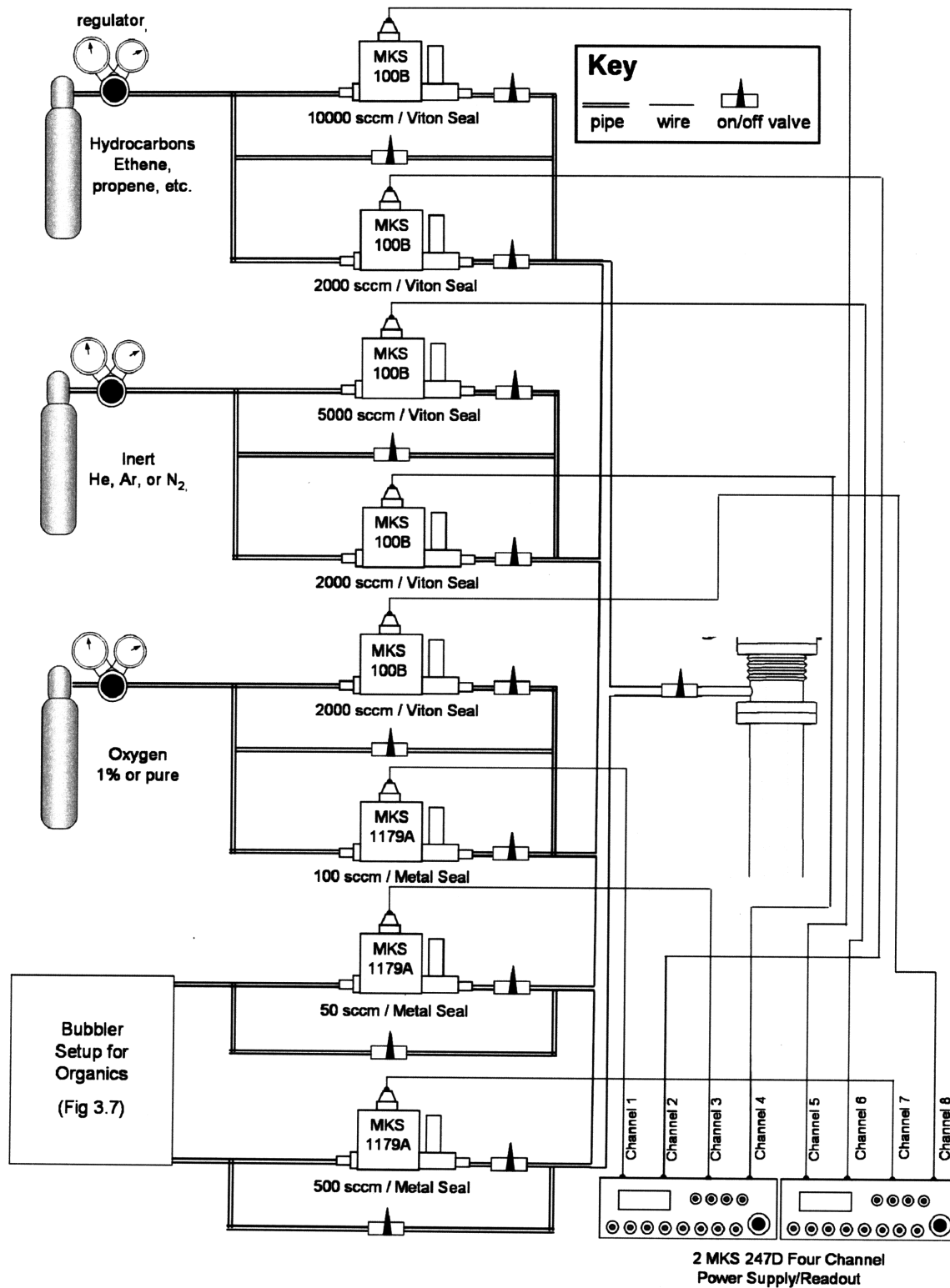


Figure 3.6: Diagram of the flow control system.

vessel – AF0096) can be connected directly to the flow controller. This setup is ideal for vinyl iodide, which has a $P_{vap} = 220$ Torr at room temperature and $P_{cell} \leq 100$ Torr.

If P_{cell} is greater than P_{vap} , then a bubbler must be used. As shown in Figure 3.7, the custom-designed bubbler is made by Lang Scientifics, a glass blowing company in Cleveland, TX. The bubbler is equipped with a special pressure equalization valve to prevent any forward or back flow of the organic liquid. The bubbler also has an extra opening to monitor the bubbler pressure ($P_{bubbler}$). The pressure inside the bubbler is regulated using a low pressure regulator (1 atm to vacuum), which is connected to the inlet of the bubbler. The outlet of the bubbler is directly connected to a MKS 1179A (500 sccm) flow controller. This bubbler setup is ideal for systems like allyl iodide, which has a $P_{vap} = 50$ Torr at room temperature and $P_{cell} = 100$ Torr.

The concentration of the organic ($c_{organic}(bubbler)$) inside the flow cell, if the bubbler setup is used, can be calculated using the following equation:

$$c_{organic}(bubbler) = \frac{P_{cell}}{RT_{cell}} \left(\frac{\dot{n}_{organic}}{\dot{n}_{total}} \right) \left(\frac{P_{vap}}{P_{bubbler}} \right) \quad (3.2)$$

where $\dot{n}_{organic}$ is the molar flow-rate of the reactants through the flow controller attached to the bubbler and \dot{n}_{total} is the total molar flow.

The internal pressure of the reactor is measured by two capacitance manometers: 100 and 1000 Torr (MKS Baratron[®] 223). The pressure is controlled with an automated Intellisys IQ throttling butterfly valve from Nor-cal. The butterfly valve is controlled by an Adaptive Pressure Controller (APC) also purchased from Nor-Cal. The APC takes in the pressure readings from

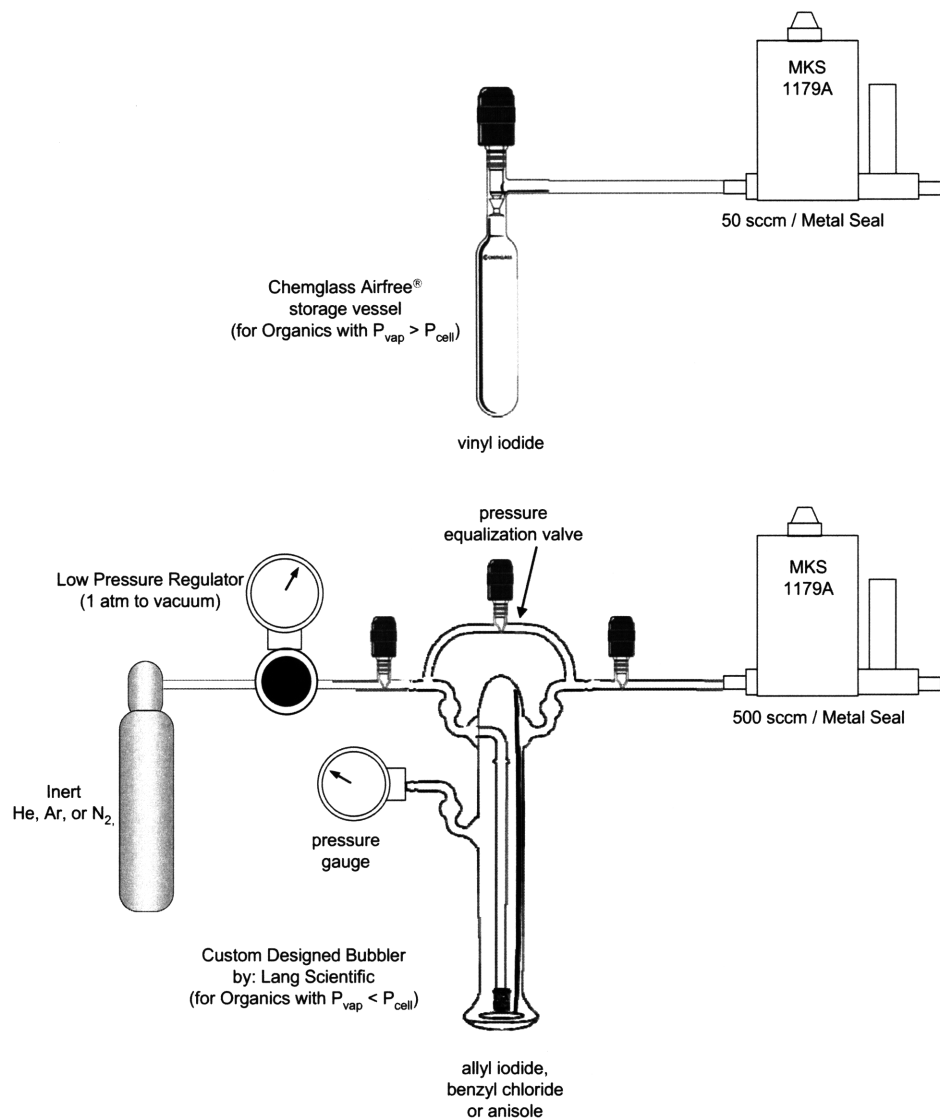


Figure 3.7: Diagram of the bubbler setup.

both Baratron, and automatically controls the butterfly valve angle to achieve a preset pressure. Both the flow controllers and automatic butterfly valve are set and adjusted via computer interface. In the present setup, the minimum achievable pressure is 10 mTorr, which is limited by the root blower vacuum system. The maximum pressure is 760 Torr. To perform experiments at higher pressures, all the fittings in the flow cell would need to be changed from ISO to Conflat flanges.

3.8. Temperature control system

It is advantageous to have a flat and controllable temperature profile across the flow cell. Version 1 of the instrument had various hot and cold temperature zones. Also, heating the flow cell to reproducible temperatures was very difficult. To address this issue, a new temperature controlled system has been incorporated in the present version of the spectrometer, as illustrated in Figure 3.8.

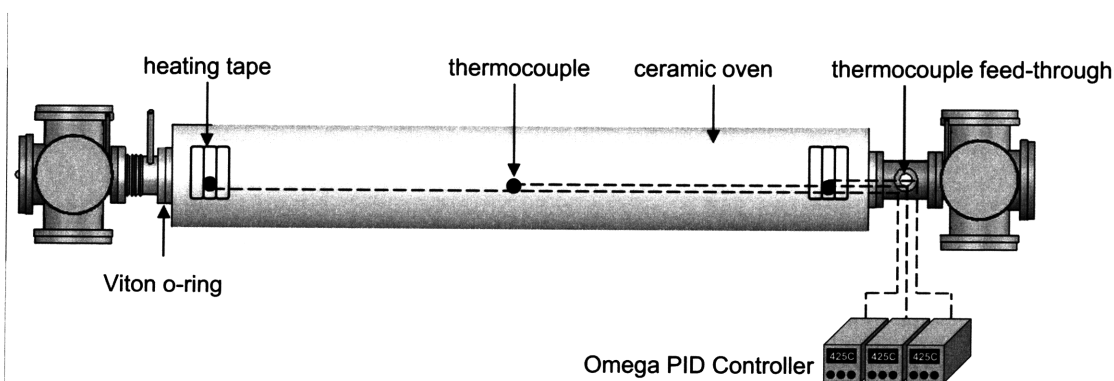


Figure 3.8: Diagram of the temperature control system.

The flow reactor is housed in a 2500 Watt cylindrical ceramic fiber heater, purchase from Watlow (VS103J40JA). The 1.2 meter heater is capable of reaching temperatures over 1200 C, but the oven alone does not provide a completely flat temperature profile over its entire length, since ambient conditions cool the two ends of the flow cell. This leads to a temperature profile that peaks in the center. Therefore, additional resistive heating is supplied using Omega heating tape at the reactor entrance and exit region, to flatten the temperature profile. Figure 3.9 shows the temperature profile provided by this three heater setup. The temperature profile is taken with a thermocouple vacuum feed-through, which can be translated in the longitudinal axial direction using Cajon[®] fitting. The ISO-100 to 1/4 inch Cajon[®] coupler is attached to one of the six-way crosses. The temperature probe is translated every 1 inch under typical experimental condition of 100 Torr total pressure and 3000 sccm of He flow to acquire the temperature profile shown in Figure 3.9.

A flat temperature profile of 700 ± 7 K is maintained over ~60 cm. The heating tapes are spaced 80 cm apart. A small temperature lag occurs on the inlet side because the cool gas entering the flow cell must be heated. This lag can be reduced by preheating the gas before it enters the flow cell.

The highest temperature achieved in the present setup is 725 K. At higher temperatures, the viton o-rings, which connect the center tube to the two six way crosses which house the Herriott mirrors, start to melt. It might be possible to achieve higher temperatures by either using Kalrez[®] o-rings or a metal-glass-metal connection (as long as the organic of interest does not thermally decompose).

The entrance, center, and exit temperatures are monitored using K-type thermocouples, which probe the temperature inside the flow cell. The fiber glass insulated thermocouples inside the flow cell connect to a thermocouple feed-through, which attach to plastic insulated thermocouple at ambient condition. These thermocouples are fed into three independent Omega PID controllers (CN 76030). The PID controllers turn on and off the power to the heat elements via a solid state relay (SSR330DC25). The power to the heating elements is supplied via three independent Variacs. The Variacs supplying power to the cylindrical oven and the two heating tapes are set at 90% and 60% current setting respectively.

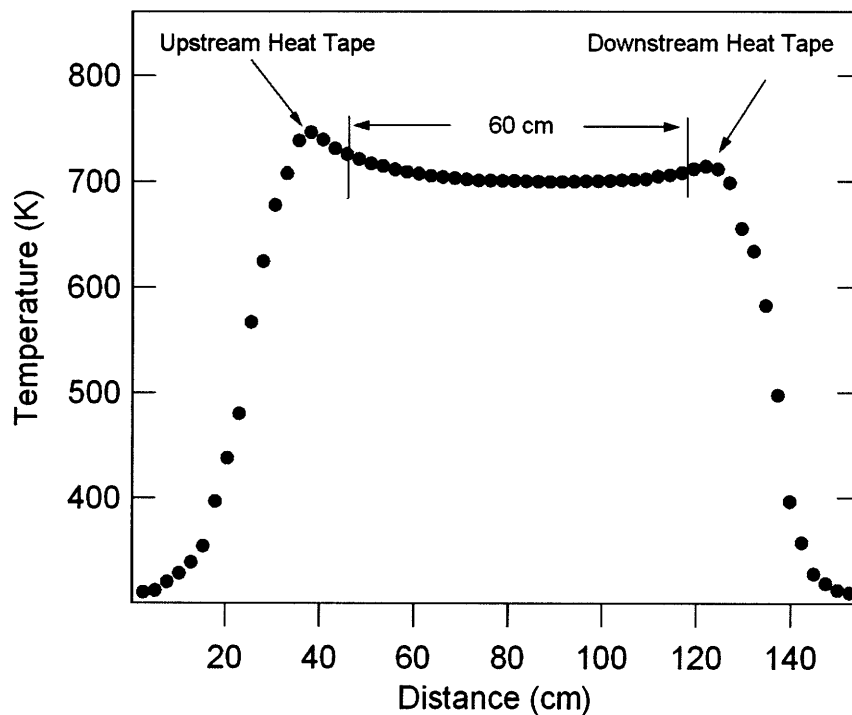


Figure 3.9: Temperature profile along the longitudinal axis of the flow cell under experimental conditions of 100 Torr and 3000 sccm of He flow. The temperature profile is taken with a thermocouple vacuum feed-through, which can be translated in the longitudinal axial direction using Cajon[®] fitting. The ISO-100 to 1/4 inch Cajon[®] coupler is attached to one of the six-way crosses. The temperature probe is translated every 1 inch to acquire this Figure.

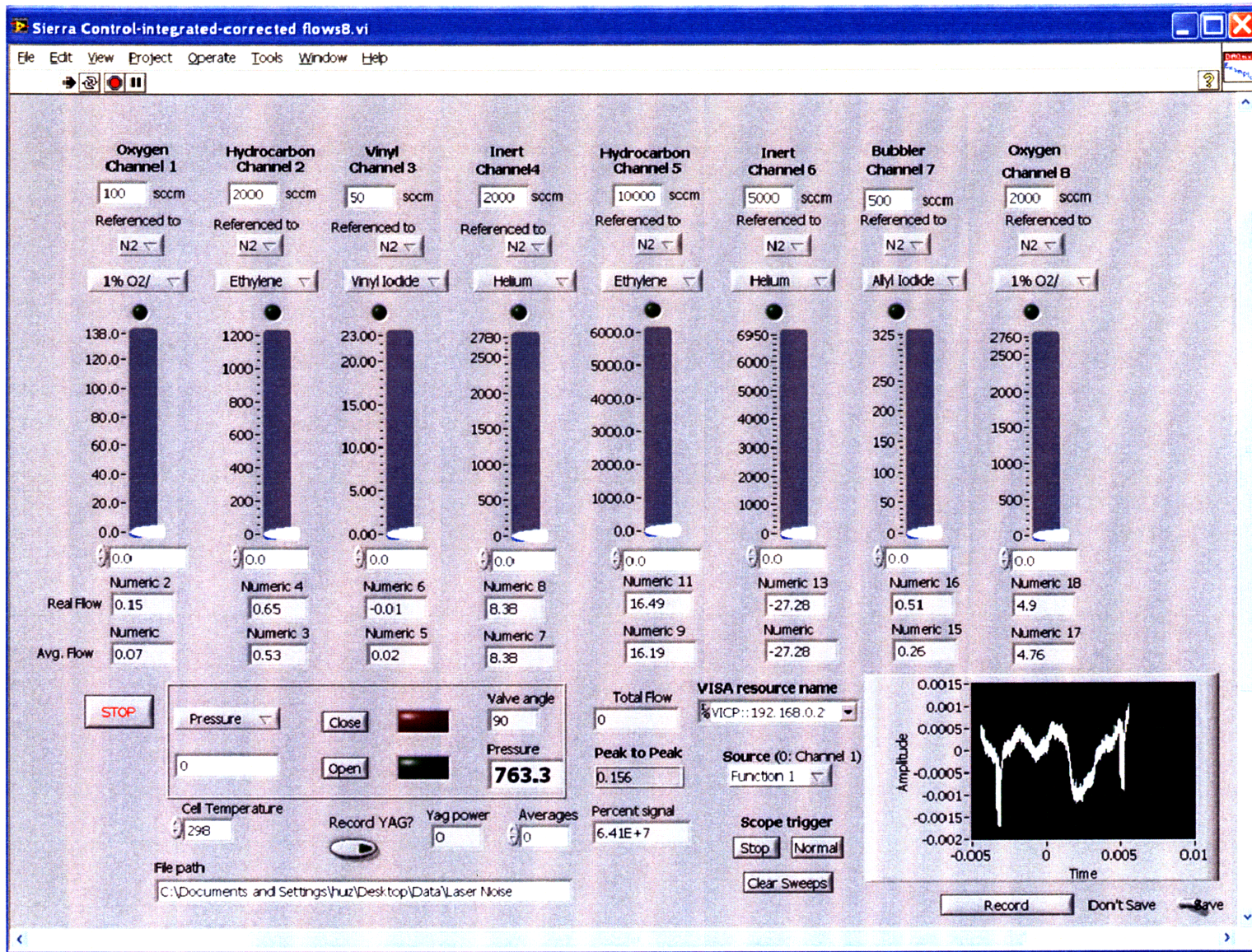
3.9. Automation & acquisition

The screen shot for the software written to control the entire laser kinetics spectrometer is shown in Figure 3.10. The software is written in LabView version 7.1. This software performs the following functions:

- Controls all eight of the flow controllers (MKS 247 D)
- Automatically corrects for the flow correction factors of various gases flowed in the cell.
- Controls the pressure (Norcal APC)
- Monitors the photolysis power (Ophir Optronics).
- Acquires data traces from the digital oscilloscope (LeCroy WaveRunner 6000 A)
- Saves the data traces along with experimental conditions (concentrations, pressure, temperature, photolysis power) in IGOR format.

To address the issue of signal digitization error, as discussed in Section 2.4.2.4, a new LeCroy 1 GHz digital oscilloscope (WaveRunner 6000 A) is incorporated in this instrument.

Figure 3.10: Instrumental control software written in LabView.



3.10. Validation

The spectrum of vinyl radical is ideal for such a probe laser, because its absorption features are broader than the laser FWHM, yet still narrow enough to allow tuning off resonance, as shown in Figure 3.11. The off-resonance signal contains contributions from thermal lensing noise; the vinyl concentration is taken to be proportional to the difference in absorption between traces taken on- and off-resonance.

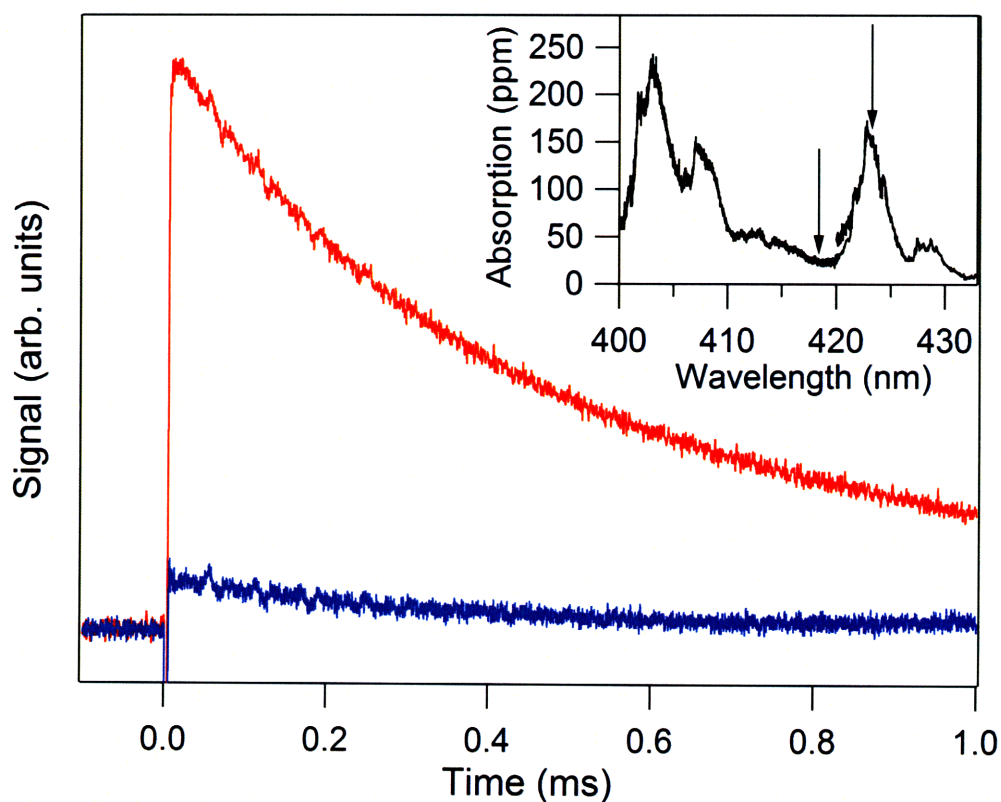


Figure 3.11: The red trace is on resonance of C_2H_3 at 423.2 nm. The blue trace is off resonance taken at 418.0 nm. The inset shows a section of the vinyl radical absorption spectrum as reported by Shahu et al.,⁶⁰ with the probe wavelengths of the two traces shown by vertical arrows.

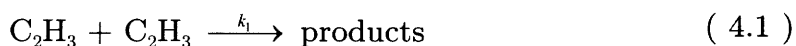
Chapter 4

4. Self Reaction of Vinyl Radical

4.1. Introduction

Reactions involving vinylic radicals are central to understanding the chemistry of planetary atmospheres and combustion processes. These reactions are important steps in carbon growth processes and soot formation⁶¹. The simplest radical of this class is vinyl (C_2H_3), which plays a pivotal role in O_2 starved environments where it decomposes to acetylene and ultimately forms soot. If O_2 is present, it burns cleanly to form CO_2 . Despite its importance, relatively little experimental work has been performed on vinyl chemistry. This lack of attention is primarily due to the difficulty in cleanly generating vinyl radicals, and due to the difficulties in detecting this radical.

There have been several studies for the self reaction of vinyl radical:



presented in the literature⁶²⁻⁶⁷. However the reported rate constants differ by a factor of 20. A complication with a second order chemical system is that it requires an accurate determination of the initial radical concentration. Three previous direct measurements^{62-64,66} had major uncertainties in the initial radical

concentration. MacFadden and Currie⁶² observed the decay of C_2H_3 via time-of-flight mass spectrometry where the initial concentration of vinyl radical ($[C_2H_3]_0$) was estimated based on the decrease in precursor ($C_2H_3OC_2H_3$) concentration, assuming unit quantum yield for C_2H_3 formation. Fahr *et al.*⁶³ measured the self reaction rate of vinyl radical via vacuum-UV flash photolysis-kinetic spectroscopy. They determined $[C_2H_3]_0$ using extinction coefficients of vinyl absorption line at 164.71 and 168.33 nm by determining the yield of 1,3 butadiene. The extinction coefficients had significant uncertainty. Their experiments were also prone to background absorption interference in the vacuum UV. More recently, Thorn *et al.*⁶⁶ determined k_1 using the discharge-flow kinetic technique coupled to mass spectrometric detection of the vinyl radical at low pressure. $[C_2H_3]_0$ was determined via direct titration. They reported an uncertainty of 33% in the self-reaction rate constant.

In the present work, vinyl iodide is used as a clean source to generate vinyl radical. One advantage of these experiments is that the production of I atoms can be optically probed at 1315.2 nm to determine the initial concentration of vinyl radical by assuming $[I]_0=[C_2H_3]_0$. The time-resolved vinyl radical concentration is fitted to a second order kinetic equation to extract the self-reaction rate constant.

4.2. Experimental details

The experimental apparatus and procedure are described in Chapter 3. The apparatus is slightly modified by the addition of a New Focus Vortex narrow line width, low noise diode laser tuned to the ($F=3 \ ^2P_{1/2} \leftarrow F=2 \ ^2P_{3/2}$) I

atom atomic transition, as shown in Figure 4.1. Direct absorption by both vinyl radicals and I atoms was used to monitor the vinyl + vinyl reaction.

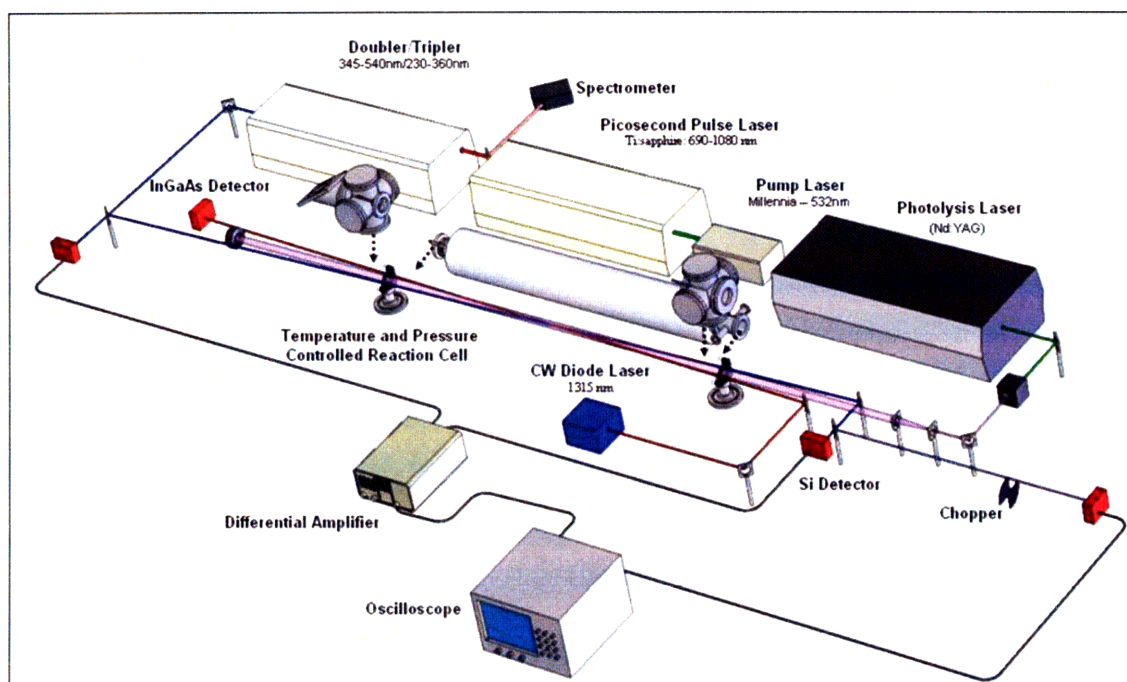
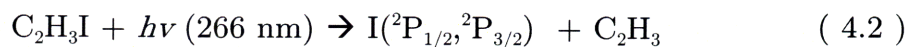


Figure 4.1: Diagram of experimental apparatus with I-atom probe laser

Vinyl radical (C_2H_3) was generated via laser photolysis of vinyl iodide at 266 nm:



Photolysis pulses were generated by frequency-doubling the 532 nm output of a short pulse Nd:YAG laser.

Chemicals were purchased from the following suppliers: $C_2H_3I \geq 85.0\%$ (Oakwood), Calibrated 1% O_2 with balanced He (Airgas), He $\geq 99.999\%$ (5.0

grade, Airgas). Vinyl iodide was processed through a freeze-pump-thaw apparatus to remove oxygen and other impurities.

The I atom probe laser was aligned through multiple apertures of the multiple pass cell to allow both lasers to probe the same reaction volume. I atoms were probed by single pass laser absorption using an external-cavity diode laser on the ($F=3 \ ^2P_{1/2} \leftarrow F=2 \ ^2P_{3/2}$) transition at 1315.28 nm. The laser was maintained at the absorption frequency by manually adjusting the laser frequency until the maximum absorption signal was achieved.

Initial vinyl radical concentrations were taken to be equal to the initial concentration of I atoms produced by the photolysis pulse. Upon photolysis, the I atoms generated from vinyl iodide are produced in both the $^2P_{3/2}$ ground state and the $^2P_{1/2}$ excited state. Three different methods were used to determine $[I]_0$:

$$[I]_0 = [I(^2P_{3/2})] + [I(^2P_{1/2})] \quad (4.3)$$

In the first method, O_2 was used to quench $I(^2P_{1/2})$ to ground state. Enough O_2 was used to ensure that the quenching rate was greater than other I loss channels. The oxygen concentration was varied from $(0.5 - 60) \times 10^{14}$ molecules cm^{-3} to determine $I^* \rightarrow I$ rate constant (k_2):



Oxygen, however also reacts very quickly with vinyl. It was not possible to quench the I atoms and measure vinyl + vinyl simultaneously, so the two measurements had to be made a few minutes apart. Fluctuations in flow conditions and photolysis power contributed to the error in determining $[I]_0$. Therefore, in the second method, ethylene was used as an alternative gas to

quench $I^* \rightarrow I$, since it reacts with vinyl much more slowly at room temperature than oxygen⁶⁸.

Ethylene concentrations were varied from $(0.9 - 30) \times 10^{15}$ molecules cm^{-3} to determine $I^* \rightarrow I$ quenching rate constant: k_3 .



All the experiments to determine quenching rate constants were conducted at room temperature, 20 Torr of pressure and two different vinyl iodide concentrations 9×10^{14} and 5×10^{15} molecules cm^{-3} .

In the third method, laser gain versus absorption spectroscopy was used to determine the $I(^2P_{1/2}, ^2P_{3/2})$ branching ratio (Φ_{I^*}) for vinyl iodide defined as:

$$\Phi_{I^*} = \frac{[I(^2P_{1/2})]_0}{[I(^2P_{3/2})]_0 + [I(^2P_{1/2})]_0} \quad (4.6)$$

The procedure for the determination of (Φ_{I^*}) is outlined in great detail by Leone and colleagues^{69,70}, who redefined Φ_{I^*} in terms of ratio of the two experimental amplitudes, the initial prompt signal before any quenching (S_i) and the final signal (S_f), which is proportional to the total I-atom concentration from photolysis. Using relations between absorption and stimulated emission cross sections and accounting for statistical weights, Leone *et al.*^{69,70} derived:

$$\Phi_{I^*} = \frac{1}{3} \left[\frac{S_i}{S_f} + 1 \right] \quad (4.7)$$

Zou *et al.*⁷¹ recently measured Φ_{I^*} for vinyl iodide upon photolysis at 266 nm. But in order to stay internally consistent, a series of experiments were

conducted in the present study to measure Φ_{I^*} . At high concentration of quenching gas, the S_i became indistinguishable from the $I^* \rightarrow I$ quenching rise time, therefore these experiments were conducted at various quenching gas concentrations ($[O_2] = (0.0 - 30) \times 10^{14}$ molecules cm^{-3} and $[C_2H_4] = (0.0 - 20) \times 10^{15}$ molecules cm^{-3}) to check for reproducibility of Φ_{I^*} . A typical transient is shown in Figure 4.2. Once Φ_{I^*} is known, the total I atom concentration can be calculated using:

$$[C_2H_3]_0 = [I]_0 = \frac{-\ln \left(1 - \frac{S_i / (3\Phi_{I^*} - 1)}{I_0} \right)}{\sigma_I \cdot \ell} \quad (4.8)$$

where I_0 is the initial probe laser power, σ_I is absorption cross section for I atom, and ℓ is the path length. The advantage of this technique is that, in principle, Φ_{I^*} can be determined in a single time-resolved transient signal. Also, Φ_{I^*} does not require knowledge of the absolute absorption or the path-length, since it is determined by the ratio of two signals. Though the fluctuations in flow conditions and photolysis power do not contribute, a disadvantage of this method is that the analysis is complicated by the fact that our measured signal is proportional to the difference between $[I(^2P_{3/2})]_0$ and $[I(^2P_{1/2})]_0$, and the need to extrapolate to $t=0$, which could lead to significant error in Φ_{I^*} .

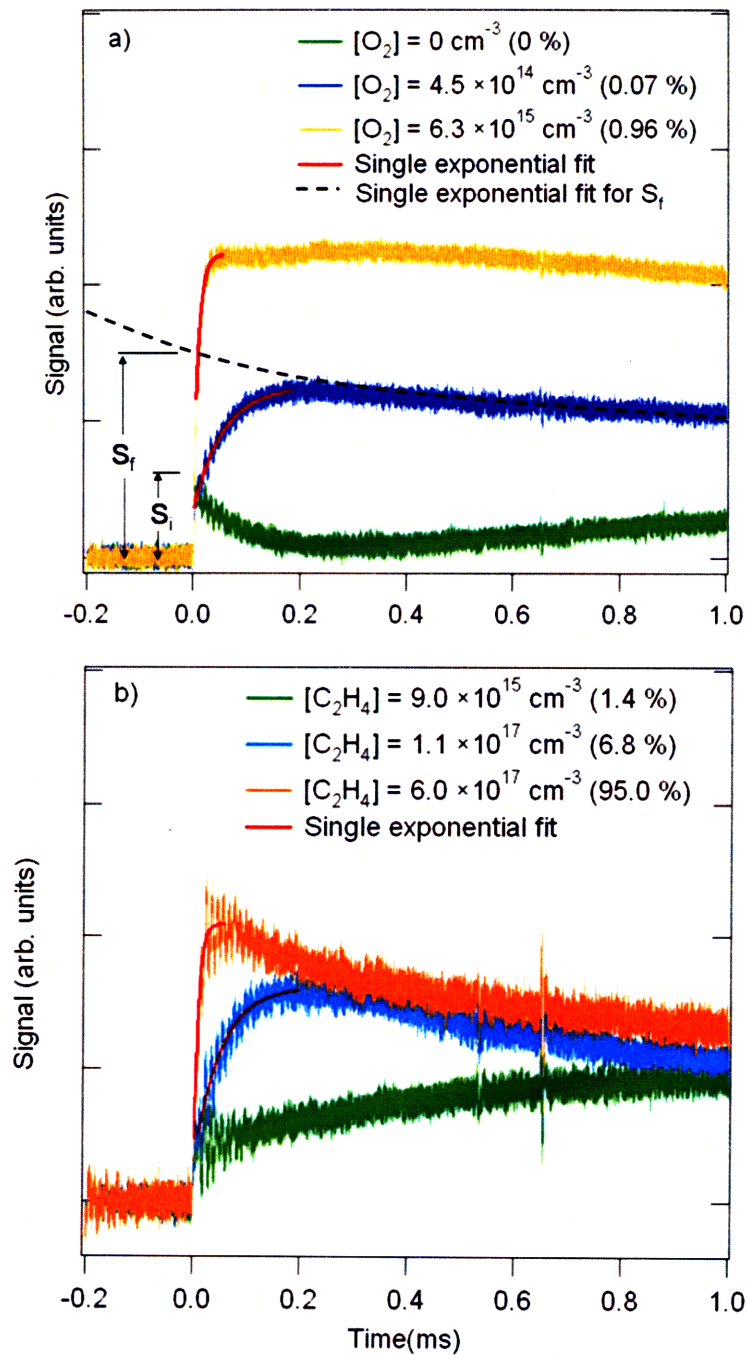


Figure 4.2: Transient absorption signal for I atom at 1315.14 nm upon photolysis of vinyl iodide at 266 nm. A prompt decay is observed on the 1315.14 nm probe laser. The $I(^2P_{1/2})$ atoms are quenched on a short time scale to yield ground state iodine atoms with a unit efficiency. $I(^2P_{3/2})$ population is solely removed via diffusion and recombination processes. O_2 (a) and ethylene (b) induced decay (S_i) and the total absorption (S_t) are obtained via back extrapolated based on single exponential fit (--).

Table 4.1: Experimental conditions for self reaction of vinyl radical

Probe Laser λ (mJ/pulse)	Photolysis energy (mJ/pulse)	YAG Diameter (cm)	$[\text{C}_2\text{H}_3\text{I}]$ (10^{15} cm^{-3})	$[\text{C}_2\text{H}_3]_0^a$ (10^{13} cm^{-3})	I overlap (cm)	Probe Laser Overlap (cm)
404	27	1.75	0.9 – 5.0	0.4 – 2.0	71	4330
404	24	1.25	0.9 – 5.0	0.6 – 4.0	44	2620
404	32	1.25	0.9 – 8.0	0.8 – 10	44	2620
423.2	28	1.75	0.9 – 5.0	0.4 – 2.0	71	4330
423.2	25	1.25	0.9 – 5.0	0.6 – 4.0	44	2620
423.2	32	1.25	0.9 – 8.0	0.8 – 10	44	2620
423.2	11-32	1.75	4.0	1.1 – 4.0	71	4330
445	27	1.75	0.9 – 5.0	0.4 – 2.0	71	4330
455	23	1.25	0.9 – 5.0	0.6 – 4.0	44	2620
445	31	1.25	0.9 – 8.0	0.8 – 10	44	2620

^a Determined using I atom concentration

The unquenched and quenched I traces were taken in every experiment; therefore all three methods were applied to determine $[C_2H_3]_0$ to every reaction condition. The kinetics experiments were performed at 293 K and 20 Torr of total pressure. All together, ten different combinations of experiments were conducted under various conditions. The summary of all these experiments are shown in Table 4.1.

In all the experiments, the concentration of vinyl iodide ranged from $(0.9 - 6.4) \times 10^{15}$ molecules cm^{-3} which yielded vinyl radical concentration ranging from $(0.5 - 1.0) \times 10^{13}$ molecules cm^{-3} . Photolysis power was varied from 11 to 32 mJ per pulse in order to verify that no competing photochemical effects were being observed. Measurements were made at two photolysis beam diameters, 1.25 and 1.75 cm in order to verify that the measured spatial overlap of the probe and photolysis beams were accurate. Photolysis power, power density and precursor concentrations gave initial vinyl concentrations of $(0.16 - 10) \times 10^{13}$ molecules cm^{-3} . Vinyl radicals were detected by multiple pass laser absorption at one of three absorption lines, 404 nm, 423.2 nm, and 445.0.⁶⁰ Multiple absorption lines were used to avoid systematic error due to the background absorption by a product species.

All three methods described above require an accurate value for the absorption cross section of I atom (σ_I). Ha *et al.*⁷² have reported line strength parameters for (I $^2P_{1/2} \leftarrow I ^2P_{3/2}$) transition at 1.3 μm . We assumed the hyperfine sub-levels to be in thermal equilibrium. Under atmospheric conditions, the I-atom line shape is given by Voigt profile (Fv) which describes the combined effects of Doppler and pressure broadening effects on the

absorption lines. To calculate F_V , we used the approximation by Whiting⁷³, which is accurate within 3%. F_V is given by:

$$\begin{aligned}
F_V(\tilde{\nu}) = & \left(1 - \frac{w_c}{w_v}\right) \exp\left\{-4 \ln 2 \left(\frac{\tilde{\nu} - \tilde{\nu}_0}{w_v}\right)^2\right\} \\
& + \left(\frac{w_c}{w_v}\right) \left[\frac{1}{1 + 4 \left(\frac{\tilde{\nu} - \tilde{\nu}_0}{w_v}\right)^2}\right] + 0.016 \left(1 - \frac{w_c}{w_v}\right) \left(\frac{w_c}{w_v}\right) \\
& \times \left\{ \exp\left(-4 \ln 2 \left(\frac{\tilde{\nu} - \tilde{\nu}_0}{w_v}\right)^2\right) - \frac{10}{10 + \left(\frac{\tilde{\nu} - \tilde{\nu}_0}{w_v}\right)^{2.25}} \right\}
\end{aligned} \tag{4.9}$$

The $\tilde{\nu}_0$ is the central wavenumber of the transition in units of cm^{-1} . The half width (w_v) of the Voigt profile is also given by Whiting⁷³ by the following approximation:

$$w_v = \frac{w_c}{2} + \sqrt{\left(\frac{w_c}{2}\right)^2 + w_d^2} \tag{4.10}$$

The w_d and w_c are respectively half widths of a purely Doppler and a purely collision broadened spectral line. The half width due to Doppler broadening⁷⁴ of any given spectral line can be calculated for any given temperature as:

$$w_d(T) = \frac{2\sqrt{2R\ln 2}}{c} \tilde{\nu}_0 \sqrt{\frac{T}{M}} \tag{4.11}$$

where, R is the gas constant and M is atomic weight of the I atom.

The expression for the collision broadening w_c is given by⁷⁵:

$$w_c(T, P) = w_{c_0} \frac{P}{P_0} \left(\frac{T_0}{T} \right)^n \quad (4.12)$$

The collision broadening of the spectral line by foreign gas molecules depends not only on temperature, but also on the number density of the collision partners. The collision cross sections are very difficult to calculate, since they are based on intermolecular potentials. They have to be determined experimentally for individual background gases. Therefore, the w_{c_0} is measured based on reference conditions T_0 and P_0 . For I atom, Davis *et al.*⁷⁵ report collision broadening parameters with various bath gases including He, N₂ and O₂. Unfortunately, collision broadening parameters for C₂H₄ have not been reported in the literature. We assumed the C₂H₄ to have the same collision broadening parameters as N₂. We believe this assumption leads to an additional 10% uncertainty if method #2 is used to determine $[I]_0$.

Using half widths w_v and w_c , the line shape factor of a Voigt line a_v can be calculated⁷³:

$$a_v = 1.065 + 0.447 \frac{w_c}{w_v} + 0.058 \left(\frac{w_c}{w_v} \right)^2 \quad (4.13)$$

Finally, for any single hyperfine atomic non overlapping line, the effective I cross section at line center is derived to be:

$$\sigma_{eff}(\tilde{\nu}_0) = \frac{\sigma_{tot}}{a_v} \quad (4.14)$$

The σ_{tot} is an integrated absorption cross section for ($I \ ^2P_{1/2} \leftarrow I \ ^2P_{3/2}$) transition of the I-atom as determined by Ha *et al.*⁷². The effective I atom cross section was calculated for every reaction condition at which we conducted the experiments.

To determine k_1 , the rate law equation is integrated to obtain the time-dependent expression:

$$\begin{aligned}
 C_2H_3 + C_2H_3 &\xrightarrow{k_1} Products \\
 \frac{d[C_2H_3]}{dt} &= -k_1[C_2H_3]^2 \\
 \frac{d[C_2H_3]}{[C_2H_3]^2} &= -k_1 dt \qquad (4.15) \\
 \frac{1}{[C_2H_3]_t} + \frac{1}{[C_2H_3]_0} &= -k_1 t \\
 [C_2H_3]_t &= \frac{1}{1 + 2k_1[C_2H_3]_0 t}
 \end{aligned}$$

To determine k_1 the transient vinyl absorption signals are normalized to 1 and fitted to a second order decay:

$$[C_2H_3]_t = \frac{1}{1 + 2k't} \qquad (4.16)$$

where $k' = k_1[C_2H_3]_0$. In principle this second-order rate constant, k' could include contributions from $C_2H_3 + I \rightarrow C_2H_3I$. However, we observe that C_2H_3 decays on a sub-millisecond timescale, while the I atom persists for ~ 5 ms, indicating that $C_2H_3 + I$ is much slower than $C_2H_3 + C_2H_3$. Dividing k' by $[I]_0$ yields the true

rate coefficient k_1 , since $[C_2H_3]_0 = [I]_0$. A typical transient absorption signal of vinyl radical and the second order fit with residuals are shown in Figure 4.3.

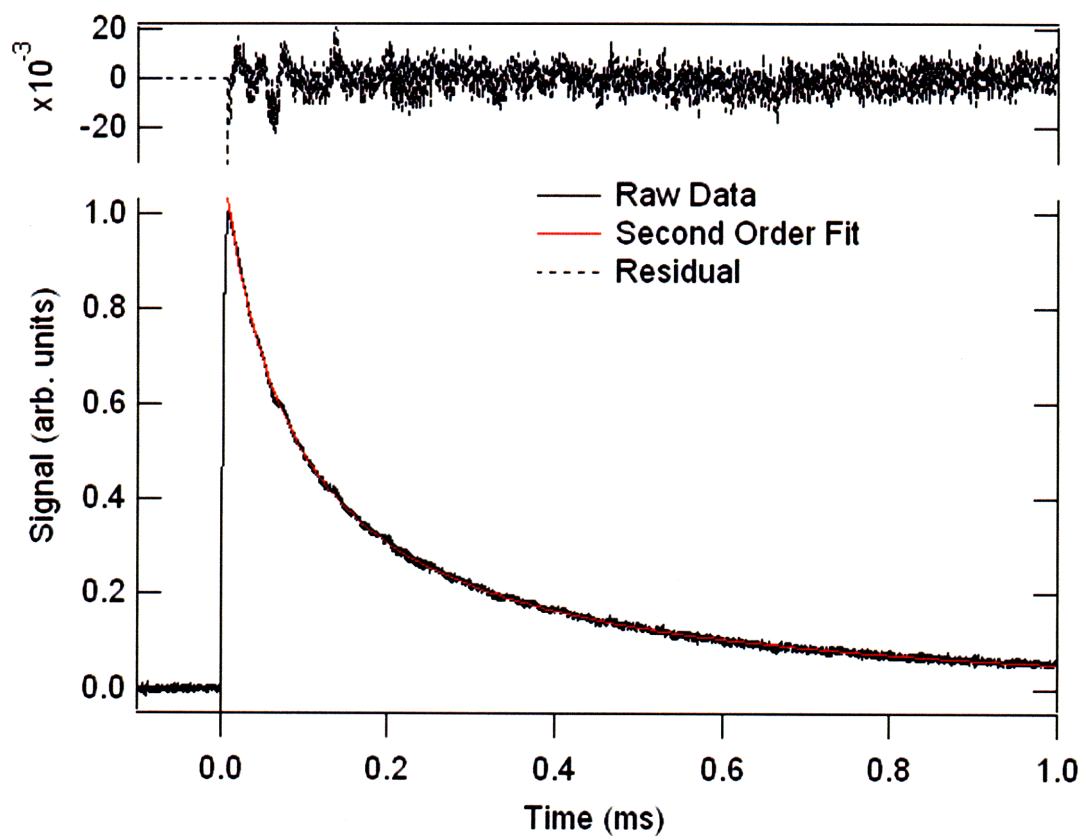


Figure 4.3: Transient absorption signal for vinyl radical. The second order fit to the decay is shown as a red line, with the corresponding residuals shown on top.

4.3. Results

4.3.1. I* quenching and Φ_{I^*} (C₂H₃I) determination

4.3.1.1. Method #1:

To determine the initial concentration of vinyl radical, three different methods were used. In the first two methods, various concentrations of quenching gases were used to determine optimal conditions to run the experiment. Transient absorption of I atom at various quenching gas concentrations is shown in Figure 4.2. The prompt decay immediately after the photolysis pulse occurs from the balance between stimulated emission from the excited level (²P_{1/2}) and absorption from the ground state (²P_{3/2}) for the I atoms. The second decay after the prompt decay occurs due to the quenching of excited I* atoms to ground state I atom by collisions with the bath gas. Oxygen is found to be a much more efficient quencher than ethylene, which is why a much higher [C₂H₄] is required to quench the I atoms. By assuming pseudo first order kinetics and fitting the second decay to a single exponential, also shown in Figure 4.2, quenching rates of I* by O₂ are determined. Plotting k' vs. [O₂] yields a straight line with constant slope, as shown in Figure 4.4. The I* quenching rate by O₂ is observed to be:

$$k_2 = (2.8 \pm 0.1) \times 10^{-11} \text{ cm}^3 \text{ molecule}^{-1} \text{ s}^{-1} \quad (4.17)$$

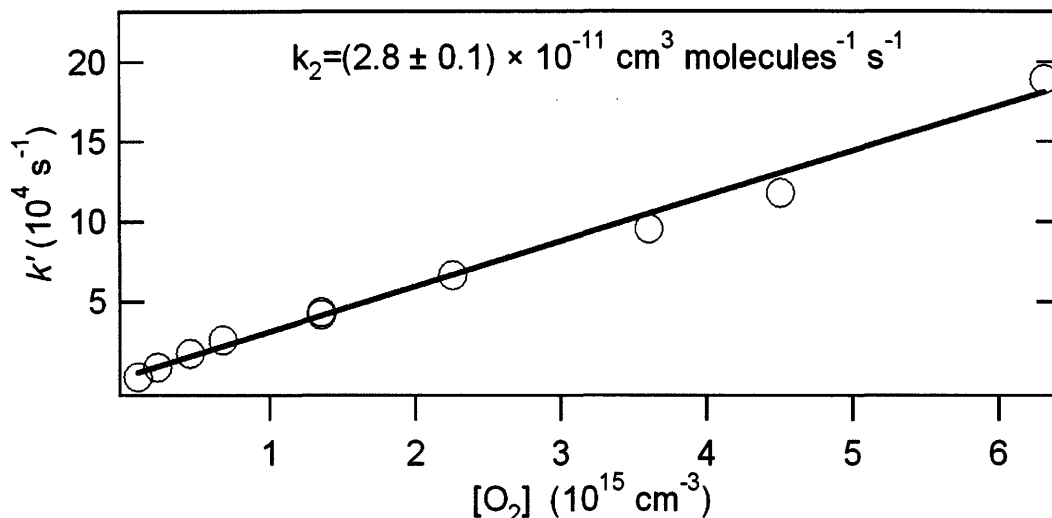


Figure 4.4: Pseudo-first-order I* quenching rate k' vs. $[O_2]$ at a temperature of 293 K and a pressure of 20 Torr

The I* quenching rate by O_2 has been reported previously in the literature^{70,76}. Burde *et al.*⁷⁶ photolyzed I_2 and probed 206.2 nm excited absorption line $I(6s^2P_{3/2}) \leftarrow I(5p^5P_{1/2})$ via vacuum UV monochrometer. They determined the quenching rate $k_2 = 2.5 \times 10^{-11} \text{ cm}^3 \text{ molecule}^{-1} \text{ s}^{-1}$. Hess *et al.*⁷⁰ produced I* via photolysis of CH_3I and $i-C_3F_7I$ and probed I atom via direct absorption at 1315 nm. Hess *et al.*⁷⁰ found $k_2 = 3.0 \times 10^{-11} \text{ cm}^3 \text{ molecule}^{-1} \text{ s}^{-1}$. Our results are situated right in the middle of these two previous studies.

In the first method, under our experimental conditions, 0.5-1.0% O_2 was found to be optimal to quench the majority of $I^* \rightarrow I$ and determine $[I]_0$. Above 1.0% O_2 concentration, a third decay was observed in the transient absorption of I atom, which we attribute to secondary I atom production from O_2 photolysis. This phenomenon is shown in Figure 4.5:

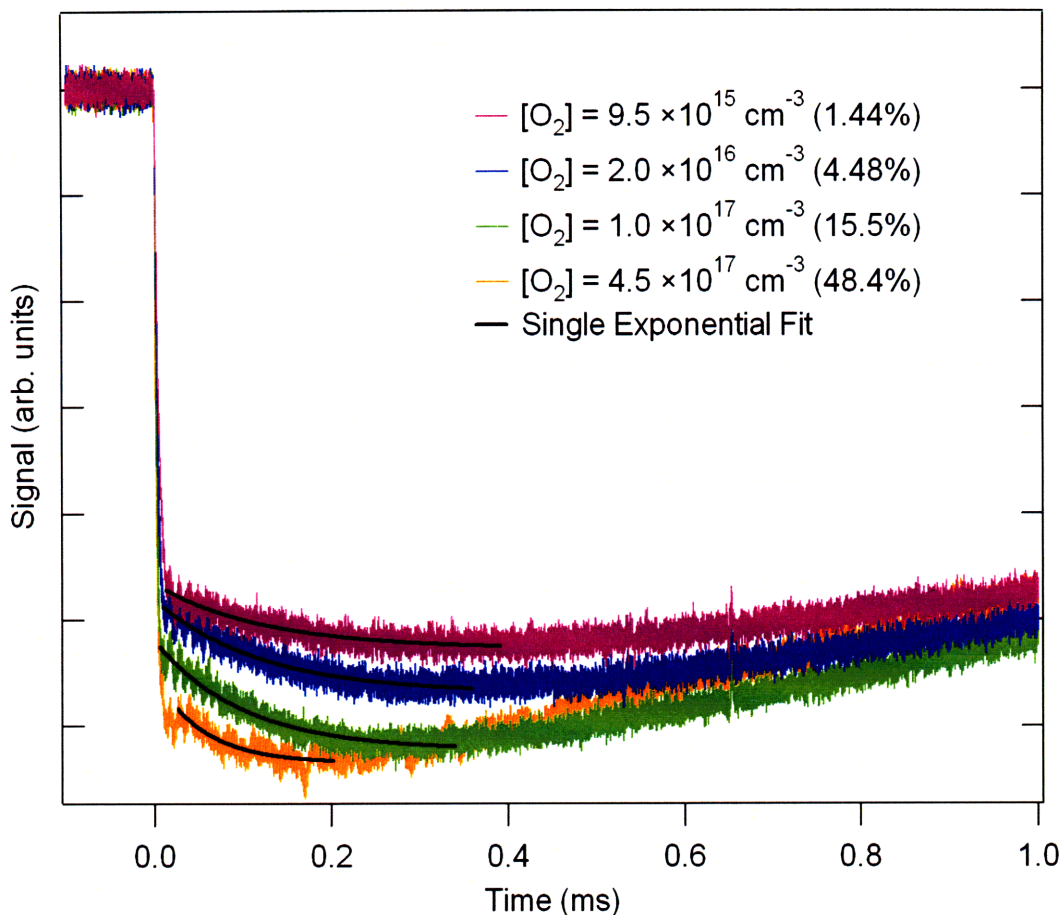
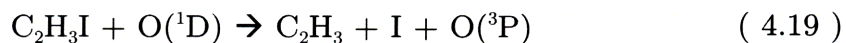
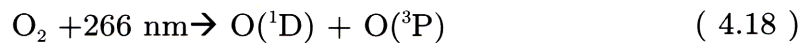


Figure 4.5: I traces with $[\text{O}_2]$ higher than 1%

Treating this third decay as pseudo first order led to an effective rate constant of $2 \times 10^{-14} \text{ cm}^3 \text{ molecule}^{-1} \text{ s}^{-1}$. The exact cause of this third decay is unknown, but we believe that additional I-atoms might be produced by following reactions:



The effective rate constant we are measuring is a combination of these two reactions. Therefore, to minimize secondary chemistry, in all I* quenching experiments for vinyl iodide, [O₂] below 1% was used.

In this first method, an additional source of uncertainty comes from flow and photolysis pulse fluctuations between the experiments which contribute to about 3% percent uncertainty in [I]₀.

4.3.1.2. Method #2:

In the second method, the optimal ethylene mole fraction was found to be between 40-95%. Plotting k' vs. [C₂H₄] yields straight line with constant slope, as shown in Figure 4.6.

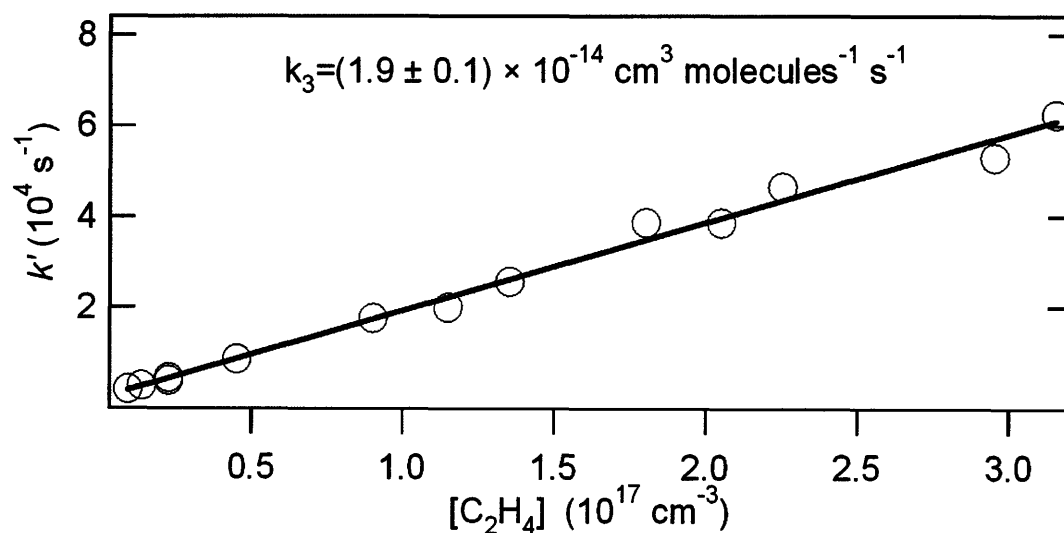


Figure 4.6: Pseudo-first-order plot of I* quenching rate k' vs. [C₂H₄] at a temperature of 293 K and a pressure of 20 Torr

The ethylene quenching rate for I* is measured to be:

$$k_3 = (1.9 \pm 0.1) \times 10^{-14} \text{ cm}^3 \text{ molecule}^{-1} \text{ s}^{-1} \quad (4.20)$$

To our knowledge, k_3 has never been reported in the literature. The error reported in k_2 & k_3 are based from 95% confidence intervals in the fits. As seen in Figure 4.2b, the high $[\text{C}_2\text{H}_4]$ led to oscillating acoustic noise in the transient I signal, which led to significant uncertainty in $[\text{I}]_0$. The reason ethylene was used as a quenching gas was that it allowed us to take both transient absorptions of vinyl radical and I atom simultaneously, but high $[\text{C}_2\text{H}_4]$ also led to beam steering of the blue probe laser which led to other uncertainties.

4.3.1.3. Method #3:

The third method used to determine $[\text{I}_0]$ was to determine the branching ratio of I* to I (Φ_{I^*}) by running a series of separate experiments. The advantage of this method is that simultaneous measurement of I atom and vinyl signal avoids problems due to fluctuations in flow conditions and photolysis laser power. Using equation (4.7), we determined:

$$\Phi_{\text{I}^*}(\text{C}_2\text{H}_3\text{I}) \text{ at } 266 \text{ nm} = 0.25 \pm 0.06 \quad (4.21)$$

The $\Phi_{\text{I}^*}(\text{C}_2\text{H}_3\text{I})$ was determined at various $[\text{O}_2]$ and $[\text{C}_2\text{H}_4]$. The error reported is based on the standard error. These results are within the error of $\Phi_{\text{I}^*} = 0.27 \pm$

0.01, reported by Zou *et al.*,⁷¹ who used a similar technique to the present study to determine Φ_{I^*} . The ~30% uncertainty in k_1 comes primarily from the large uncertainty in Φ_{I^*} . We believe the lower standard error Φ_{I^*} reported by Zou *et al.*⁷¹ occurs because they did not vary the quenching gas concentration as we did in the present study.

4.3.2. Vinyl radical self reaction rate constant (k_1)

To determine the self reaction rate constant for vinyl radical (k_1), all three methods were used to determine $[C_2H_3]_0$ were applied to every experimental trace. Table 4.2 summarizes the results. We found that all these experiments yielded values of k_1 within 15%, regardless of the method we used to analyze the signal. One of the principal sources of uncertainty in determining k_1 comes from the uncertainty in $[C_2H_3]_0$. In all three methods used to determine $[C_2H_3]_0$, a dominant source of uncertainty came from the uncertainty in σ_I . Ha *et al.*⁷² did not report error bars in the line strength for the ${}^2P_{1/2} \leftarrow {}^2P_{3/2}$ transition of the I atom, but Davis *et al.*⁷⁵, reported the uncertainties for the temperature-dependent-collision-broadening parameters, which yielded a propagated uncertainty of ~10% in σ_I . The combined effect of Doppler and pressure broadening effects on the I atom absorption line is given by the Voigt profile. The half width of the Voigt profile is calculated according to the approximation calculated by Whiting *et al.*⁷⁷ This approximation has an error of ~3%. The combined effect led to a propagated uncertainty of ~11% in k_1 .

Table 4.2: Determination of k_1 using various methods to determine $[C_2H_3]_0$

Vinyl Self Reaction Rate Constant $k_1 \pm \text{error (cm}^3/\text{molecules/s)}$			
	Average Rate	Average Propagated Error (Percentage)	Standard Error (Percentage)
Method #1 (Using 1% O ₂)	6.4×10^{-11}	$\pm 7.2 \times 10^{-12}$ ($\pm 12\%$)	$\pm 7.0 \times 10^{-12}$ ($\pm 12\%$)
Method #2 (Using C ₂ H ₄)	6.6×10^{-11}	$\pm 1.7 \times 10^{-11}$ ($\pm 25\%$)	$\pm 1.2 \times 10^{-11}$ ($\pm 18\%$)
Method #3 (Using ($\Phi_{1^*}=0.25$))	6.7×10^{-11}	$\pm 2.0 \times 10^{-11}$ ($\pm 30\%$)	$\pm 1.3 \times 10^{-11}$ ($\pm 20\%$)
Zou <i>et al.</i> ⁷¹ (Using ($\Phi_{1^*}=0.27$))	5.5×10^{-11}		

As seen in Table 4.2, method 1 yields the smallest values for propagated and standard error in k_1 . The large errors in method 2 and 3 occur because of acoustic noise caused by ethylene in the transient absorption signal and error in Φ_{1^*} . Since the 1% oxygen method yielded less error, we recommend using this method to determine $[C_2H_3]_0$. The self reaction rate constant and the cross section of vinyl radical determined using this method will be considered for the rest of the discussion.

The present study finds the mean k_1 at 293 K to be:

$$k_1 = (6.4 \pm 0.7) \times 10^{-11} \text{ cm}^3 \text{ molecule}^{-1} \text{ s}^{-1} \quad (4.22)$$

A summary k_1 vs $[\text{C}_2\text{H}_3]_0$ at room temperature is shown in Figure 4.7. The error limits are based on 1σ standard deviation based on the average of all the runs. Likewise, the propagated error based on 1% O_2 method also yields ~12% error in k_1 .

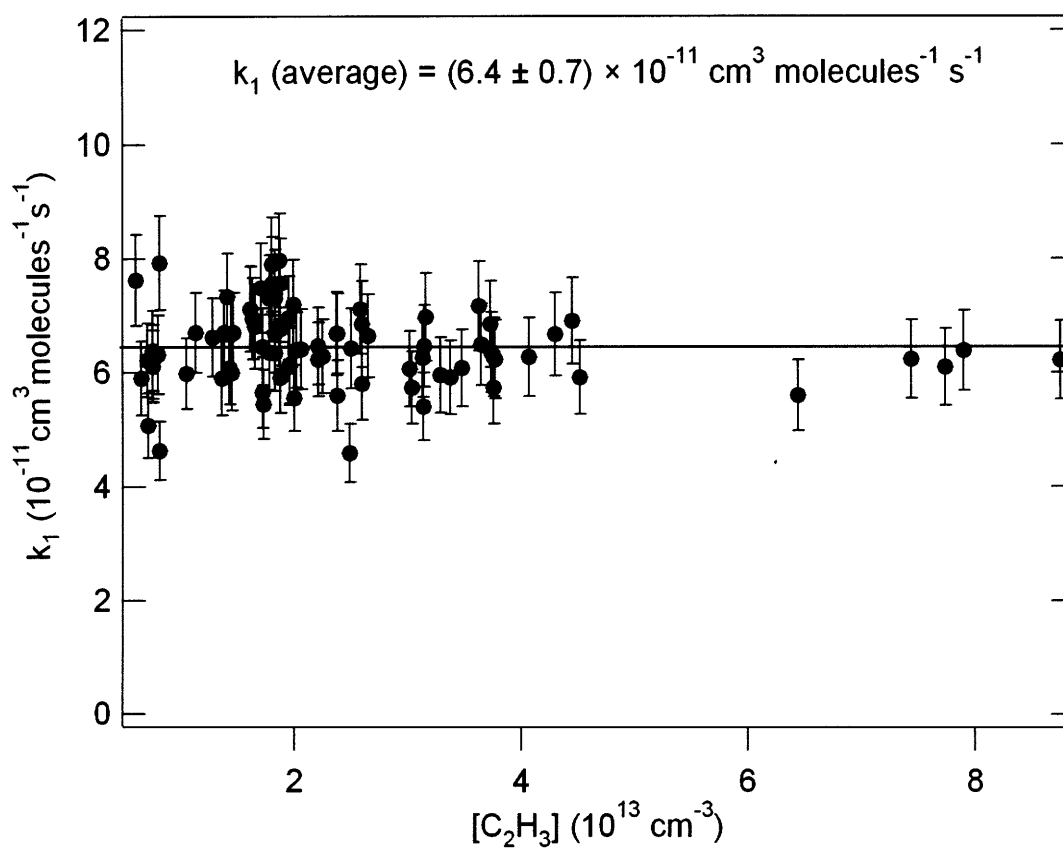


Figure 4.7: Measured rate constant for the self reaction of vinyl radical at various initial vinyl concentrations. The error bar on each data point is based on propagated error.

4.3.3. Vinyl radical spectrum & visible cross section

The visible/near ultraviolet absorption spectrum of vinyl radical has been studied by several authors previously. Hunziker *et al.*⁷⁸ generated vinyl radical by mercury-sensitized photo-chemical modulation. They observed a visible absorption structure, with band origin at 499.5 nm, which was attributed to electronic transition between the ground (\tilde{X}^2A') and the first excited state (\tilde{A}^2A'') of the vinyl radical. Hunziker *et al.*⁷⁸ reported the spectrum at a low resolution of 1.6 nm, which peaked at 400 nm. Pibel *et al.*⁵⁴, used tunable dye laser with cavity ring-down spectroscopy (CDRS) and reported visible vinyl spectrum between 415 nm and 530 nm at a resolution of 0.002 nm. They calculated the band origin rotational contour, using an excited state geometry calculated by Mebel *et al.*⁷⁹. The modeled spectrum had reasonable agreement with the observed experimental spectrum. Tonokura *et al.*⁵⁸ also measured the vinyl spectrum from 440-460 nm using CDRS and determined the cross section at 446.5 nm. Recently, Shahu *et al.*⁸⁰ extended upon Pibel's work and reported vinyl absorption high resolution vinyl radical spectrum from 385-530 nm. Shahu *et al.*⁸⁰ found the first four vibrational features of the vinyl radical $\tilde{A} \leftarrow \tilde{X}$ transition. In the present study, we have acquired low resolution spectrum of vinyl radical from 395 nm to 480 nm. This spectrum compares well with Shahu *et al.*⁸⁰ as shown in Figure 4.8. The present study did not conduct any vibronic analysis.

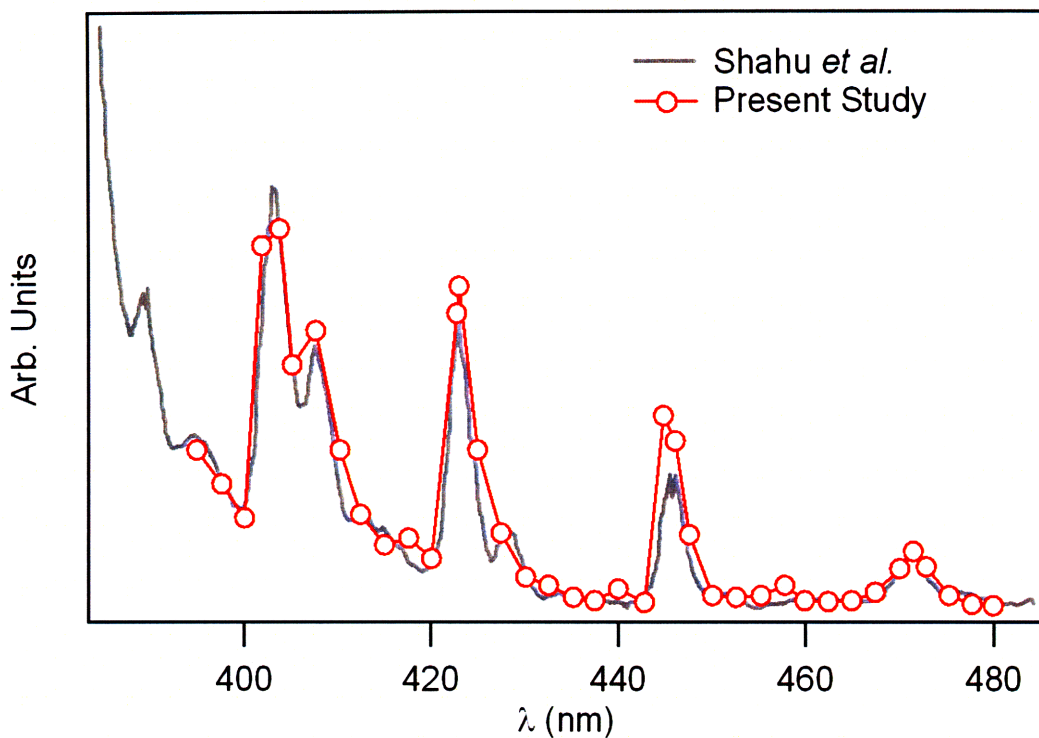


Figure 4.8: Low resolution spectrum attained in the present study for vinyl radical and it is compared to high resolution spectrum by Shahu *et al.*⁸⁰

Additionally, using direct absorption by I atom, we determined the vinyl radical absolute absorption cross section at three different probe wavelengths.

From Beer's Law, we can solve for $\sigma_{C_2H_3}$:

$$\sigma_{C_2H_3} = \frac{-A_{C_2H_3}}{[I]_0 \times \ell} \quad (4.23)$$

where, ℓ is path length of the probe laser for vinyl radical, $A_{C_2H_3}$ is the base e absorbance ($A = -\ln(I/I_0)$) for probe laser, and $[I]_0$ is the concentration of I atoms. The results from are summarized in Figure 4.9, where $\sigma_{C_2H_3}$ is shown vs. $[C_2H_3]$.

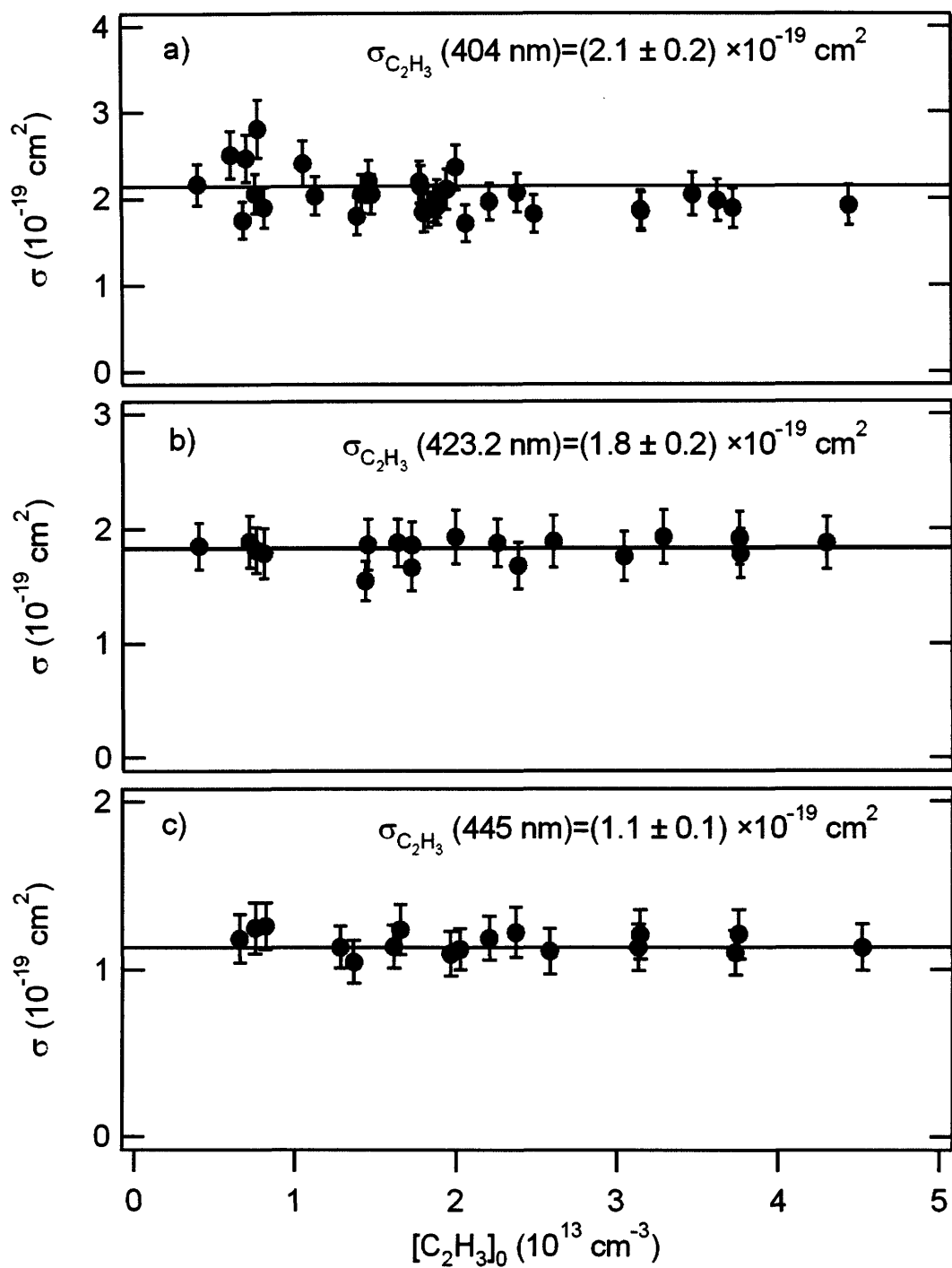


Figure 4.9: Plots of the absorption cross sections at 404nm (a), 423.2nm (b), and 445nm (c) for the vinyl radical as a function of initial vinyl concentration. The error bars are based on propagated error.

The photolysis power, photolysis diameter, and vinyl iodide concentration were varied to determine the reproducibility and consistency of $\sigma_{C_2H_3}$. The average cross-sections determined from all these measurements are:

$$\sigma_{C_2H_3}(404 \text{ nm}) = (2.1 \pm 0.2) \times 10^{-19} \text{ cm}^2 \quad (4.24)$$

$$\sigma_{C_2H_3}(423.2 \text{ nm}) = (1.8 \pm 0.2) \times 10^{-19} \text{ cm}^2 \quad (4.25)$$

$$\sigma_{C_2H_3}(445 \text{ nm}) = (1.1 \pm 0.1) \times 10^{-19} \text{ cm}^2 \quad (4.26)$$

The error reported is based on 1σ standard deviation. The spectrum of vinyl, published by several authors^{54,78,80} seems to suggest that the $\sigma_{C_2H_3}(445 \text{ nm})$ is about 70% smaller than the $\sigma_{C_2H_3}(404 \text{ nm})$. And, $\sigma_{C_2H_3}(445 \text{ nm})$ is approximately 30% smaller than $\sigma_{C_2H_3}(404 \text{ nm})$. Recently, DeSain³⁹ *et al.* reported the $\sigma_{C_2H_3}(404 \text{ nm}) = (2.9 \pm 0.8) \times 10^{-19} \text{ cm}^2$ using a similar technique to that in the present study. Using the spectrum and $\sigma_{C_2H_3}(404 \text{ nm})$ as reported by DeSain³⁹, we can estimate $\sigma_{C_2H_3}(423 \text{ nm})$ to be $2 \times 10^{-19} \text{ cm}^2$ and $\sigma_{C_2H_3}(446 \text{ nm})$ to be $0.9 \times 10^{-19} \text{ cm}^2$. Hunziker *et al.*⁷⁸ determined $\sigma_{C_2H_3}(445 \text{ nm})$ to be $0.8 \times 10^{-19} \text{ cm}^2$, which agrees well with previous spectra and DeSain³⁹. However, in a separate study, Tonokura *et al.*⁵⁸ determined the $\sigma_{C_2H_3}(446.5 \text{ nm}) = (4.8 \pm 0.3) \times 10^{-19} \text{ cm}^2$. They derived initial concentration of vinyl radical by back fitting the time dependent vinyl traces to a self reaction rate constant determined by Fahr *et al.*⁶⁴. To resolve all these discrepancies, we decided to measure $\sigma_{C_2H_3}$ at

all three wavelengths simultaneously using a more accurate way of determining $[\text{C}_2\text{H}_3]_0$.

Our results for $\sigma_{\text{C}_2\text{H}_3}$ (404 nm) agree to within 30% to the results from DeSain³⁹. Even though $\sigma_{\text{C}_2\text{H}_3}$ (423.2 nm) has never been reported in the literature, our results compare well to the estimate based on previous spectra and cross section of DeSain³⁹. Lastly, the $\sigma_{\text{C}_2\text{H}_3}$ (445 nm) determined by the present study is approximately 25% larger than the number reported by Hunziker *et al.*⁷⁸ Our results clearly disagree with Tonokura⁵⁸. The reliability of their method depends on the accuracy of the self reaction rate measured by Fahr *et al.*⁶⁴.

Potential sources of error in the $\sigma_{\text{C}_2\text{H}_3}$ determination include the uncertainty in I atom absorption cross section and loss of vinyl radical to secondary disassociation, which would lead to an underestimation of the visible cross section for vinyl radical.

4.4. Discussion

The self reaction of vinyl radical has been investigated previously by several authors⁶²⁻⁶⁷. The results from these studies have been summarized in Table 4.3. MacFadden and Currie⁶² measured k_1 to be $5.3 \times 10^{-12} \text{ cm}^3 \text{ molecule}^{-1} \text{ s}^{-1}$ using a time of flight mass spectrometer⁶². Tsang and Hampson⁶⁵ revised this value based on a thermochemical estimate of the self reaction rate to be $1.76 \times 10^{-11} \text{ cm}^3 \text{ molecule}^{-1} \text{ s}^{-1}$. Thorn *et al.*⁶⁶ determined k_1 to be $1.41 \times 10^{-10} \text{ cm}^3$

molecule⁻¹ s⁻¹ employing a discharge-flow kinetic technique, where a mass spectrometer was used to detect C₂H₃. Fahr and Laufer measured the self reaction rate to be 1.0×10^{-10} cm³ molecule⁻¹ s⁻¹ based on vacuum UV flash photolysis⁶³. Later, Fahr and coworkers revised this number after extensive literature review to be 1.21×10^{-10} cm³ molecule⁻¹ s⁻¹⁶⁷. Our study finds the vinyl radical self reaction rate to be a factor of 2 slower than the rate recommended by Laufer and Fahr⁶⁷.

Table 4.3: Comparison of self reaction rate of vinyl radical from literature and from the current study

	Method	Pressure	k_1 (cm ³ molecule ⁻¹ s ⁻¹)
MacFadden & Currie ⁶² (1972)	Time-of-flight mass spectrometry	65-200 mTorr	$(5.3 \pm 0.5) \times 10^{-12}$
Tsang & Hampson ⁶⁵ (1986)	Thermo-chemical Analysis		1.76×10^{-11}
Fahr & Laufer ⁶³ (1990)	Vacuum UV / Flash photolysis	400 Torr	$(1.0 \pm 0.25) \times 10^{-10}$
Thorn et. al. ⁶⁶ (1996)	Discharge-flow / Mass spectrometer	1 Torr	$(1.41 \pm 0.60) \times 10^{-10}$
Fahr & Laufer ⁶⁷ (2004)	Literature Review		$(1.2 \pm 0.3) \times 10^{-10}$
Present Study (2007)	Laser Photolysis / Laser absorption (using 1% O ₂)	20 Torr	$(6.4 \pm 0.7) \times 10^{-11}$

4.5. Conclusion

The recombination rate constant of vinyl radical has been studied at a temperature of 293 K and a pressure of 20 Torr using a novel low noise flash photolysis laser kinetic spectrometer. Vinyl iodide is incorporated as a precursor. Accurate determination of the initial radical concentration was obtained via direct laser absorption by I atom at 1315 nm. Vinyl radicals were probed at three different wavelengths: 404, 423.2, and 445 nm. The branching ratio between excited and ground state I atom production from 266 nm photolysis of vinyl iodide was found to be 0.25 ± 0.06 . Additionally, the quenching rate constant of $I^* \rightarrow I$ via oxygen and ethylene was found to be $k_2=(2.8 \pm 0.1) \times 10^{-11} \text{ cm}^3 \text{ molecule}^{-1} \text{ s}^{-1}$ and $k_3=(1.9 \pm 0.1) \times 10^{-14} \text{ cm}^3 \text{ molecule}^{-1} \text{ s}^{-1}$ respectively.

The self-reaction rate constant for vinyl radical at room temperature was found to be:

$$k_1=(6.4 \pm 0.7) \times 10^{-11} \text{ cm}^3 \text{ molecule}^{-1} \text{ s}^{-1} \quad (4.22)$$

These results are ~50% slower than the results in previous studies, but are superior measurements because of a more accurate measurement of initial vinyl radical concentration. Absorption cross sections of the vinyl radical at 404, 423.2, and 445 nm were also measured to be: $(2.1 \pm 0.2) \times 10^{-19} \text{ cm}^2$, $(1.8 \pm 0.2) \times 10^{-19} \text{ cm}^2$ and $(1.1 \pm 0.1) \times 10^{-19} \text{ cm}^2$ respectively at 293 K.

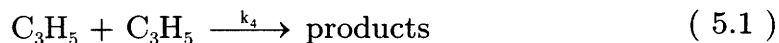
Chapter 5

5. Self reaction of allyl radical

5.1. Introduction

The reaction chemistry of allyl radical (CH_2CHCH_2) is interesting because it is one of the simplest resonantly-stabilized radicals. The resonance makes it unusually stable. Under combustion conditions, many resonantly-stabilized radicals accumulate and subsequently react via radical-radical processes. Edelson *et al.*⁸¹ showed that allyl radical has a fairly slow H abstraction rate constant, predominately due to its thermodynamic stability. Therefore, recombination reactions dominate in pyrolysis of C_n ($n \geq 3$) alkanes. Accurate determination of the allyl self-reaction rate constant is important for modeling such systems. The allyl + allyl reaction is one of the few resonantly-stabilized radical recombinations which have been studied using high level theoretical methods⁸². Recently, Klippenstein *et al.* applied variable reaction coordinate transition state theory (VRC-TST) to predict the self reaction rate of allyl radical. An accurate measurement of the rate would be very helpful in assessing the accuracy of the theoretical methods used by Klippenstein *et al.*

There have been several direct measurements of the self reaction of allyl radical in the literature⁸³⁻⁸⁹.



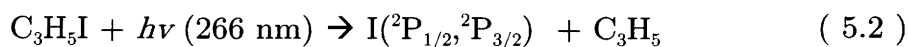
However, the same complication exists as seen in Chapter 4, for determining the rate constant for allyl radical, that it requires an accurate determination of the initial radical concentration. The accuracy of the self-reaction rate determined via spectroscopic techniques is therefore dependent upon the accuracy of absorption coefficient of the allyl radical. Almost 40 years ago, van den Bergh and Callear⁸⁴ measured the far ultraviolet (UV) spectrum and the room temperature allyl cross section ($\sigma_{\text{C}_3\text{H}_5}$) at 223 nm by referencing it to the UV absorption of co-produced methyl radicals. Tulloch *et al.*⁸⁶, using the laser flash photolysis technique, reported the allyl recombination rate constant over a temperature range of 295-571K by using van den Bergh and Callear's⁸⁴ UV absorption cross section for allyl, and assuming it to be independent of temperature. Jenkin *et al.*⁸⁷ also used laser flash photolysis to measure the far-UV spectrum, and derived $\sigma_{\text{C}_3\text{H}_5}$ at 220 nm and k_4 , relying on UV absorption of allyl iodide to calibrate their allyl radical spectrum. Most recently, Boyd *et al.*,⁸⁸ using flash-photolysis/UV absorption, determined allyl self reaction rate constant using the absorption cross section reported by Jenkin *et al.*⁸⁷ and determined the temperature dependence of k_4 again assuming the UV absorption of allyl is independent of temperature. Boyd's⁸⁸ rate constant agreed very well with Jenkin's⁸⁷ and Tulloch's⁸⁶ work.

The problem with the three previous studies is that they were based on determinations of the absolute UV absorption cross-section of allyl. Some were based on the literature absolute absorption coefficient of methyl radical, a measurement which could have significant uncertainty. Others were based on

the complicated de-convolution procedure of Jenkin *et al.*⁸⁷ Additionally, their experiments were also prone to background absorption interference due to the fact that many organic species have diffuse absorption in this spectral region. In the present work, laser photolysis of allyl iodide is used as a clean source to generate allyl radical. One advantage of these experiments is that the co-produced I atoms can be optically probed at 1315.28 nm to determine the initial concentration of iodine atoms. It is assumed that flash photolysis of allyl iodide produces equal concentrations of iodine atoms and allyl radicals. The near-IR absorption coefficient of I atoms is known much more precisely than the far-UV absorption coefficient of methyl or allyl iodide, so it provides a better absolute reference. Additionally, allyl radical is probed in the visible region of the spectrum at wavelengths of 404 and 407.5 nm, where there is a much lower probability of interference from other chemical species.

5.2. Experimental details

The same apparatus described in Section 4.1 and shown in Figure 4.1, was used to conduct experiments to determine the self reaction of allyl radical. Allyl radical (C_3H_5) was generated via laser photolysis of allyl iodide at 266 nm:



Allyl radicals were detected by multiple-pass laser absorption at one of two absorption lines, 404 nm and 407.5 nm^{30,39}.

Chemicals were purchased from following suppliers and were used without further purification: $C_3H_5I \geq 98.0\%$ (Sigma Aldrich), Calibrated 1% O_2 with balanced He (Airgas), $He \geq 99.999\%$ (5.0 grade, Airgas). At room temperature, allyl iodide has a vapor pressure ~ 25 Torr. Therefore, a bubbler setup, as described in Figure 3.7, was used to flow allyl iodide into the flow cell. The bubbler pressure was maintained at 750 Torr using a low pressure regulator.

The allyl self-reaction experiments were performed from 293 K to 550 K and 20 Torr of total pressure. As in the vinyl system, upon photolysis, the I atoms generated from allyl iodide are produced in both the $^2P_{3/2}$ ground state and the $^2P_{1/2}$ excited state. Therefore, method 1 and method 3, as discussed in Chapter 4, were used to determine $[I]_0$ (or $[C_3H_3]_0$). Since the quenching gas, oxygen, reacts with allyl it was not possible to quench the I atoms and to measure allyl + allyl simultaneously.

To determine Φ_{I^*} (C_3H_5I) for photolysis at 266 nm, the experiments were conducted at various O_2 concentrations (6×10^{14} - 6×10^{15} molecules cm^{-3}) to check Φ_{I^*} reproducibility. Once the yield of excited state I atoms (Φ_{I^*}) is known, the time-resolved absorption data for allyl and I atom can be acquired simultaneously with no O_2 present, and $[I]_0$ (where $[I]_0 = [C_3H_5]_0$) can be determined using equations (4.3), (4.6), and (4.7). The simultaneous measurement avoids problems due to fluctuations in flow conditions and photolysis power. The major source of error in this method is the experimental determination of Φ_{I^*} which causes an error in $[C_3H_5]_0$.

Table 5.1: Experimental conditions for the self reaction of allyl radical at 20 Torr.

Temperature (K)	Probe Laser λ (mJ/pulse)	Photolysis energy (mJ/pulse)	YAG Diameter (cm)	$[\text{C}_3\text{H}_5\text{I}]$ (10^{15} cm^{-3})	$[\text{C}_3\text{H}_5]_0^a$ (10^{13} cm^{-3})	I overlap (cm)	Probe Laser Overlap (cm)
293	407.5	28	1.65	0.2 – 1.9	0.6 – 3.0	70	3570
293	407.5	28	1.15	0.2 – 1.9	0.7 – 5.0	40	2345
293	404	24	1.65	0.2 – 1.9	0.6 – 3.0	70	3570
293	404	24	1.15	0.2 – 1.9	0.8 – 5.0	40	2345
350	407.5	29	1.65	0.3 – 1.9	0.6 – 3.3	70	3570
400	407.5	27	1.65	0.3 – 1.9	0.7 – 2.7	70	3570
450	407.5	29	1.65	0.9 – 1.9	0.6 – 2.5	70	3570
500	407.5	27	1.65	0.3 – 1.9	0.6 – 2.6	70	2310
550	407.5	27	1.65	0.2 – 1.9	0.5 – 2.3	70	2310

^a Determined using I atom concentration

Both methods 1 and 3 were applied for every reaction condition to determine $[C_3H_5]_0$. Experiments were performed under various concentrations of allyl iodide, at different photolysis pulse energies, at different photolysis beam diameters, and at two different visible probe wavelengths. Table 5.1 has a summary of all the experiments conducted at these various conditions.

To determine k_4 , the time dependent allyl absorption signal is normalized to 1 and fitted to a second order decay (equation (4.16)). In principle this second-order rate constant, k' could include contributions from $C_3H_5 + I \rightarrow C_3H_5I$. However, we observe that C_3H_5 decays on a sub-millisecond timescale, while the I atom persists for >5 ms, indicating that $C_3H_5 + I$ is much slower than $C_3H_5 + C_3H_5$. Dividing k' by $[I]_0$ yields the true rate coefficient k_4 , since $[C_3H_5]_0 = [I]_0$. A typical transient absorption signal of allyl radical and the second order fit with residuals are shown in Figure 5.1.

5.3. Results

5.3.1. Φ_{I^*} (C_3H_5I) determination

The quantum yields of the spin-orbit sublevels of I^* and I at 266 nm have been measured using transient gain vs. absorption spectroscopy. This technique is described in great detail in Chapter 4 and has been proven

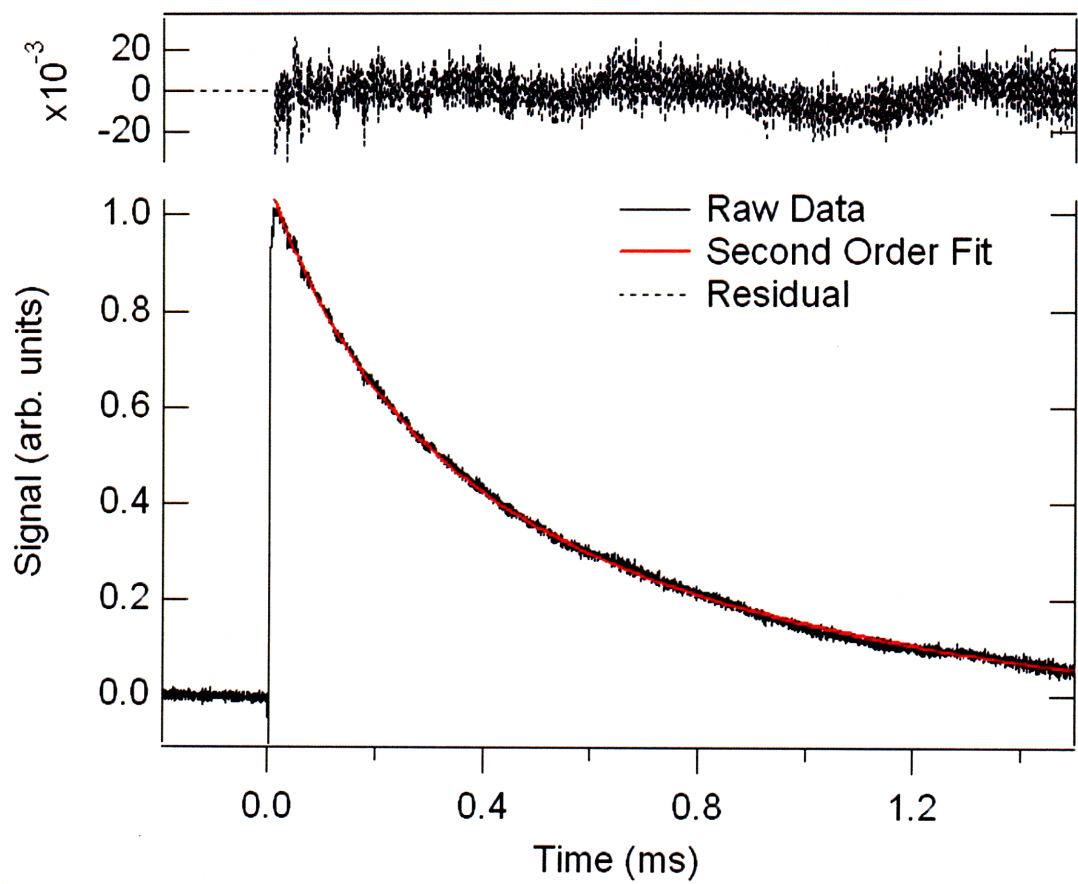


Figure 5.1: Transient absorption signal for allyl radical. The second order fit to the decay is shown as a red line, with the corresponding residuals shown on top.

accurate in several previous studies^{69,70} for spin-orbit sublevel quantum yield measurement of Br and I.

A typical transient absorption of I absorption signal after 266 nm photolysis of allyl iodide is shown in Figure 5.2 at various $[O_2]$. For the traces with no oxygen and $[O_2] = 1.6 \times 10^{15}$ molecules/cm³, the prompt gain immediately after the photolysis pulse occurs from the balance between stimulated emission from the $^2P_{1/2}$ excited level and absorption from the $^2P_{3/2}$ ground state for the I atoms. In comparison to the vinyl iodide system, in allyl iodide, significantly more I* are produced than ground state I atoms. As time evolves, the sign of the signal depends on the relative intensities of stimulated emission and absorption. The fast change in the gain occurs due to the quenching of excited I* atoms to ground state I atom by collisions with the bath gas. Oxygen is much more efficient quencher than helium, which is why the fast decay from prompt gain varies with $[O_2]$. The slow recovery of the signal at long time is due to diffusion and ground state I atom recombination.

The diode laser is tuned to a particular spin-orbit component of the hyperfine transition, measuring the difference in the populations of the corresponding hyperfine sublevels in the absorption signal of the I atom. Given the multiplicities of the hyperfine sublevels, and assuming that the sublevels are in thermal equilibrium, the branching ratio (Φ_{I^*}) can be calculated as stated in equation (4.7). In it, S_i represents the prompt signal before any quenching and S_f is proportional to the total I-atom concentration from photolysis. As shown in Figure 5.2, S_i and S_f at $t=0$ are experimentally determined by fitting the respective decays to a single exponential.

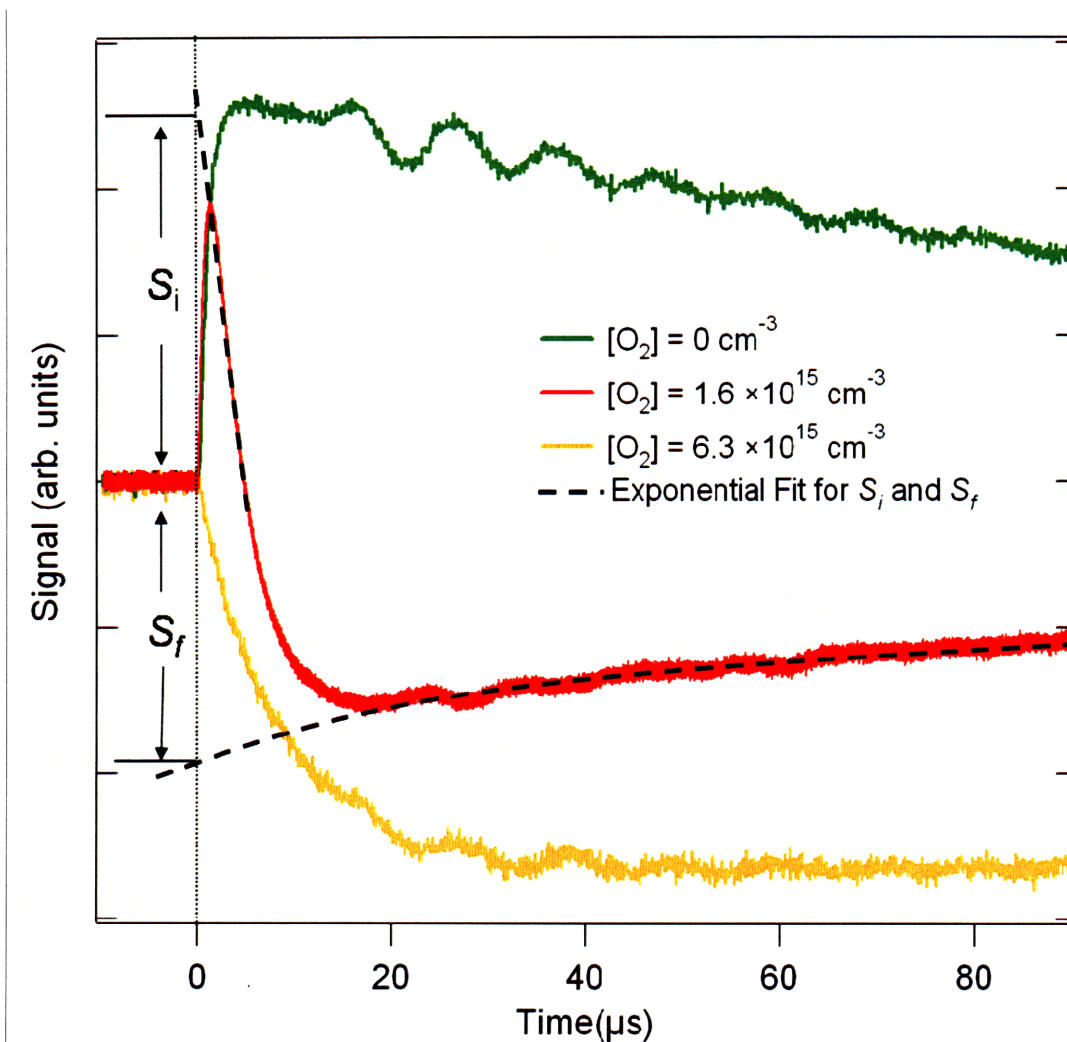


Figure 5.2: Transient absorption signal for I atom at 1315.14 nm upon photolysis of allyl iodide at 266 nm. All the traces were taken at room temperature, 100 Torr of total pressure, $[C_3H_5I] \approx 4 \times 10^{15}$ molecules/cm³, and $[C_3H_5] = 1.7 \times 10^{13}$ molecules/cm³. A prompt gain is observed on the 1315.14 nm probe laser. The $I(^2P_{1/2})$ atoms are quenched on a short time scale to yield ground state iodine atoms. $I(^2P_{3/2})$ population is removed via diffusion slowly and recombination processes. The signals S_i and S_f are obtained via extrapolating to $t=0$ based on single exponential fit (--).

The resulting branching ratio for allyl iodide at 266 nm is summarized in Figure 5.3.

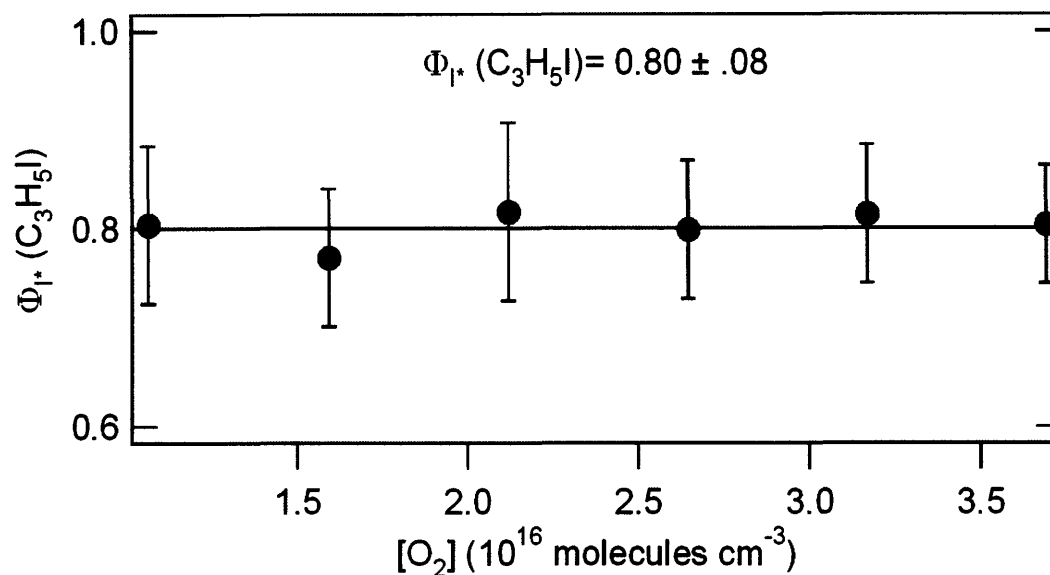


Figure 5.3: Branching ratio (Φ_{1^*}) for Allyl Iodide at 266 nm at various oxygen concentrations.

The average Φ_{1^*} from various $[O_2]$ yield:

$$\Phi_{1^*} (C_3H_5I) \text{ at } 266 \text{ nm} = 0.80 \pm 0.08 \quad (5.3)$$

The error in Φ_{1^*} is based on the standard deviation of several independent runs at various oxygen concentrations. To our knowledge, this is the first ever measurement reported for $\Phi_{1^*} (C_3H_5I)$ at 266 nm.

5.3.2. Allyl radical self reaction rate constant (k_4)

To determine the self reaction rate constant for allyl radical (k_4), two methods were used to determine $[C_3H_5]_0$. Table 5.2 summarizes the results at room temperature.

Table 5.2: k_4 determination using various methods to determine $[C_3H_5]_0$

Allyl Self Reaction Rate Constant $k_4 \pm \text{error (cm}^3/\text{molecules/s)}$			
	Average Rate	Average Propagated Error (Percentage)	Standard Error (Percentage)
Method #1 (Using O_2)	4.3×10^{-11}	$\pm 5.3 \times 10^{-12}$ ($\pm 12\%$)	$\pm 5.6 \times 10^{-12}$ ($\pm 13\%$)
Method #3 (Using ($\Phi_{1*}=0.80$))	4.4×10^{-11}	$\pm 7.5 \times 10^{-12}$ ($\pm 17\%$)	$\pm 6.9 \times 10^{-11}$ ($\pm 16\%$)

We found that all these experiments yielded the same self reaction rate constant (within 5%), regardless of the method we used to analyze the signal. The only difference is the error bars; therefore, all the uncertainties reported are based on the first method, which is slightly more precise in this case. Also, $[I]_0$ determined using O_2 as quenching gas, will be used to determine the self reaction rate constant and allyl cross section for the remainder of the discussion.

A summary of k_4 vs $[C_3H_5]_0$ at room temperature is shown in Figure 5.4.

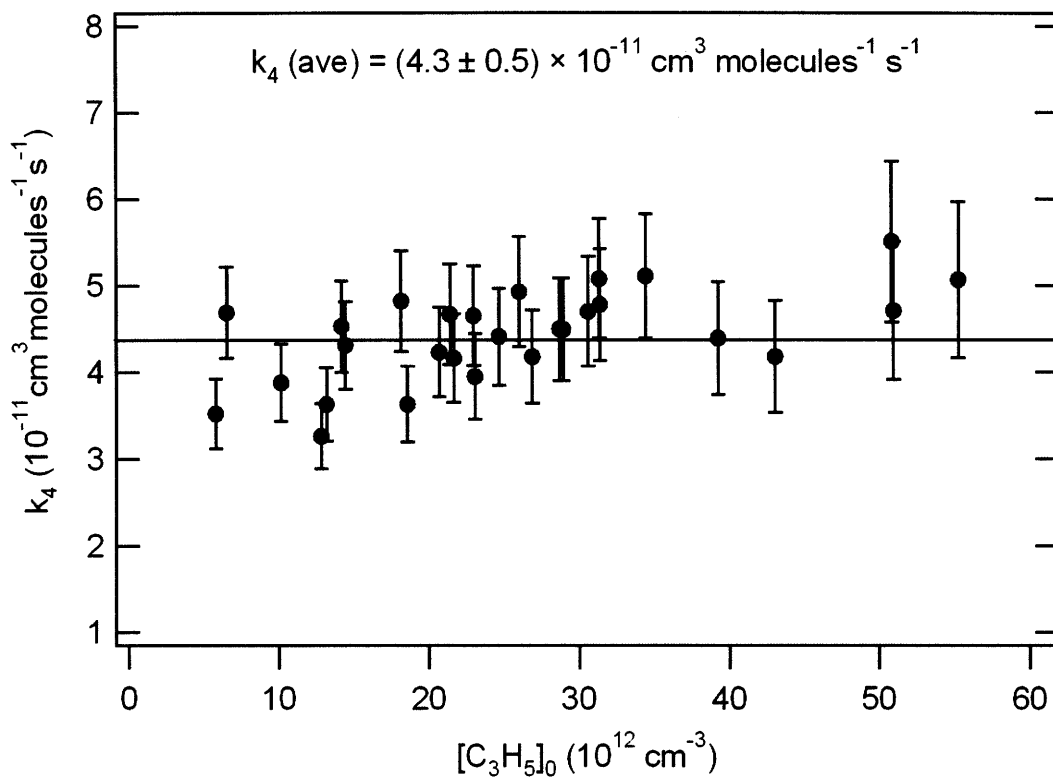


Figure 5.4: Measured rate constant for the self reaction of allyl radical at various initial allyl concentrations. The error bars on each data point are based on propagated error.

The present study finds the mean k_4 at 298 K to be:

$$k_4 = (4.3 \pm 0.5) \times 10^{-11} \text{ cm}^3 \text{ molecule}^{-1} \text{ s}^{-1} \quad (5.4)$$

The Arrhenius plot of k_4 is shown in Figure 5.5. The Arrhenius fit to the measured rate coefficient for reaction (5.1) at 20 Torr, weighted by the uncertainties in the individual data points, yields:

$$k_4 = (2.5 \pm 0.4) \times 10^{-11} \text{ cm}^3 \text{ molecules}^{-1} \text{ s}^{-1} \exp((174 \pm 40) \text{ K}/T) \quad (5.5)$$

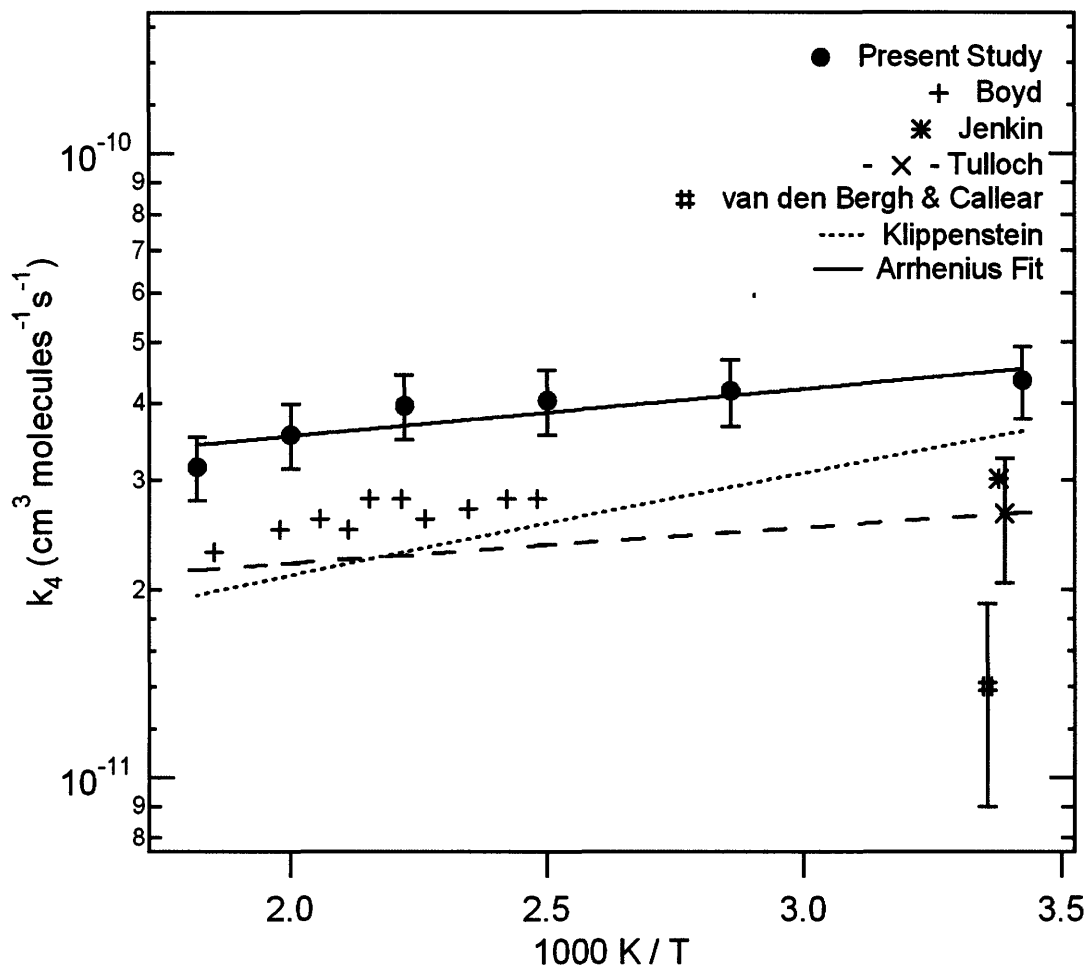


Figure 5.5: Temperature dependence of the allyl self reaction rate constant (k_1). Solid circles: experimental results of the current study at 20 Torr. The error bars on each experimental data point is based on propagated error. Solid line is the Arrhenius fit for the present data (solid circles); Dotted line is the result from Klippenstein *et al.* Number sign (#) measured by van den Bergh & Callear. Dashed line and cross (x) are the results reported by Tulloch *et al.*, using our estimate of the propagated uncertainty. Plus (+) are results from Boyd *et al.* and star (*) is rate reported by Jenkin *et al.* at room temperature.

The error limits in the Arrhenius expression (5.5) are the uncertainty in the fit parameters, weighted by the precision in the individual rate constants determined from the least-square fit of the k' data to an exponential. We attempted to make measurements of allyl at 575 K and higher temperatures, but no transient signal was observed, probably because of decomposition of the precursor before the photolysis flash. Thermochemical analysis showed that allyl iodide thermally decomposes between 500-600 K.

5.3.3. Allyl visible spectrum and cross section (σ)

Allyl radical is the simplest π -conjugated hydrocarbon radical having an open-shell electronic structure due to its unpaired electron. Several absorption measurements of the allyl radical in the visible^{30,90,91} and ultraviolet^{84,86,87,91-94} have been reported in the literature. The \tilde{B} and \tilde{C} states have been studied using resonance-enhanced multi-photon ionization spectroscopy⁹⁵⁻⁹⁹. The UV absorptions have been studied predominately to obtain various rate coefficients associated with allyl radical^{84,86,87}. But relatively few studies have been done on the electronic spectral properties of the transition from the ground (\tilde{X}^2A_2) state to the first excited (\tilde{A}^2B_1) state.

Currie *et al.*⁹⁰ first reported a weak absorption in the range of 370-410 nm by photolyzing various allylic compounds. They attributed this band to the electronic transition between ground state and first excited state with a band

origin at 408.3 nm. Maier *et al.*⁹¹ reported the UV/Vis absorption spectrum of the allyl radical in an Argon matrix, where an absorption peak occurred at 408.5 nm. Recently, Tonokura *et al.*³⁰ photolyzed 1,5 hexadiene at 193 nm to generate allyl radicals, and measured the CRDS spectrum from 370 nm to 420 nm. They attributed the diffuse structure of vibronic bands to pre-dissociation or to isomerization. We acquired a low resolution spectrum from 380 nm to 425 nm, which qualitatively agrees very well with the Tonokura *et al.*³⁰ spectrum as shown in Figure 5.6. We found that the absorption maxima occurred at 407.5 nm.

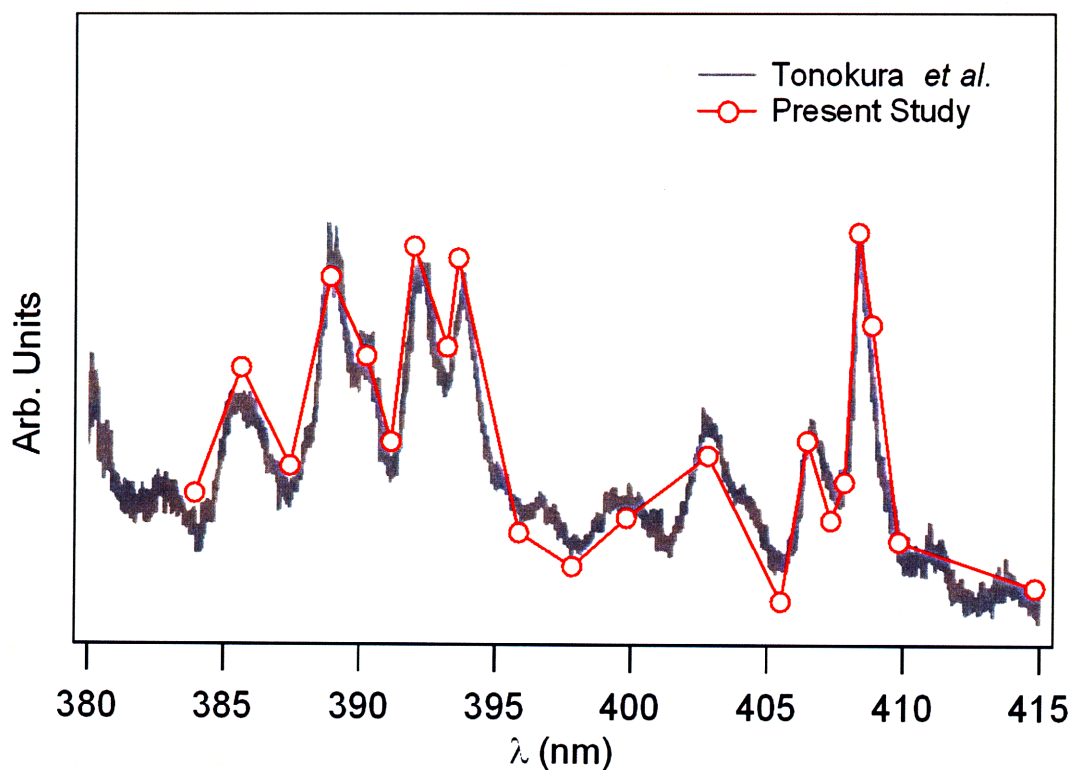


Figure 5.6: Low resolution spectrum acquired in the present study for allyl radical and it is compared to high resolution spectrum by Tonokura *et al.*³⁰

The cross section for the $\tilde{A} \leftarrow \tilde{X}$ transition for allyl radical has not been widely reported in the literature. Using equation similar to (4.23), accurate absorption cross-sections for allyl radical were determined at 404 and 407.5 nm. The results from the current study are summarized in Figure 5.7, where $\sigma_{\text{C}_3\text{H}_5}$ is shown vs. $[\text{C}_3\text{H}_5]$. The photolysis power, photolysis diameter, and allyl iodide concentration were varied to determine the reproducibility and consistency of $\sigma_{\text{C}_3\text{H}_5}$. The average cross-sections determined from all these measurements are:

$$\sigma_{\text{C}_3\text{H}_5}(404 \text{ nm}) = (1.8 \pm 0.3) \times 10^{-19} \text{ cm}^2 \quad (5.6)$$

$$\sigma_{\text{C}_3\text{H}_5}(407.5 \text{ nm}) = (4.2 \pm 0.5) \times 10^{-19} \text{ cm}^2 \quad (5.7)$$

The error reported is based on propagated uncertainty. Additionally, since the absorbance of allyl radical and I atom are measured at all temperatures, we were also able to determine the temperature dependence for $\sigma_{\text{C}_3\text{H}_5}$ at 407.5 nm. The results are shown in Table 5.3.

Tonokura *et al.*³⁰ reported a cross section of $(2.0 \pm 0.4) \times 10^{-19} \text{ cm}^2$ at 402.9 nm. Their measurements were based on fitting the transient absorption of allyl radical to second order rate coefficients of Jenkins *et al.* and Tulloch *et al.* In their reported spectrum, the cross section at 402.9 nm is roughly 30% larger than the cross section at 404 nm. Therefore, the σ_{404} can be estimated to be $1.4 \times 10^{-19} \text{ cm}^2$. DeSain *et al.*³⁹, using similar experimental technique to that in the present study, found $\sigma_{\text{C}_3\text{H}_5}(404 \text{ nm}) = (3.6 \pm 0.8) \times 10^{-19} \text{ cm}^2$.

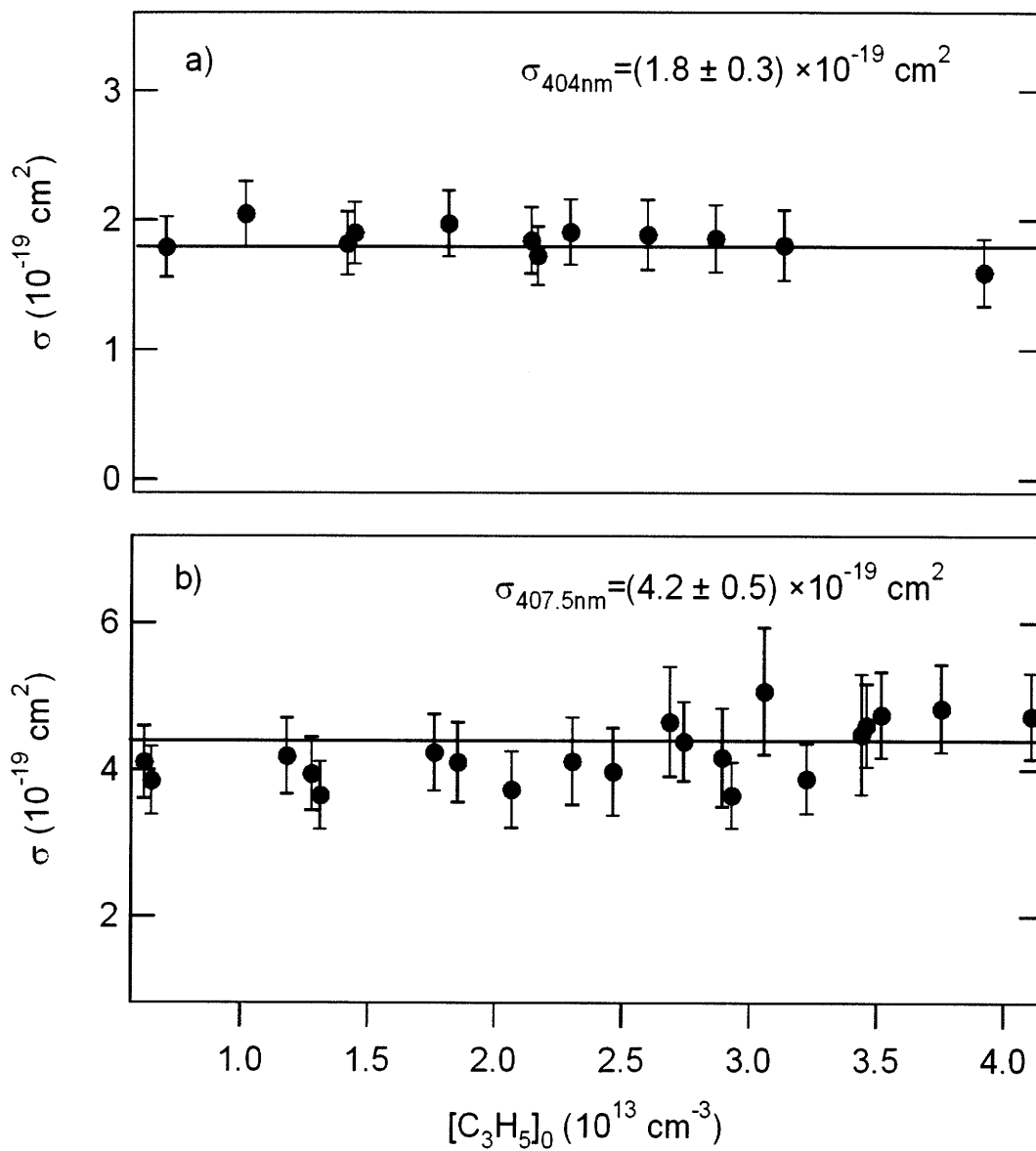


Figure 5.7: Plots of the absorption cross sections at 404nm (a) and 407.5nm (b) for the allyl radical as a function of initial allyl concentration. The error bars are based on propagated error.

Table 5.3: Temperature dependence of $\sigma_{\text{C}_3\text{H}_5}$ at 408 nm and at 20 Torr.

Temperature (K)	$\sigma_{\text{C}_3\text{H}_5}$ at 408 nm (cm^2)*
298	$(4.2 \pm 0.5) \times 10^{-19}$
350	$(3.6 \pm 0.3) \times 10^{-19}$
400	$(3.2 \pm 0.3) \times 10^{-19}$
450	$(2.8 \pm 0.2) \times 10^{-19}$
500	$(2.6 \pm 0.1) \times 10^{-19}$
550	$(2.5 \pm 0.1) \times 10^{-19}$

* Error based on 1σ standard deviation

Our value of $\sigma_{\text{C}_3\text{H}_5}$ (404 nm) agrees well with Tonokura *et al.*'s³⁰ spectrum based cross section, but is approximately a factor of two smaller than DeSain's results. This discrepancy can likely be attributed to the difference in laser line width; DeSain used a multimode diode probe laser (1 nm) whereas the present study used a narrower mode-locked laser (0.15 nm).

The strongest absorption feature for the $\tilde{\text{A}} \leftarrow \tilde{\text{X}}$ transition occurs at 408 nm. The cross-section, $\sigma_{\text{C}_3\text{H}_5}$ (407.5 nm), has never been reported in the literature, but it can be estimated to be $4.0 \times 10^{-19} \text{ cm}^2$ based on the allyl spectrum and $\sigma_{\text{C}_3\text{H}_5}$ (402.9 nm) reported by Tonokura *et al.*³⁰ Our results agree very well with Tonokura *et al.*'s³⁰ estimated results.

Potential sources of error in the $\sigma_{\text{C}_3\text{H}_5}$ determination include the uncertainty in σ_1 and secondary dissociation of allyl radical. If a fraction of the allyl radicals are dissociating after the photolysis of allyl iodide, the measured visible cross section for the radical would be too small. This in turn would produce an over estimate of the radical yield in photolysis. Szpunar *et al.*¹⁰⁰ observed secondary dissociation in a supersonic jet upon 193 nm photolysis of allyl iodide. The allyl radical in the present study can undergo collisional relaxation, which was absent in the study by Szpunar *et al.*¹⁰⁰ Additionally, the photon energy used in the present experiment is 170 kJ/mol less than Szpunar¹⁰⁰, therefore, we do not expect substantial secondary dissociation.

5.4. Discussion

The self reaction of allyl radical has been investigated previously by several authors⁸³⁻⁸⁹. The results from these studies have been summarized in Table 5.4. Van den Bergh and Callear⁸⁴ determined the absorption cross of allyl radical using 1-butene as a precursor. They assumed that 1-butene photolysis produces equal concentration allyl and methyl radicals and derived the room temperature allyl cross section, $\sigma_{\text{C}_3\text{H}_5}$ (223 nm), based on methyl oscillator strength at 216.0 nm, which was also determined by their group in an earlier study¹⁰¹. The $\sigma_{\text{C}_3\text{H}_5}$ (223nm) had an uncertainty of 20% which was propagated

from 15% uncertainty in σ_{CH_3} . Van den Bergh and Callear⁸⁴ photolyzed 1,5-hexadiene, and reported $k_4(298\text{ K}) = (1.4 \pm 0.50) \times 10^{-11} \text{ cm}^3 \text{ molecule}^{-1} \text{ s}^{-1}$.

Tulloch *et al.*⁸⁶ determined k_4 by using van den Bergh and Callear's⁸⁴ $\sigma_{\text{C}_3\text{H}_5}$ (223nm). They performed a comprehensive study on the self reaction of allyl radical at a temperature and pressure range of 295-571K and 1-250 Torr respectively. Allyl radicals were generated via flash photolysis of 1,5-hexadiene. A Xenon arc lamp coupled with a monochromator were used to probe allyl radicals at 223 nm and obtained $k_4(295\text{ K}) = (2.65 \pm 0.60) \times 10^{-11} \text{ cm}^3 \text{ molecule}^{-1} \text{ s}^{-1}$. The error reported here and in Figure 5.5, are based on propagated error from van den Bergh and Callear's⁸⁴ cross section, since Tulloch *et al.*⁸⁶ underestimated the uncertainty by reporting 1σ error of 7% for k_4 . As seen in Figure 5.5, our study's range in k_4 falls close to the error bars of Tulloch *et al.*⁸⁶

To obtain rate constants at higher temperatures, Tulloch *et al.*⁸⁶ assumed van den Bergh and Callear's⁸⁴ $\sigma_{\text{C}_3\text{H}_5}$ to be temperature independent and obtained Arrhenius parameters $A = (1.69 \pm 0.03) \times 10^{-11} \text{ cm}^3 \text{ molecule}^{-1} \text{ s}^{-1}$ and $E_a = -(1.1 \pm 0.1) \text{ kJ mol}^{-1}$. Glanzer *et al.*¹⁰² calculated the temperature dependence of the UV absorption cross section for methyl radical and found it could decrease as much as a factor of two over the temperature range of 298 to 700K. A similar trend might be expected for $\sigma_{\text{C}_3\text{H}_5}$ in the UV, and as seen in Table 5.3, our study finds that $\sigma_{\text{C}_3\text{H}_5}$ (408nm) changes by over 40% at 550 K. Not taking the temperature dependence of $\sigma_{\text{C}_3\text{H}_5}$ into account could significantly affect the Arrhenius parameters determined by Tulloch *et al.*⁸⁶

Table 5.4: Comparison of allyl radical self-reaction rate constants with previous literature

	Method	Temp range (K)	Pressure (Torr)	Reaction rate constant (cm ³ molecule ⁻¹ s ⁻¹)
van den Bergh and Callear ⁸⁴ (1970)	UV-Flash photolysis (allyl probed at 223 nm)	298	40-200	$k_4(298 \text{ K}) = 1.4 \times 10^{-11}$
Tulloch <i>et al.</i> ⁸⁶ (1982)*	UV-Flash photolysis (allyl probed at 223 nm)	293-579	1-500	$k_4 = (1.69 \pm 0.03) \times 10^{-11} \exp((132 \pm 13)/T)$ $k_4(295 \text{ K}) = 2.65 \times 10^{-11}$
Jenkins <i>et al.</i> ⁸⁷ (1989)	UV-Flash photolysis (allyl probed at 220 nm)	296	760	$k_4(296 \text{ K}) = 3.01 \times 10^{-11}$
Boyd <i>et al.</i> ⁸⁸ (1995)	UV-Flash photolysis (allyl probed at 220 nm)	400-540	760	$k_{4(\text{ave})} = 2.61 \times 10^{-11}$
Klippenstein <i>et al.</i> ⁸² (2007)	Variable reaction coordinate transition state theory (VRC-TST)	200-2000	760	$k_4 = 3.17 \times 10^{-11} T^{-0.166} \exp(312.2/T)$
Current Study (2008)	Laser Photolysis / Laser absorption (allyl probed at 404 & 408 nm)	298-550	20	$k_4 = (2.5 \pm 0.4) \times 10^{-11} \exp((174 \pm 40)/T)$ $k_4(298 \text{ K}) = 4.3 \times 10^{-11}$

*The published uncertainty neglected larger uncertainty in $[\text{C}_3\text{H}_5]_0$.

Tulloch *et al.*⁸⁶ also concluded that the allyl self-reaction rate is already in the high pressure limit at 1 Torr. Therefore, the present work at 20 Torr is also expected to be in the high pressure limit. We measured several data points at 100 Torr and no significant change in the self-reaction rate was observed.

Jenkin *et al.*⁸⁷ photolyzed 1,5-hexadiene at 193 nm, and fitted the allyl radical absorption at 220 nm time traces to determine $k_4/\sigma_{\text{C}_3\text{H}_5}$ (220 nm). They also measured the allyl iodide absorption spectrum at 205-365 nm. Jenkin *et al.*⁸⁷ photolyzed allyl iodide at 248 nm and measured several time dependent traces in the wavelength range of 217-230 nm. A set of three of these traces were then fitted to a kinetic model based on four reactions: instantaneous dissociation of allyl iodide, the self reaction of ally radical ($k_4/\sigma_{\text{C}_3\text{H}_5}$ (220nm) based on the 1,5-hexadiene experiment), self reaction of I atom ($k_1=2.5\times 10^{-13}$) and reaction of allyl radical with I atom(k_{4-I}). The model was fitted to three parameters: initial radical concentration, k_{4-I} and $\sigma_{\text{C}_3\text{H}_5}$ (220 nm). Since the UV allyl spectrum overlaps with allyl iodide spectrum, Jenkin *et al.*⁸⁷ had to use a three parameter fit to three different time dependent traces at different wavelengths to de-convolute $\sigma_{\text{C}_3\text{H}_5}$. By varying k_{12} , they optimized $\sigma_{\text{C}_3\text{H}_5}$ (220 nm)= $(5.8. \pm 0.8) \times 10^{-17} \text{ cm}^2$ and determined k_4 (296 K)= $(3.01 \pm 0.5) \times 10^{-11} \text{ cm}^3 \text{ molecule}^{-1} \text{ s}^{-1}$. However, their reported $k_{12}= (1.6 \pm 0.6) \times 10^{-10} \text{ cm}^3 \text{ molecule}^{-1} \text{ s}^{-1}$ is more than an order of magnitude too fast, based on results from the present study which finds allyl decay trace to be more than a factor of 10 faster than I decay trace. In essence, Jenkin *et al.*⁸⁷ calibrated the allyl spectrum based on the allyl iodide spectrum using a complex non-linear kinetic model, where at least one of the parameters had a significant error. Jenkin *et al.*⁸⁷ did not report

an uncertainty in allyl iodide cross section, and their kinetic model did not factor in chemistry due to excited I atoms. Though they only reported 1σ error and did not propagate the error for k_4 , all three of these factors could lead to significant error bars in k_4 .

Jenkin *et al.*'s⁸⁷ work was extended by Boyd *et al.*⁸⁸ to measure the temperature dependence of k_4 over the range of 400-540 K. They employed Jenkin *et al.*'s⁸⁷ $\sigma_{\text{C}_3\text{H}_5}$ (220 nm) to determine k_4 and they also did not consider temperature dependence of $\sigma_{\text{C}_3\text{H}_5}$ (220 nm). Due to experimental scatter and a small temperature range, Boyd *et al.*⁸⁸ were unable to determine the temperature dependence of the rate coefficient. Therefore, they reported the averaged k_4 (400-540 K) = $(2.61 \pm 0.2) \times 10^{-11} \text{ cm}^3 \text{ molecule}^{-1} \text{ s}^{-1}$. Since Boyd *et al.* relied solely on Jenkin *et al.*'s⁸⁷ $\sigma_{\text{C}_3\text{H}_5}$ (220 nm), their k_4 should have the same inherent uncertainties which were present in the studies by Jenkin *et al.*⁸⁷

More recently, Klippenstein *et al.*⁸² calculated the theoretical rate constant for allyl radical self reaction. They applied state-of-the-art electronic structure calculations in combination with variable reaction coordinate transition state theory (VRC-TST) and master equation methodology to derive k_4 (200-2000 K) = $3.17 \times 10^{-11} \text{ cm}^3 \text{ molecule}^{-1} \text{ s}^{-1} T^{-0.166} \exp(312.2/T)$.

As seen in Table 5.4 and Figure 5.5 our results agree reasonably well with previous studies. The results of the present study are faster by ~50% compared to previous experimental work. The present work agrees with Klippenstein *et al.*⁸² at low temperatures, but deviates by about 50% at higher temperatures. The advantage of the present work is that it is free from background interferences which might have been present in all three previous

studies. Also, the temperature dependence of $\sigma_{\text{C}_3\text{H}_5}$ is effectively accounted by applying Doppler and temperature dependent collision broadening parameters to σ_1 . The present study's determination of $[\text{C}_3\text{H}_5]_0$ relies on a straightforward method based on an atomic line strength, instead of molecular line strength or complicated models on which previous studies depended, and also led to significantly less propagated uncertainty in k_4 .

5.5. Conclusion

The recombination rate constant of allyl radical was measured from 298 K to 550 K at 20 Torr using a novel low noise flash photolysis laser kinetic spectrometer. Allyl iodide was used as a precursor. Accurate determination of the initial radical concentration was obtained via direct laser absorption by I atom at 1315 nm. The branching ratio between ground and excited state I atom production from 266 nm photolysis of allyl iodide was measured to be 0.80 ± 0.08 . Allyl radicals were probed at two different wavelengths: 404 and 408 nm. The self-reaction rate constant for allyl radical at room temperature was found to be:

$$k_4 = (4.3 \pm 0.5) \times 10^{-11} \text{ cm}^3 \text{ molecule}^{-1} \text{ s}^{-1} \quad (5.4)$$

Arrhenius parameters for allyl recombination rate were determined between 298-550 K to be:

$$k_4 = (2.5 \pm 0.4) \times 10^{-11} \text{ cm}^3 \text{ molecules}^{-1} \text{ s}^{-1} \exp((174 \pm 40) \text{ K}/T) \quad (5.5)$$

These results are ~50% faster than the results in previous studies, but are superior measurements due to a more accurate measurement of initial allyl radical concentration. Absorption cross sections of the allyl radical at 404 and 407.5 nm were also measured to be: $(1.8 \pm 0.3) \times 10^{-19} \text{ cm}^2$ and $(4.2 \pm 0.5) \times 10^{-19} \text{ cm}^2$ respectively at 298 K.

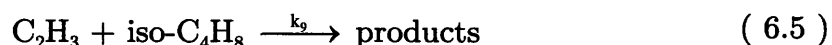
Chapter 6

6. Reaction of vinyl radical with various alkenes

6.1. Introduction

Reactions involving the vinyl radical ($\text{H}_2\text{C}=\text{CH}$) addition to alkenes play an important role in combustion processes¹⁰³. These reactions are important in olefin pyrolysis and molecular weight growth chemistry. The only vinyl + alkene reaction that has been experimentally studied is the reaction of vinyl with ethylene (C_2H_4)⁶⁸, which were conducted under a narrow set of conditions. To our knowledge, vinyl additions to C3 and C4 alkenes have never been studied experimentally or theoretically. This chapter will discuss experimental studies of vinyl addition five different alkenes:





Reaction (6.1) is interesting because ethylene is the simplest olefin, therefore its thermal chemistry serves as the basis for understanding the thermal chemistry of other olefins. At temperatures below 1000 K, C_2H_4 decomposition proceeds primarily through disproportionation to give C_2H_5 and C_2H_3 .^{104,105} Although the chemistry of C_2H_5 is fairly well understood, the chemistry of C_2H_3 remains relatively unexplored. For example, there have been few direct studies of the kinetics and product branching of the C_2H_3 self-reaction,¹⁰⁶⁻¹¹⁰ although a number of studies have treated the combination / disproportionation channels of the vinyl self-reaction in models of complex reaction systems.^{107,111-115}

An understanding of the $\text{C}_2\text{H}_3 + \text{C}_2\text{H}_4$ reaction system supports a more accurate description of C_2H_4 pyrolysis in particular and olefin pyrolysis in general. Moreover, polyethylene is one of the most important synthetic polymers. It is a widely used multipurpose material and has the largest annual production among all synthetic commodity polymers. In recent years, gas phase polymerization has emerged as the most versatile process for the production of polyethylene. However, many fundamental microscopic processes involved in gas phase ethylene polymerization are not completely understood¹¹⁶. Reaction (6.1) has potential importance as the initiating and/or propagating step in gas phase ethylene polymerization. Furthermore, it has been suggested^{117,118} that reaction (6.1) may produce resonance-stabilized 1-methylallyl radicals, possible

contributors to molecular weight growth in rich hydrocarbon flames.¹¹⁹ Surprisingly, there have been only a limited number of studies on the $C_2H_3 + C_2H_4$ reaction to date.

Fahr and Stein¹²⁰ employed the Very Low Pressure Pyrolysis (VLPP) technique to study the kinetics and products of the $C_2H_3 + C_2H_4$ reaction over a temperature range of 1023-1273 K and at low pressure between 1.3 - 13 μ bar. Temperature dependent rate parameters for the $C_2H_3 + C_2H_4$ reaction were derived relative to the vinyl self- reaction, $C_2H_3 + C_2H_3$. More recently, Shestov and coworkers¹¹⁸ reported kinetic studies of the $C_2H_3 + C_2H_4$ reaction from 625-950 K and at pressures between 5 and 11 Torr, using the Laser Photolysis/Photoionization Mass Spectroscopy (LP/PIMS) technique. Under the conditions of these two previous studies C_4H_6 and C_4H_7 were detected as the only major products. Both of the previous studies were done under conditions of low pressures and high temperature.

Vinyl + propene chemical system is of particular interest since it can lead to the formation of several resonantly-stabilized free radicals as well as three, four, and five-member ring structures. Propene is the simplest olefin with a methyl group and thus this is the easiest case for comparing the rate of vinyl addition with the rate of vinyl direct H-abstraction.

There have been no experimental or theoretical rate coefficient reported for reaction (6.2). The only attempt was made by Tsang⁸⁹, who estimated various rate coefficients of the vinyl + propene system, all based upon other reaction systems. The rate coefficient for vinyl + propene \rightarrow allyl + ethylene via direct H-abstraction, $3.68 \times 10^{-24} \times T^{3.5} \times \exp[- 2365 / T]$ $cm^3 \text{ molecule}^{-1} s^{-1}$, was based upon the thermochemically-derived estimate for methyl + propene¹²¹. Similarly, the rate coefficients for vinyl + propene \rightarrow 1,3-butadiene + methyl,

$1.2 \times 10^{-12} \exp[-2520 / T] \text{ cm}^3 \text{ molecule}^{-1} \text{ s}^{-1}$, and 1,3-pentadiene + H, $1.2 \times 10^{-12} \exp[-3240 / T] \text{ cm}^3 \text{ molecule}^{-1} \text{ s}^{-1}$, were based upon vinyl addition to ethylene and acetylene¹²². No estimate has been provided for the formation of cyclic species, including cyclopentene + H.

Vinyl addition to butenes (reaction (6.3), (6.4), and (6.5)) have never been estimated nor experimentally measured. Though recently, Radom *et al.*¹²³ performed a detailed study of methyl radical addition to C2, C3 & C4 olefin species. They reported barriers, enthalpies, and rate constants for a selection of alkenes including ethylene, propene and 1-butene. Radom concluded that reaction of methyl radical with C=C species is dominated by the reaction exothermicities. Additionally, as expected, the methyl addition to unsubstituted C=C carbon center was found to be favored over addition to substituted carbon center, both kinetically and thermodynamically.

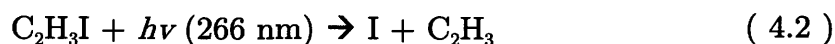
In the present work, the rate coefficients of vinyl addition various alkenes has been measured over a temperature range of 300 K to 700 K and at pressures of 15, 20 and 100 Torr. The potential energy surfaces of these reactions are calculated using *ab initio* methodology and modeled with Rice-Ramsperger-Kassel-Marcus (RRKM) master equation simulations, yielding pressure-dependent rate coefficients and branching fractions into various primary products.

Lastly, Prof. Askar Fahr and colleagues⁶⁸ conducted a product channels study the for reaction (6.1) at temperatures of 523-723 K, and pressures of 20-700 Torr. The product studies employed excimer laser photolysis to generate the vinyl radicals and GC/MS product analysis, for identifying and quantifying the final products. We modeled this reaction system using RMG and simulated product yields of 1-butene, 1,3-butadiene, 1,5-hexadiene and 1,7-octadiene. A

comparison of experimental product yields to an RMG model will also be presented for vinyl + ethylene system.

6.2. Experimental details

The experimental apparatus has been described in Chapter 3. Here, brief experimental details will be given that pertains to the specific set of conditions that were used to measure the rate constants of vinyl + alkenes. Once again, the vinyl radicals were generated using vinyl iodide.



Direct absorption by vinyl radical was used to monitor the reaction of vinyl + ethylene. Vinyl radicals were detected by multiple pass laser absorption at one of two absorption lines, 423.2 nm or 472.0^{54,78,80}.

Chemicals were purchased from following suppliers and were used without further purifications: C₂H₄ ≥ 99.0% (2.0 grade from Airgas), C₃H₆ ≥ 99.0% (2.0 grade from Advanced Gas Technologies Inc.), 1-butene ≥ 99.0% (2.0 grade from Advanced Gas Technologies Inc.), 2-butene ≥ 99.0% (2.0 grade from Advanced Gas Technologies Inc.) Isobutene ≥ 99.0% (2.0 grade from Advanced Gas Technologies Inc.), C₂H₃I ≥ 90.0% (Oakwood Products Inc), & He ≥ 99.999% (5.0 grade, Airgas). 2-butene gas had approximately equal mixture of cis and trans isomers (~49 % of each).

Calibrated mass flow controllers were used to maintain a constant flow of the reactant and buffer gases. A very small portion of the photolyte ($\sim 0.2\%$) in the path of the laser is dissociated on each pulse, and the photolysis laser intersects less than about 20% of the total cell volume. If higher flows were used such that the cell refreshed every 1 shot at 1 Hz repetition rate of the photolysis laser, then the probe beam started stirring and missed the detector. On the other hand, running at lower photolysis repetition rate was not feasible since it took too long to conduct the experiments. Therefore, an experiment was conducted where observed decay rate (k') of vinyl + ethylene was measured at various repetition rate of the photolysis laser. Figure 6.1 contains a summary of the results. Varying the laser repetition rate over a factor of 50 produced no systematic change in the observed decay rate. We expect similar trends for the reaction with other alkenes. Therefore, in all the vinyl + alkenes experiments, sufficient flows were used to completely refresh the cell every 4-5 shots at the 1 Hz repetition of the photolysis laser.

To maintain pseudo-first-order conditions, alkene concentrations were in large excess over the vinyl concentration. Also, this difference in concentrations ensured that the pseudo-first order decays were at least five times greater than the decays without added alkenes. For most of the experiments, vinyl iodide concentrations were maintained at $[C_2H_3I] = 1 \times 10^{15}$ molecules cm^{-3} . Some experiments were performed at several concentrations of vinyl by varying photolysis laser intensity and C_2H_3I concentration. It was found that the rate constants did not depend on $[C_2H_3]$ or on photolysis energy, confirming the validity of a pseudo-first-order approximation and suggesting a negligible role for photolytic interferences. Details for all the experimental condition for determining $k_{5,9}$ are outline in Tables 6.1-6.5.

Although dissociation of ethylene has been reported in other experiments from irradiation at 248 nm,¹¹⁸ no photolysis of ethylene at 266 nm was observed in the present experiments, and no transient absorption of the 423.2 nm probe laser could be detected from 266 nm irradiation of pure ethylene, even at 100 Torr and 700 K. Excitation at 266 nm is near or below the origin of the first singlet excitation in ethylene, and the only absorption is expected to be in the extremely weak first triplet band¹²⁴. Furthermore, the 107.5 kcal mol⁻¹ energy of a 266 nm photon (7.8 kcal mol⁻¹ less energy than a 248 nm photon) is less than the C-H bond energy in ethylene ($D_0 = (109.7 \pm 0.8)$ kcal mol⁻¹)¹²⁵.

To determine $k_{5,9}$, the decay rate of C₂H₃ was measured as a function of the alkene concentration. A typical raw data trace, as shown in Figure 6.2a, was fitted to a single exponential decay. Rate constants were obtained in the usual manner as the slope of a plot of the pseudo-first order rate constant for vinyl loss, k' (where $k' = k_{5,9} [C_nH_{2n}] + k_0$), versus $[C_nH_{2n}]$ which yielded a linear slope as shown in Figure 6.2b. The effective rate constant k_0 , represented by the zero-alkene intercept of this plot, is attributable to all other loss processes for vinyl radical, including self-reaction, reaction with the photolytic precursor, and diffusion out of the beam. The uncertainty limits of k' shown in Figure 6.2b represent the statistical uncertainty resulting from the fit of the C₂H₃ decay data to a single exponential. Alkene concentrations used were large enough that the error in simply including the second-order contribution from self-reaction in the intercept was small. Extracting k' from the first-order component of a fit to the functional form for a combined first- and second-order decay resulted in identical values of $k_{5,9}$ to within experimental uncertainty.

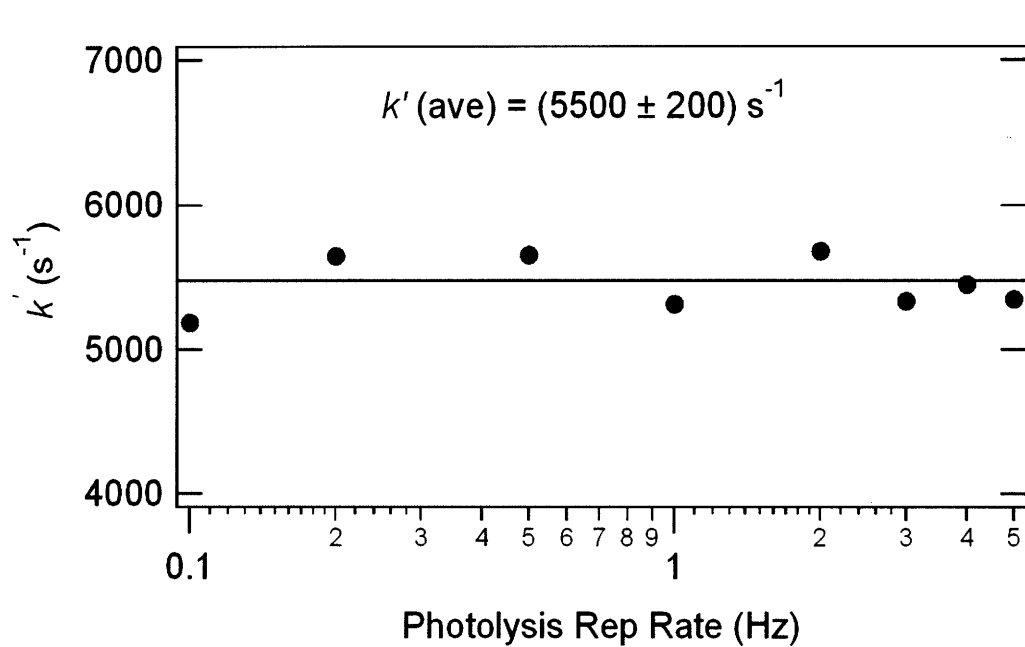


Figure 6.1: Observed decay rate (k') of vinyl + ethylene, measured at various repetition rates of the photolysis laser. The k' fluctuated by only 3% and produced no systematic changes.

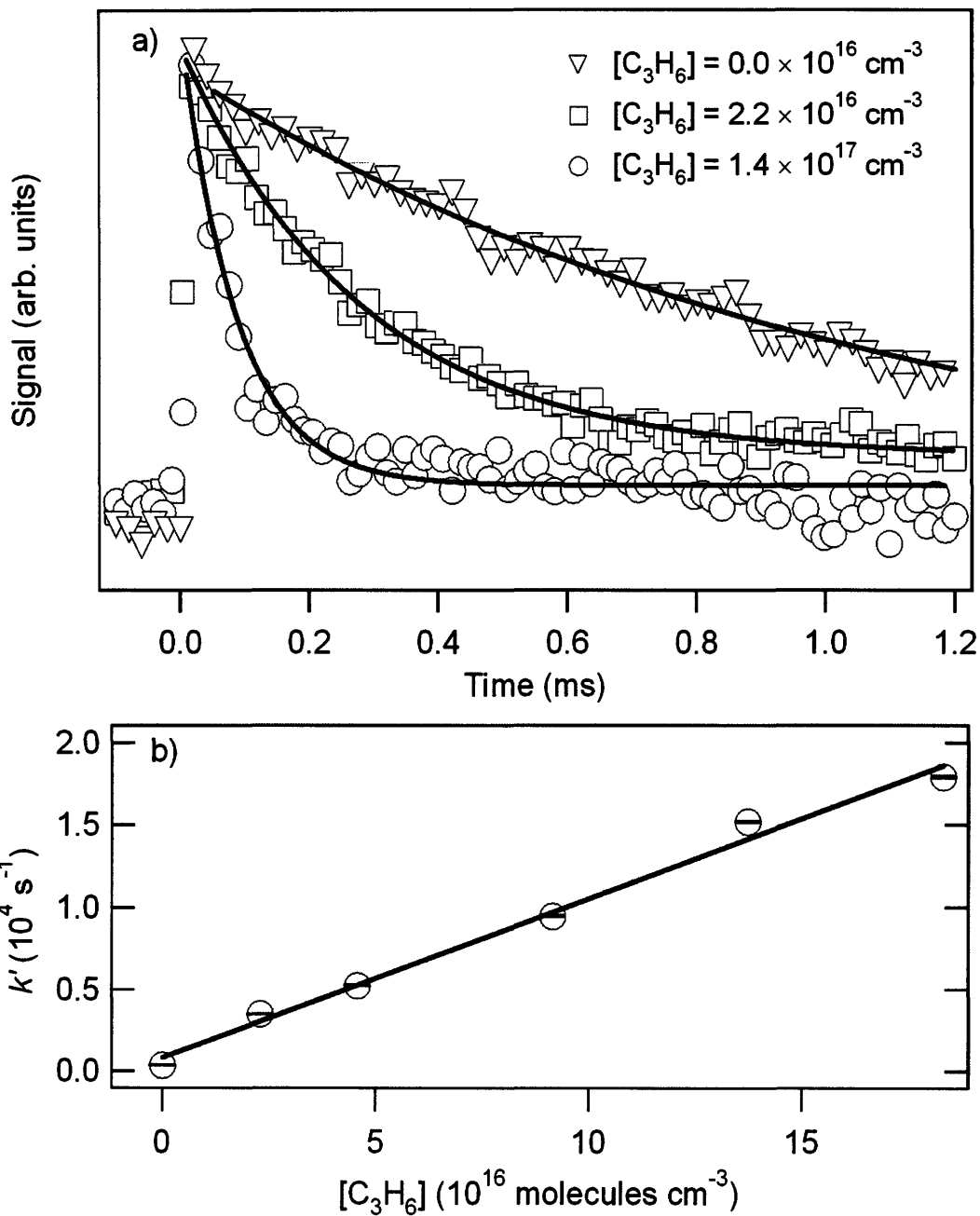


Figure 6.2: Recorded decay of C_2H_3 at 700 K and 100 Torr for the conditions $[C_3H_6] = 0 \text{ molecules cm}^{-3}$ (triangles), $[C_3H_6] = 2.2 \times 10^{16} \text{ molecules cm}^{-3}$ (squares) and $[C_3H_6] = 1.4 \times 10^{17} \text{ molecules cm}^{-3}$ (circles). Every 150th point is shown for clarity. b) Pseudo-first-order C_2H_3 decay rate k' vs. $[C_3H_6]$, at 700 K and 100 Torr.

Table 6.1: Conditions and results for experiments to measure k_5 .

Temperature (K)	Pressure (Torr)	[C ₂ H ₃ I] (10 ¹⁵ cm ⁻³)	[C ₂ H ₃] ₀ ^a (10 ¹² cm ⁻³)	[Ethylene] (10 ¹⁷ cm ⁻³)	k_5^b (10 ⁻¹⁵ cm ³ molecule ⁻¹ s ⁻¹)	k_0^c (s ⁻¹)
298	100	1.30	3.90	4.0 – 33.0	0.60 ± 0.1	816
325	100	1.16	3.20	3.0 – 30.0	0.99 ± 0.1	636
350	100	1.32	3.80	2.0 – 7.5	2.30 ± 0.3	926
375	100	1.23	3.44	1.2 – 7.0	3.15 ± 0.3	826
400	100	1.15	2.50	1.1 – 6.5	3.64 ± 0.4	913
425	100	1.08	2.24	1.0 – 6.1	4.73 ± 0.6	900
450	100	1.02	2.11	0.9 – 4.8	7.02 ± 0.6	672
475	100	1.06	2.81	0.9 – 4.6	9.61 ± 0.6	701
500	100	1.01	2.14	0.9 – 4.3	11.7 ± 0.7	557
525	100	0.96	1.81	0.8 – 4.0	14.0 ± 0.4	430
550	100	1.04	2.20	0.8 – 3.9	19.0 ± 1.2	347
575	100	1.03	3.70	0.8 – 3.8	23.0 ± 2.0	279
600	100	1.06	2.15	0.7 – 3.7	22.4 ± 2.0	901
625	100	1.09	1.90	0.7 – 3.5	27.6 ± 2.8	846
650	100	1.05	1.60	0.6 – 3.4	44.0 ± 4.0	280
675	100	1.05	2.62	0.4 – 2.3	43.0 ± 3.0	784
700	100	1.05	3.37	0.2 – 1.8	54.0 ± 3.0	339
500	15	1.06	2.51	1.0 – 2.9	9.10 ± 0.9	763
550	15	1.04	2.04	0.6 – 2.6	14.9 ± 1.0	582
600	15	1.05	1.90	0.5 – 2.4	19.0 ± 1.1	894
650	15	1.05	1.89	0.4 – 2.2	28.2 ± 3.1	808
700	15	1.03	1.75	0.2 – 2.0	40.0 ± 4.2	839

^a Determined using C₂H₃ cross section of 2×10^{-19} cm²³⁹

^b Uncertainty limits ($\pm 1\sigma$) based on statistical uncertainties in the fits.

^c The y -intercept of the plot of pseudo-first-order rate constant vs. ethylene concentration.

Table 6.2: Conditions and results for experiments to measure k_6

Temperature (K)	Pressure (Torr)	$[\text{C}_2\text{H}_3\text{I}]$ (10^{15} cm^{-3})	$[\text{C}_2\text{H}_3\text{I}]^a$ (10^{12} cm^{-3})	[Propene] (10^{17} cm^{-3})	k_6^b ($10^{-15} \text{ cm}^3 \text{ molecule}^{-1} \text{ s}^{-1}$)	k_0^c (s^{-1})
298	100	1.42	5.29	2.8 – 18.1	1.07 ± 0.3	293
325	100	1.39	5.49	2.7 – 10.2	2.08 ± 0.4	400
350	100	1.37	4.80	2.7 – 10.0	3.44 ± 0.3	509
375	100	1.37	4.79	1.8 – 7.3	4.38 ± 0.5	291
400	100	1.39	4.82	1.8 – 7.3	7.60 ± 0.4	320
425	100	1.06	2.53	1.4 – 4.6	10.4 ± 0.9	249
450	100	1.07	2.49	0.9 – 2.8	13.5 ± 1.5	217
475	100	1.06	2.73	0.9 – 2.8	15.7 ± 1.0	272
500	100	1.05	2.82	0.5 – 2.8	21.0 ± 1.3	349
525	100	1.05	2.30	0.5 – 2.3	23.1 ± 2.1	428
550	100	1.06	2.70	0.5 – 2.3	29.2 ± 2.8	381
575	100	1.07	2.58	0.5 – 2.2	38.8 ± 3.0	674
600	100	1.05	2.41	0.3 – 2.2	46.2 ± 4.7	293
625	100	1.04	2.00	0.3 – 1.8	47.6 ± 3.3	387
650	100	1.05	2.54	0.3 – 1.8	67.0 ± 4.2	343
675	100	1.06	2.18	0.3 – 1.8	76.6 ± 4.9	252
700	100	1.05	2.04	0.3 – 1.8	97.1 ± 4.5	350
298	25	1.21	5.29	3.2 – 8.1	1.32 ± 0.4	422
325	25	1.23	6.33	2.5 – 7.4	2.29 ± 0.3	412
350	25	1.29	5.03	2.6 – 6.9	3.75 ± 0.5	320
375	25	1.37	5.71	2.7 – 6.3	3.77 ± 0.4	701
400	25	1.38	4.93	1.8 – 5.5	7.80 ± 0.7	360

Table 6.2: Conditions and results for experiments to measure k_6 (*continued*)

Temperature (K)	Pressure (Torr)	[C ₂ H ₃ I] (10 ¹⁵ cm ⁻³)	[C ₂ H ₃] ^a (10 ¹² cm ⁻³)	[Propene] (10 ¹⁷ cm ⁻³)	k_6^b (10 ⁻¹⁵ cm ³ molecule ⁻¹ s ⁻¹)	k_0^c (s ⁻¹)
425	15	1.05	2.89	1.4 – 3.3	7.85 ± 0.9	440
450	15	1.05	4.15	0.9 – 3.2	11.5 ± 0.7	364
475	15	1.05	3.61	0.9 – 2.7	11.3 ± 1.3	324
500	15	1.06	3.58	0.5 – 2.3	17.2 ± 1.4	620
525	15	1.05	3.38	0.4 – 2.3	22.8 ± 1.5	319
550	15	1.05	3.63	0.4 – 2.3	26.5 ± 3.0	686
575	15	1.07	2.93	0.4 – 2.3	34.4 ± 3.6	306
600	15	1.05	2.98	0.3 – 2.4	47.3 ± 3.5	286
625	15	1.06	2.49	0.3 – 2.2	50.1 ± 3.2	347
650	15	1.05	3.05	0.3 – 1.8	64.0 ± 8.1	390
675	15	1.05	2.69	0.3 – 1.8	72.8 ± 8.9	290
700	15	1.05	2.46	0.3 – 1.8	91.6 ± 5.9	540

^a Determined using C₂H₃ cross section of 2×10^{-19} cm² ³⁹

^b Uncertainty limits ($\pm 1\sigma$) based on statistical uncertainties in the fits.

^c The y -intercept of the plot of pseudo-first-order rate constant vs. propene concentration.

Table 6.3: Conditions and results for experiments to measure k_7 for 1-butene.

Temperature (K)	Pressure (Torr)	$[\text{C}_2\text{H}_3\text{I}]$ (10^{14} cm^{-3})	$[\text{C}_2\text{H}_3]_0^a$ (10^{12} cm^{-3})	[1-butene] (10^{17} cm^{-3})	k_7^b ($10^{-15} \text{ cm}^3 \text{ molecule}^{-1} \text{ s}^{-1}$)	k_0^c (s^{-1})
292	100	5.49	7.49	2.2 – 18.1	0.78 ± 0.1	740
350	100	5.49	7.42	1.8 – 10.9	2.55 ± 0.3	601
400	100	5.55	4.91	0.9 – 6.5	5.92 ± 0.4	557
450	100	4.64	5.23	0.9 – 5.6	10.0 ± 0.7	457
500	100	4.58	3.18	0.5 – 3.7	14.3 ± 1.3	312
550	100	4.60	3.59	0.5 – 3.2	21.1 ± 1.1	448
600	100	4.58	3.58	0.2 – 2.3	32.4 ± 1.7	447
650	100	4.58	4.48	0.2 – 2.3	48.6 ± 2.4	330
700	100	4.58	2.90	0.2 – 1.8	64.6 ± 8.6	356

^a Determined using C_2H_3 cross section of $2 \times 10^{-19} \text{ cm}^2$ ³⁹

^b Uncertainty limits ($\pm 1\sigma$) based on statistical uncertainties in the fits.

^c The y -intercept of the plot of pseudo-first-order rate constant vs. 1-butene concentration.

Table 6.4: Conditions and results for experiments to measure k_8 for 2-butene.

Temperature (K)	Pressure (Torr)	$[C_2H_3I]$ (10^{14} cm^{-3})	$[C_2H_3]_0^a$ (10^{12} cm^{-3})	[2-butene] (10^{17} cm^{-3})	k_8^b ($10^{-15} \text{ cm}^3 \text{ molecule}^{-1} \text{ s}^{-1}$)	k_0^c (s^{-1})
292	100	5.49	9.80	2.7 – 19.2	0.39 ± 0.1	733
350	100	5.49	8.65	1.8 – 10.9	1.05 ± 0.1	700
400	100	5.55	6.77	1.4 – 8.3	2.17 ± 0.2	519
450	100	4.64	5.06	0.9 – 7.4	5.33 ± 0.6	909
500	100	4.58	4.36	0.9 – 4.6	9.25 ± 1.2	725
550	100	4.60	4.48	0.7 – 4.1	14.6 ± 1.3	714
600	100	4.58	3.62	0.7 – 4.1	21.9 ± 0.6	777
650	100	4.55	3.62	0.5 – 2.7	27.8 ± 1.1	382
700	100	4.58	4.44	0.5 – 3.2	41.4 ± 1.1	630

^a Determined using C_2H_3 cross section of $2 \times 10^{-19} \text{ cm}^2$ ³⁹

^b Uncertainty limits ($\pm 1\sigma$) based on statistical uncertainties in the fits.

^c The y -intercept of the plot of pseudo-first-order rate constant vs. 2-butene concentration.

Table 6.5: Conditions and results for experiments to measure k_0 for isobutene

Temperature (K)	Pressure (Torr)	$[\text{C}_2\text{H}_3\text{I}]$ (10^{15} cm^{-3})	$[\text{C}_2\text{H}_3]_0^a$ (10^{13} cm^{-3})	[isobutene] (10^{17} cm^{-3})	k_9^b ($10^{-15} \text{ cm}^3 \text{ molecule}^{-1} \text{ s}^{-1}$)	k_0^c (s^{-1})
292	100	1.60	1.27	2.1 – 10.1	0.85 ± 0.1	650
350	100	1.65	1.26	3.2 – 9.8	2.54 ± 0.8	505
400	100	1.85	1.34	1.4 – 8.3	6.75 ± 0.6	588
450	100	1.85	1.34	0.9 – 5.2	10.2 ± 1.0	585
500	100	1.83	1.61	0.9 – 5.0	16.8 ± 1.0	824
550	100	2.30	1.07	0.4 – 3.6	21.1 ± 0.8	755
600	100	1.83	0.57	0.6 – 4.8	28.0 ± 1.0	459
650	100	1.79	0.57	0.2 – 2.3	40.8 ± 3.5	683
700	100	1.83	0.57	0.2 – 2.3	63.5 ± 5.2	388

^a Determined using C_2H_3 cross section of $2 \times 10^{-19} \text{ cm}^2$ ³⁹

^b Uncertainty limits ($\pm 1\sigma$) based on statistical uncertainties in the fits.

^c The y -intercept of the plot of pseudo-first-order rate constant vs. isobutene concentration.

6.3. Theoretical calculations

6.3.1. *Ab initio* calculations

The potential energy surface (PES) calculations were performed by C. Franklin Goldsmith, a fellow group member of the Green Group at MIT. Here, a brief description is given as an aid in understanding the experimental results. A generic reaction scheme is shown in Figure 6.3.

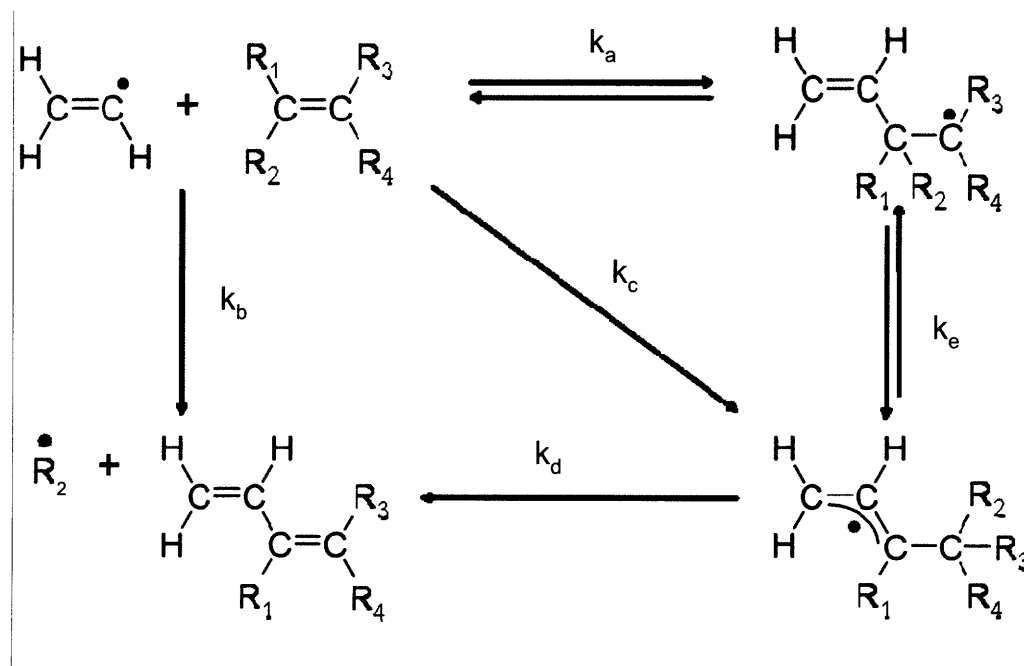


Figure 6.3: A simplified reaction scheme for the vinyl + alkene reaction system. $k_{5,9} = k_a + k_b + k_c$.

For the case where $R_n=H$, represents the ethylene case and yields the simplest PES among all the vinyl + alkene chemical system. The optimized geometries, zero-point corrected energies and the transition states for the C_4H_7 isomers in the vinyl + ethylene system have been calculated by Miller¹¹⁷. For vinyl + propene and vinyl + butenes systems, the optimized geometries, the zero-point corrected energies for the stationary points, transition states, and product channels on the various alkenes potential energy surface were calculated using the G3 compound method¹²⁶ within the Gaussian 03 software package¹²⁷. The PES for C_5H_9 and C_6H_{10} isomers were fairly complex with a lot more wells and product channels, the details for which can be found in various publications^{68,128}

6.3.2. Pressure dependence calculations

The $k_{5,9}(T, P)$ calculation were performed by also C. Franklin Goldsmith using RRKM/ME in the program package, VariFlex¹²⁹, to determine microcanonical rate constants for our experimental conditions. The PES does not explicitly contain all the possible conformers for a given species; instead, the lowest energy conformer was selected, and other conformers (e.g. cis and trans) were treated as hindered internal rotors in the kinetics model. The potential barrier for each hindered internal rotor, here assumed to be any single carbon-carbon bond not included in a ring, was calculated at the HF/6-31G(d) level with Gaussian 03. The partition function and density of state for each rotor was treated as a one-dimensional hindered rotor with a semi-classical Pizer-Gwinn¹³⁰-like approximation.

Tunneling was included for all transition states by use of an Eckart approximation. For energy transfer in the master equation, a single-exponential down model was used, with an average ΔE_{down} given by $100 \text{ cm}^{-1} (T/298)^{0.8}$ ¹³¹⁻¹³³. The collision frequency was estimated using a Lennard-Jones model, with LJ parameters of $\sigma = 5.78 \text{ \AA}$ and $\varepsilon = 273.8 \text{ cm}^{-1}$. The LJ parameters were estimated from literature values for c-C₆H₁₂¹³⁴; the same source was used for the bath gas LJ-parameters: $\sigma = 2.55 \text{ \AA}$ and $\varepsilon = 6.95 \text{ cm}^{-1}$. For the isomer-bath gas complex, σ was calculated by the arithmetic mean of the values for the two species, and ε was calculated by the geometric mean^{131,135}.

6.3.3. End product studies in RMG

The reaction mechanism for the product analysis was generated using RMG, an open-source automatic reaction model generating program.¹ The algorithm for mechanism generation has been described in detail previously^{1,3}. In brief, the complete reaction system is calculated, with rate constants for all possible reactions between the available species estimated based on rules for classes of reactions. Thus a model is generated that is comprehensive (in the sense that it includes all relevant reactions), albeit with approximate rate coefficients. Thermodynamic parameters and high-pressure-limit rate parameters are stored in a hierarchical database based on functional groups. Thermodynamic parameters for specific molecules are included in a primary thermodynamic library, and thermodynamic properties for all other molecules are estimated using group additivity. RMG's kinetics database is divided into

34 reaction families. Small molecule reactions that cannot be described by reaction families are included in a primary reaction library. The temperature, pressure, and initial concentrations of vinyl radical, ethylene, and helium were provided to RMG as input; it was assumed that 1% of the initial vinyl iodide is photolyzed to form the vinyl radical. RMG uses the high-pressure limit for all the rate constants in the mechanism. The rate constants pertaining to the vinyl + ethylene potential energy surface were added as a reaction library, replacing the RMG-estimated high-pressure rate constant with the pressure-dependent rate constants generated from the master equation calculations. The error tolerance value was set to 0.1. This process was repeated for 523, 623, and 723 K and for 20, 150, 400, and 700 Torr, thereby yielding twelve different mechanisms.

6.4. Results

6.4.1. Vinyl + ethylene

6.4.1.1. Kinetic study

The measured values for k_5 at various temperatures and pressures are given in Table 6.1 and an Arrhenius plot of k_5 is shown in Figure 6.4. A simple Arrhenius fit to the measured rate coefficient for reaction 1 at 100 Torr, weighted by the uncertainties in the individual data points, yields:

$$k_5 = (1.2 \pm 0.2) \times 10^{-12} \text{ cm}^3 \text{ molecule}^{-1} \text{ s}^{-1} \exp(-(2310 \pm 70) \text{ K}/T) \quad (6.6)$$

and a similar fit to the present results at 15 Torr gives

$$k_5 = 8.8 \times 10^{-13} \text{ cm}^3 \text{ molecule}^{-1} \text{ s}^{-1} \exp(-2330 \text{ K}/T) \quad (6.7)$$

where the limited number of determinations at 15 Torr does not permit useful uncertainty analysis of the fitting parameters. The error limits in the Arrhenius expression are the 95% uncertainty in the fit parameters, weighted by the precision in the individual rate constants determined from the linear fit of the k' data to an exponential. A better fit to the observed data at 100 Torr is given by a modified Arrhenius form, with the temperature exponent fixed at 1.6:

$$k_5 = (1.1 \pm 1) \times 10^{-13} \text{ cm}^3 \text{ molecules}^{-1} \text{ s}^{-1} (T/298 \text{ K})^{1.6} \exp(-(1600 \pm 100) \text{ K}/T) \quad (6.8)$$

This is the fit shown in Figure 6.4.

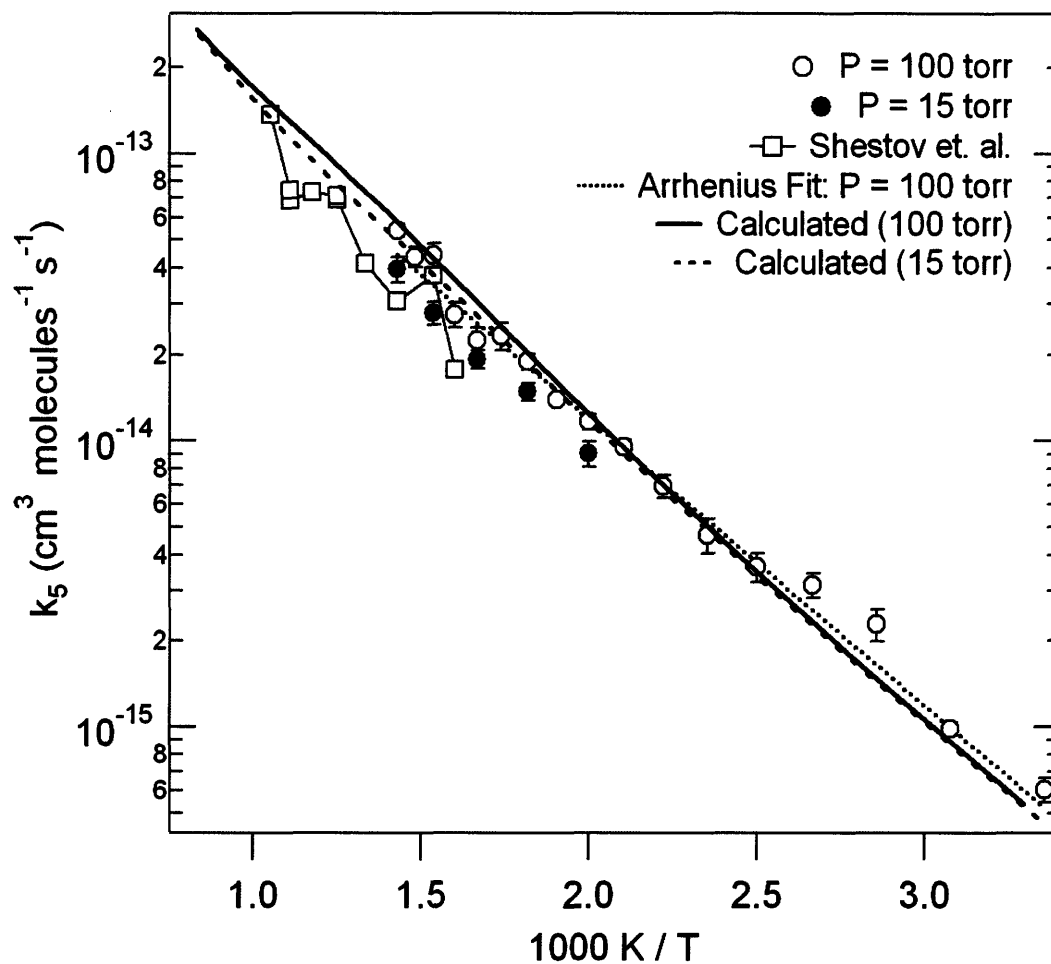


Figure 6.4: Temperature dependence of the total rate constant of the reaction of vinyl with ethylene. Open circles: experimental results of the current study at 100 Torr; filled circles: experimental results of the current study at 15 Torr; open squares: results reported by Shestov *et al.*¹¹⁸ Dotted line is the Arrhenius fits for high pressure data set for present study. Master equation calculations for 15 Torr (dashed line) and 100 Torr (solid line) are shown.

Table 6.6: Comparison of Vinyl + Ethylene (k_5) rate constants from literature and from the current study.

	Method	Temperature range (K)	Pressure (Torr)	A-factor ($\text{cm}^3 \text{ molecule}^{-1} \text{ s}^{-1}$)	E_a/R (K)
Benson and Haugen ¹³⁶ (1967)	Thermochemical Estimate	1170-1430		8.3×10^{-13}	0
Fahr and Stein ¹²⁰ (1989)	Very Low Pressure Pyrolysis (VLPP)	1023-1273	0.0010 - 0.010	1.04×10^{-12}	1560
Miller ¹¹⁷ (2004)	Computational Quantum Chemistry				1810 ^a
Shestov ¹¹⁸ (2005)	Laser Photolysis/Photoionization Mass Spectrometry	625-950		2.04×10^{-12}	2830 ± 790
Current Study	Laser Photolysis / Laser absorption	300-700	100	$(1.2 \pm 0.2) \times 10^{-12}$	2310 ± 70
		500-700	15	8.8×10^{-13}	2330

^a Relative enthalpy of transition state on potential energy surface

6.4.1.2. Comparison to previous studies

The reaction of vinyl radical with ethylene has been investigated previously by several authors. The results from all these studies have been summarized in Table 6.6. The previous experiments were generally carried out at conditions of lower pressure and higher temperature than the present experiments. Benson and Haugen¹³⁶ indirectly determined the rate constant for reaction (6.1) between 1100 K and 1430 K via kinetic modeling of the ethylene pyrolysis study performed by Skinner and Sokoloski¹³⁷. This rate coefficient is approximately a factor of 3 to 4 higher than an extrapolation of the Arrhenius fits to the results from many of the recent studies, including the current work.

Fahr and Stein¹²⁰ determined the rate constant for reaction (6.1) for the temperature range 1023 K to 1273 K relative to the vinyl radical recombination reaction. Using an assumed rate constant for the vinyl recombination of $3.3 \times 10^{-11} \text{ cm}^3 \text{ molecule}^{-1} \text{ s}^{-1}$ at low pressure and high temperature conditions, their derived k_5 values are in reasonable agreement with an extrapolation of the Arrhenius fit reported by Shestov *et al.*¹¹⁸

The activation energy from an Arrhenius fit to the present data taken at 100 Torr is found to be $(4.6 \pm 0.2) \text{ kcal mol}^{-1}$. This activation energy is approximately 1 kcal mol^{-1} lower than the activation energy obtained from an Arrhenius fit to the data of Shestov *et al.*¹¹⁸ and $\sim 1 \text{ kcal mol}^{-1}$ greater than the entrance barrier calculated by Miller¹¹⁷. Shestov *et al.*¹¹⁸ found that raising the energy for the entrance transition state from Miller's value by $1.3 \text{ kcal mol}^{-1}$ gave good agreement of their master equation calculations with the experimental data. This correction is within the accuracy of the G3//B3LYP

method used by Miller¹¹⁷. As shown in Figure 6.4, the present master equation calculations fit the 100 Torr data reasonably well without modification to the G3 energies. The present data at 15 Torr agrees with the data of Shestov *et al.*,¹¹⁸ whereas the rate coefficient at 100 Torr appears consistently ~20% - 30% higher at all temperatures, suggesting the vinyl + ethylene reaction is in the falloff region at the present experimental conditions and those of Shestov *et al.* The master equations predict a very slight falloff, as shown in Figure 6.4 with $k_5(15 \text{ Torr}) \sim 20\%$ smaller than $k_5(100 \text{ Torr})$ at 700 K.

One of the intriguing aspects of the vinyl + ethylene reaction in the context of molecular weight growth and soot formation in combustion is the possibility of forming resonance-stabilized C_4H_7 radicals. Resonance-stabilized radicals are less reactive than their unstabilized isomeric counterparts, and tend to reach larger concentrations in flames. As a result, resonance-stabilized radicals, in particular the propargyl (C_3H_3) radical, play a prominent role in aromatic formation and soot production. Miller¹¹⁷ predicted formation of delocalized 1-methylallyl isomer in the vinyl + ethylene reaction. Shestov *et al.*¹¹⁸ concluded from the thermal stability of the observed C_4H_7 product that substantial 1-methylallyl formation occurs in the reaction, and their master equation simulations suggested 40 % of the reaction proceeded by this pathway under the low-pressure (total densities of $6 \times 10^{16} \text{ cm}^{-3}$) conditions of their experiments. The present master equation calculations predict 1-methylallyl yields that (in general) rise with temperature and fall with increasing pressure, as shown in Figure 6.5.

An attempt was made to directly observe 1-methylallyl radical in the laser absorption experiments. Tonokura and Koshi¹³⁸ found allyl radical absorption to be in the same region as vinyl (370-420 nm). It is to be expected

that 1-methylallyl would also have absorption bands in this region, except that it may be more diffuse. Under the conditions of high temperature (650 K), low pressure (15 Torr), and high ethylene concentration, a low resolution spectrum of this system was taken from 390 nm to 440 nm. However, no features appeared that could be attributed to absorption by a 1-methylallyl reaction product. The visible absorption cross sections of vinyl radical and allyl radical are similar,¹³⁸⁻¹⁴⁰ and the signal-to-noise for the vinyl radical under these conditions is > 20 . However, the master equation simulations predict a relatively small yield of 1-methylallyl under these conditions, and it is possible that a 1-methylallyl yield consistent with the calculations simply is too small to be observed. Higher sensitivity measurements, possibly in other wavelength regions, may be required to observe absorption from 1-methylallyl produced in this reaction.

At temperatures below 500 K, the reaction between vinyl radical and ethylene predominantly forms the 3-buten-1-yl radical adduct, and the rate of 1-methylallyl formation is nearly negligible. As shown in Figure 6.5, the calculated production of 1-methylallyl formation at higher temperatures is strongly dependent upon the pressure; at 15 Torr 1-methylallyl becomes significant for temperatures between 650 and 900 K, whereas at 100 Torr the channel is predicted to be significant for temperatures between 800 and 1000 K. At still higher temperatures, the vinyl + ethylene reaction proceeds directly to the bimolecular products H + 1,3-butadiene via a chemically activated channel, and the yield of stabilized C_4H_7 is predicted to be very small. The steep decrease in 1-methylallyl yields as the pressure increases make the vinyl + ethylene reaction unlikely to be an important source of resonance-stabilized radicals in realistic combustion systems.

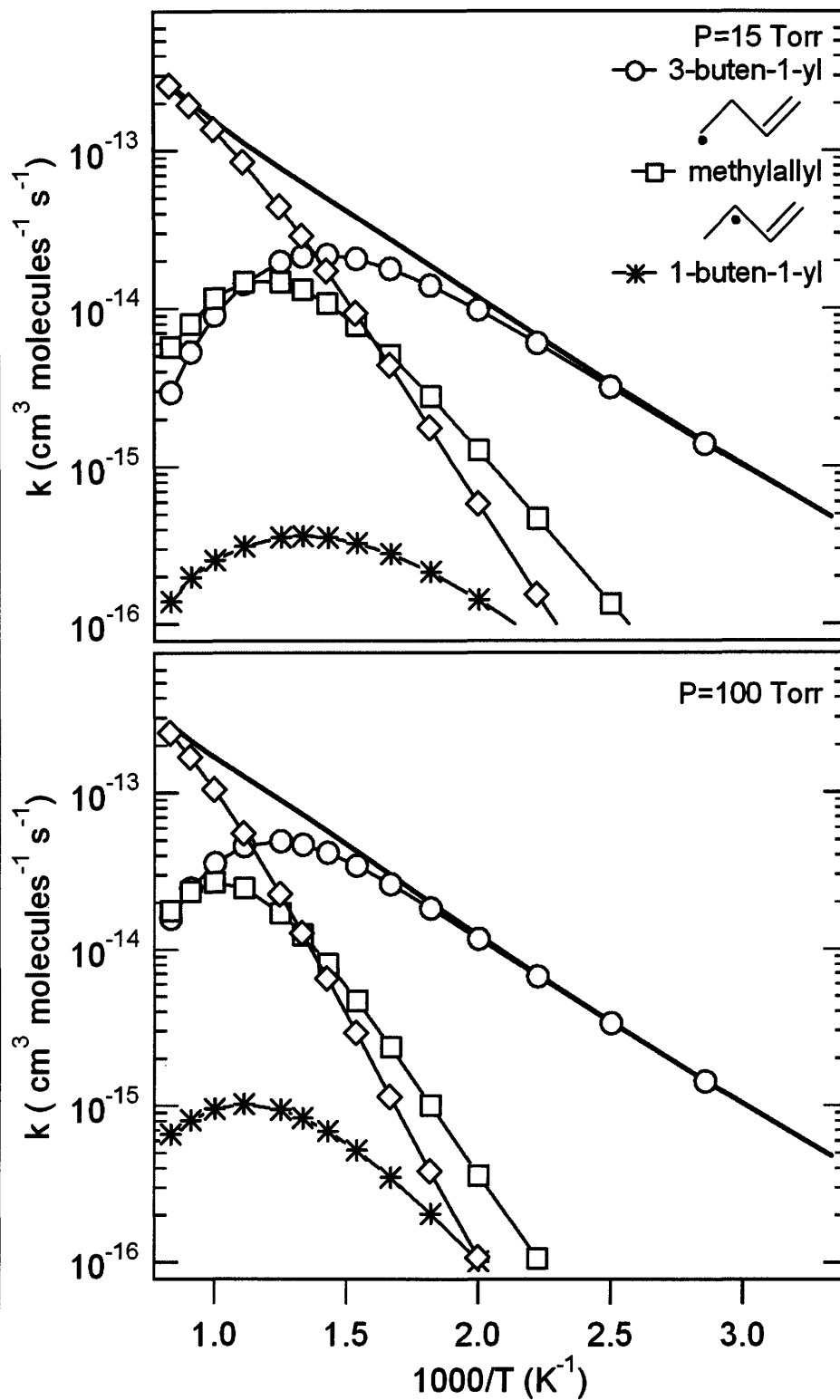


Figure 6.5: Master equation predictions for the product branching of the reaction between vinyl radical and ethylene at 15 Torr and 100 Torr.

6.4.1.3. Modeling of product studies using RMG

Earlier studies^{118,120} identified C_4H_7 and $H + C_4H_6$ as the only products of the $C_2H_3 + C_2H_4$ reaction. The subsequent reactions of different C_4H_7 isomers should produce distinguishable end products. In the 248 nm photolysis of vinyl iodide / ethylene mixtures carried out in Fahr's Lab, the primary products suffer secondary reactions before the stable final products are detected. Acetylene, 1,3-butadiene, 1-butene, 1,5-hexadiene, cyclohexene, and 1,7-octadiene have been identified as end products. In addition, an unidentified product of molecular weight of 82 was detected. It is likely that the products 1-butene, 1,5-hexadiene, cyclohexene, and the unidentified mass 82 product are formed mainly from the reactions of C_4H_7 radicals. The rule-based estimates in the RMG model predict the secondary chemistry based on families of known reactions, and the RMG mechanism therefore provides a framework for interpreting the observed stable products of the complex reaction system following 248 nm photolysis of vinyl iodide / ethylene mixtures. The RMG-generated mechanism consisted of 114 species and ~7500 reactions.

The RMG model predicts a roughly similar molar balance to that observed in the experiments, suggesting that the overall loss to secondary chemistry is approximately consistent with known hydrocarbon chemistry. However, the quantitative agreement for the major products is relatively poor, as seen in Figure 6.6 - 6.9 for 1,3-butadiene. In view of the disappointing quantitative predictions, inferences from comparisons of the model and the end product measurements are limited to qualitative information regarding relative yields.

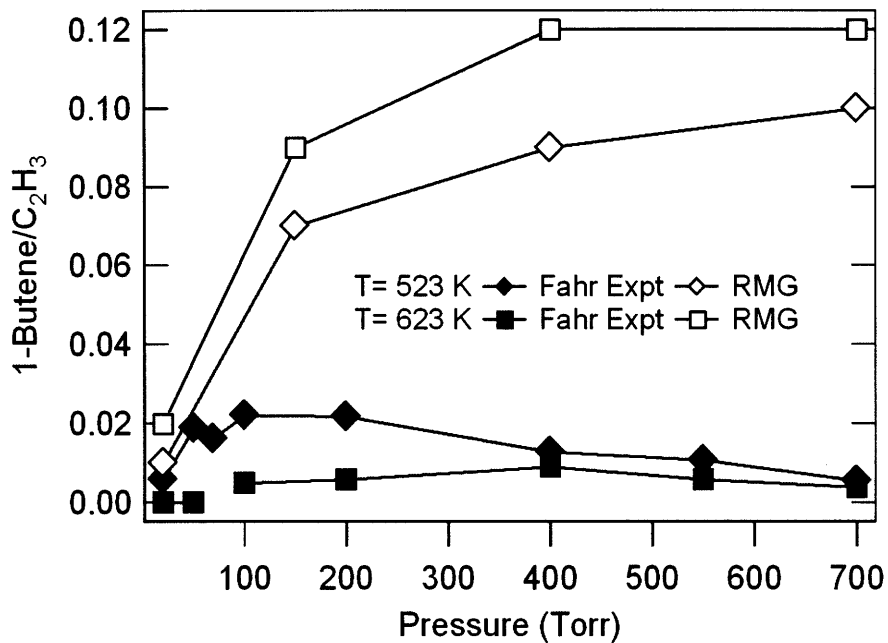


Figure 6.6: Experimental and RMG predicted yield of 1-butene versus total pressure

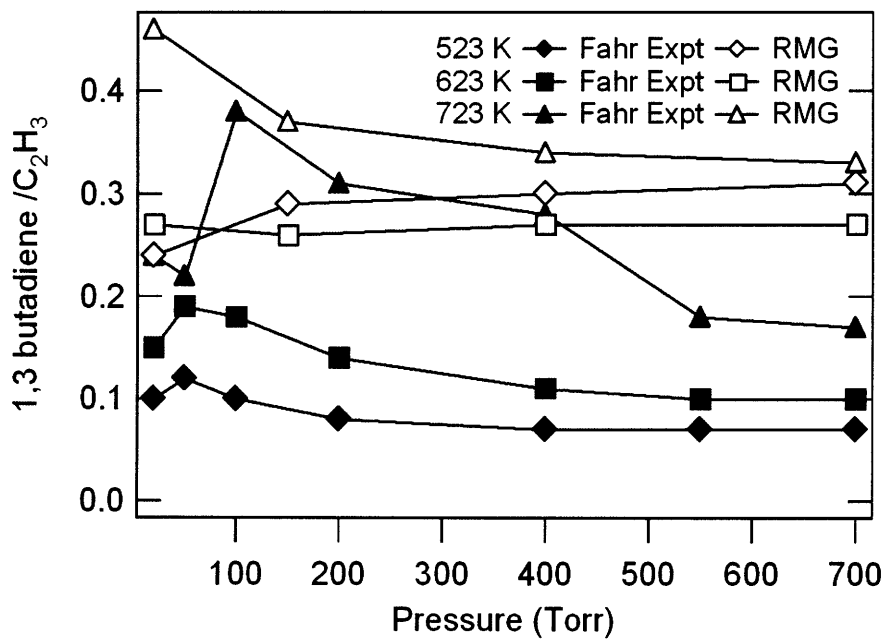


Figure 6.7: Experimental and RMG predicted yield of 1,3-butadiene versus total pressure

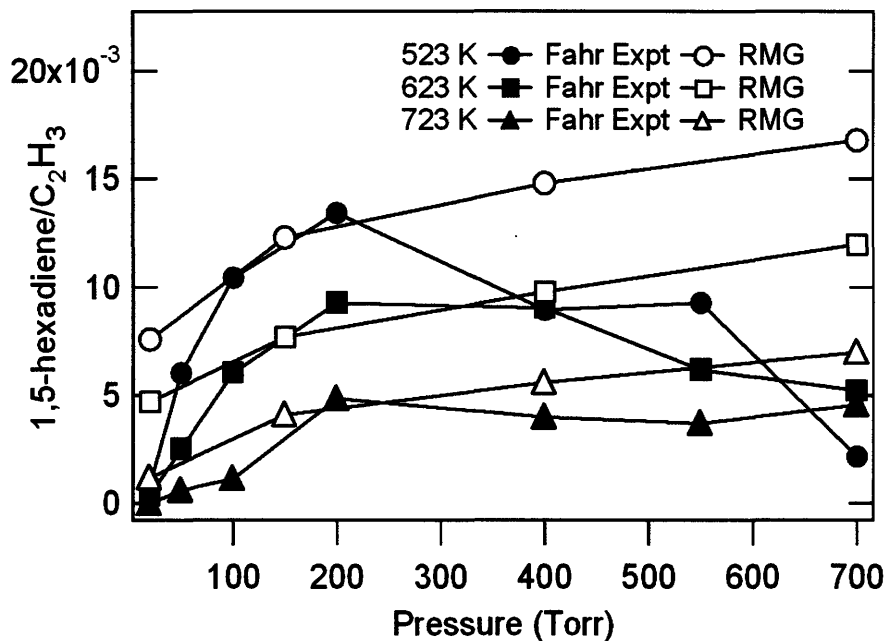


Figure 6.8: Experimental and RMG predicted yield of 1,5-hexadiene versus total pressure

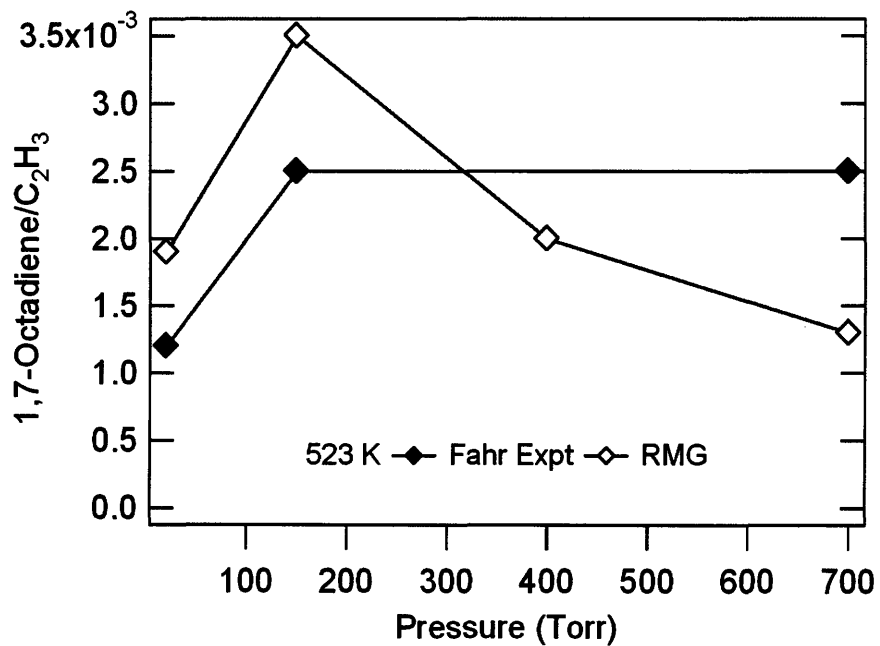


Figure 6.9: Experimental and RMG predicted yield of 1,7-Octadiene versus total pressure

The yield of 1-butene versus total pressure at selected temperatures is plotted in Figure 6.6. Contributions from the ethylene photochemistry to the 1-butene yield have not been deducted from the total 1-butene yield. The 1-butene yield rises rapidly with pressure, reaching a maximum at around 150 Torr. However, above 150 Torr total pressure, the 1-butene yield decreases. At 623 K, 1-butene yield shows a broad maximum centered at ~400 Torr. Interestingly, at high temperatures the 1-butene yield falls to a negligible level. The RMG mechanism predicts too high a concentration of 1-butene, perhaps for similar reasons as those that lead to the overestimate of 1,3-butadiene, which is shown in Figure 6.7. Both 1-butene and 1,3-butadiene may be products of H atom reactions with C_4H_7 , and it is possible that the H-atom chemistry is inaccurately modeled in the automatically generated mechanism.

The formation of 1-butene may arise from reactions of vinyl or H with either C_4H_7 isomer. Production of 2-butene, not experimentally observed, would also be expected from reactions of 1-methylallyl; the RMG model predicts 2-butene at about one-tenth the level of 1-butene. The C_4H_7 radicals predicted to be products of the reaction of vinyl with ethylene will yield various C_6H_{10} isomers from reactions with vinyl or with ethylene and isomers of C_8H_{14} from recombination reactions.

Figure 6.8 displays the observed and RMG-modeled yield of 1,5-hexadiene versus total pressure. At 523 and 623 K, 1,5-hexadiene yield increases with pressure up to about 225-300 Torr and then decreases at higher pressures. The yield of 1,5-hexadiene decreases as temperature is increased. At 723 K, 1,5-hexadiene yield increases with pressure up to about 225 Torr and remains nearly unchanged at higher pressures. The RMG model captures the qualitative behavior of the 1,5-hexadiene yields and reasonably matches the quantitative

yields, although the increased removal of 1,5-hexadiene at higher pressures is poorly modeled. The observed 1,5-hexadiene is likely a product of the 3-buten-1-yl radical reacting with vinyl or ethylene. Cyclohexene is another likely product of the reaction of 3-buten-1-yl with ethylene, not observed in RMG model but seen experimentally by Fahr. The 5-penten-1-yl radical initially formed by the addition of 3-buten-1-yl to ethylene rapidly cyclizes¹⁴¹ and formation of cyclohexene + H is predicted to be facile.¹⁴² Production of cyclohexene from 1-methylallyl seems rather less likely. Formation of cyclohexene + H in the reaction of 3-buten-1-yl with ethylene should be accompanied by a similar but smaller production of methylenecyclopentane + H.¹⁴³

Other isomers of C₆H₁₀, 1,4-hexadiene and 3-methyl-1,4-pentadiene, would be expected to arise, in approximately equal quantities, from 1-methylallyl reactions with vinyl (formation of H + linear C₆H₁₀ isomers is substantially endothermic from 1-methylallyl + ethylene). These isomers are not observed in the experiments; if one of them were responsible for the unidentified signal, a second unidentified mass 82 peak would be expected, corresponding to products of vinyl addition to the other radical site on 1-methylallyl.

Figure 6.9 shows the yield of 1,7-octadiene at 523 K and P= 20 Torr, 150 Torr and 700 Torr. The yield increases monotonically with pressure. This yield is modeled fairly well by the RMG mechanism. Recombination reactions of the 1-methylallyl radicals might be expected to be a more prominent loss pathway than for the 3-buten-1-yl radical because the resonance stabilization makes 1-methylallyl less reactive with stable molecules. The RMG mechanism predicts other C₈H₁₄ isomers, such as 2,6-octadiene, that may be expected to result from

recombination reactions of the 1-methylallyl radical or reactions of 1-methylallyl with 3-buten-1-yl, in concentrations similar to that of 1,7-octadiene. However, these isomers remain unobserved experimentally.

In conclusion, the observed products from the photolysis system can be rationalized as arising from secondary reactions of the primary 3-buten-1-yl and 1,3-butadiene products. Attempted in situ laser absorption detection of the 1-methylallyl product was also unsuccessful. Shestov et al.¹¹⁸ directly observed C_4H_7 radicals by photoionization mass spectrometry, and their master equation calculations, as well as those reported here, predict larger 1-methylallyl production at the lower pressures of their experiments. Perhaps similar measurements with tunable photoionization¹⁴⁴ could be used to experimentally determine the relative importance of the C_4H_7 isomers.

6.4.2. Vinyl + propene

The measured values for k_6 are listed in Table 6.2. A standard Arrhenius fit to the measured rate coefficient at 100 Torr, weighted by the uncertainties in the individual data points, yields:

$$k_6 = (2.15 \pm 0.40) \times 10^{-12} \text{ cm}^3 \text{ molecule}^{-1} \text{ s}^{-1} \exp[- (2320 \pm 70) / T] \quad (6.9)$$

The error limits in the Arrhenius equation are the 95% confidence intervals. A better fit to the observed data at 100 Torr is given by a modified Arrhenius rate equation, with the temperature exponent fixed at 1.6:

$$k_6 = (1.90 \pm 0.32) \times 10^{-13} \text{ cm}^3 \text{ molecule}^{-1} \text{ s}^{-1} (T/298)^{1.6} \exp[- (1550 \pm 70) / T] \quad (6.10)$$

At 15 Torr, a similar Arrhenius expression for the rate is given by:

$$k_6 = (7.1 \pm 1) \times 10^{-14} \text{ cm}^3 \text{ molecule}^{-1} \text{ s}^{-1} (T/298)^{1.6} \exp[- (1430 \pm 70) / T] \quad (6.11)$$

The results for the high- and low-pressure experiments, as well as the modified Arrhenius expression for the high-pressure experiments, and the VariFlex results for the high-pressure experiments (100 Torr) are shown in Figure 6.10.

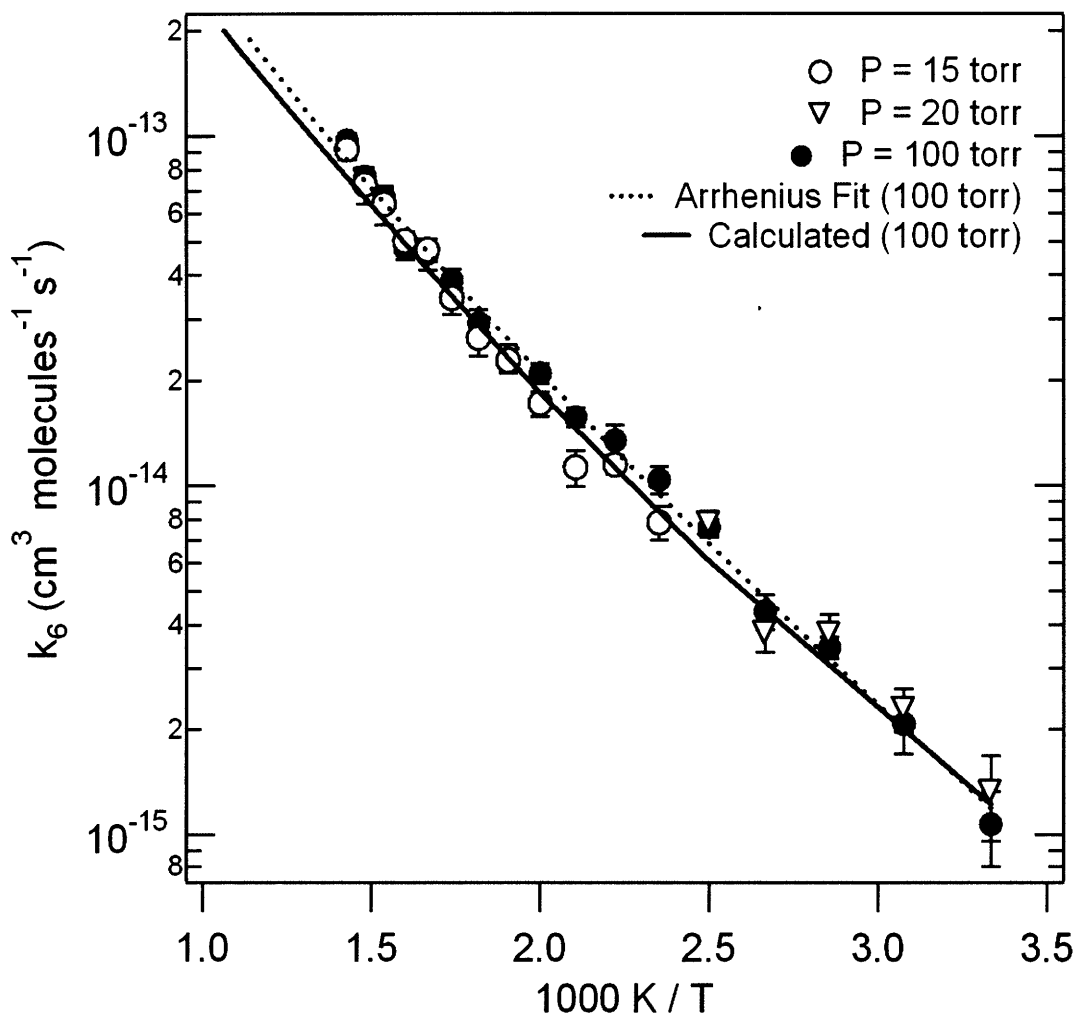


Figure 6.10: Temperature dependence of the total rate constant of the reaction of vinyl with propene. Filled circles: experimental results for 100 Torr; Open circles: experimental results for 15 Torr; open triangles: experimental results for 25 Torr. The dotted line is the Arrhenius fits (100 Torr) for the present data sets, and master equation calculations (100 Torr) are shown as the solid line.

6.4.3. Vinyl + butenes

The measured rate constant vinyl + 1-butene, vinyl + 2-butene and vinyl + iso-butene are given in Table 6.3, Table 6.4, and Table 6.5 respectively. An Arrhenius fit to the measured rate coefficient for reaction (6.3), (6.4), and (6.5) at 100 Torr, weighted by the uncertainties in the individual data points respectively yields following expressions:

$$k_7 = (1.29 \pm 0.3) \times 10^{-12} \text{ cm}^3 \text{ molecules}^{-1} \text{ s}^{-1} \exp(-(2197 \pm 121) \text{ K}/T) \quad (6.12)$$

$$k_8 = (1.67 \pm 0.4) \times 10^{-12} \text{ cm}^3 \text{ molecules}^{-1} \text{ s}^{-1} \exp(-(2610 \pm 128) \text{ K}/T) \quad (6.13)$$

$$k_9 = (1.04 \pm 0.4) \times 10^{-12} \text{ cm}^3 \text{ molecules}^{-1} \text{ s}^{-1} \exp(-(2129 \pm 55) \text{ K}/T) \quad (6.14)$$

The measured values, the Arrhenius fit and the Variflex simulations are shown in Figure 6.11.

A better fit to the observed data is given by a modified Arrhenius rate equation with the temperature exponent fixed at 1.6:

$$k_7 = (1.27 \pm 0.3) \times 10^{-13} \text{ cm}^3 \text{ molecules}^{-1} \text{ s}^{-1} (T/298 \text{ K})^{1.6} \exp(-(1475 \pm 115) \text{ K}/T) \quad (6.15)$$

$$k_8 = (1.36 \pm 0.3) \times 10^{-13} \text{ cm}^3 \text{ molecules}^{-1} \text{ s}^{-1} (T/298 \text{ K})^{1.6} \exp(-(1795 \pm 122) \text{ K}/T) \quad (6.16)$$

$$k_8 = (0.72 \pm 0.2) \times 10^{-13} \text{ cm}^3 \text{ molecules}^{-1} \text{ s}^{-1} (T/298 \text{ K})^{1.6} \exp(-(1200 \pm 170) \text{ K}/T) \quad (6.17)$$

In the vinyl + propene system, no pressure dependence was observed between 15 Torr and 100 Torr. Additionally, the RRKM calculation predicted no significant fall-off in the accessible experimental temperature and pressure regime. Therefore, the vinyl + butenes rate constants were measured at only high pressure of 100 Torr.

All the experiments for the vinyl + alkenes were conducted by probing vinyl radical at 423.2 nm, except for vinyl + isobutene. The vinyl + isobutene data exhibited a base-line offset. A spectrum was taken for the baseline offset from 422nm to 480nm as shown in Figure 6.12a. The transient absorption from this background is shown in Figure 6.12b. The rise time of this signal is ~20 μ s. The fall time of this signal is ~3 ms, which is comparable to radical-radical recombination rate (Chapter 4 & 5).

As seen in the spectrum, no background absorption is seen between 470 and 480 nm. The spectrum was taken at 700 K and 100 Torr of pressure. Vinyl radical has a weak absorption feature at 475 nm^{54,80}. At this wavelength, the baseline offset disappeared, therefore all the measurements for k_9 was taken using this wavelength. Since the background spectrum was taken at low resolution and lacked distinct features, it was very hard to optically identify which species was causing the background absorption.

Of the five vinyl + alkenes reactions considered, vinyl + iso-butene is unique in that it is the only reaction in which the initial adduct is a tertiary

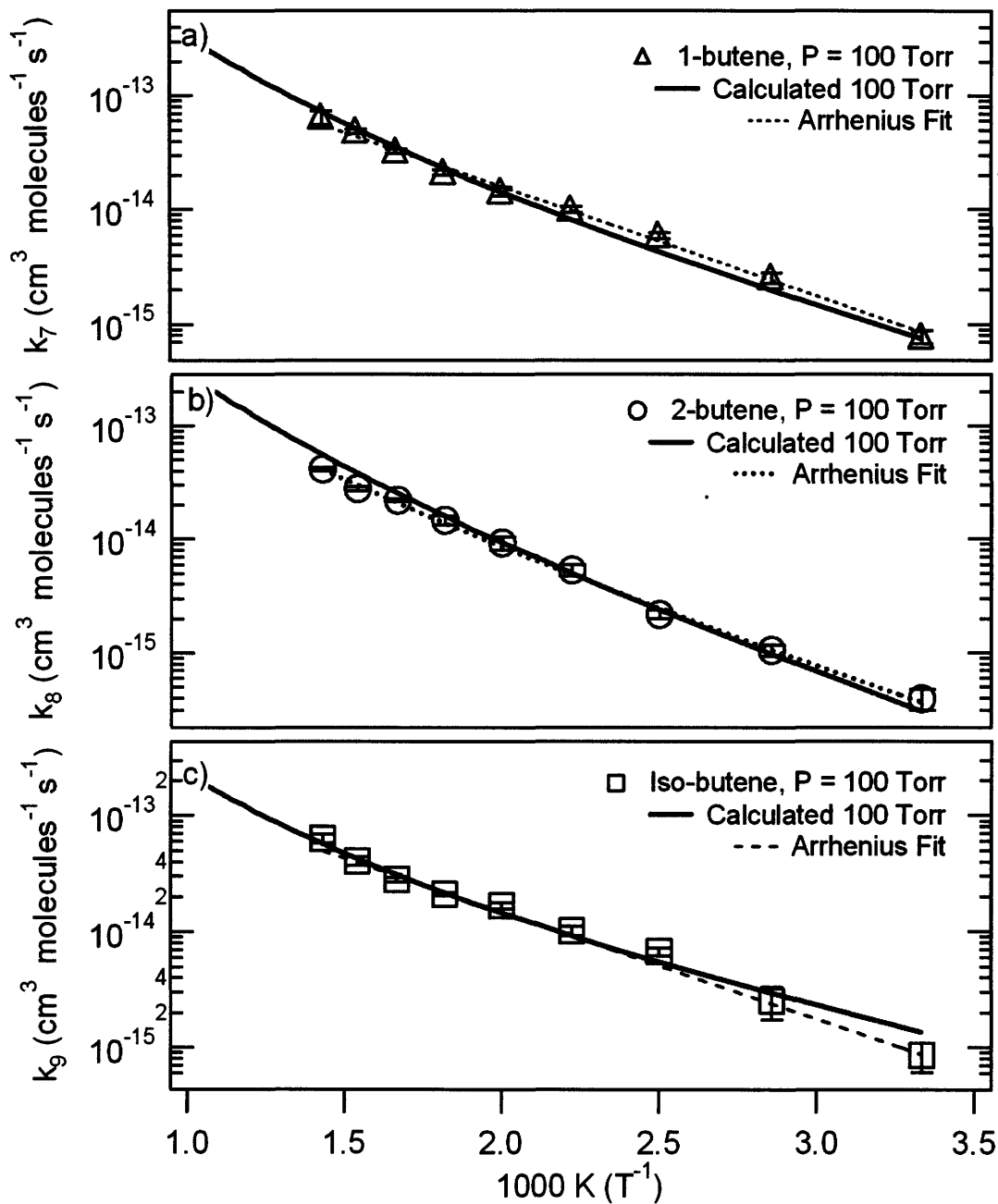


Figure 6.11: Temperature dependence of the total rate constant of the reaction of vinyl with various butene. Experimental results of the current study at 100 Torr; Open triangle: 1-butene; open circle: 2-butene; open square: isobutene; Dotted lines are the 2 parameter Arrhenius fits for each data sets. Master equation calculations (100 Torr) are shown as the solid line.

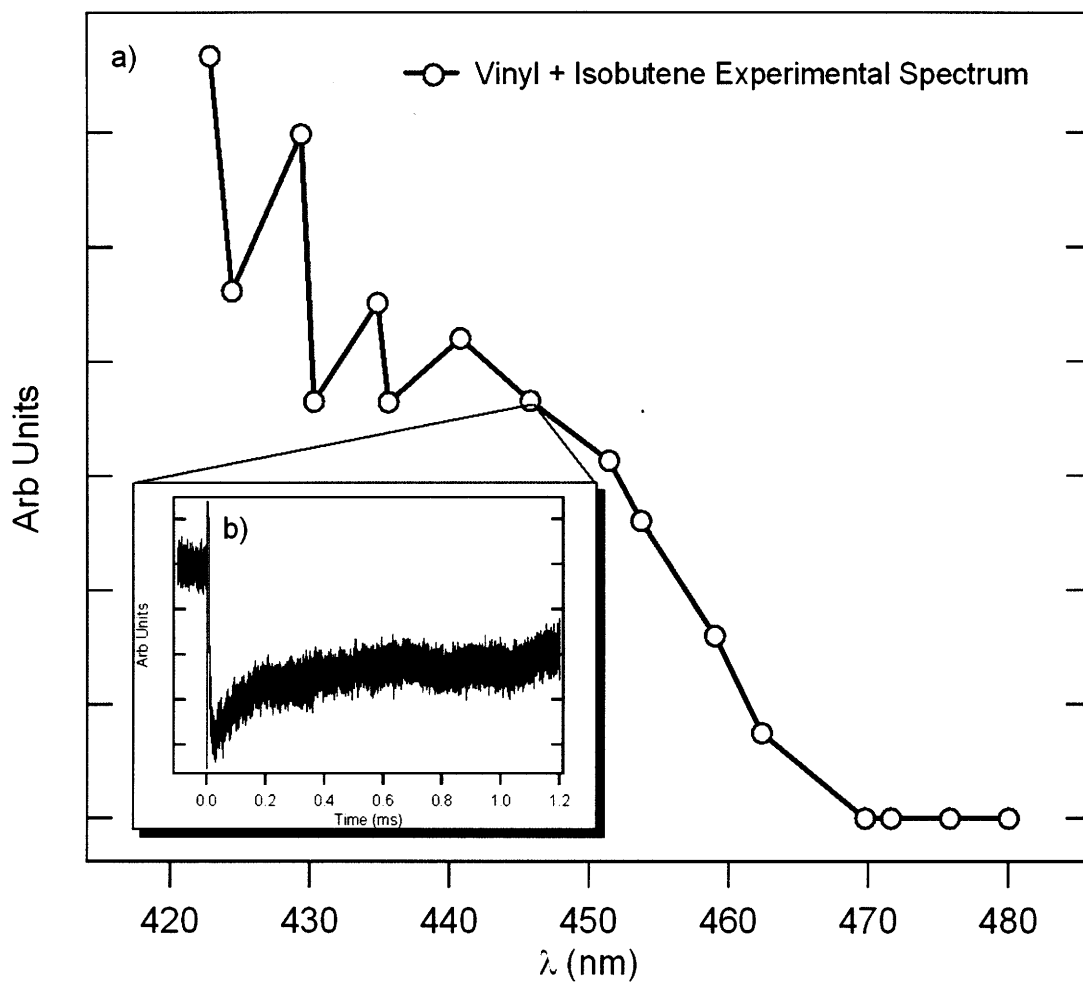


Figure 6.12: a) Low resolution spectrum of the background signal for vinyl + isobutene system taken at 700 K and 100 Torr. The background signal is attributed to 2-methylallyl radical b) Transient absorption of the background signal. The spectrum is taken at 0.8 ms. The background signal lasts for ~ 5 ms, before returning to baseline.

radical. The increased stability of the initial adduct implies that it is more difficult for chemically activated product formation to occur; at 100 torr, chemical activation doesn't occur until temperatures in excess of 850 K, according to the VariFlex calculations. Additionally, unlike vinyl + propene, 1-butene, and 2-butene, for temperatures above 700 K the dominant product channel for vinyl + iso-butene is the direct H-abstraction, yielding ethene + 2-methyl-allyl. Between 300 and 700 K, the H-abstraction channel increases from 5% to 25% of the total rate of disappearance of vinyl. The rate of H-abstraction from 1-butene is slightly faster than the abstraction from iso-butene, yet there is no baseline offset for the vinyl + 1-butene experiments. One difference between these two systems is that iso-butene yields 2-methyl-allyl, whereas 1-butene leads to 1-methyl-allyl. Thus, if 2-methyl-allyl has a strong absorption at 423.2 nm and 1-methyl-allyl does not, and then 2-methyl-allyl could be the source for the background absorption signal at 423.2 nm. The spectrum of the methyl-allyl species have never been measured in this wavelength range. Unsubstituted allyl has a strong absorption for $\lambda \leq 408$ nm as discussed in Chapter 5.

6.5. Discussion

The experimental data, combined with the quantum calculations and Arrhenius fits, show some interesting trends. Although the experimental rates are quite similar, the ordering of the rates cannot be explained easily by molecular weight or reaction enthalpy alone. The relative rate is determined by several effects: the structure of the adduct radical, the degree of substitution on the alkene bond, the high rotational constants for smaller molecular weight species, and the reaction path degeneracy. In general, the presence of a rotor will slow down the rate, unless the adduct being formed is a more stable radical. Beginning with the rate for vinyl + ethylene, even though there is no methyl substitution to hinder vinyl addition, the rate of vinyl + ethylene is comparatively slow because the adduct (3-buten-1-yl) is a primary radical. Vinyl + propene is faster than vinyl + ethylene, even though half of the vinyl addition sites are hindered by the methyl group, because the adduct (4-penten-2-yl) is a secondary radical. Vinyl + 1-butene is slightly slower than vinyl + propene, despite the fact that the ethyl group on 1-butene provides less of an obstruction to vinyl addition than does the methyl group on propene, because propene has one high rotational constant (details below). For vinyl + propene, 1-butene, and iso-butene, the dominant adduct is formed when the vinyl radical adds to the CH₂ end (i.e. "head") of the double bond; additionally, a primary radical can also be formed when the vinyl radical adds to the substituted end (i.e. "tail"), though these rates are typically an order of magnitude slower. 2-butene, in contrast, has no CH₂ group. Although the adduct is a secondary radical, the vinyl + 2-butene transition state is hindered by the presence of

methyl groups on both of the double-bonded carbons, effectively making it the slowest rate. Finally, vinyl + iso-butene is the only case in which the dominant adduct, 2-methyl-3-buten-2-yl, is a tertiary radical. Compared with vinyl + propene, even though the extra methyl group on the tail end of iso-butene provides additional obstruction to vinyl addition, the gain in stability due to the formation of a tertiary radical adduct is enough to decrease the relative barrier height. Vinyl + propene is still slightly faster than vinyl + iso-butene, however, due to the high rotational constant of propene.

6.6. Conclusion

The reaction kinetics of vinyl addition to various alkenes has been studied at temperatures ranging from 300 K to 700 K and at pressures of 15, 25, and 100 Torr. Arrhenius parameters for vinyl + ethylene (k_5), propene (k_6), 1-butene (k_7), 2-butene (k_8) and iso-butene (k_9) have been reported:

$$k_5 = (1.2 \pm 0.2) \times 10^{-12} \text{ cm}^3 \text{ molecule}^{-1} \text{ s}^{-1} \exp(-(2310 \pm 70) \text{ K}/T) \quad (6.6)$$

$$k_6 = (2.15 \pm 0.38) \times 10^{-12} \text{ cm}^3 \text{ molecule}^{-1} \text{ s}^{-1} \exp[-(2290 \pm 89) / T] \quad (6.9)$$

$$k_7 = (1.29 \pm 0.3) \times 10^{-12} \text{ cm}^3 \text{ molecules}^{-1} \text{ s}^{-1} \exp(-(2197 \pm 121) \text{ K}/T) \quad (6.12)$$

$$k_8 = (1.67 \pm 0.4) \times 10^{-12} \text{ cm}^3 \text{ molecules}^{-1} \text{ s}^{-1} \exp(-(2610 \pm 128) \text{ K}/T) \quad (6.13)$$

$$k_9 = (1.04 \pm 0.4) \times 10^{-12} \text{ cm}^3 \text{ molecules}^{-1} \text{ s}^{-1} \exp(-(2129 \pm 55) \text{ K}/T) \quad (6.14)$$

The current results for vinyl + ethylene at 15 Torr agree with results of Shestov *et al.*,¹¹⁸ and extrapolation of these data sets agrees well with the data of Fahr and Stein.¹²⁰ The rate constant measured at 100 Torr is consistently slightly higher than both the rate constant at 15 Torr and the data of Shestov *et al.*, suggesting the vinyl + ethylene reaction is in the falloff region in the present work and at the lower pressure conditions of the studies done by Fahr and Stein¹²⁰ and Shestov *et al.*¹¹⁸ The predicted branching to 1-methylallyl product is relatively small under the conditions of the vinyl + ethylene, experiments and we were not able to detect this radical directly. Analysis of end products of 248 nm photolysis of vinyl iodide / ethylene mixtures at total pressures between 20 Torr and 700 Torr using RMG provides no direct evidence for participation of 1-methylallyl.

The VariFlex simulations were in excellent agreement with experimental results. The background interference signal in vinyl + isobutene system was attributed to 2-methyl allyl radical.

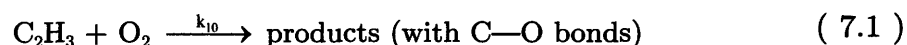
Chapter 7

7. Ongoing & Future Chemical Systems

7.1. Vinyl + O₂

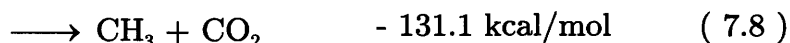
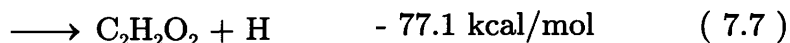
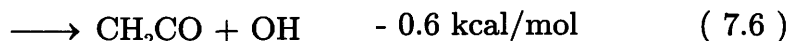
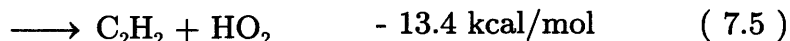
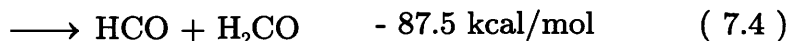
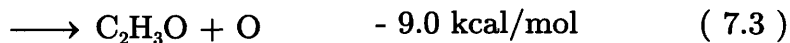
7.1.1. Introduction

In flame chemistry, the reaction of vinyl with molecular oxygen:



is very important because it competes with $\text{C}_2\text{H}_3 \rightarrow \text{H} + \text{C}_2\text{H}_2$ and other channels, which effectively lead to soot formation. In addition, Reaction (7.1) is also believed to play a role in the hydrocarbon chemistry of the Jovian atmosphere¹⁴⁵.

Though the reaction of vinyl with O₂ looks deceptively simple, because of its high exothermicity, many reaction channels are thermodynamically accessible^{146,147}:



The mechanism by Baldwin *et al.*¹⁴⁸ assumes reaction (7.4) to be the dominant channel. Using mass spectroscopy, Gutman and co-workers^{149,150} subsequently confirmed that reaction (7.4) is the dominant channel at low pressures and low temperatures. Their study was conducted between 297-602 K and a range of low pressures from 0.4-3.0 Torr. By detecting C₂H₃, HCO and H₂CO, they found reaction (7.1) to have a slight negative temperature dependence and found $k_{10} = (6.6 \pm 1.3) \times 10^{-12} \text{ cm}^3 \text{ molecules}^{-1} \text{ s}^{-1} \exp((126 \pm 50) \text{ K}/T)$. The relatively high value of the room-temperature rate constant ($k_{10} (298 \text{ K}) = (1.06 \pm 0.21) \times 10^{-11} \text{ cm}^3 \text{ molecules}^{-1} \text{ s}^{-1}$) determined by Gutman and co-workers^{149,150} was later corroborated by Krueger *et al.*¹⁵¹ who obtained $k_{10} (298 \text{ K}) = (1.0 \pm 0.4) \times 10^{-11} \text{ cm}^3 \text{ molecules}^{-1} \text{ s}^{-1}$ by using a tunable diode laser to probe C₂H₄. Using vacuum ultraviolet flash photolysis spectroscopy, Fahr and Laufer¹⁴⁶ also measured k_{10} at room temperature to be $(6.7 \pm 2.7) \times 10^{-12} \text{ cm}^3 \text{ molecules}^{-1} \text{ s}^{-1}$. Knyazev and Slagle,¹⁵² using laser photolysis/photoionization mass

spectrometry, repeated Gutman's original experiment and measured k_{10} at a higher temperature range (299-1005 K) and obtained an Arrhenius expression of $(6.92 \pm 0.17) \times 10^{-12} \text{ cm}^3 \text{ molecules}^{-1} \text{ s}^{-1} \exp((120 \pm 12) \text{ K}/T)$.

The importance of the reaction (7.1) has also prompted several theoretical studies aimed at predicting the overall rate constant and product branching ratio as a function of temperature and pressure. Based on the *ab initio* quantum calculations coupled with QRRK analysis, Westmoreland¹⁴⁷ and Bozzelli *et al.*¹⁵³ each estimated rate constants of several possible channels for reaction (7.1) over the temperature range of 300-2500 K. Carpenter^{154,155} used semi-empirical and *ab initio* quantum chemistry calculations to determine the overall rate constant and activation parameters at 297-602 K. The true complexity of reaction (7.1) is addressed by Mebel *et al.*,¹⁵⁶ who found more than 40 separate transition states in the PES. Mebel *et al.*¹⁵⁶ applied *ab initio* and density functional theory and found that the reaction (7.1) is predicted to proceed through the formation of vibrationally excited vinylperoxy radical ($\text{C}_2\text{H}_3\text{O}_2$). They calculated that under low pressure and low temperature conditions, the most favorable reaction channel is $\text{HCO} + \text{H}_2\text{CO}$. At low pressure and $T \geq 900 \text{ K}$, $\text{C}_2\text{H}_3\text{O} + \text{O}$ are major products and at very high temperatures, the $\text{C}_2\text{H}_2 + \text{HO}_2$ channel become competitive. Under high pressure and low temperature, Mebel *et al.*'s¹⁵⁶ calculation showed that it might be possible to trap vinylperoxy radical.

Based on Mebel *et al.*'s¹⁵⁶ study, Fahr and Laufer⁵⁷ obtained a gas phase, low-resolution spectrum of the products of 193 nm photolysis of $\text{C}_2\text{H}_3\text{Br}/\text{N}_2/\text{O}_2$ mixture at high pressure (50-70 Torr). In the absorption spectrum, ranging from 220-550 nm, they observed three peaks. They attributed the 230 nm and

smaller 420 nm peaks to vinylperoxy radical, whereas the 340 nm peak was attributed to other background species (e.g. vinoxyl radical or formaldehyde). Recently, Wang *et al.*,¹⁵⁷ using time-resolved Fourier transform infrared emission spectroscopy, detected various vibrationally excited products of 248 nm photolysis of C₂H₃Br/O₂ mixtures at 2 Torr and 460 K. They found H₂CO and HCO and CO₂ to be the main emitters, leading them to conclude that along with reaction (7.4), reaction (7.8) is also a significant channel at low temperatures and low pressures.

In the present study, we wanted to re-measure the vinyl + O₂ rate constant and attempt to probe for the appearance of vinylperoxy radical. Due to limitations of their experimental apparatus, Gutman *et al.*^{149,150} and Knyazev *et al.*'s¹⁵² conducted their experiments under fairly low pressures (< 2 Torr). Fahr and Laufer's⁵⁷ experimental setup lacked sufficient sensitivity and resolution to make definitive spectroscopic assignments; therefore it is possible that the absorption at 420nm, attributed to vinylperoxy radical, could be due to other species. The high sensitivity, tunability, and broad temperature and pressure range of our apparatus make it ideal to revisit the vinyl + O₂ system. The rate coefficient for the reaction (7.1) has been measured over a temperature range of 300 K to 700 K, and for pressures of 5, 10, 100 and 150 Torr. Additionally, a low resolution spectrum of C₂H₃I/He/O₂ mixture after 266 nm photolysis is recorded in an attempt to detect vinylperoxy radical and obtain its absorption spectrum.

7.1.2. Experimental details

The apparatus design for this experiment is described in Chapter 3. Vinyl iodide was used as a precursor to generate vinyl radical via 266 nm photolysis. GC grade 1% O₂ with balance Helium (Airgas) was used since the mass flow controller could not maintain sufficiently low flow rates of pure oxygen required for these experiments.

The vinyl radical was probed at 423.2 nm⁶⁰. The kinetic experiments to determine k_{10} were performed between 300 K and 700 K and at pressures of 5, 15, 100, and 150 Torr. To maintain pseudo-first-order conditions, [O₂] was in large excess over [C₂H₃]. Also, it was ensured that the pseudo-first order decays were at least ten times faster than the decay without added O₂. For most of the experiments, vinyl iodide concentrations were maintained at [C₂H₃I] = 1 × 10¹⁵ molecules cm⁻³. Details for all the experimental conditions for determining k_{10} are outlined in Table 7.1.

The low resolution spectrum of the C₂H₃I/He/O₂ mixture after 266 nm photolysis is recorded from 402-472 nm. The variation of the maximum absorbance ($\ln I_0/I$) was determined as a function of wavelength derived from the real-time absorption signals, 2 milliseconds after photolysis, for mixtures with identical sample composition and pressure. The spectrum was taken at room temperature, 5 Torr of total pressure, [C₂H₃I] = 2.2 × 10¹⁵ molecules cm⁻³ and [O₂] = 6.5 × 10¹⁴ molecules cm⁻³. A few points were taken at a high pressure of 100 Torr to resemble Fahr and Laufer's⁵⁷ experiments.

Table 7.1: Conditions and results of experiments to measure the reaction of vinyl with O₂(k₁₀).

Temperature (K)	Pressure (Torr)	[C ₂ H ₃ I] (10 ¹⁴ cm ⁻³)	[C ₂ H ₃] ₀ ^a (10 ¹² cm ⁻³)	[O ₂] (10 ¹⁴ cm ⁻³)	k ₁₀ ^b (10 ⁻¹² cm ³ molecule ⁻¹ s ⁻¹)	k ₀ ^c (s ⁻¹)
292	5	9.7	4.6	0.3 – 4.9	9.7 ± 0.5	600
400	5	9.6	4.5	0.3 – 2.5	8.5 ± 0.8	750
500	5	9.6	3.4	0.3 – 5.0	6.5 ± 0.3	1000
600	5	9.5	3.3	0.3 – 4.5	6.6 ± 0.3	1125
700	5	9.1	3.1	0.1 – 4.0	14.5 ± 0.8	1175
292	10	9.2	4.1	1.0 – 9.4	10.6 ± 0.4	620
325	10	8.4	4.9	1.0 – 8.6	10.8 ± 0.4	700
350	10	9.3	3.7	1.0 – 8.6	10.6 ± 0.5	743
375	10	9.8	5.3	1.1 – 9.1	10.6 ± 0.5	738
400	10	9.6	3.1	1.0 – 24.5	9.5 ± 0.5	760
425	10	9.9	3.8	1.1 – 8.9	9.6 ± 1.0	660
450	10	9.4	4.8	0.9 – 8.2	8.5 ± 0.5	650
475	10	9.8	4.4	1.0 – 6.0	8.6 ± 0.7	700
500	10	9.8	2.8	1.0 – 4.0	7.1 ± 0.8	780
525	10	10.2	3.8	1.0 – 6.0	7.4 ± 0.4	630
550	10	10.3	3.2	0.9 – 5.8	7.1 ± 0.4	890
575	10	10.4	3.1	1.0 – 5.9	6.6 ± 0.7	800
600	10	10.5	3.0	1.0 – 6.0	7.6 ± 1.0	830
625	10	10.1	3.9	1.0 – 6.0	8.5 ± 0.9	930
650	10	10.5	4.3	1.0 – 6.0	9.6 ± 0.9	550
675	10	10.1	3.6	1.0 – 14.0	1.2 ± 0.9	720
700	10	10.1	5.6	1.0 – 8.1	1.3 ± 1.5	950

Table 7.1: (continued): Conditions and results of experiments to measure the reaction of vinyl with O₂(k₁₀).

<i>Temperature</i> (K)	<i>Pressure</i> (Torr)	[C ₂ H ₃ I] (10 ¹⁴ cm ⁻³)	[C ₂ H ₃] ^a (10 ¹² cm ⁻³)	[O ₂] (10 ¹⁴ cm ⁻³)	k ₁₀ ^b (10 ⁻¹² cm ³ molecule ⁻¹ s ⁻¹)	k ₀ ^c (s ⁻¹)
292	100	9.7	4.5	0.3 – 5.3	10.6 ± 0.4	660
400	100	10.5	4.3	0.4 – 5.1	9.6 ± 0.2	650
500	100	9.7	3.6	0.3 – 4.9	8.8 ± 0.7	860
600	100	9.6	3.7	0.3 – 4.9	7.7 ± 0.7	640
700	100	9.8	3.3	0.3 – 4.1	13.7 ± 0.5	770
292	150	5.49	2.8	1.0 – 8.6	11.9 ± 0.1	560
350	150	5.49	2.8	0.9 – 5.5	10.7 ± 0.1	400
400	150	5.49	3.4	1.2 – 6.7	9.2 ± 0.1	667
450	150	5.49	2.2	1.0 – 5.9	9.2 ± 0.1	500
500	150	5.49	2.0	1.0 – 6.1	7.7 ± 0.1	930
550	150	5.49	2.3	1.0 – 5.8	7.8 ± 0.1	740
600	150	5.49	3.0	1.1 – 8.5	8.7 ± 0.1	890
650	150	5.49	2.7	1.5 – 8.8	1.1 ± 0.1	740
700	150	5.49	4.1	1.2 – 8.5	1.5 ± 0.1	560

^a Determined using C₂H₃ cross section of 2 × 10⁻¹⁹ cm² ³⁹

^b Uncertainty limits (± 1σ) based on statistical uncertainties in the fits.

^c The y-intercept of the plot of pseudo-first-order rate constant vs.[O₂].

The rate constant of the reaction of vinyl with molecular oxygen was determined using the procedure described in Section 6.2. A typical raw data trace is shown in Figure 7.1a at various $[O_2]$. At high $[O_2]$, significant interference from a background species was observed, causing considerable error in k' determination. Therefore, an off-resonance trace was acquired at 426.2 nm and subtracted from the on-resonance trace, and the resulting trace was then fitted to a single exponential decay to determine k' , as illustrated Figure 7.1b. This procedure was repeated at all temperatures and pressures at high $[O_2]$.

7.1.3. Results

7.1.3.1. Spectrum

The low resolution spectrum of the photolysis products of the $C_2H_3I/He/O_2$ mixture is obtained from 402-472 nm. Our initial hypothesis was that mysterious background signal seen in transient absorption signal at 423.2 nm as shown in Figure 7.1, were due to vinylperoxy radical, as reported by Fahr and Laufer⁵⁷. But this assessment was not kinetically consistent with our absorption signal since the fall time of the vinyl decay was about a factor of 4 faster than the rise time of the background signal. We would expect the fall time to be same as the rise time for the background signal if it were due to vinylperoxy radical.

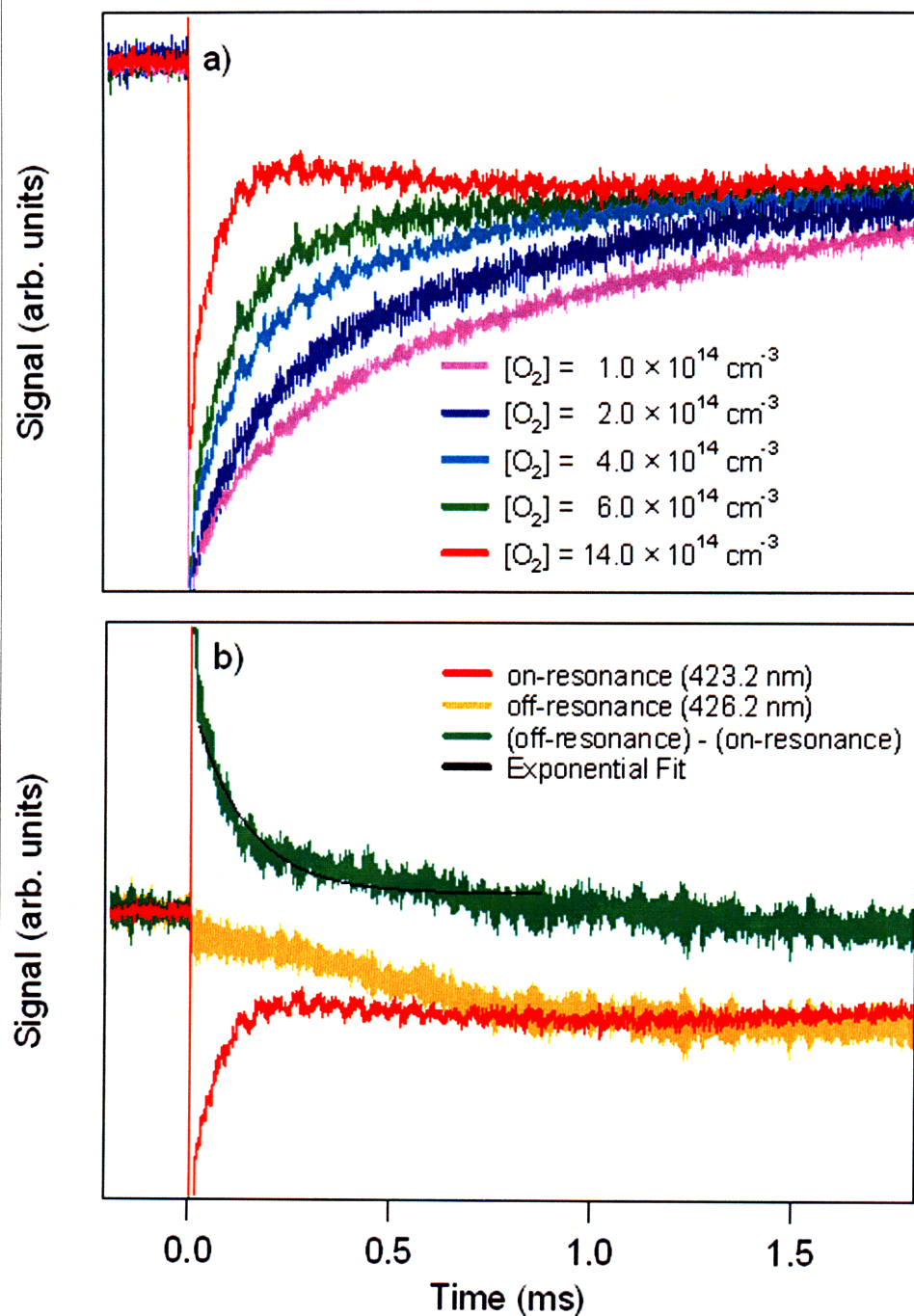


Figure 7.1. a) Recorded decay of C_2H_3 at 675 K and 10 Torr at various $[O_2]$. At high $[O_2]$, red and the green trace, the interference from the background signal is significant. b) A vinyl off-resonance trace was acquired at 426.2 nm and subtracted from the on-resonance signal and the resultant trace is fitted to a single exponential.

The spectrum obtained in the present study is shown in Figure 7.2a. The background signal was identified to be caused by iodine monoxide radical (IO). The spectrum of IO radical has been measured by several authors^{45,158-160}. As shown in Figure 7.2a, our results are in excellent agreement with spectrum published by Spietz *et al.*⁴⁵ The absorption cross section of IO radical, reported by Spietz *et al.*,⁴⁵ is more than an order of magnitude stronger than vinyl radical. Even though IO production is a fairly minor channel (<1%), its strong transition strength causes significant interference in the transient absorption signal of vinyl radical.

We also observed IO production to be highly pressure dependent. The [IO] at 100 Torr was approximately twice as high as [IO] at 5 Torr. The mechanism of IO production will be addressed in Section 7.3.

Due to the interference from IO radical, we were unable to replicate Fahr and Laufer's⁵⁷ vinylperoxy spectrum. If the present spectrum is subtracted from Spietz *et al.*'s⁴⁵ IO spectrum, the resultant spectrum yields a broad absorption feature from 400 to 432 nm, as shown in Figure 7.2b. This feature could be due to the vinylperoxy radical as Fahr and Laufer⁵⁷ predicted. Although, they reported this feature to be almost nonexistent at 10 Torr of total pressure, while we see a significant signal at 5 Torr of total pressure.

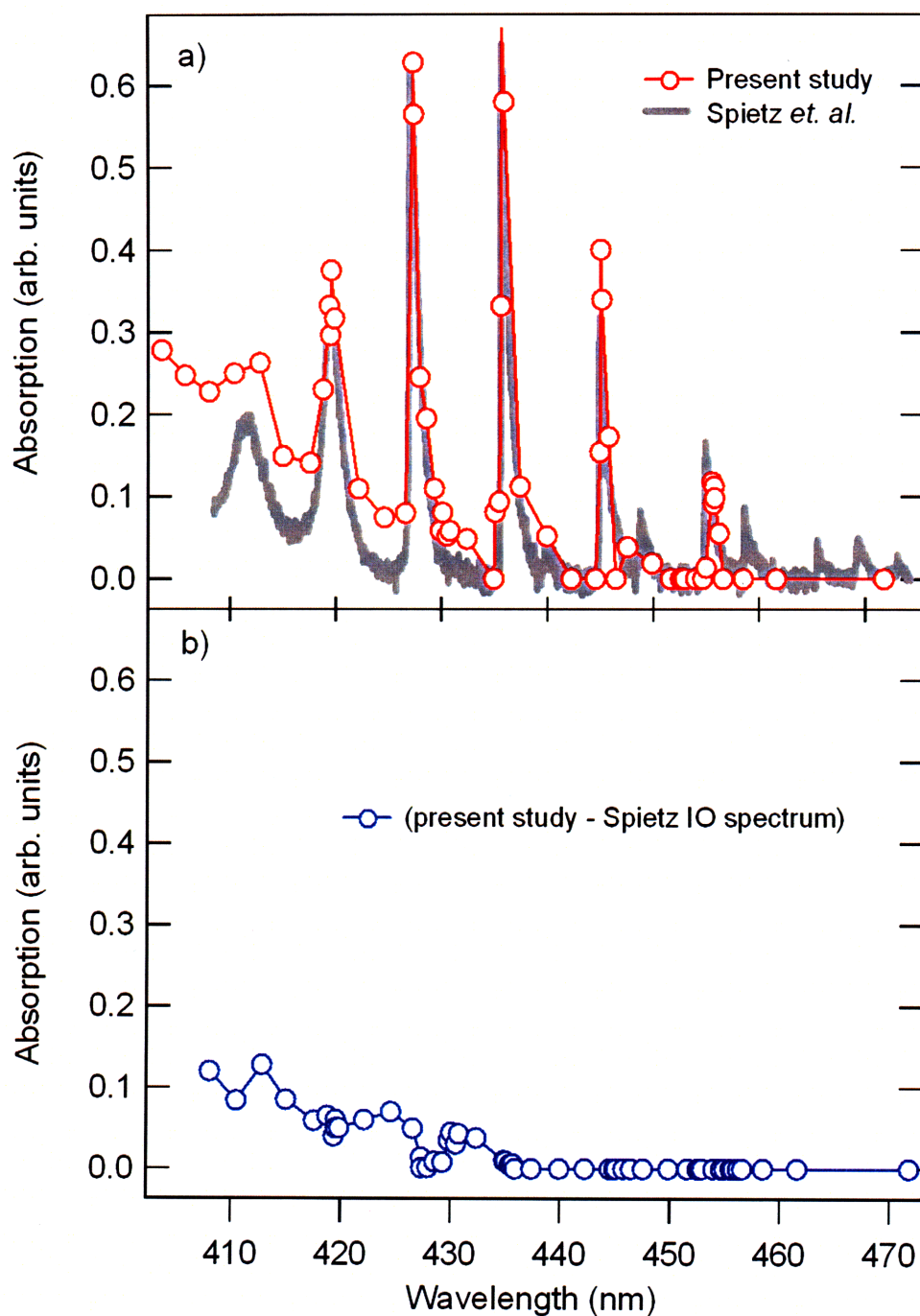


Figure 7.2. a) Low resolution spectrum recorded in the present study of photo-products of $C_2H_3I/He/O_2$ mixture after 266 nm photolysis (red trace) at 298 K and 5 Torr. It is compared to high resolution spectrum of Spietz *et al.* (grey trace). b) Spietz's spectrum is subtracted from the spectrum in the present study (blue trace), which yields a diffuse band from 400 to 432 nm.

7.1.3.2. Kinetic study (k_{10})

In the present study, k_{10} at room temperature showed no pressure dependence, therefore, the value reported below is the average of all pressures:

$$k_{10} (298 \text{ K}) = (10.7 \pm 0.9) \times 10^{-12} \text{ cm}^3 \text{ molecule}^{-1} \text{ s}^{-1} \quad (7.9)$$

Our room temperature rate constant value agrees very well with previous studies including Gutman *et al.*,^{149,150} Krueger *et al.*,¹⁵¹ and Knyazev *et al.*¹⁵² Our results are approximately 30% faster than Fahr and Laufer's¹⁴⁶ value, who used vacuum UV flash photolysis of $\text{Sn}(\text{C}_2\text{H}_3)_4$ and $\text{Hg}(\text{C}_2\text{H}_3)_2$ to measure k_{10} . As discussed in Chapter 4, Fahr and Laufer's¹⁴⁶ experimental technique is prone to interference from background species, which could account for the 30% discrepancy.

We also measured the temperature dependence (298-700K) of k_{10} at various pressures (5, 10, 100, and 150 Torr). The measured values for k_{10} are given in Table 7.1 and an Arrhenius plot is shown in Figure 7.3. The results from previous experimental and theoretical studies are also summarized in Figure 7.3. The Arrhenius plots for the current results exhibit rather strange behavior. From 298-600 K, we find k_{10} to have negative temperature dependence, as reported by previous studies^{149,150}. At 600 K, there is a 'turning point' in the Arrhenius plot, where the apparent rate constant of vinyl with oxygen becomes faster as temperature increases. In the previous studies, k_{10} continues to decrease with temperature (up to 1000 K).

Since this 'V-shaped' Arrhenius behavior occurs at all pressures, we do not believe this could be due to an error caused by thermal lensing. One

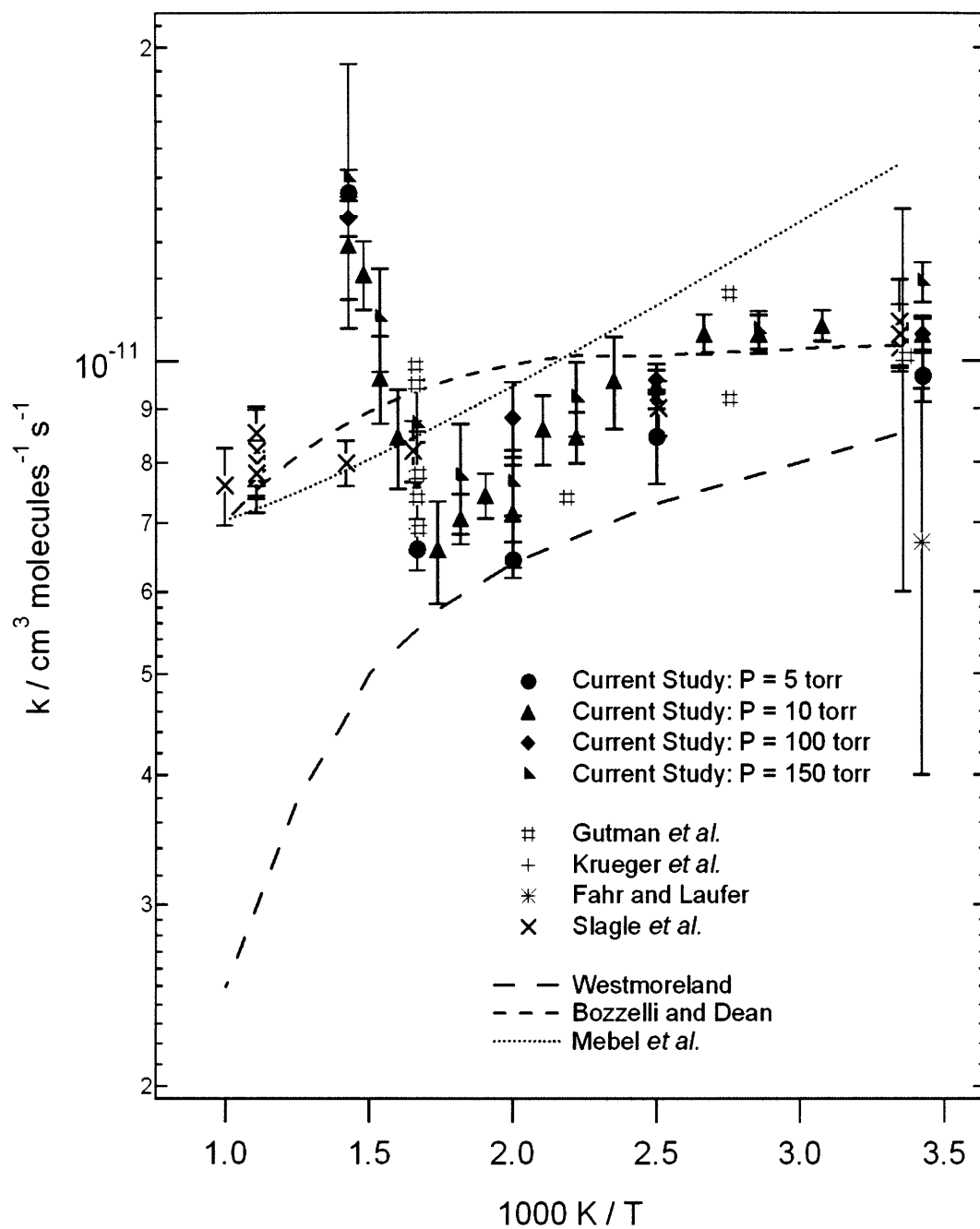
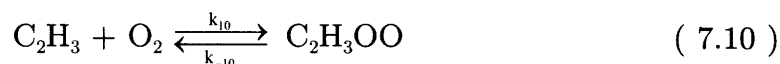


Figure 7.3. Temperature dependence of the total rate constant of the reaction of vinyl with O₂. Solid markers are experimental results of the current study at various pressures; The line markers are experimental results from various previous studies; Dotted lines are theoretical results from previous studies.

possibility is that at approximately 600 K, this reaction reaches equilibrium and mechanism switches as temperature rises:



Slagle and Gutman¹⁶¹ observed a similar 'V-shaped' Arrhenius behavior in the reaction of propargyl (C_3H_3) with molecular oxygen. They investigated this reaction from 293-900 K using a tubular reactor coupled with a photoionization mass spectrometer, where they monitored the disappearance of propargyl radical. From 293-333 K, they observed the propargyl decay to be a simple single exponential, and they were able to apply pseudo-first-order kinetics to solve for the forward rate for $\text{C}_3\text{H}_3 + \text{O}_2 \rightarrow \text{C}_3\text{H}_3\text{O}_2$. They also found, in this temperature range, the Arrhenius expression to have negative temperature dependence. Between 380 and 430 K, the propargyl decay became bi-exponential which is characteristic of the equilibrium $\text{C}_3\text{H}_3 + \text{O}_2 \rightleftharpoons \text{C}_3\text{H}_3\text{O}_2$. At high temperature (from 500-900 K), the mechanism for this reaction switches to yield $\text{C}_3\text{H}_3 + \text{O}_2 \rightarrow \text{H}_2\text{C}_2\text{O} + \text{HCO}$. Slagle and Gutman¹⁶¹ found the high temperature process to have normal Arrhenius dependence.

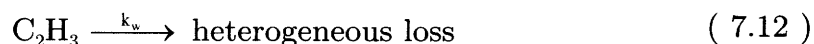
It is possible that vinyl + O_2 kinetic resembles Slagle and Gutman's¹⁶¹ propargyl oxidation system. At low temperatures (292 – 525 K), we find the rate constant for reaction (7.1), which corresponds to a simple reversible addition reaction. As observed in the previous studies^{149,150}, reaction (7.1) has a negative Arrhenius dependence of :

$$k_{10} (292-525 \text{ K}) = (4.5 \pm 2) \times 10^{-12} \text{ cm}^3 \text{ molecule}^{-1} \text{ s}^{-1} \exp((270 \pm 120) \text{ K}/T) \quad (7.11)$$

This expression is fitted to experiment data at all pressures and the error limits in the Arrhenius expression (7.11) are the uncertainty in the fit parameters, weighted by the precision in the individual rate constants determined from the linear fit of the k' data to an exponential. At low temperatures, the Arrhenius expression from the present study quantitatively agrees with previous experimental^{149,150,152} and theoretical studies^{147,153,156}.

At some temperature, the reverse reaction, $C_2H_3OO \rightarrow C_2H_3 + O_2$, is expected to become important and reaction 7.10 becomes equilibrated. Using Bozzelli and Dean's¹⁵³ thermochemistry for C_2H_3 and C_2H_3OO and at $[O_2] = 5 \times 10^{14}$ molecules cm^{-3} , we find that $C_2H_3 + O_2 \rightleftharpoons C_2H_3OO$ reaches equilibrium around 425 K. As seen in Figure 7.3, the current experimental data suggests that this reaction does not reach equilibrium below 575 K. The discrepancy of 150 K in the equilibrium constant could be caused by an error in the thermochemical estimate for C_2H_3OO by Bozzelli and Dean,¹⁵³ which was determined by using group additivity¹⁶².

Attempts were made to fit the data, between 550 and 600 K, to a simple equilibrium model. Reaction (7.10) and the heterogeneous loss channel: are the only reactions that need to be considered in the analysis of the transient absorption of vinyl radical, which considered the simple equilibrium model:



Under low concentrations of vinyl radical and high concentration of O_2 , the transient absorption of vinyl radical is simply given by a sum of two exponential¹⁶¹ terms:

$$[C_2H_3]_t = Ae^{-m_1t} + Be^{-m_2t} \quad (7.13)$$

The three parameters (A/B , m_1 , and m_2) are functions of the three rate constants k_{10} , k_{-10} and k_w and the oxygen partial pressure. The equations for these dependencies can be readily inverted to yield the equilibrium constant (K_p) for reaction (7.10) can be solved using following expression:

$$K_p = \frac{A}{B} \left(1 + \frac{\left(\frac{A}{B} + 1 \right) (m_2 - k_w)}{\left(\frac{A}{B} \right) (m_1 - m_2)} \right)^2 \quad (7.14)$$

Transient absorption of vinyl radical were fitted to equation (7.13) to obtain A , B , m_1 and m_2 by using a standard non-linear least-squares procedure and equation (7.14). These results were then used to determine K_p . To determine the thermodynamic parameters, ΔH and ΔS , a van't Hoff plot was constructed by plotting $\ln(K_p)$ vs. $1/T$.

Unfortunately, no clear trend was observed in the van't Hoff plot. We believe this occurred because of the interference from absorption from background species causing a breakdown in the bi-exponential model. Even though off-resonance trace was subtracted from each on-resonance transient absorption signal of vinyl radical, the subtraction process caused significant error in the B parameter of equation (7.13).

To minimize the interference from background species, the ideal solution is to generate vinyl radical with different precursors (i.e. methyl vinyl ketone (MVK) or vinyl bromide) and rerunning these experiments. The photolysis of MVK ($C_2H_3COCH_3$) was attempted. The absorption spectrum of MVK contains two bands. The first band spans from 160 – 250 nm. Fahr *et al.*¹⁶³ found that

193 nm photolysis of MVK led unity quantum yield of vinyl radical. Our lab did not have a source for generating 193 nm. The second absorption for MVK spans from 255-365 nm. The photolysis of MVK with quadrupled YAG (266nm) and tripling the YAG (355 nm), unfortunately, produced no evidence of vinyl radical production.

In the previous experiments using laser photolysis/photoionization mass spectrometry and detecting $C_2H_3^+$, HCO^+ and H_2CO^+ , Gutman & co-workers^{149,150} and Knyazev & Slagle¹⁵² concluded that the dominant channel for reaction 7.1 was HCO and H_2CO . In all three papers, the low temperature experiments (< 500 K) were conducted at relatively low pressure (< 1 Torr). The reaction of C_2H_3 with O_2 is predicted^{147,153,156} to begin through the vinylperoxy (C_2H_3OO) intermediate. Under the experimental conditions of Gutman & co-workers^{149,150} and Knyazev & Slagle¹⁵², the internal energy of the $C_2H_3OO^*$ generated upon formation of the C—O bond does not deactivate fast enough to stabilize the radical, and $C_2H_3OO^*$ rapidly dissociates to form HCO and H_2CO . Since our experiments are conducted at higher pressures, $C_2H_3OO^*$ could thermally stabilize to form C_2H_3OO and live long enough for us to monitor the equilibrium for reaction (7.2).

A good way to test that the dominant product for reaction (7.2) is C_2H_3OO under our experimental conditions is to probe for potential products. As discussed previously, we attempted to probe for C_2H_3OO radical but the results were inconclusive due to interference from the IO radical. In the propargyl oxidation experiment of Slagle and Gutman¹⁶¹, they monitored the $C_2H_2O^+$ ion and detected no signal under low temperature conditions, but at intermediate and high temperatures, a $C_2H_2O^+$ ion signal was observed, leading the authors to conclude $C_3H_3 + O_2$ to be in equilibrium with C_3H_3OO and that

the mechanism switches over to produce $\text{HCO} + \text{C}_2\text{H}_2\text{O}$ at high temperature. Our experimental apparatus would be ideal to potentially probe for HCO, since its absorption spectrum spans from 460 nm to 750 nm¹⁶⁴. If the vinyl radical is indeed trapped as vinylperoxy, the HCO signal should increase steadily as temperature is increased or as pressure is decreased.

7.1.4. Conclusions and future work

We have determined the rate constant of vinyl with molecular oxygen at room temperature and found to be in excellent agreement with previous literature values. We also acquired a low resolution spectrum of photolysis products of $\text{C}_2\text{H}_3\text{I}/\text{He}/\text{O}_2$ mixtures, which was dominated by features from IO radical. We also found some tentative evidence of vinylperoxy radical in this spectrum. Additionally, the temperature and pressure dependence of k_{10} was determined, but the results were inconclusive. The ‘u-shaped’ Arrhenius dependence for k_{10} was attributed to either mechanism changing due to equilibrium or interference from background species.

For future work, we recommend re-running these experiments with 248 nm photolysis of vinyl bromide and 193 nm photolysis of methyl vinyl ketone. Also, probing for potential products like HCO could provide insights into the equilibrium reaction.

Analogous to vinyl iodide, vinyl bromide could pose potential problems by producing bromine monoxide (BrO) and bromine dioxide OBrO, which could interfere with vinyl absorption signal. The BrO and OBrO spectra have been published in the literature by Wilmouth *et al.*⁴¹ (280-380 nm) and Knight *et*

*al.*⁴⁰ (400-560 nm), respectively. Similar to IO, both BrO and OBrO have sharp absorption band structure with $\sim 100\times$ stronger absorption cross section than vinyl radical. In the low resolution vinylperoxy spectrum recorded from a $C_2H_3Br/O_2/N_2$ mixture after 248 nm photolysis, Fahr and Laufer⁵⁷ observed an unidentifiable absorption feature from 300-380 nm, which they hypothesized to be due to be either vinoxyl radical or formaldehyde, and the band from 400-450 nm was attributed to vinylperoxy radical. In their paper, Fahr and Laufer⁵⁷ never discussed the possibility of generating BrO and OBrO. Also, their spectrum consisted of only approximately 25 data points over the span of 300-500 nm, which would make it impossible to identify the sharp features of BrO and OBrO. Therefore, it is possible that Fahr and Laufer⁵⁷ misidentified the two bands in their spectrum and that the bands were actually caused by BrO and OBrO. The sharp band features of BrO and OBrO should make them easily distinguishable from diffuse band structure of vinyloxy and vinylperoxy radical.

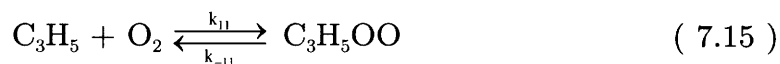
In the 248 nm photolysis of $C_2H_3Br/O_2/He$ mixture, if BrO and/or OBrO are identified as the absorbing species, then 193 nm photolysis of MVK/ O_2/He mixtures should be attempted. This chemical system would yield photo products of CO, CH_3 and C_2H_3 ¹⁶³. Methoxyl¹⁶⁵ and methylperoxyl¹⁶⁶ radical could be potential photoproducts, but both of these radicals do not absorb from 400-500nm. If BrO and OBrO are not formed in the 248 nm photolysis of $C_2H_3Br/O_2/He$ mixture, an interesting mechanistic question can be addressed on why IO is formed in our vinyl iodide experiments. Production of IO, OIO, BrO and OBrO are of great of interest in the field of atmospheric chemistry with respect to ozone depletion and aerosol formation^{167,168}.

7.2. Allyl + O₂

7.2.1. Introduction

The reaction of allyl and allyl-like radicals with oxygen plays an important role in the elementary steps of many oxidation processes including combustion and atmospheric chemistry. The double bond in the precursor of these radicals provides both an unsaturated site for addition reactions and an allylic site for abstraction reactions, where the corresponding activation energy is lowered due to electron delocalization. The stability and low reactivity of allyl-related radicals have been linked to the anti-knock effect of fuel additives such as ethyl *tert*-butyl ether¹⁶⁹. Additionally, the high octane ratings for olefin blending suggest that they play a critical role in pre-ignition chemistry. Therefore, for accurate low-temperature combustion model development, it is important to understand the fundamental chemical reaction pathways and kinetics of olefin oxidation.

Due to the stability of the allyl radical, it is found to be in equilibrium with allylperoxy radical at low temperatures.



The reaction of allyl radical with molecular oxygen has been addressed by several authors¹⁷⁰⁻¹⁷⁵. Ruiz *et al.*¹⁷⁰ and Slagle *et al.*¹⁷² using photoionization mass spectroscopy and Morgan *et al.*¹⁷¹ via UV absorption spectroscopy reported equilibrium constants for reaction (7.15). Ruiz *et al.*¹⁷⁰ and Slagle *et al.*'s¹⁷² study was conducted under fairly low pressures (< 1 Torr) whereas Morgan *et*

*al.*¹⁷¹ measured reaction (7.15) at higher pressure (~50 Torr). All three studies found reaction (7.15) equilibrated between 350 - 425 K. Using colorimetry and gas chromatography for product analysis, Walker *et al.*^{173,174} determined forward rates of various pathways for $C_3H_5 + O_2$. Their experiments were conducted between 673 - 750 K and found several accessible reaction pathways once equilibrium had been established. Recently, Lee and Bozzelli¹⁷⁵ performed thorough thermochemical and kinetic analysis of the $C_3H_5 + O_2$ chemical system and found several other reaction pathways in addition to the ones recommended by Walker *et al.*^{173,174}. They found that the allyl radical adds to O_2 to form an excited peroxy adduct $CH_2=CHCH_2OO^*$ which has a relatively small barrier (~20 kcal/mol) for dissociation. The energized peroxy adduct could also stabilize to form $CH_2=CHCH_2OO$ or isomerize via a hydrogen shift to form $CH_2=CHCHO$ and OH . Other important channels include: allene + HO_2 and $C_2H_2 + CH_2O + OH$ which are calculated to become significant above 600 K.

While conducting the experiments to determine the self-reaction rate constant of allyl (Chapter 5), we observed a background absorption signal at 408 nm when O_2 was added to quench $I^* \rightarrow I$. In the present study, we investigate the mysterious background signal, by acquiring a low resolution spectrum of $C_3H_5I/He/O_2$ mixture after 266 nm photolysis. Also, we determined the forward rate constant for reaction (7.15) at room temperature since none of the previous authors¹⁷⁰⁻¹⁷⁵ reported it. Lastly, we attempted to measure the equilibrium constant for reaction (7.15) and its temperature dependence to see if such measurements can be made using our apparatus.

7.2.2. Experimental details

The low resolution spectrum of the photoproducts of $C_3H_5I/He/O_2$ mixture after 266 nm photolysis was taken from 404-481 nm, at room temperature, 20 Torr of total pressure, $[C_3H_5I]= 9.0 \times 10^{14}$ molecules cm^{-3} and $[O_2]= 3.0 \times 10^{15}$ molecules cm^{-3} . The absorption signal after 2-4 milliseconds was plotted against wavelength to obtain the low resolution spectrum.

The kinetic experiments were conducted from 300 to 550 K and at pressures of 20 and 100 Torr. The details for the experimental conditions are summarized in Table 7.2 and Table 7.3. The forward rate constant for reaction (7.15) at room temperature was determined using the pseudo first order assumption (Figure 7.4). Similar to the vinyl + O_2 kinetic system (Section 7.1.2), significant interference from background species was observed at high $[O_2]$ and an off-line trace taken at 435 nm was subtracted from the on-resonance trace. The data at 350, 400 and 450 K were fitted to biexponential (equation (7.13) and equilibrium constants were determined using equation (7.14). A typical data trace and the bi-exponential fit are shown in Figure 7.4.

7.2.3. Results

7.2.3.1. Spectrum

The low resolution spectrum of the photoproducts for $C_3H_5I/He/O_2$ mixture is shown in Figure 7.5a. Based on the kinetics data, we believe there

Table 7.2: Conditions and results of experiments to measure reaction of allyl with O₂

T (K)	P (Torr)	$[C_3H_5I]$ (10 ¹⁴ cm ⁻³)	$[C_3H_5]_0^a$ (10 ¹² cm ⁻³)	$[O_2]$ (10 ¹⁵ cm ⁻³)	k_{11}^b (10 ⁻¹³ cm ³ molecule ⁻¹ s ⁻¹)	k_w^c (s ⁻¹)
300	20	4.5	7.1	0.4 – 6.2	8.3 ± 0.5	390
300	100	4.5	7.8	0.8 – 8.2	10.1 ± 0.8	360
500	20	9.1	7.1	0.4 – 2.4	-	310
500	100	9.7	6.3	0.4 – 2.4	-	340
550	20	9.0	6.1	0.2 – 1.3	-	330
550	100	9.0	6.2	0.4 – 3.5	-	310

^a Determined using C₃H₅ cross section of 4 × 10⁻¹⁹ cm²

^b Uncertainty limits (± 1σ) based on statistical uncertainties in the fits.

^c k_w is the first order rate constant for the heterogeneous loss of C₃H₅

Table 7.3: Conditions and results of experiments to measure equilibrium constants for $C_3H_5 + O_2 \leftrightarrow C_3H_5OO^a$

T (K)	P (Torr)	$[C_3H_5I]$ (10^{14} cm^{-3})	$[C_3H_5]_0^b$ (10^{12} cm^{-3})	$[O_2]$ (10^{14} cm^{-3})	k_w^c (s^{-1})	m_1 (s^{-1})	m_2 (s^{-1})	A/B (s^{-1})	K_p^d (atm^{-1})
350	20	4.9	8.1	4.8	490	5870	1060	1.62	88000
350	20	4.9	8.1	9.8	440	6550	1380	1.62	46950
350	100	3.9	7.7	4.9	460	6320	1180	1.70	107800
350	100	3.9	7.7	9.7	450	5900	1110	2.10	64600
400	20	5.0	5.2	48	510	5480	740	2.66	9760
400	20	5.0	5.2	72	460	6080	730	3.18	7740
400	100	5.0	5.1	68	590	8660	680	3.33	6340
400	100	5.0	5.1	93	580	10600	690	3.20	3860
450	20	5.1	5.0	24	600	7120	700	0.09	540
450	20	5.1	5.0	49	560	13540	810	0.11	360
450	100	4.9	4.9	24	680	8420	850	0.14	980
450	100	4.9	4.9	47	540	9450	650	0.06	200

$$^a [C_3H_5]_t = Ae^{-k_1t} + Be^{-k_2t}$$

^b Determined using C_3H_5 cross section of $4 \times 10^{-19} \text{ cm}^2$

^c k_w is the first order rate constant for the heterogeneous loss of C_3H_5

$$^d K_p = (A/B) [1 + (((A/B)+1)(k_2-k_w)) / ((A/B)(k_1-k_2))]^2$$

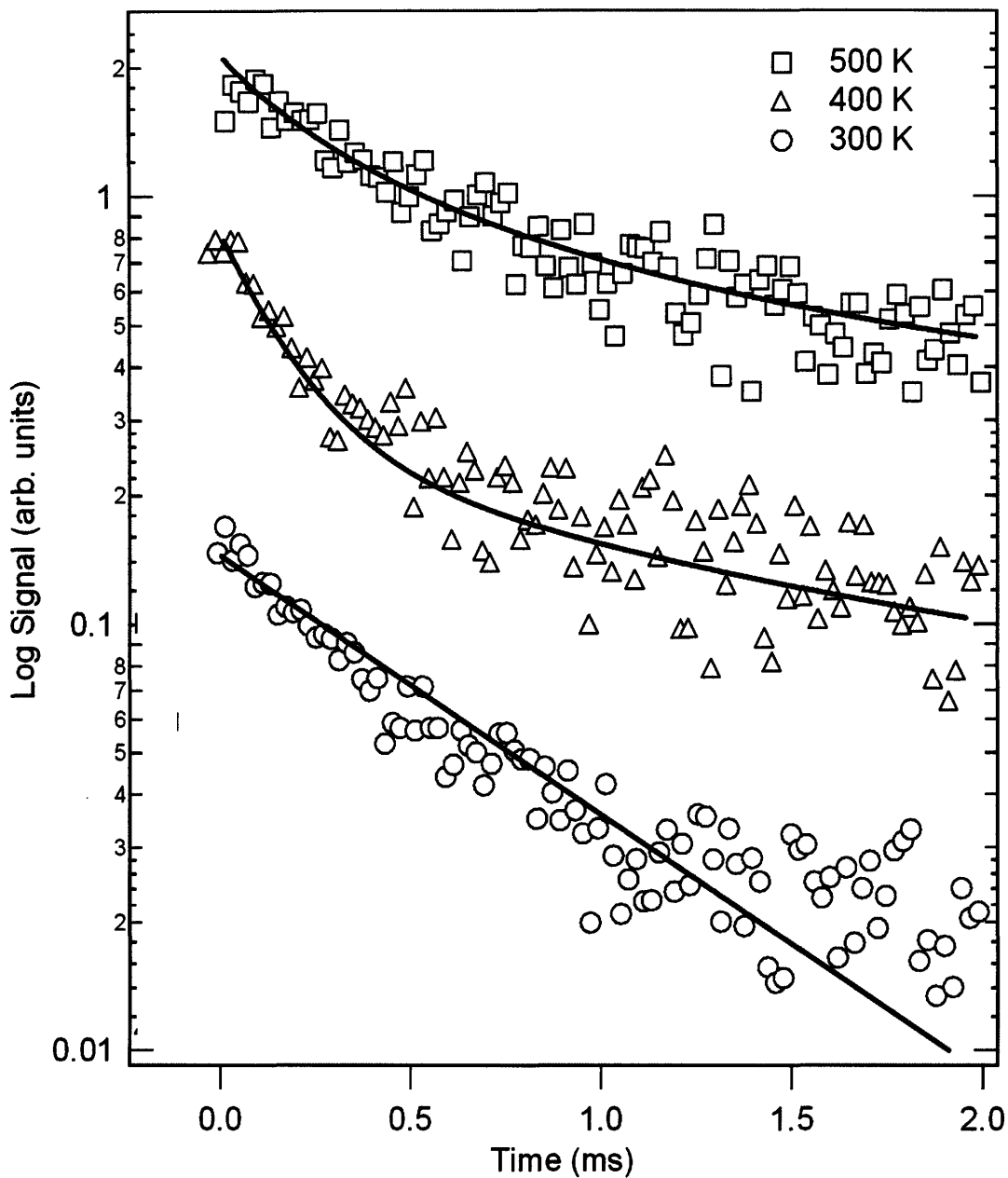


Figure 7.4. Transient absorption of allyl radical at three different temperatures; data are offset for clarity. All three traces are taken at 20 Torr total pressure and $[O_2] = 1.8 \times 10^{15}$ molecules cm^{-3} . At 300 K (circle) the decay is fitted to simple exponential. At 400 K (triangle), equilibrium is established between $C_3H_5 + O_2 \leftrightarrow C_3H_5OO$, therefore, a biexponential model is fitted to the ally decay. At 500 K (square), the decay reverts to a second order decay, corresponding to allyl reacting with itself or I atoms. Oxygen has little effect on the decay of allyl radical at 500 K.

are, in addition to allyl, two other chemically distinct species convoluted in the spectrum. The absorption signal from 400-410 nm occurs from the tail end of the allyl absorption spectrum, which appears as a fast spike followed by a slow decay in Figure 7.5b. A second distinct species also appears from 400-440 nm, which has a characteristic rise time of 0.6 ms under our experimental conditions (Figure 7.5c). Since the fall time of allyl is a factor of ~ 3 faster than the rise time of the signal of the unknown species, we believe this signal could not be due to allylperoxy radical. Lee and Bozzelli's¹⁷⁵ thermochemical calculation predicts allylperoxy radical could rapidly perform an internal H transfer to form various isomers including $\text{CH}=\text{CHCH}_2\text{OOH}$ or $\text{CH}_2\text{CCH}_2\text{OOH}$. It is possible that this absorption signal is due to one of these isomers and the characteristic 0.6 ms rise represents the isomerization rate. Interestingly enough, at 550 K, we did not observe an absorption signal at 435 nm. The reverse reaction (k_{-11}) dominates at this temperature, so allylperoxy does not accumulate. This suggests that whatever species is causing the absorption from 400-440 nm at room temperature is formed via allylperoxy.

From 440-490 nm, the rise-time in the transient absorption signal changes from 0.6 ms to 1.5 ms, as shown in Figure 7.5d. We believe this signal is caused by iodine dioxide (OIO). The spectrum of OIO radical has been reported by several authors^{45,46}. As shown in Figure 7.5a, our results compare well with recent spectrum published by Spietz *et al.*⁴⁵ Like IO, OIO's absorption cross section is approximately an order magnitude stronger than allyl radical, therefore OIO is fairly a minor channel (<1%) in our chemical system. The mechanism for OIO production still needs to be resolved. But at

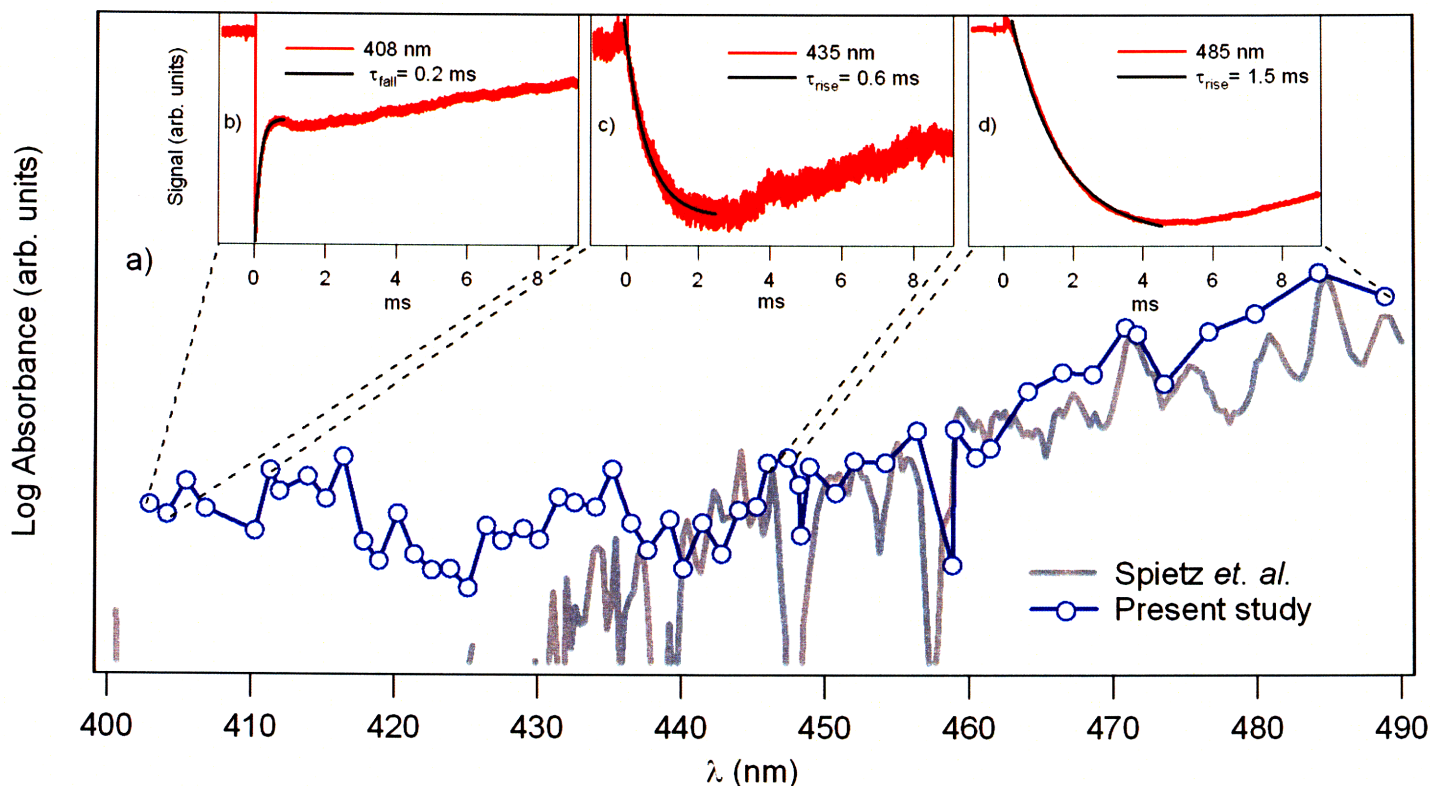


Figure 7.5. a) Low resolution spectrum for $\text{C}_3\text{H}_5\text{I}/\text{He}/\text{O}_2$ mixture after 266 nm photolysis (blue trace) at 300 K, 20 Torr, and $[\text{O}_2] = 3.0 \times 10^{15}$ molecules cm^{-3} . Three different transient species are thought to be convoluted in the spectrum. b) From 400-410 nm, the initial fast spike is due to absorption from allyl radical. The slow background signal is due to absorption unknown species. c) The absorption from the unknown species, which we believe is from $\text{C}_3\text{H}_5\text{OO}$ isomers, ends at ~ 440 nm. The rise time for the unknown species is 0.6 ms under our experimental conditions. d) From 440-490 nm, the absorption is due to OIO radical and rise this is species changes to 1.5 ms. Our spectrum for OIO compares well with the high resolution spectrum of Spietz *et al.* (grey trace).

550 K, OIO signal decreased by a factor of 15 compared to the room temperature signal, leading us to conclude that allylperoxy once again must be included in the mechanism for OIO production.

7.2.3.2. Kinetic study (k_{11})

At room temperature, the forward rate constant for reaction (7.15) showed very little pressure dependence, therefore the reported value below is an average from measurements made at all pressures:

$$k_{11} (300 \text{ K}) = (1.0 \pm 3) \times 10^{-12} \text{ cm}^3 \text{ molecule}^{-1} \text{ s}^{-1} \quad (7.16)$$

Morgan *et al.*¹⁷¹ reported an Arrhenius expression for k_{-11} based on experiments conducted between 382-673 K. They also reported ΔH_{298}° and ΔS_{298}° for reaction (7.15), hence the equilibrium constant (K_p) can be calculated. The forward rate ($k_{11} = k_{-11} \cdot K_p \cdot RT$) was found to be $k_{11} (300 \text{ K}) = 2.0 \times 10^{-12} \text{ cm}^3 \text{ molecule}^{-1} \text{ s}^{-1}$. Our value is within 50% Morgan's *et al.*¹⁷¹ extrapolated value for the forward rate constant for the reaction of allyl with O₂ at 300K.

The transient absorption of allyl at 350, 400, and 450 K were fitted to a biexponential function (equation (7.13)). The results are summarized in Table 7.3. The values of ΔH_{298}° and ΔS_{298}° for reaction (7.15) can be determined by plotting $\ln(K_p)$ vs. $1/T$ and fitting it to straight line. A van't Hoff plot is shown in Figure 7.6 for our experimental data. The values obtained for the thermodynamic variables by applying the Second law procedure are: $\Delta H_{298}^\circ = -$

$(66 \pm 14) \text{ kJ mol}^{-1}$ and $\Delta S_{298}^{\circ} = -(96 \pm 33) \text{ kJ mol}^{-1} \text{ K}^{-1}$. Our values are in reasonable agreement with the literature¹⁷⁰⁻¹⁷² values: $\Delta H_{298}^{\circ} = -77 \text{ kJ mol}^{-1}$ and $\Delta S_{298}^{\circ} = -127 \text{ kJ mol}^{-1} \text{ K}^{-1}$. There is a ~30% discrepancy between our value and the literature values for ΔH_{298}° and ΔS_{298}° because there is great deal of scatter in the data, which stems predominately from uncertainty in the biexponential fit parameters to determine K_p . The allyl data traces were acquired at S/N of approximately 5:1, sufficient for accurate single exponential fits, but for biexponential fits, higher S/N is required to determine the A and B amplitude parameters accurately. Therefore, it is recommended that if such experiments are attempted in the future, data should be acquired at S/N at least 10/1.

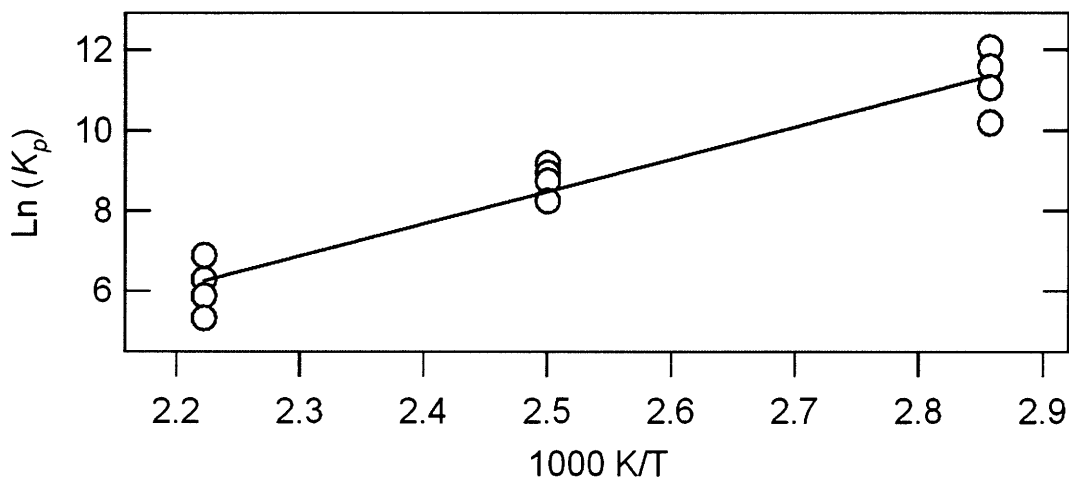


Figure 7.6. A van't Hoff plot of the measured equilibrium constants (K_p) for $\text{C}_3\text{H}_5 + \text{O}_2 \leftrightarrow \text{C}_3\text{H}_5\text{OO}$. The experimental data (O) were taken at various oxygen concentrations. The straight line through the data points was obtained by a least squares fit to determine the thermodynamic parameters for the equilibrium reaction. The slope of this line is $\Delta H^{\circ}/R$ and the y-intercept is $\Delta S^{\circ}/R$.

7.2.4. Conclusions and future work

The rate constant of the reaction of allyl radical with molecular oxygen at room temperature has been determined and found to be in good agreement with previous literature values. We also acquired a low resolution spectrum of $C_3H_5I/He/O_2$ mixtures, which was found to have features from at least two distinct chemical species, OIO and an unknown species. Lastly, we measured the temperature dependence equilibrium constant for the reaction (7.15) and found ΔH_{298}° and ΔS_{298}° for the reaction, which are in reasonable agreement with previous studies. Such measurements can be made using our apparatus, but accuracy can be improved by obtaining the data at higher S/N.

For future work, we recommend re-running these experiments with different allyl radical precursors to try identify the unknown background species. In the present study, there was considerable interference by OIO radical, which can be avoided using a non-iodated precursor such as 193 nm photolysis of 1-5 hexadiene or 248 nm photolysis of allyl bromide.

7.3. IO & OIO

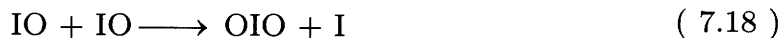
One of the key issues not resolved in vinyl and allyl oxidation experiments is why only iodine monoxide (IO) is observed in 266 nm photolysis $C_2H_3I/He/O_2$ mixture and why only iodine dioxide (OIO) signal is seen in $C_3H_5I/He/O_2$ mixture after 266 nm photolysis. Investigations of these questions are very important for atmospheric chemistry with respect to ozone (O_3) reactions. Iodine atoms are released in the stratosphere and troposphere by photolysis of molecular iodine and volatile iodocarbons, mostly released by the marine biosphere¹⁷⁶. The fate of the I atom is to react predominately with ozone, producing IO. Reactions that convert IO back to iodine atoms can lead to catalytic loss of ozone¹⁷⁷.

The atmospheric fate of OIO is also of great interest since its low reactivity and a slow photolysis rate yield an enhancement of its potential to form aerosol nuclei¹⁶⁸. The irreversible accumulation of iodine oxides are thought to be the main cause for aerosols enriched with iodine¹⁶⁸. Iodine condensable vapors are also linked to new particle formation in the coastal marine boundary layer¹⁷⁸.

In current atmospheric models, IO formation is primarily attributed to the following reaction¹⁷⁹:



IO can react with itself to lead to iodine oxides in the atmosphere¹⁷⁹:



Our experiments on C₂H₃I/O₂ and C₃H₅I/O₂ mixtures reveal that IO and OIO can form via pathways involving volatile organic compounds (VOC), which the current atmospheric models ignore. Additionally, these models also do not take into account the chemistry of excited I atoms. Both of these classes of reactions could have a significant impact on the current atmospheric models. Although we were not able to determine the exact mechanism for IO and OIO production, a detailed thermodynamic analysis is briefly presented to probe for possible reaction pathways.

The thermochemical data were acquired from various sources^{153,180}. The thermochemistry of oxygen containing hydrocarbon species was taken from Bozzelli and Dean¹⁵³, who calculated the thermodynamic parameters in THERM¹⁶². Thermochemistry for iodine oxides were obtained from Chase¹⁸⁰, which are based on an extensive literature review.

The IO formation in the vinyl oxidation system is relatively straightforward if vinylperoxy is stabilized. The reaction of vinylperoxy radical with I atom to make IO radical is relatively exothermic reaction:

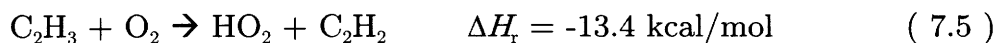


The reason we do not detect OIO in vinyl oxidation is because its formation is highly endothermic:



Via email correspondence, another possible mechanism was proposed by Professor John P. Burrows from Institute of Environmental Physics at University of Bremen¹⁸¹. This mechanism involves production of HO₂ radical and its reaction with I radical to make IO. There are two potential pathways

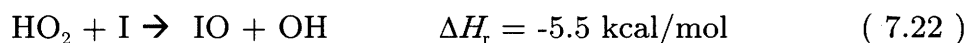
for production of HO₂ in our systems. The first pathway involves direct production of HO₂ via chemically activated pathways:



The second pathway is indirect production of HO₂, also via a chemically activated pathway:



The HO₂ from both pathways can then react with I to form IO:



In our experiments, IO production was found to be highly pressure dependant. As the total pressure was changed from 20 Torr to 100 Torr by adding He, the peak IO concentration increased by a factor of 3. In Burrow's mechanism, [IO]_{peak} should decrease as total pressure is increased since HO₂ forms via a chemically activated pathway. Whereas in the mechanism proposed in reaction(7.19), [C₂H₃OO] increases as the pressure increases due to stabilization of activated C₂H₃OO*. Therefore, a likely mechanism for IO production in our experiments is vinylperoxy radical reacting directly with I atoms. This is strong indirect evidence for C₂H₃OO formation in our system.

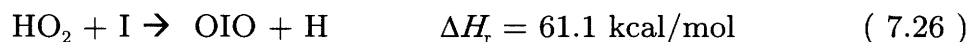
The mechanism of OIO production in the allyl oxidation system is far more complex. The question of why IO is not observed in the allyl system is addressed first. The reaction of I atom with allylperoxy radical yields IO and highly unstable allyloxy radical (CH₂CHCHO). Therefore, this reaction is not favored in the forward direction:



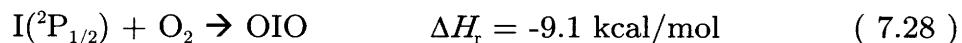
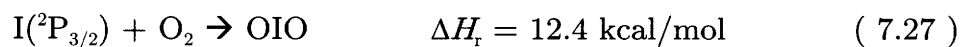
Another possibility is that allylperoxy radical reacts with I atoms to form OIO. But this reaction is also highly endothermic:



Applying Burrow's mechanism to the allyl system also leads to an endothermic pathway for OIO production:



One interesting aspect of allyl iodide photolysis at 266 nm is that 80% of the I atoms produced were in the electronically excited state ($\text{I}({}^2\text{P}_{1/2})$), as discussed in Chapter 5. Whereas in the vinyl iodide photolysis at 266 nm, only 25% of the I atoms are produced in the ${}^2\text{P}_{1/2}$ state. According to Husain *et al.*¹⁸², the electronic energy difference between the $\text{I}({}^2\text{P}_{1/2}) - \text{I}({}^2\text{P}_{3/2}) = 21.7 \text{ kcal/mol}$, which could render a number of atomic abstraction reactions exothermic whereas the analogous reaction of the $\text{I}({}^2\text{P}_{3/2})$ ground state atom would be endothermic. Therefore, the reaction of I^* with molecular oxygen becomes favorable to produce OIO:



Though this mechanism is thermodynamically possible, it cannot explain our observations because $\text{I}({}^2\text{P}_{1/2})$ atom decays on a microsecond timescale, but the rise time of OIO is $\tau_{\text{OIO}} = \sim 1.5 \text{ ms}$.

The thermodynamic analysis of OIO in the allyl oxidation system indicates that a more complex mechanism is required to model the temporal profile of OIO. Understanding the mechanism of IO and OIO in our experiment would not only be of interest to atmospheric chemistry, but it might also give us insight into the pressure dependence of the oxidation of vinyl and allyl radical.

7.4. Benzyl & Phenoxy Radical

Oxidation of aromatic compounds such as benzene and toluene are of much interest because they are major components in gasoline and significantly affect fuel ignition (octane number). Typical gasoline blends have an aromatic content of 20-30% by volume¹⁸³. This results in significant emissions of aromatics in the atmosphere and leads to ozone and aerosol formation in urban air¹⁸⁴. There have been relatively few kinetics studies performed on reactions involving benzyl ($C_6H_5CH_2$) and phenoxy (C_6H_5O) radical, which are key intermediates in the oxidation of aromatics. Therefore, spectroscopic and kinetic data for benzyl and phenoxy radicals is vital for better understanding and modeling of oxidation of aromatic hydrocarbons.

The benzyl radical gas phase absorption spectrum in the UV^{185,186} and the visible^{32,187} has been reported by several authors. Similarly, the UV^{51,188,189} and visible^{52,190,191} absorption spectrum for phenoxy radical have also been widely studied. Recently, Tonokura and Koshi published cavity ring-down spectrum for both benzyl³² and phenoxy⁵² radicals. Their benzyl absorption was in the

region of vibrationally mixed 1^2A_2 - 2^2B_1 excited states spanning from 445 - 455 nm. Tonokura and Koshi³² used 193 nm photolysis of benzyl chloride ($C_6H_5C_2H_2Cl$) as photolytic precursor for benzyl radicals. Their phenoxy spectrum was taken from 375-410 nm and assigned to the $2^2B_1 \leftarrow X^2B_1$ transition⁵². Anisole ($C_6H_5OCH_3$) was used as precursor for phenoxy radical via 193 nm photolysis⁵².

In this present study, we replicated Tonokura and Koshi's experiments, to ensure that we could detect these radicals in our experimental setup with using a different photolysis wavelength (266 nm). Since both anisole and benzyl chloride have relatively low vapor pressures, a bubbler setup was used to flow precursors into the flow cell. The spectrum was taken at time delay of 5 μ sec for phenoxy and 250 μ sec for benzyl radical. Both spectra were taken at 20 Torr, 300 K, $[C_6H_5CH_2Cl] = 3.0 \times 10^{14}$ molecules cm^{-3} and $[C_6H_5OCH_3] = 1.5 \times 10^{14}$ molecules cm^{-3} .

In both chemical systems, we observed a transient absorption signal after 266 nm photolysis, and excellent S/N was achieved. In particular, the phenoxy radical can easily be detected using a single pass configuration of the probe laser.

The low resolution spectrum of benzyl radical is shown in Figure 7.7 and phenoxy radical in Figure 7.8. The phenoxy radical absorption spectrum is in excellent agreement with Tonokura and Koshi⁵². On the other hand, our measured spectrum of benzyl radical agrees reasonably well from 446 - 449 nm with Tonokura and Koshi³², but significantly disagrees from 449 - 455 nm. It is possible benzyl chloride photoproducts differ as photolysis wavelength is changed from 193 to 266 nm. Additionally, upon further examination, the rise

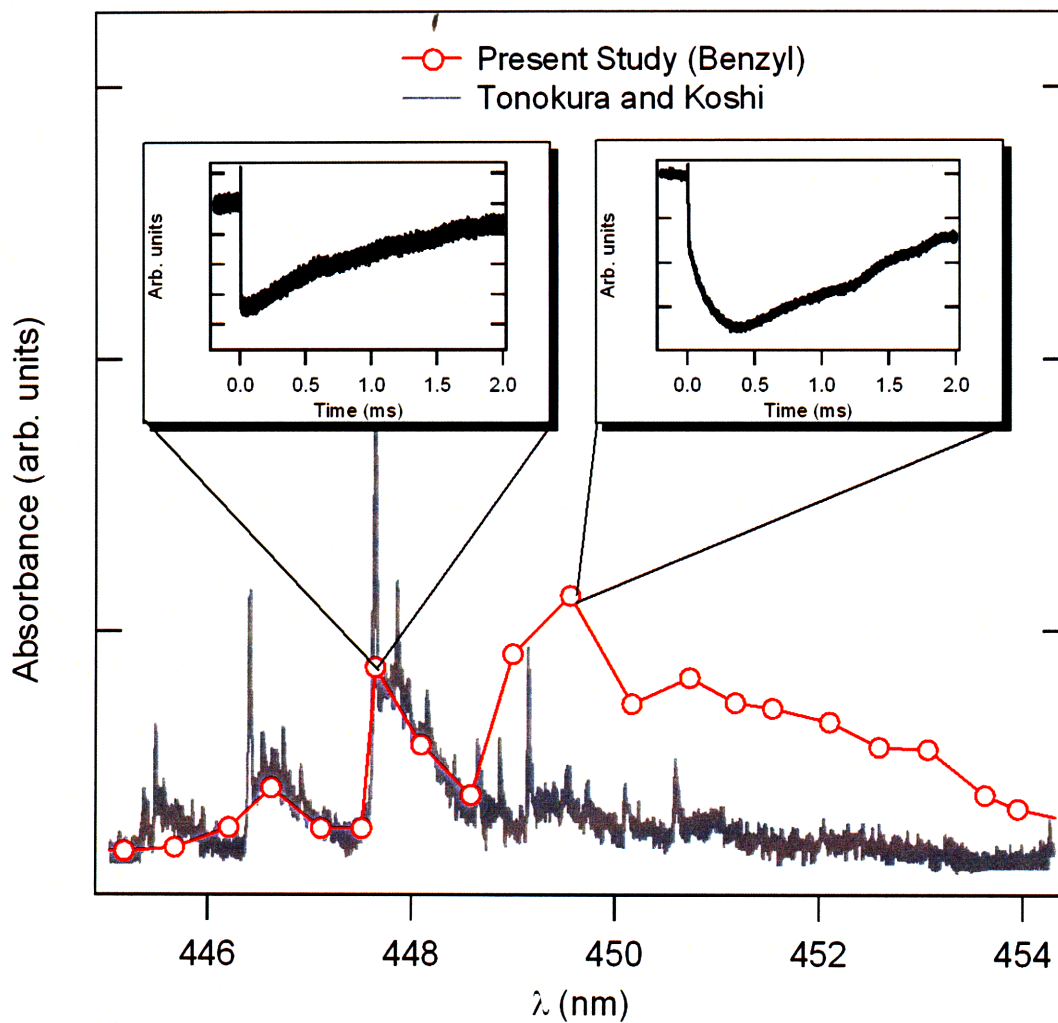


Figure 7.7: a) Low resolution spectrum recorded in the present study of photoproducts of $C_6H_5C_2H_2Cl/He$ mixture after 266 nm photolysis (circle) at 300 K and 20 Torr. Inserts are transient absorption signals at different wavelengths.

time of the transient absorption traces for benzyl from 446-449 nm versus traces from 449-455 nm slightly differed. The rise time from 446-449 nm is almost instantaneous ($\tau_{\text{rise}} = 5 \mu\text{sec}$). Whereas, the rise time from 449 - 455 nm has a fast ($\tau_{\text{rise}}(\text{fast}) = 5 \mu\text{sec}$) and a slow component ($\tau_{\text{rise}}(\text{slow}) = 300 \mu\text{sec}$). This is shown in Figure 7.7 as inserts. The kinetics data indicate that the absorption from 449-455 nm in the spectrum could be due to another chemical species or to absorption from excited states of benzyl chloride.

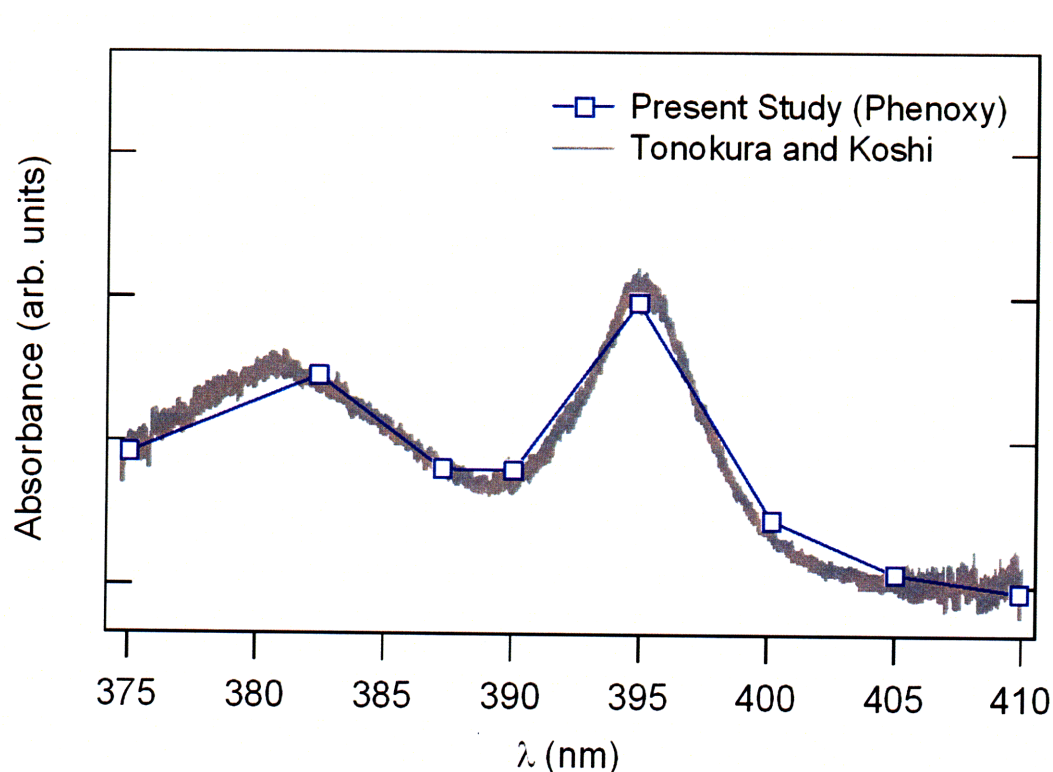


Figure 7.8: Low resolution spectrum recorded in the present study of photoproducts of $\text{C}_6\text{H}_5\text{OCH}_3/\text{He}$ mixture after 266 nm photolysis at 300 K and 20 Torr (square). High resolution spectrum of Tonokura and Koshi (grey traces) compare well with the present study.

We also attempted a kinetic study of benzyl and phenoxy radical with molecular oxygen:



The experiments to determine k_{12} were conducted at 300 K, 20 Torr of pressure and $[\text{O}_2] = (0.1 - 2.0) \times 10^{15}$ molecules cm^{-3} . The benzyl radicals were probed at 447.8 nm and the pseudo-first-order assumption was used to analyze the data. The reaction rate for benzyl radical with molecular oxygen at 300K was found to be:

$$k_{12} = (1.0 \pm 0.5) \times 10^{-12} \text{ cm}^3 \text{ molecule}^{-1} \text{ s}^{-1} \quad (7.31)$$

Our value agrees very well with the literature value of $9.9 \times 10^{-13} \text{ cm}^3 \text{ molecule}^{-1} \text{ s}^{-1}$, reported by Ebata *et al.*¹⁹²

The experiments for phenoxy radical with molecular oxygen were conducted at 300 K and pressures 20 and 100 Torr. The decay constant of the transient absorption of phenoxy radical showed no change as $[\text{O}_2]$ was changed from 1×10^{14} - 1×10^{18} molecules cm^{-3} . Therefore, phenoxy radical was found unreactive with molecular oxygen.

For future experiments, we recommend performing a temperature- and pressure-dependent kinetic study of benzyl and phenoxy radical reactions with NO and NO_2 . Additionally, the benzyl absorption spectrum should be reexamined, using a different precursor (e.g. ethyl benzene) or using different

photolysis wavelengths (193, 248 & 266 nm) to help resolve the discrepancy between Tonokura and Koshi's study and the present work.

References

- [1] Song, J. Building Robust Chemical Reaction Mechanisms: Next Generation of Automatic Model Construction Software. Ph.D dissertation, Massachusetts Institute of Technology, 2004.
- [2] Matheu, D. M. Integrated Pressure-Dependence in Automated Mechanism Generation: A New Tool for Building Gas-Phase Kinetic Models, Massachusetts Institute of Technology, 2002.
- [3] Van Geem, K. M.; Reyniers, M.-F.; Marin, G. B.; Song, J.; Green, W. H.; Matheu, D. M. *AIChE Journal* **2006**, *52*, 718.
- [4] Matheu, D. M.; Grenda, J. M. *Journal of Physical Chemistry A* **2005**, *109*, 5332.
- [5] Matheu, D. M.; Grenda, J. M. *Journal of Physical Chemistry A* **2005**, *109*, 5343.
- [6] Petway, S. V.; Ismail, H.; Green, W. H.; Estupinan, E. G.; Jusinski, L. E.; Taatjes, C. A. *Journal of Physical Chemistry A* **2007**, *111*, 3891.
- [7] Paraskevopoulos, G.; Singleton, D. L.; Irwin, R. S. *Journal of Physical Chemistry* **1981**, *85*, 561.
- [8] Farhataziz. *Journal of Physical Chemistry* **1977**, *81*, 827.
- [9] Herzberg, G.; Shoosmith, J. *Canadian Journal of Physics* **1956**, *34*, 523.
- [10] Kochi, J. K.; Editor *Free Radicals, Vol. 1 & 2*, 1973.
- [11] Herriott, D.; Kogelnik, H.; Kompener, R. *Applied Optics* **1964**, *3*, 523.
- [12] Trutna, W. R.; Byer, R. L. *Applied Optics* **1980**, *19*, 301.
- [13] Ruslen, L. M. Application of Sensitive Spectroscopic Techniques to Intramolecular Dynamics and Combustion Kinetics, Massachusetts Institute of Technology, 2002.
- [14] Taylor, J. W. Direct Measurement and Analysis of Cyclohexadienyl Oxidation, Massachusetts Institute of Technology, 2005.
- [15] Park, J.; Lin, M. C. *ACS Symposium Series* **1999**, *720*, 196.
- [16] Shida, T.; Hamill, W. H. *Journal of the American Chemical Society* **1966**, *88*, 3689.

- [17] Ohnishi, S.; Tanei, T.; Nitta, I. *Journal of Chemical Physics* **1962**, *37*, 2402.
- [18] Sauer, M. C., Jr.; Ward, B. *Journal of Physical Chemistry* **1967**, *71*, 3971.
- [19] Cooper, R.; Thomas, J. K. *Journal of Chemical Physics* **1968**, *48*, 5097.
- [20] Shida, T.; Hanazaki, I. *Bulletin of the Chemical Society of Japan* **1970**, *43*, 646.
- [21] Jordan, J. E.; Pratt, D. W.; Wood, D. E. *Journal of the American Chemical Society* **1974**, *96*, 5588.
- [22] Berho, F.; Rayez, M.-T.; Lesclaux, R. *Journal of Physical Chemistry A* **1999**, *103*, 5501.
- [23] Effio, A.; Griller, D.; Ingold, K. U.; Scaiano, J. C.; Sheng, S. J. *Journal of the American Chemical Society* **1980**, *102*, 6063.
- [24] Berho, F.; Lesclaux, R. *Physical Chemistry Chemical Physics* **2001**, *3*, 970.
- [25] Pan, X. M.; Bastian, E.; Von Sonntag, C. *Zeitschrift fuer Naturforschung, B: Chemical Sciences* **1988**, *43*, 1201.
- [26] Pan, X. M.; Schuchmann, M. N.; von Sonntag, C. *Journal of the Chemical Society, Perkin Transactions 2: Physical Organic Chemistry (1972-1999)* **1993**, 1021.
- [27] Maillard, B.; Ingold, K. U.; Scaiano, J. C. *Journal of the American Chemical Society* **1983**, *105*, 5095.
- [28] Estupinan, E.; Villenave, E.; Raoult, S.; Rayez, J. C.; Rayez, M. T.; Lesclaux, R. *Physical Chemistry Chemical Physics* **2003**, *5*, 4840.
- [29] Taylor, J. W.; Ehlker, G.; Carstensen, H.-H.; Ruslen, L.; Field, R. W.; Green, W. H. *Journal of Physical Chemistry A* **2004**, *108*, 7193.
- [30] Tonokura, K.; Koshi, M. *Journal of Physical Chemistry A* **2000**, *104*, 8456.
- [31] Tonokura, K.; Norikane, Y.; Koshi, M.; Nakano, Y.; Nakamichi, S.; Goto, M.; Hashimoto, S.; Kawasaki, M.; Andersen, M. P. S.; Hurley, M. D.; Wallington, T. J. *Journal of Physical Chemistry A* **2002**, *106*, 5908.
- [32] Tonokura, K.; Koshi, M. *Journal of Physical Chemistry A* **2003**, *107*, 4457.
- [33] *Chemical Properties Handbook*; Yaw, C. L., Ed.; McGraw-Hill, 1999.

- [34] Nakashima, N.; Inoue, H.; Sumitani, M.; Yoshihara, K. *Journal of Chemical Physics* **1980**, *73*, 5976.
- [35] Yokoyama, A.; Zhao, X.; Hints, E. J.; Continetti, R. E.; Lee, Y. T. *Journal of Chemical Physics* **1990**, *92*, 4222.
- [36] Orttung, W. H. *Journal of Physical Chemistry* **1985**, *89*, 3011.
- [37] Hayon, E.; Nakashima, M. *Journal of Physical Chemistry* **1971**, *75*, 1910.
- [38] Bridier, I.; Veyret, B.; Lesciaux, R.; Jenkin, M. E. *Journal of the Chemical Society, Faraday Transactions* **1993**, *89*, 2993.
- [39] DeSain, J. D.; Jusinski, L. E.; Taatjes, C. A. *Physical Chemistry Chemical Physics* **2006**, *8*, 2240.
- [40] Knight, G.; Ravishankara, A. R.; Burkholder, J. B. *Journal of Physical Chemistry A* **2000**, *104*, 11121.
- [41] Wilmouth, D. M.; Hanisco, T. F.; Donahue, N. M.; Anderson, J. G. *Journal of Physical Chemistry A* **1999**, *103*, 8935.
- [42] Lesclaux, R.; Roussel, P.; Veyret, B.; Pouchan, C. *Journal of the American Chemical Society* **1986**, *108*, 3872.
- [43] Zhu, L.; Kellis, D.; Ding, C.-F. *Chemical Physics Letters* **1996**, *257*, 487.
- [44] Maricq, M. M.; Szente, J. J.; Dibble, T. S.; Francisco, J. S. *Journal of Physical Chemistry* **1994**, *98*, 12294.
- [45] Spietz, P.; Gomez Martin, J. C.; Burrows, J. P. *Journal of Photochemistry and Photobiology, A: Chemistry* **2005**, *176*, 50.
- [46] Himmelmann, S.; Orphal, J.; Bovensmann, H.; Richter, A.; Ladstaetter-Weissenmayer, A.; Burrows, J. P. *Chemical Physics Letters* **1996**, *251*, 330.
- [47] Sehested, J.; Ellermann, T.; Nielsen, O. J. *International Journal of Chemical Kinetics* **1994**, *26*, 259.
- [48] Langer, S.; Ljungstroem, E.; Ellermann, T.; Nielsen, O. J.; Sehested, J. *Chemical Physics Letters* **1995**, *240*, 53.
- [49] Black, G.; Jusinski, L. E. *Journal of the Chemical Society, Faraday Transactions 2: Molecular and Chemical Physics* **1986**, *82*, 2143.
- [50] Alfassi, Z. B.; Khaikin, G. I.; Neta, P. *Journal of Physical Chemistry* **1995**, *99*, 265.
- [51] Platz, J.; Nielsen, O. J.; Wallington, T. J.; Ball, J. C.; Hurley, M. D.; Straccia, A. M.; Schneider, W. F.; Sehested, J. *Journal of Physical Chemistry A* **1998**, *102*, 7964.

- [52] Tonokura, K.; Ogura, T.; Koshi, M. *Journal of Physical Chemistry A* **2004**, *108*, 7801.
- [53] Atkinson, D. B.; Hudgens, J. W. *Journal of Physical Chemistry A* **1999**, *103*, 4242.
- [54] Pibel, C. D.; McIlroy, A.; Taatjes, C. A.; Alfred, S.; Patrick, K.; Halpern, J. B. *Journal of Chemical Physics* **1999**, *110*, 1841.
- [55] Anastasi, C.; Sanderson, M. G.; Pagsberg, P.; Sillesen, A. *Journal of the Chemical Society, Faraday Transactions* **1994**, *90*, 3625.
- [56] Zhu, L.; Johnston, G. *Journal of Physical Chemistry* **1995**, *99*, 15114.
- [57] Fahr, A.; Laufer, A. H.; Krauss, M.; Osman, R. *Journal of Physical Chemistry A* **1997**, *101*, 4879.
- [58] Tonokura, K.; Marui, S.; Koshi, M. *Chemical Physics Letters* **1999**, *313*, 771.
- [59] Pilgrim, J. S.; Jennings, R. T.; Taatjes, C. A. *Review of Scientific Instruments* **1997**, *68*, 1875.
- [60] Shahu, M.; Yang, C.-H.; Pibel, C. D.; McIlroy, A.; Taatjes, C. A.; Halpern, J. B. *J. Chem. Phys.* **2002**, *116*, 8343.
- [61] Richter, H.; Howard, J. B. *Progress in Energy and Combustion Science* **2000**, *26*, 565.
- [62] MacFadden, K. O.; Currie, C. L. *Journal of Chemical Physics* **1973**, *58*, 1213.
- [63] Fahr, A.; Laufer, A. H. *Journal of Physical Chemistry* **1990**, *94*, 726.
- [64] Fahr, A.; Laufer, A.; Klein, R.; Braun, W. *Journal of Physical Chemistry* **1991**, *95*, 3218.
- [65] Tsang, W.; Hampson, R. F. *Journal Of Physical and Chemical Reference Data* **1986**, *15*, 1087.
- [66] Thorn, R. P.; Payne, W. A.; Stief, L. J.; Tardy, D. C. *Journal of Physical Chemistry* **1996**, *100*, 13594.
- [67] Laufer, A. H.; Fahr, A. *Chemical Reviews (Washington, DC, United States)* **2004**, *104*, 2813.
- [68] Ismail, H.; Goldsmith, C. F.; Abel, P. R.; Howe, P.-T.; Fahr, A.; Halpern, J. B.; Jusinski, L. E.; Georgievskii, Y.; Taatjes, C. A.; Green, W. H. *Journal of Physical Chemistry A* **2007**, *111*, 6843.
- [69] Haugen, H. K.; Weitz, E.; Leone, S. R. *Journal of Chemical Physics* **1985**, *83*, 3402.

- [70] Hess, W. P.; Kohler, S. J.; Haugen, H. K.; Leone, S. R. *Journal of Chemical Physics* **1986**, *84*, 2143.
- [71] Zou, P.; Strecker, K. E.; Ramirez-Serrano, J.; Jusinski, L. E.; Taatjes, C. A.; Osborn, D. L. *Physical Chemistry Chemical Physics* **2008**, *10*, 713.
- [72] Ha, T.-K.; He, Y.; Pochert, J.; Quack, M.; Ranz, R.; Seyfang, G.; Thanopoulos, I. *Berichte der Bunsen-Gesellschaft* **1995**, *99*, 384.
- [73] Whiting, E. E. *J. Quant. Spectry. Radiative Transfer* **1968**, *8*, 1379.
- [74] Okabe, I. *Photochemistry of Small Molecules*; John Wiley: New York, 1978.
- [75] Davis, S. J.; Mulhall, P. A.; Bachman, M.; Kessler, W. J.; Keating, P. B. *Journal of Physical Chemistry A* **2002**, *106*, 8323.
- [76] Burde, D. H.; McFarlane, R. A. *Journal of Chemical Physics* **1976**, *64*, 1850.
- [77] Arnold, J. O.; Whiting, E. E.; Lyle, G. C. *Journal of Quantitative Spectroscopy & Radiative Transfer* **1969**, *9*, 775.
- [78] Hunziker, H. E.; Knepe, H.; McLean, A. D.; Siegbahn, P.; Wendt, H. R. *Canadian Journal of Chemistry* **1983**, *61*, 993.
- [79] Mebel, A. M.; Chen, Y.-T.; Lin, S.-H. *Chemical Physics Letters* **1997**, *275*, 19.
- [80] Shahu, M.; Yang, C.-H.; Pibel, C. D.; McIlroy, A.; Taatjes, C. A.; Halpern, J. B. *Journal of Chemical Physics* **2002**, *116*, 8343.
- [81] Allara, D. L.; Edelson, D. *International Journal of Chemical Kinetics* **1975**, *7*, 479.
- [82] Georgievskii, Y.; Miller, J. A.; Klippenstein, S. J. *Physical Chemistry Chemical Physics* **2007**, *9*, 4259.
- [83] Golden, D. M.; Gac, N. A.; Benson, S. W. *Journal of the American Chemical Society* **1969**, *91*, 2136.
- [84] van den Bergh, H. E.; Callear, A. B. *Transactions of the Faraday Society* **1970**, *66*, 2681.
- [85] Rossi, M.; King, K. D.; Golden, D. M. *Journal of the American Chemical Society* **1979**, *101*, 1223.
- [86] Tulloch, J. M.; Macpherson, M. T.; Morgan, C. A.; Pilling, M. J. *Journal of Physical Chemistry* **1982**, *86*, 3812.
- [87] Jenkin, M. E.; Murrells, T. P.; Shalliker, S. J.; Hayman, G. D. *Journal of the Chemical Society, Faraday Transactions* **1993**, *89*, 433.

- [88] Boyd, A. A.; Noziere, B.; Lesclaux, R. *Journal of Physical Chemistry* **1995**, *99*, 10815.
- [89] Tsang, W. *Journal of Physical and Chemical Reference Data* **1991**, *20*, 221.
- [90] Currie, C. L.; Ramsay, D. A. *Journal of Chemical Physics* **1966**, *45*, 488.
- [91] Maier, G.; Reisenauer, H. P.; Rohde, B.; Dehnicke, K. *Chemische Berichte* **1983**, *116*, 732.
- [92] Callear, A. B.; Lee, H. K. *Transactions of the Faraday Society* **1968**, *64*, 308.
- [93] Shimo, N.; Nakashima, N.; Ikeda, N.; Yoshihara, K. *Journal of Photochemistry* **1986**, *33*, 279.
- [94] Nakashima, N.; Yoshihara, K. *Laser Chemistry* **1987**, *7*, 177.
- [95] Hudgens, J. W.; Dulcey, C. S. *Journal of Physical Chemistry* **1985**, *89*, 1505.
- [96] Sappey, A. D.; Weisshaar, J. C. *Journal of Physical Chemistry* **1987**, *91*, 3731.
- [97] Blush, J. A.; Minsek, D. W.; Chen, P. *Journal of Physical Chemistry* **1992**, *96*, 10150.
- [98] Minsek, D. W.; Blush, J. A.; Chen, P. *Journal of Physical Chemistry* **1993**, *97*, 8674.
- [99] Minsek, D. W.; Blush, J. A.; Chen, P. *Journal of Physical Chemistry* **1992**, *96*, 2025.
- [100] Szpunar, D. E.; Morton, M. L.; Butler, L. J.; Regan, P. M. *Journal of Physical Chemistry B* **2002**, *106*, 8086.
- [101] van den Bergh, H. E.; Callear, A. B.; Norstrom, R. J. *Chemical Physics Letters* **1969**, *4*, 101.
- [102] Glaenger, K.; Quack, M.; Troe, J. *Symposium (International) on Combustion, [Proceedings]* **1977**, *16*, 949.
- [103] Tsang, W.; Hampson, R. F. *J. Phys. Chem. Ref. Data* **1986**, *15*, 1087.
- [104] Sakai, T. In *Pyrolysis: theory and industrial practice*; Albright, L. F., Crynes, B. L., Corcoran, W. H., Eds.; Academic Press: New York, 1983; pp 89.
- [105] Roscoe, J. M.; Bossard, A. R.; Back, M. H. *Can. J. Chem.* **2000**, *78*, 16.
- [106] Thorn, R. P.; Payne, W. A.; Stief, L. J.; Tardy, D. C. *J. Phys. Chem.* **1996**, *100*, 13594.

- [107] Fahr, A.; Braun, W.; Laufer, A. H. *J. Phys. Chem.* **1993**, *97*, 1502.
- [108] Fahr, A.; Laufer, A.; Klein, R.; Braun, W. *J. Phys. Chem.* **1990**, *95*, 3218.
- [109] Fahr, A.; Laufer, A. H. *J. Phys. Chem.* **1990**, *94*, 726.
- [110] MacFadden, K. O.; Currie, C. L. *J. Chem. Phys.* **1973**, *58*, 1213.
- [111] Tickner, A. W.; LeRoy, D. J. *J. Chem. Phys.* **1951**, *19*, 1247.
- [112] Sherwood, A. G.; Gunning, H. E. *J. Phys. Chem.* **1965**, *69*, 2323.
- [113] Weir, N. A. *J. Chem. Soc.* **1965**, 6870.
- [114] Takita, S.; Mori, Y.; Tanaka, I. *J. Phys. Chem.* **1968**, *72*, 4360.
- [115] Szivovicza, L. *Int. J. Chem. Kinet.* **1985**, *17*, 117.
- [116] Xie, T.; McAuley, K. B.; Hsu, J. C. C.; Bacon, D. W. *Ind. Eng. Chem. Res.* **1994**, *33*, 449.
- [117] Miller, J. L. *J. Phys. Chem. A* **2004**, *108*, 2268.
- [118] Shestov, A. A.; Popov, K. V.; Slagle, I. R.; Knyazev, V. D. *Chem. Phys. Lett.* **2005**, *408*, 339–343.
- [119] Richter, H.; Howard, J. B. *Prog. Energy Combust. Sci.* **2000**, *26*, 565.
- [120] Fahr, A.; Stein, S. E. *Proc. Combust. Inst.* **1989**, *22*, 1023.
- [121] Kerr, J. A.; Parsonage, A. M. J.; Butterworths: London, 1976.
- [122] Fahr, A.; Stein, S. E. *Symposium (International) on Combustion, [Proceedings]* **1989**, *22nd*, 1023.
- [123] Henry David, J.; Coote Michelle, L.; Gomez-Balderas, R.; Radom, L. *Journal of the American Chemical Society* **2004**, *126*, 1732.
- [124] Merer, A. J.; Mulliken, R. S. *Chem. Rev.* **1969**, *69*, 639.
- [125] Ervin, K. M.; Gronert, S.; Barlow, S. E.; Gilles, M. K.; Harrison, A. G.; Bierbaum, V. M.; DePuy, C. H.; Lineberger, W. C.; Ellison, G. B. *J. Am. Chem. Soc.* **1990**, *112*, 5750.
- [126] Curtiss, L. A.; Raghavachari, K.; Redfern, P. C.; Rassolov, V.; Pople, J. A. *Journal of Chemical Physics* **1998**, *109*, 7764.
- [127] Frisch, M. J.; Trucks, G. W.; Schlegel, H. B.; Scuseria, G. E.; Robb, M. A.; Cheeseman, J. R.; Montgomery, J., J. A.; Vreven, T.; Kudin, K. N.; Burant, J. C.; Millam, J. M.; Iyengar, S. S.; Tomasi, J.; Barone, V.; Mennucci, B.; Cossi, M. S., G.; Rega, N.; Petersson, G. A. N., H.; Hada, M.; Ehara, M.; Toyota, K.; Fukuda, R.; Hasegawa, J.; Ishida, M.; Nakajima, T.; Honda, Y.; Kitao, O.; Nakai, H.; Klene, M.; Li, X.; Knox, J. E.; Hratchian, H. P.; Cross, J. B.; Bakken, V.; Adamo, C.; Jaramillo,

- J.; Gomperts, R.; Stratmann, R. E.; Yazyev, O.; Austin, A. J.; Cammi, R.; Pomelli, C.; Ochterski, J. W.; Ayala, P. Y.; Morokuma, K.; Voth, G. A.; Salvador, P.; Dannenberg, J. J.; Zakrzewski, V. G.; Dapprich, S.; Daniels, A. D.; Strain, M. C.; Farkas, O.; Malick, D. K.; Rabuck, A. D.; Raghavachari, K.; Foresman, J. B.; Ortiz, J. V.; Cui, Q.; Baboul, A. G.; Clifford, S.; Cioslowski, J.; Stefanov, B. B.; Liu, G.; Liashenko, A.; Piskorz, P.; Komaromi, I.; Martin, R. L.; Fox, D. J.; Keith, T.; Al-Laham, M. A.; Peng, C. Y.; Nanayakkara, A.; Challacombe, M.; Gill, P. M. W.; Johnson, B.; Chen, W.; Wong, M. W.; Gonzalez, C.; Pople, J. A. In *Gaussian 03*; Gaussian, Inc., 2004.
- [128] Goldsmith, C. F.; Ismail, H.; Green, W. H., Jr. *Proceedings of the Combustion Institute* **2008**, Submitted for Review.
- [129] Klippenstein, S. J.; Wagner, A. F.; Dunbar, R. C.; Wardlaw, D. M.; Robertson, S. H.; Miller, J. A. *VARIFLEX* **2002**.
- [130] Pitzer, K. S.; Gwinn, W. D. *Journal of Chemical Physics* **1942**, *10*, 428.
- [131] Golden, D. M.
- [132] Miller, J. A.; Klippenstein, S. J.; Raffy, C. *Journal of Physical Chemistry A* **2002**, *106*, 4904.
- [133] Miller, J. A.; Klippenstein, S. J. *Journal of Physical Chemistry A* **2003**, *107*, 2680.
- [134] Hippler, H.; Troe, J.; Wendelken, H. J. *Journal of Chemical Physics* **1983**, *78*, 6709.
- [135] Barker, J. R.; Ortiz, N. F.; Preses, J. M.; Lohr, L. L.; Maranzana, A.; Stimac, P. J. MultiWell-2.08 Software University of Michigan, Ann Arbor, MI, 2007.
- [136] Benson, S. W.; Haugen, G. R. *J. Phys. Chem.* **1967**, *71*, 1735.
- [137] Skinner, G. B.; Sokoloski, E. M. *J. Phys. Chem.* **1960**, *64*, 1028.
- [138] Tonokura, K.; Koshi, M. *J. Phys. Chem. A* **2000**, *104*, 8456.
- [139] Tonokura, K.; Marui, S.; Koshi, M. *Chem. Phys. Lett.* **1999**, *313*, 771.
- [140] DeSain, J. D.; Jusinski, L. E.; Taatjes, C. A. *Phys. Chem. Chem. Phys.* **2006**, *8*, 2240–2248.
- [141] Handford-Styring, S. M.; Walker, R. W. *Phys. Chem. Chem. Phys.* **2001**, *3*, 2043.
- [142] Matheu, D. M.; Green Jr., W. H.; Grenda, J. M. *Int. J. Chem. Kinet.* **2003**, *35*, 95.

- [143] Stein, S. E.; Rabinovitch, B. S. *J. Phys. Chem.* **1975**, *79*, 191.
- [144] Meloni, G.; Zou, P.; Klippenstein, S. J.; Ahmed, M.; Leone, S. R.; Taatjes, C. A.; Osborn, D. L. *J. Am. Chem. Soc.* **2006**, *128*, 13559.
- [145] Yung, Y. L.; Strobel, D. F. *Astrophysical Journal* **1980**, *239*, 395.
- [146] Fahr, A.; Laufer, A. H. *Journal of Physical Chemistry* **1988**, *92*, 7229.
- [147] Westmoreland, P. R. *Combustion Science and Technology* **1992**, *82*, 151.
- [148] Baldwin, R. R.; Walker, R. W. *Symposium (International) on Combustion, [Proceedings]* **1981**, *18th*, 819.
- [149] Park, J. Y.; Heaven, M. C.; Gutman, D. *Chemical Physics Letters* **1984**, *104*, 469.
- [150] Slagle, I. R.; Park, J. Y.; Heaven, M. C.; Gutman, D. *Journal of the American Chemical Society* **1984**, *106*, 4356.
- [151] Krueger, H.; Weitz, E. *Journal of Chemical Physics* **1988**, *88*, 1608.
- [152] Knyazev, V. D.; Slagle, I. R. *Journal of Physical Chemistry* **1995**, *99*, 2247.
- [153] Bozzelli, J. W.; Dean, A. M. *Journal of Physical Chemistry* **1993**, *97*, 4427.
- [154] Carpenter, B. K. *Journal of the American Chemical Society* **1993**, *115*, 9806.
- [155] Carpenter, B. K. *Journal of Physical Chemistry* **1995**, *99*, 9801.
- [156] Mebel, A. M.; Diau, E. W. G.; Lin, M. C.; Morokuma, K. *Journal of the American Chemical Society* **1996**, *118*, 9759.
- [157] Wang, H.; Wang, B.; He, Y.; Kong, F. *Journal of Chemical Physics* **2001**, *115*, 1742.
- [158] Cox, R. A.; Coker, G. B. *Journal of Physical Chemistry* **1983**, *87*, 4478.
- [159] Laszlo, B.; Kurylo, M. J.; Huie, R. E. *Journal of Physical Chemistry* **1995**, *99*, 11701.
- [160] Harwood, M. H.; Burkholder, J. B.; Hunter, M.; Fox, R. W.; Ravishankara, A. R. *Journal of Physical Chemistry A* **1997**, *101*, 853.
- [161] Slagle, I. R.; Gutman, D. *Symposium (International) on Combustion, [Proceedings]* **1988**, *21st.*, 875.
- [162] Ritter, E. R.; Bozzelli, J. W. *International Journal of Chemical Kinetics* **1991**, *23*, 767.
- [163] Fahr, A.; Braun, W.; Laufer, A. H. *Journal of Physical Chemistry* **1993**, *97*, 1502.

- [164] Herzberg, G.; Ramsey, D. A. *Proceedings of the Royal Society of London. Series A, Mathematical and Physical Sciences* **1955**, Vol. 233, 34.
- [165] Williams, B. A.; Fleming, J. W. *Chemical Physics Letters* **1994**, 221, 27.
- [166] Nielsen, O. J.; Johnson, M. S.; Wallington, T. J.; Christensen, L. K.; Platz, J. *International Journal of Chemical Kinetics* **2002**, 34, 283.
- [167] Solomon, S.; Albritton, D. L. *Nature (London, United Kingdom)* **1992**, 357, 33.
- [168] O'Dowd Colin, D.; Jimenez Jose, L.; Bahreini, R.; Flagan Richard, C.; Seinfeld John, H.; Hameri, K.; Pirjola, L.; Kulmala, M.; Jennings, S. G.; Hoffmann, T. *Nature* **2002**, 417, 632.
- [169] Bach, R. D.; Ayala, P. Y.; Schlegel, H. B. *Journal of the American Chemical Society* **1996**, 118, 12758.
- [170] Ruiz, R. P.; Bayes, K. D.; Macpherson, M. T.; Pilling, M. J. *Journal of Physical Chemistry* **1981**, 85, 1622.
- [171] Morgan, C. A.; Pilling, M. J.; Tulloch, J. M.; Ruiz, R. P.; Bayes, K. D. *Journal of the Chemical Society, Faraday Transactions 2: Molecular and Chemical Physics* **1982**, 78, 1323.
- [172] Slagle, I. R.; Ratajczak, E.; Heaven, M. C.; Gutman, D.; Wagner, A. F. *Journal of the American Chemical Society* **1985**, 107, 1838.
- [173] Lodhi, Z. H.; Walker, R. W. *Journal of the Chemical Society, Faraday Transactions* **1991**, 87, 2361.
- [174] Stothard, N. D.; Walker, R. W. *Journal of the Chemical Society, Faraday Transactions* **1992**, 88, 2621.
- [175] Lee, J.; Bozzelli, J. W. *Proceedings of the Combustion Institute* **2005**, 30, 1015.
- [176] Saiz-Lopez, A.; Plane, J. M. C. *Geophysical Research Letters* **2004**, 31, L04112/1.
- [177] Davis, D.; Crawford, J.; Liu, S.; McKeen, S.; Bandy, A.; Thornton, D.; Rowland, F.; Blake, D. *Journal of Geophysical Research, [Atmospheres]* **1996**, 101, 2135.
- [178] Allan, B. J.; McFiggans, G.; Plane, J. M. C.; Coe, H. *Journal of Geophysical Research, [Atmospheres]* **2000**, 105, 14363.
- [179] Carlos Gomez Martin, J.; Spietz, P.; Burrows, J. P. *Journal of Photochemistry and Photobiology, A: Chemistry* **2005**, 176, 15.

- [180] Chase, M. W. *Journal of Physical and Chemical Reference Data* 1996, 25, 1297.
- [181] Burrows, J. P. Email correspondence. In *Journal of Photochemistry and Photobiology, A: Chemistry*; Institute of Environmental Physics at University of Bremen, 2008; Vol. 176.
- [182] Donovan, R. J.; Hathorn, F. G. M.; Husain, D. *Transactions of the Faraday Society* 1968, 64, 3192.
- [183] Owen, K. *Mod. Petrol. Technol., 4th Ed.* 1973, 573.
- [184] Liao, H.; Chen, W.-T.; Seinfeld, J. H. *Journal of Geophysical Research, [Atmospheres]* 2006, 111, D12304/1.
- [185] Ikeda, N.; Nakashima, N.; Yoshihara, K. *Journal of Physical Chemistry* 1984, 88, 5803.
- [186] Markert, F.; Pagsberg, P. *Chemical Physics Letters* 1993, 209, 445.
- [187] Porter, G.; Ward, B. *Journal de Chimie Physique et de Physico-Chimie Biologique* 1964, 61, 1517.
- [188] Kajii, Y.; Obi, K.; Nakashima, N.; Yoshihara, K. *Journal of Chemical Physics* 1987, 87, 5059.
- [189] Berho, F.; Lesclaux, R. *Chemical Physics Letters* 1997, 279, 289.
- [190] Ward, B. *Spectrochimica Acta, Part A: Molecular and Biomolecular Spectroscopy* 1968, 24, 813.
- [191] Yu, T.; Mebel, A. M.; Lin, M. C. *Journal of Physical Organic Chemistry* 1995, 8, 47.
- [192] Ebata, T.; Obi, K.; Tanaka, I. *Chemical Physics Letters* 1981, 77, 480.